Phenomenology of the Higgs and Flavour Physics In the Standard Model and Beyond

D I S S E R T A T I O N

zur Erlangung des akademischen Grades

doctor rerum naturalium
(Dr. rer. nat.)
im Fach Physik

eingereicht an der
Mathematisch-Wissenschaftlichen Fakultät
Humboldt-Universität zu Berlin

von
M.Sc. Lina Alasfar
geboren am 27. 09. 1994 in Riad

Präsidentin der Humboldt-Universität zu Berlin:
Prof. Dr.-Ing. Dr. Sabine Kunst

Dekan der Mathematisch-Wissenschaftlichen Fakultät:
Prof. Dr. Elmar Kulke

Gutachter:
1. Prof. Dr. R. Gröber, Humboldt-Universität zu Berlin
2. Prof. Dr. Dr. M. Musterman, Potsdam-Institut fur Klimafolgenforschung
3. Prof. Dr. M. Mustermann2, Heidelberg

Tag der mündlichen Prüfung: 06. November 2013

Contents

List of publications

1. **L. Alasfar**, G. Degrassi, P. P. Giardino, R. Gröber and M. Vitti
   Virtual corrections to $gg \to ZH$ via a transverse momentum expansion
   JHEP **05** (2021), 168
   arXiv:2103.06225 [hep-ph].

2. **L. Alasfar**, A. Azatov, J. de Blas, A. Paul and M. Valli
   B anomalies under the lens of electroweak precision
   JHEP **12** (2020), 016
   arXiv:2007.04400 [hep-ph].

3. **L. Alasfar**, R. Corral Lopez and R. Gröber
   Probing Higgs couplings to light quarks via Higgs pair production
   JHEP **11** (2019), 088
   arXiv:1909.05279 [hep-ph].

Part I

Higgs Physics

1 The Standard Model Higgs boson

> It's very nice to be right sometimes...
> it has certainly been a long wait.
>
> *Peter Higgs*

1.1 Spontaneous symmetry breaking

Before talking about symmetry breaking, we need to discuss the concept of symmetry in physics. Symmetry has an essential role in studying physical systems. It manifests not only as a geometric feature of physical objects but also in the dynamics of physical systems. For example, one can find symmetries in the equation of motion, Lagrangians/Hamiltonians and actions. The magnetisation of materials is a good example of the role that symmetry plays in describing physical behaviour. For instance, **paramagnetic** materials have a positive magnetic susceptibility χ_B due to the random arrangement of their electrons' spins. The paramagnetic material spins arrangement will therefore possess rotational symmetry. The material has no *preferred direction* in space [1]. On the contrary, **ferromagnetic** materials with the electrons' spins aligned in a certain direction, will not have such symmetry as there will be a preferred direction, see Figure 1.1.

In particle physics and quantum field theory, symmetry plays an essential role in the taxonomy and dynamics of elementary particles and their bound states, i.e. hadrons, cf. [2, 3]. There are two types of symmetries considered when studying elementary particles and their quantum fields: external and internal symmetries. The first is the symmetry of the spacetime background. Typically, this is a four-dimensional Poincaré symmetry. However, in some models, higher spacetime dimensions or non-flat geometries are considered. Though there is no current evidence of higher dimensions or indications of non-flat spacetime from colliders and cosmological observations [4]. The second class of symmetries is internal symmetries stemming from the quantum nature of these particles/fields. Because their state is described by a **ray** in complex Hilbert/Fock spaces, internal symmetries are simply symmetries of rotations in these spaces that keep the action variation unchanged. Internal symmetries are usually described in terms of simple or product of simple **Lie groups**, e.g. $SU(N)$ [1], and particles/fields will be arranged

[1] Gauge theories based on finite groups have been investigated in the literature, but their phenomeno-

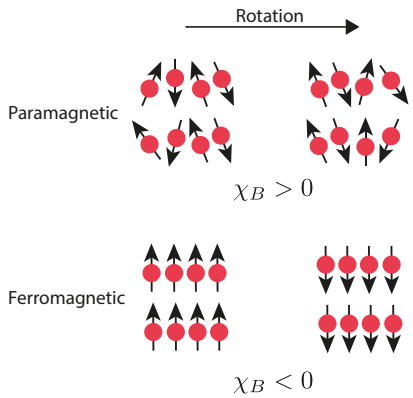

Figure 1.1. In paramagnetic materials, the spins are randomly distributed such that a rotation performed on the system will keep the spin distribution invariant. However, for ferromagnetic materials, where the spins are aligned in a single direction, the symmetry is broken, and the system has a preferred direction.

as multiplets in some representation of the groups. The rotations of the states could be parametrised by constants. In this case, the symmetry is called **global**, or fields of spacetime, where the symmetry is then called **local** or **gauged**.

Gauge symmetries describe rotations in the state space that depend on spacetime, the generator of the gauge transformations could propagate between two spacetime points. This is the way particle/field interactions are described in quantum field theory. The generators of these gauge transformations are called gauge bosons, and they mediate the interactions between the particles/fields and transform under the adjoint representation of the gauge group. Hence, we observe that gauge symmetries are the basis of describing the fundamental interactions of nature, which we call **gauge theories**.

An example of a gauge theory that is realised in nature is the **Standard Model** (SM). Which is a gauge theory based on the group $G_{\text{SM}} := SU(3)_C \otimes SU(2)_L \otimes U(1)_Y$. The first simple group is for the *strong* interaction described by quantum chromodynamics (QCD). The product of the two remaining groups $SU(2)_L \otimes U(1)_Y$ forms the Weinberg-Salam *electroweak* (EW) model [7–9], where $SU(2)_L$ describes the weak interaction which only couples to *left handed* fermions and $U(1)_Y$ is the weak hypercharge Y gauge group, defined by the formula

$$Y = 2(Q - T_3). \tag{1.1}$$

Where Q is the electric charge and T_3 is the third component of the weak isospin. A description of the matter content of the SM and their multiplicities with respect to G_{SM} is shown in Table 1.1

The SM has been very successful at describing particle interactions even when chal-

logical significance is yet to be further investigated [5, 6]

Particle/Field	G_{SM} multiplicity	mass [GeV]
	Quarks	
$Q = \binom{u_L}{d_L}, \binom{c_L}{s_L}, \binom{t_L}{b_L}$	$(\mathbf{3}, \mathbf{2}, 1/6)$	$m_u = 2.16 \cdot 10^{-3}$, $m_d = 2.67 \cdot 10^{-3}$
$U = u_R, c_R, t_R$	$(\mathbf{3}, \mathbf{1}, 2/3)$	$m_c = 0.93 \cdot 10^{-2}$, $m_s = 1.27$
$D = d_R, s_R, b_R$	$(\mathbf{3}, \mathbf{1}, -1/3)$	$m_t = 172.4$, $m_b = 4.18$
	Leptons	
$L = \binom{\nu_{e,L}}{e_L}, \binom{\nu_{\mu,L}}{\mu_L}, \binom{\nu_{\tau,L}}{\tau_L}$	$(\mathbf{1}, \mathbf{2}, -1/2)$	$m_e = 0.511 \cdot 10^{-3}$, $m_\mu = 1.05 \cdot 10^{-2}$
$E = e_R, \mu_R, \tau_R$	$(\mathbf{1}, \mathbf{1}, -1)$	$m_\tau = 1.77$,m_ν =??
	Gauge bosons	
$g/G^A_\mu, \;\; A = 1 \dots 8$	$(\mathbf{8}, \mathbf{1}, 0)$	0.0
γ/A_μ	$(\mathbf{1}, \mathbf{1}, 0)$	0.0
$W^\pm_\mu$	$(\mathbf{1}, \mathbf{3}, 0)$	80.379
Z_μ	$(\mathbf{1}, \mathbf{3}, 0)$	91.1876
	The Higgs boson	
h	$(\mathbf{1}, \mathbf{2}, 1/2)$	125.10

Table 1.1. The SM constituents, their multiplicities with respect to the SM gauge group $G_{\text{SM}} := SU(3)_C \otimes SU(2)_L \otimes U(1)_Y$ and masses. The mass of the neutrinos ν is zero according to the SM prediction, but observations suggest that they are massive, and only the difference between the three masses is known [10]. The values of the masses are taken from the Particle Data Group (PDG) [4], and used throughout this thesis.

lenged by numerous precision tests at LEP and SLD [11–14] and later at DØ [15] and the LHC [16, 17] Nevertheless, it fails to describe the ground state if only the fermion and gauge sectors are considered. The reason for this shortcoming is that the $W^{\pm}$ and Z bosons have a mass, this violates the EW gauge symmetry. This can be easily seen by looking at the mass term of a spin 1 field B_{μ}^{A}

$$\mathcal{L} = m_B B^{A,\mu} B_{\mu}^{A}, \tag{1.2}$$

and performing an $SU(N)$ gauge transformation

$$B_{\mu}^{A} \to B_{\mu}^{A} + \partial_{\mu}\Lambda^{A} + g\,\varepsilon_{BC}^{A} B_{\mu}^{B}\Lambda^{C}. \tag{1.3}$$

We see that the mass term is invariant under these transformations. Secondly, because the SM is a chiral theory, as only left-handed fermions would be doublets under $SU(2)_L$, the Dirac mass term

$$\mathcal{L}_{\mathrm{D}} = m_D \overline{\psi}_L \psi_R + \mathrm{h.c.}, \tag{1.4}$$

cannot be a singlet under $SU(2)_L$, hence also violating the EW symmetry. Despite quark and lepton masses being forbidden by the EW symmetry, we indeed observe that they do have a mass, and since they also carry charges this mass has to be a Dirac mass.

In order for the EW model to be consistent at the ground state like it is in the interaction states. A mechanism for spontaneous symmetry breaking going from an interaction state to the vacuum ought to be introduced.

1.1.1 Nambu-Goldstone theorem

Coming back to the example of the paramagnetic-ferromagnetic materials, when heated above a certain temperature, known as the **Curie Temperature** T_C will undergo a phase transition and become paramagnetic (losing their permanent magnet property), in the mean-field theory approximation the magnetic susceptibility is related to the temperature of the metal via the relation

$$\chi_B \sim (T - T_C)^{-\gamma}, \tag{1.5}$$

where γ is a critical exponent. We see that if the metal temperature $T > T_C$ the metal is in an *disordered phase* and when $T < T_C$ it is in the *ordered phase*,i.e. χ_B is the **order parameter** of this system. At the Curie temperature, the system will be at the *critical point* where the susceptibility is divergent. The exponent γ is not used to describe the system at the critical point. There is a "pictorial" description of the metal at the critical point which is helpful in picturing the Goldstone theorem. Starting at $T > T_C$, the metal would be in a paramagnetic phase, where the spins are randomly arranged. As the temperature becomes lower and lower, thermal fluctuations start to lessen. One or

more regions of the metal, some of the spins will start to get aligned With continued cooling, nearing T_C, these turned spins will affect their neighbours turning them into their directions. At the critical point $T = T_C$, the system behaves in a peculiar manner, when one would see regions of spins in "up" and others in "down" directions. The system will resemble a fractal of these regions, becoming scale-invariant. Additionally, waves of oscillating local magnetisation will propagate. These waves, or spinless quasiparticles (called **Magnons**) are Goldstone bosons emerging from spontaneous symmetry breaking. Which will manifest at $T < T_C$ as the spins will be arranged in a certain single direction and the metal becomes ferromagnetic.

Theorem 1 (Nambu-Goldstone)**.** When a continuous symmetry has a conserved currents but broken in the ground state (vacuum) is called to be spontaneously broken. There is a scalar boson associated with each broken generator of this spontaneously broken symmetry. The modes of these bosons are fluctuations of the order parameter.

This theorem first emerged from condensed matter physics, particularly superconductors [18, 19]. However, it soon got applied to relativistic quantum field theories [20].

1.2 The Higgs mechanism

In order to solve the aforementioned shortcomings of the Weinberg-Salam model, Nambu-Goldstone theorem has been first proposed by P. W. Anderson [21]. However, the way that Anderson formulated his theory was unfamiliar to particle physicists and used a non-relativistic picture to illustrate how photons could gain mass in an electron plasma with a plasma frequency ω_p

$$m_\gamma^{\text{plasma}} = \frac{\hbar\omega_p}{c^2} \tag{1.6}$$

Later on, a theory that explains the mass generation of the EW gauge bosons has been published in an almost simultaneous manner by R. Braut and F. Englert [22], P. Higgs [23] and G. Guralnik, C. R. Hagen, and T. Kibble [24, 25][2]. The Higgs mechanism starts by considering the spontaneous symmetry breaking (SSB) of the EW sector of the SM via the pattern

$$SU(2)_L \otimes U(1)_Y \longrightarrow U(1)_Q \tag{1.7}$$

This is achieved by the vacuum expectation value (vev) of a complex scalar field $\phi \sim (\mathbf{1}, \mathbf{2}, +1/2)$, with the Lagrangian

$$\mathcal{L} = D_\mu\phi^* D^\mu\phi - V, \qquad V := \mu^2\phi^*\phi + \lambda(\phi^*\phi)^2, \tag{1.8}$$

[2] All of these authors have contributed to the theory of SM spontaneous symmetry breaking (SSB). By calling it the "Higgs" mechanism or boson. I, by no means, have intended to ignore the role played by the rest, rather, I wanted to stick the most widely-used terminology in the field.

were ϕ is given explicitly by

$$\phi = \begin{pmatrix} \phi^1 + i\phi^2 \\ \frac{1}{\sqrt{2}}(h+v) - i\phi^3 \end{pmatrix} \tag{1.9}$$

The covariant derivative

$$D_\mu = \partial_\mu - ig_2\frac{\sigma_a}{2}W_\mu^a - ig_1\frac{1}{2}B_\mu, \tag{1.10}$$

dictates the coupling between the Higgs field and the EW gauge bosons and g_3, g_2 and g_1 are, respectively, the coupling constants of $SU(3)_C$, $SU(2)_L$ and $U(1)_Y$. The minimum of the scalar potential is then obtained by

$$\frac{\partial V}{\partial \phi} \mid_{\phi \to v} = 0, \tag{1.11}$$

which for a tachyonic mass $\mu^2 < 0$ will have a real non-vanishing values v corresponding to the vev of this field $\langle\phi\rangle = (\frac{0}{\frac{v}{\sqrt{2}}})$.

According to Nambu-Goldstone theorem, the three broken generators of $SU(2)_L \otimes U(1)_Y$ will become massive, and they are the $W^\pm$ and Z bosons, while the photon will remain massless. We will have three massless Goldstone bosons $G^\pm = \frac{1}{2}(\phi^1 \pm i\phi^2)$ and $G^0 = \phi^3$ that are "eaten" by the aforementioned massive photons. Where they become the longitudinal polarisations of $W^\pm$ and Z boson. In order to see this more concretely, we start by looking at the terms of the EW Lagrangian where the field ϕ couples to the gauge bosons, in the unbroken phase

$$D_\mu\phi^* D^\mu\phi = \frac{1}{2}|\partial_\mu\phi|^2 + \frac{1}{8}g_2^2|\phi|^2|W_\mu^1 + iW_\mu^2|^2 + \frac{1}{8}|\phi|^2|g_2W_\mu^3 - g_1B_\mu|^2 \tag{1.12}$$

After SSB, we write the gauge bosons in the mass basis

$$\begin{aligned} W_\mu^\pm &= \frac{1}{\sqrt{2}}(W_\mu^1 \pm iW_\mu^2), \\ Z_\mu &= \frac{1}{\sqrt{g_1^2+g_2^2}}\left(g_2W_\mu^3 - g_1B_\mu\right), \\ A_\mu &= \frac{1}{\sqrt{g_1^2+g_2^2}}\left(g_2W_\mu^3 + g_1B_\mu\right). \end{aligned} \tag{1.13}$$

From this, the electric change is identified as the coupling constant to the photon A_μ

$$e = \frac{g_1}{\sqrt{g_1^2+g_2^2}}. \tag{1.14}$$

It is useful to define **Weinberg angle** θ_W, an important EW parameter relating the electric charge to the weak coupling g_2

$$\sin\theta_W = \frac{e}{g_2} \approx 0.231214, \tag{1.15}$$

typically the sin and cos of the Weinberg angle are denoted by s_W and c_W, respectively. We use the unitary gauge, to absorb the Goldstone bosons into the $W^\pm$ and Z longitudinal polarisations. In this gauge the Higgs doublet can be written as

$$\phi \to \begin{pmatrix} 0 \\ \frac{1}{\sqrt{2}}(h+v). \end{pmatrix}, \qquad v = 246\,\text{GeV}. \tag{1.16}$$

With these substitutions, one can read off the masses of the gauge bosons their bilinear terms in (1.12)

$$m_W = \frac{vg_2}{2} \qquad m_Z = \frac{v}{2}\sqrt{g_1^2+g_2^2} \qquad m_A = 0. \tag{1.17}$$

Since ϕ is a complex doublet. We have seen that it has four components, and three of them correspond to the Goldstone bosons, thus one remains physical h which is what we now identify with the "Higgs boson" discovered in the Summer of 2012 [26, 27]. The couplings between the Higgs and the electroweak bosons is related to their mass via the vev

$$g_{hVV} = \frac{2m_V^2}{v}, \qquad g_{hhVV} = \frac{2m_V^2}{v^2}. \tag{1.18}$$

By substituting (1.16), into the Higgs potential (1.8) one can write the mass of the physical Higgs boson in terms of the vev

$$m_h = \sqrt{2\lambda}v. \tag{1.19}$$

The physical Higgs mass is related to the μ parameter via the relation

$$m_h^2 = -2\mu^2, \tag{1.20}$$

One can see that the mass term after SSB changes its sign, characterising the order-parameter for this system, analogous to the magnetic susceptibility for the magnetisation of materials example. One could also identify the self-couplings of h, the trilinear and quartic couplings

$$g_{hhh} = 3\lambda v = 3\frac{m_h^2}{v}, \qquad g_{hhhh} = 3\lambda = 3\frac{m_h^2}{v^2}. \tag{1.21}$$

1.3 Yukawa interaction

It is possible to also use the Higgs vev to give fermions their masses by introducing a Yukawa-interaction terms, first introduced by S. Weinberg [9]

$$\mathcal{L}_{\text{Yuk}} = -y_e\,\overline{L}\,\phi\,E - y_d\,\overline{Q}\,\phi\,D - y_u\,\overline{Q}\,\tilde{\phi}\,U \;\; + \text{h.c.}, \tag{1.22}$$

with $\tilde{\phi} = i\sigma_2\phi$ and y_e, y_d, y_u are 3×3 matrices. These matrices are free parameters in the SM. As the Higgs boson acquires a the vev, the fermions will acquire a mass $m_f = vy'_f$ and the Higgs boson coupling to the fermions is given by

$$g_{h\overline{f}f} = \frac{m_f}{v}, \tag{1.23}$$

and the Yukawa matrices will be fixed in the mass basis y'_f by measurements of the fermion masses.
Leptonic Yukawa matrix is diagonal, with a degeneracy between the flavour and masses basis, this manifests as lepton family number conservation (the lepton family operator commutes with the Hamiltonian.). However, for the quarks, the situation is more complicated. One can rotate these matrices to the mass basis via a bi-unitary transformation via the unitary matrices $\mathcal{V}_Q, \mathcal{U}_Q$ for $q = u, d$

$$y_q \longrightarrow y'_f = \mathcal{V}_q^\dagger\, y_q\, \mathcal{U}_q = \text{diag}\,(m_{q_1}, m_{q_2}, m_{q_3})\,. \tag{1.24}$$

However, the is no degeneracy here as the Hamiltonian does not commute with the quark flavour operator. This is because the transformation matrices for the up and down-type quarks are not the same. The charged EW quark currents contains flavour mixing described by the Kabibbo-Kobayashi-Maskawa (CKM) matrix [28, 29]. More details on the flavour sector of the SM is discussed in Update the section
Figure 1.2 shows all the SM couplings' strengths, with the thickness of the chord is proportional to the strength of the coupling, on can see the Higgs couplings in orange.

1.4 The Higgs and EW precision observables

Higgs physics is intertwined with the EW sector for example, the Higgs vev is determined from Fermi's constant $v = (\sqrt{2}G_F)^{-1/2}$, and is fixed by muon lifetime measurements, and comparing it with the theoretical predictions [30–33]

$$\tau_\mu^{-1} = \frac{G_F^2 m_\mu^5}{192\pi^3}\left(1 - \frac{8m_e^2}{m_\mu}\right)\left[1 - 1.810\frac{\alpha}{\pi} + (6.701 \pm 0.002)\left(\frac{\alpha}{\pi}\right)^2\right], \tag{1.25}$$

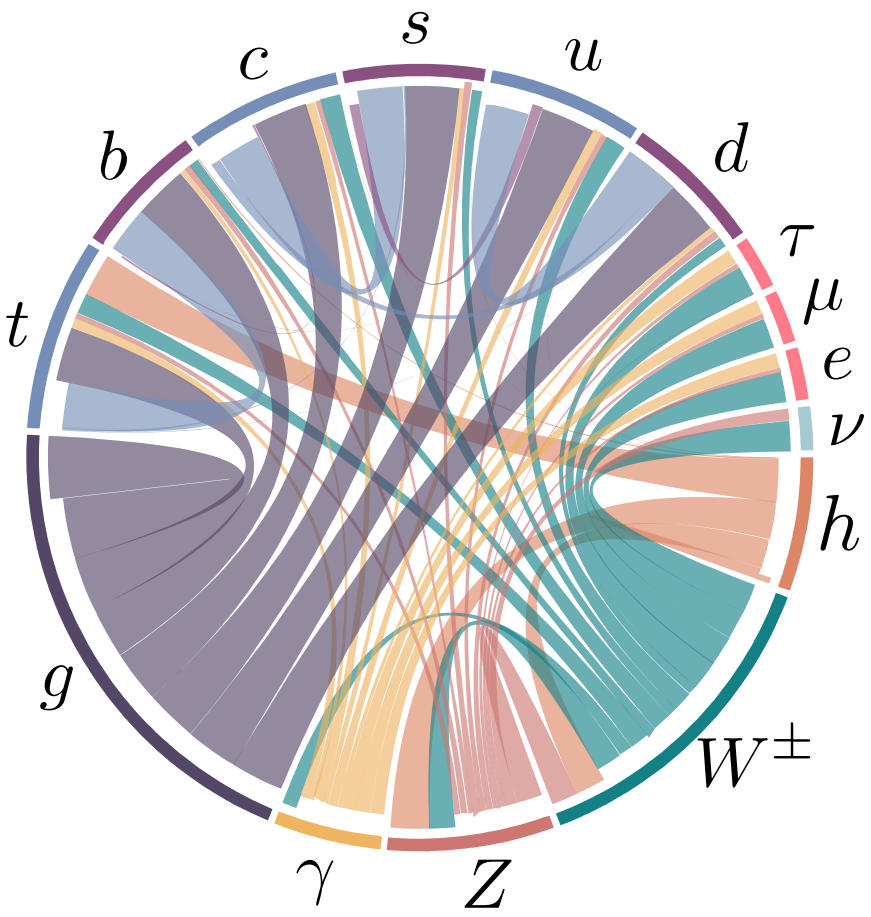

Figure 1.2. A chord diagram showing the SM couplings, with the coupling strength illustrated by the chord thickness. Higgs couplings are coloured in orange.

which leads to the numerical value of G_F [4]

$$G_F = 1.1663787(6) \cdot 10^{-5}\text{GeV}^{-2}, \tag{1.26}$$

given the value of the fine structure constant $\alpha^{-1} = 137.03599976(50)$.

Another important EW precision observable (EWPO) is the ratio between the W and Z masses

$$\rho = \frac{m_W^2}{c_W^2 m_Z^2}. \tag{1.27}$$

At leading order, this parameter is equal to unity in the SM. The ρ parameter depends on the representation of the scalar sector of the EW model having ϕ_i scalars with T_i weak isospin and $T_{3,i}$ being its third component, and a vev v_i, via the relation [34, 35]

$$\rho = \frac{\sum_i [T_i(T_i+1) - T_{3,i}^2] v_i^2}{2\sum_i T_{3,i}^2 v_i^2}. \tag{1.28}$$

From (1.28) one can see that a real triplet scalar, for instance, would not fit the experimental EW measurement of ρ. Hence, a complex doublet is the simplest scalar possible for the EW symmetry breaking, and the Higgs boson was expected to be seen almost four decades before its discovery. However, radiative corrections to the EW gauge bosons mass from vacuum polarisation diagrams could potentially cause ρ to deviate significantly from unity. This is not the case, as the experimentally measured value of ρ [4]

$$\rho_{\text{exp}} = 1.00038 \pm 0.00020 \tag{1.29}$$

Additionally, it is possible to think of an extended Higgs sector, where there are multiple scalars with different $SU(2)_L$ multiplicities. Or, a composite Higgs sector, where the Higgs boson is a pseudo Nambu-Goldstone boson, cf. [36, 37]. How can such models be built assuring the ρ parameter is protected from change ? The answer to this question lies in a symmetry of the Higgs Lagrangian known as custodial symmetry.

1.4.1 Custodial symmetry

After SSB, a residual global symmetry known as the custodial symmetry protects the ρ parameter from obtaining large radiative corrections at higher orders in perturbation theory. This symmetry must be kept in extended or composite Higgs models. This symmetry can be seen by rewriting the Higgs potential as

$$V = \frac{\lambda}{4}\left(\phi_1^2 + \phi_2^2 + \phi_3^2 + \phi_4^2 - 2\mu^2\right)^2. \tag{1.30}$$

This potential is invariant under $SO(4) \simeq SU(2)_L \otimes SU(2)_R$ rotations. However, when the Higgs field squires a non-vanishing vev, $\phi_4 \to h + v$, the potential becomes

$$V = \frac{\lambda}{4}\left(\phi_1^2 + \phi_2^2 + \phi_3^2 + h^2 + 2vh + v^2 - 2\mu^2\right)^2, \tag{1.31}$$

which is only invariant under $SO(3) \simeq SU(2)_V$ transformations, the diagonal part of the original group. This global SSB pattern comes alongside the EW SSB of the gauge group $SU(2)_L \otimes U(1)_Y$ as global $SU(2)_L$ is itself the gauged $SU(2)_L$ group. Additionally the T^3 component of the $SU(2)_R$ global group is the gauged $U(1)_Y$ and the T^3 component of the custodial group $SU(2)_V$ is gauged as well and identified to be the electric charge operator, i.e. the generator of $U(1)_Q$.

$$\underbrace{SU(2)_R}_{\supset U(1)_Y} \otimes \overbrace{SU(2)_L}^{\text{gauged}} \longrightarrow \underbrace{SU(2)_V}_{\supset U(1)_Q}. \tag{1.32}$$

This pattern indicates that the symmetry is already broken by the gauging of the diagonal part of $SU(2)_R$ (the hypercharge). The custodial symmetry is only *approximate* in the limit of $g_1 \to 0$, and $\rho = 1$ is a consequence of $g_1 \neq 0$. The symmetry breaking pattern $\mathbf{2} \otimes \mathbf{2} = \mathbf{3} \oplus \mathbf{1}$ also allows us to identify the Goldstone bosons as the custodial triplet and the physical Higgs h as the custodial singlet, explaining the electric charge pattern they have.
We could use the isomorphism between the special orthogonal and special unitary groups to parametrise the Higgs doublet as an $SU(2)_L \otimes SU(2)_R$ bidoublet

$$\mathcal{H} = (\tilde{\phi} \;\; \phi) = \frac{1}{\sqrt{2}}\begin{pmatrix} \phi_4 - i\phi_3 & \phi_1 + i\phi_2 \\ \phi_1 - i\phi_2 & \phi_4 + i\phi_3 \end{pmatrix}, \tag{1.33}$$

with the bi-unitary transformations

$$\mathcal{H} \longrightarrow \mathcal{U}_L \mathcal{H} \mathcal{U}_R^\dagger \tag{1.34}$$

which leaves any traces of the form $\mathrm{Tr}(\mathcal{H}^\dagger \mathcal{H})$, invariant. The Higgs potential could be rewritten in terms of the bidoublet

$$V = -\frac{\mu^2}{2}\mathrm{Tr}(\mathcal{H}^\dagger \mathcal{H} + \frac{\lambda}{4}\left(\mathrm{Tr}(\mathcal{H}^\dagger \mathcal{H}\right)^2 \tag{1.35}$$

The vev is hence written in this representation as

$$\langle \mathcal{H} \rangle = \frac{v}{\sqrt{2}}\, \mathbb{1}_{2\times 2}. \tag{1.36}$$

We can also look at the Yukawa sector, and observe that in the case where $y_u = y_d = y$, we can also write the left-handed and right-handed quarks as $SU(2)_L \otimes SU(2)_R$ bidoublets and $SU(2)_R$ doublets, respectively. Hence, the quark part of the Yukawa Lagrangian in (1.22) becomes

$$\mathcal{L}_{yuk} \supset \frac{y}{\sqrt{2}}(\overline{u}_L \;\; \overline{d}_L) \begin{pmatrix} \phi_4 - i\phi_3 & \phi_1 + i\phi_2 \\ \phi_1 - i\phi_2 & \phi_4 + i\phi_3 \end{pmatrix} \begin{pmatrix} u_R \\ d_R \end{pmatrix}, \tag{1.37}$$

which is invariant under custodial transformations, but when $y_u \neq y_d$, this Lagrangian term breaks custodial symmetry. Thus, the differences between the up-type and down-type quark masses $m_u - m_d$ are considered **spurions** of the custodial symmetry and one expects to see radiative corrections to ρ being proportional to these spurions.

In order to see this more concretely, we start by examining the radiative corrections that could contribute to the deviation of ρ from unity, i.e. $\Delta\rho$ these corrections are known as the **oblique correction**. These oblique corrections come from electroweak vacuum polarisations $\Pi_{VV}(p^2)$, as shown in Figure 1.3, for more details on these corrections and their calculation see Refs.. [38, 39]

The 1-loop correction to the ρ parameter is given in terms of the Π_{VV} by

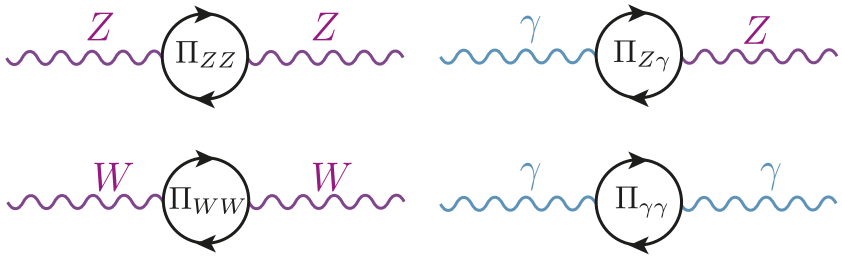

Figure 1.3. The oblique corrections, are radiative correction with electroweak gauge bosons propagators. Namely vacuum polarisations of the Z, $W^{\pm}$ and γ bosons.

$$\Delta\rho = \frac{\Pi_{WW}(0)}{m_W^2} - \frac{\Pi_{ZZ}(0)}{m_Z^2} \tag{1.38}$$

Where the dominant contributions are given by [40]

$$\Delta\rho = \frac{3G_F}{8\sqrt{2}\pi^2}\left((m_t^2 + m_b^2) - \frac{2m_t^2 m_b^2}{m_t^2 - m_b^2}\ln\frac{m_t^2}{m_b^2}\right) + \dots. \tag{1.39}$$

Since $m_b \ll m_t$, the correction is non-vanishing, and (1.39) shows clearly how the radiative corrections are proportional to the spurions of the custodial symmetry. However, this radiative correction is absorbed into the SM definition of ρ, i.e. the $\overline{\text{MS}}$ definition of the ρ-parameter $\rho^{\overline{\text{MS}}}$.

One can study new physics (NP) effects that violates custodial symmetry, by looking at deviations from $\rho = 1$ from it. Given the experimentally measured value of ρ (1.29) many NP models violating custodial symmetry can already be excluded. Nevertheless, ρ alone does not capture the full story of EWPO's. For instance, adding a new quark doublet would not necessarily violate the custodial symmetry though it still can be excluded by EWPO. It is hence useful to introduce new parameters known as **Peskin-Takeuchi parameters** [39, 41, 42]

$$\begin{aligned} S &:= \frac{4c_W^2 s_W^2}{\alpha}\left[\frac{\Pi_{ZZ}^{\rm NP}(m_Z^2)-\Pi_{ZZ}^{\rm NP}(0)}{m_Z^2} - \frac{c_W^2-s_W^2}{c_W s_W}\frac{\Pi_{Z\gamma}^{\rm NP}(m_Z^2)}{m_Z^2} - \frac{\Pi_{\gamma\gamma}^{\rm NP}(m_Z^2)}{m_Z^2}\right], \\ T &:= \frac{\rho^{\overline{\rm MS}}-1}{\alpha} = \frac{1}{\alpha}\left[\frac{\Pi_{WW}^{\rm NP}(0)}{m_W^2} - \frac{\Pi_{ZZ}^{\rm NP}(0)}{m_Z^2}\right], \\ U &:= \frac{4s_W^2}{\alpha}\left[\frac{\Pi_{WW}^{\rm NP}(m_W^2)-\Pi_{WW}^{\rm NP}(0)}{m_W^2} - \frac{c_W}{s_W}\frac{\Pi_{Z\gamma}^{\rm NP}(m_Z^2)}{m_Z^2} - \frac{\Pi_{\gamma\gamma}^{\rm NP}(m_Z^2)}{m_Z^2}\right] - S. \end{aligned} \tag{1.40}$$

The NP contributions to the EW vacuum polarisations $\Pi_{VV}^{\rm NP}(p^2)$) could either come from loop or tree-level effects. Typically both T and U are related to custodial symmetry violation. However, U has an extra suppression factor of $m_{\rm NP}^2/m_Z^2$ compared to T and S. The most recent fit result for these parameters is [4]

$$\begin{aligned} S &= -0.01 \pm 0.10, \\ T &= 0.03 \pm 0.13, \\ U &:= 0.02 \pm 0.11. \end{aligned} \tag{1.41}$$

But since T and S tend to give stronger constraint on NP, due to the suppression factor of U. One can preform a two-parameter fit of S and T setting $U = 0$, thas shown in Figure 1.4, with the numerical values [4],

$$\begin{aligned} S &= 0.00 \pm 0.07, \\ T &= 0.05 \pm 0.06. \end{aligned} \tag{1.42}$$

The Peskin-Takeuchi parameters are important in constraining effective operators in the Higgs sector , namely

$$\begin{aligned} \hat{O}_S &= \phi^\dagger \sigma_i \phi W^i_{\mu\nu} B^{\mu\nu}, \\ \hat{O}_T &= |\phi^\dagger D_\mu \phi|^2. \end{aligned} \tag{1.43}$$

For example, $\hat{O}_S$ appears in Technicolour models causing large deviations of S compared

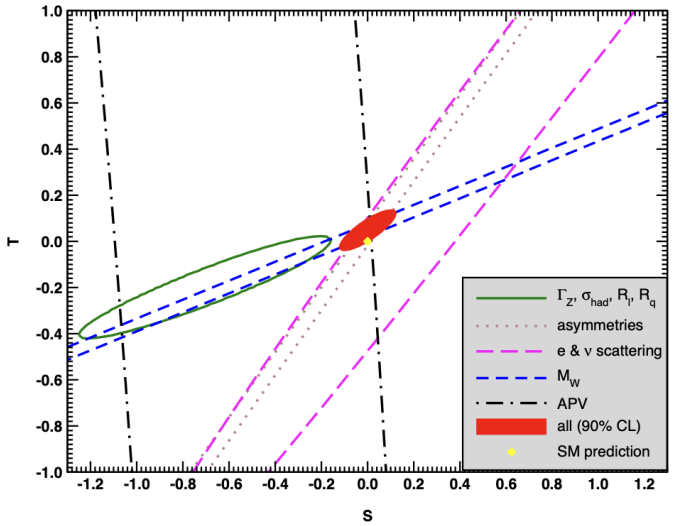

Figure 1.4. Fit results from various EWPO's for T and S setting $U =$. The contours show $1\,\sigma$ contours (39.35% for closed contours and 68% for the rest). This plot is obtained from the PDG [4]

to its measured value [41, 43–45]. Moreover, The constraints on T parameter is important for top mass generation ans well as modifications to $Zb\bar{b}$ coupling in such models [46, 47]. We will revisit the $\hat{O}_T$ when we discuss the Higgs and effective field theories in section update here.

2 Constraints on the Higgs properties

In this chapter, the bounds on the Higgs sector will be discussed. Starting from an overview of the theoretical constraints on the Higgs potential, like the quantum triviality and unitarity. Then, the state-of-the-art experimental results on Higgs properties and couplings measurements will be discussed. However, despite many of the Higgs boson properties have been measured with good accuracy, there are still difficult observables in the Higgs sector and some open problems. These will be addressed at the end of this chapter.

2.1 Theoretical constraints

2.1.1 Partial-wave unitarity

Recall that in particle scattering process, the **S** matrix is defined via the relation

$$| \, out \, \rangle = \mathbf{S} | \, in \, \rangle \tag{2.1}$$

Since the S-matrix S describes the transition probability, it must satisfy the unitarity condition

$$\mathbf{S}^\dagger \mathbf{S} = \mathbf{S}\mathbf{S}^\dagger = \mathbb{1}, \tag{2.2}$$

in order to have probability / quantum numbers conservation.
Moreover, we can remove the identity operator **1** by defining the operator T such as

$$\mathbf{S} = \mathbb{1} + i\mathbf{T}. \tag{2.3}$$

For small coupling, **T** is small, enabling the use of perturbation theory. Now, we apply the unitarity condition to find a new relation for **T**

$$\begin{aligned} \mathbf{S}^\dagger \mathbf{S} = \mathbb{1} &= (\mathbf{1} - i\mathbf{T}^\dagger)(\mathbf{1} + i\mathbf{T}) \\ &\Rightarrow -i\mathbf{T}^\dagger + i\mathbf{T} + \mathbf{T}^\dagger\mathbf{T} = 0 \\ &\Rightarrow \mathbf{T}^\dagger\mathbf{T} = \underbrace{-i(\mathbf{T} - \mathbf{T}^\dagger)}_{=2\Im(\mathbf{T})}. \end{aligned} \tag{2.4}$$

With the matrix element given by

$$\langle\, a \,|\mathbf{T}|\, b \,\rangle = \mathcal{M}_{ab}(2\pi)^4\delta^4(p_a - p_b), \tag{2.5}$$

and using the completeness relations, we define the unity operator in terms of some states $|\, f \,\rangle$

$$\mathbb{1} = \sum_f \prod_i \int \frac{d^3p'}{(8\pi^3)\, 2E_i^f}(2\pi)^4 |\, f \,\rangle\langle\, f \,|. \tag{2.6}$$

Thus, the matrix element should satisfy

$$\sum_f \prod_i \int \frac{d^3p'}{(2\pi)^3\, 2E_i^f}(2\pi)^4\delta^4(p_i - \sum_i p_i^f)\mathcal{M}_{bf}\mathcal{M}^*_{af} = -i(\mathcal{M}_{ba} - \mathcal{M}^*_{ab}). \tag{2.7}$$

. Here, f denotes any set of intermediate states between $|\, a \,\rangle$ and $|\, b \,\rangle$. For the elastic scattering case, where $a = b$, we arrive at the **Optical Theorem** [1]

$$\sum_f \int d\Phi_n(p_a, p_i^f)|\mathcal{M}_{af}|^2 = 2\Im(\mathcal{M}_{aa}). \tag{2.8}$$

Where $d\Phi_n(p_a, p_i^f)$ is the n-particle phase space, for the $2 \to 2$ case, the equality is substituted by $\leq$.
From now one, we shall only consider the $2 \to 2$ case ($|\, p_1, p_2 \,\rangle \to |\, k_1, k_2 \,\rangle$) in which we could simplify the phase space further, rewriting the LHS of (2.8) as

$$\begin{aligned}&\int \frac{d^3k_1}{(2\pi)^3\, 2E_1}\int \frac{d^3k_2}{(2\pi)^3\, 2E_2}(2\pi)^4\delta^4(p_1 + p_2 - k_1 - k_2)\,|\mathcal{M}(s,t)|^2,\\ &= \frac{1}{16\pi}\int_{-1}^{1} d(\cos\theta)|\mathcal{M}(s,t)|^2.\end{aligned} \tag{2.9}$$

Recall that the relation between the Mandelstam variable t, and the scattering angle for the elastic scattering is given by

$$t = \frac{1}{2}(s - 4m^2)(\cos\theta - 1) \tag{2.10}$$

We could expand the matrix element $\mathcal{M}(s,t)$ in terms of *partial waves*, isolating s from scattering angle dependence

$$\mathcal{M}(s,t) = 16\pi\sum_j (2j+1)a_j P_j(\cos\theta). \tag{2.11}$$

Where a_j are called the jth partial wave amplitude, and $P_j(\cos\theta)$ are the Legendre

[1] Note that $\mathcal{M}_{af}$ is diagonalisable since T is normal as a result from the S-matrix unitarity.

polynomials

$$P_j(z) = \frac{1}{j!}\frac{1}{2^j}\frac{d^j}{dz^j}(z^2-1)^j \tag{2.12}$$

Which satisfies the orthonormality condition

$$\int_{-1}^{1} dz\, P_j(z)P_k(z) = \frac{1}{2j+1}\delta_{jk} \tag{2.13a}$$

$$P_j(1) = 1 \;\; \forall j. \tag{2.13b}$$

We hence get for the LHS of (2.8) scattering

$$\begin{aligned}
&\int \frac{d^3k_1}{(2\pi)^3\,2E_1}\int \frac{d^3k_2}{(2\pi)^3\,2E_2}(2\pi)^4\delta^4(p_1+p_2-k_1-k_2)\,|\mathcal{M}(s,t)|^2,\\
&= \frac{1}{16\pi}\int_{-1}^{1} d(\cos\theta)\left[16\pi\sum_j (2j+1)a_j(s)P_j(\cos\theta)\right]\times\\
&\quad\left[16\pi\sum_k (2k+1)a_k^*(s)P_k(\cos\theta)\right],\\
&\Rightarrow = 32\pi\sum_j (2j+1)|a_j(s)|^2.
\end{aligned} \tag{2.14}$$

And the RHS of (2.8)

$$2\mathfrak{I}(\mathcal{M}_{aa}) = \underbrace{2\mathfrak{I}(\mathcal{M}(s,0))}_{t \text{ is integrated out.}} = 32\pi\sum_j (2j+1)\mathfrak{I}(a_j(s)). \tag{2.15}$$

Otherwise large cancellations needed, $a_j(s)$'s are hierarchal. Thus, we could compare the partial wave amplitudes term-by-term

$$|a_j(s)|^2 \le \mathfrak{I}(a_j(s)) \quad \Rightarrow \mathfrak{R}(a_j(s))^2 + \mathfrak{I}(a_j(s))^2 \le \mathfrak{I}(a_j(s)) \tag{2.16}$$

Rearrainging terms, we get

$$\mathfrak{R}(a_j(s)) + \left(\mathfrak{I}(a_j(s)) - \frac{1}{2}\right)^2 \le \frac{1}{4} \tag{2.17}$$

The partial wave amplitude has to lie within the unitarity circle, see figure **??** . We use though perturbation theory if the the partial wave amplitude respects the inequality

$$\mathfrak{R}(a_j(s)) \le \frac{1}{2} \tag{2.18}$$

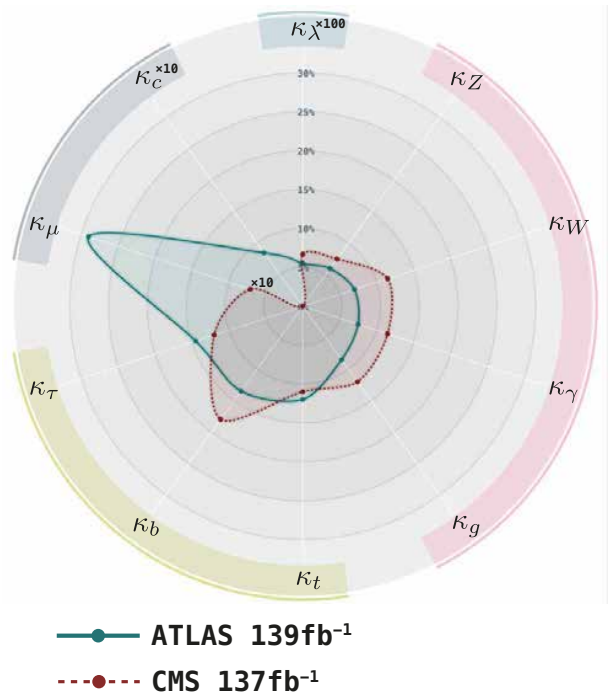

Figure 2.1. ff.

2.2 Experimental

We also provide in this appendix the experimental measurements of the signal strengths at the LHC Run II and the CMS projections for the HL-LHC (scenario S2, see [48]) that we used in the fits in this paper. These inputs are summarised in table 2.1.

Production	Decay	$\mu_{\rm Exp} \pm \delta\mu_{\rm Exp}$ (symmetrised) **LHC Run-II**	**HL-LHC**	Ref.
		CMS $137\,\text{fb}^{-1}$ ATLAS $139\,\text{fb}^{-1}$	CMS $3\,\text{ab}^{-1}$	
ggF	$h \to \gamma\gamma$	0.99 ± 0.12 1.030 ± 0.110	1.000 ± 0.042	[49–51]
	$h \to ZZ^*$	0.985 ± 0.115 0.945 ± 0.105	1.000 ± 0.040	[49, 51, 52]
	$h \to WW^*$	1.285 ± 0.195 1.085 ± 0.185	1.000 ± 0.037	
	$h \to \tau^+\tau^-$	0.385 ± 0.385 1.045 ± 0.575	1.000 ± 0.055	
	$h \to b\bar{b}$	2.54 ± 2.44 –	1.000 ± 0.247	[51, 52]
	$h \to \mu^+\mu^-$	0.315 ± 1.815 –	1.000 ± 0.138	[51, 52]
VBF	$h \to \gamma\gamma$	1.175 ± 0.335 1.325 ± 0.245	1.000 ± 0.128	[49–51]
	$h \to ZZ^*$	0.62 ± 0.41 1.295 ± 0.455	1.000 ± 0.134	[49, 51, 52]
	$h \to WW^*$	0.65 ± 0.63 0.61 ± 0.35	1.000 ± 0.073	
	$h \to \tau^+\tau^-$	1.055 ± 0.295 1.17 ± 0.55	1.000 ± 0.044	
	$h \to b\bar{b}$	– 3.055 ± 1.645	–	[49]
	$h \to \mu^+\mu^-$	3.325 ± 8.075 –	1.000 ± 0.540	[51]
$t\bar{t}h$	$h \to \gamma\gamma$	1.43 ± 0.30 0.915 ± 0.255	1.000 ± 0.094	[49–51]
	$h \to VV^*$	$0.64 \pm 0.64 (ZZ^*)$ 0.945 ± 0.465 (WW^*) 1.735 ± 0.545	1.000 ± 0.246 (ZZ^*) 1.000 ± 0.097 (WW^*) –	[49, 51, 52]
	$h \to \tau^+\tau^-$	0.845 ± 0.705 1.27 ± 1.0	1.000 ± 0.149	
	$h \to b\bar{b}$	1.145 ± 0.315 0.795 ± 0.595	1.000 ± 0.116	
Vh	$h \to \gamma\gamma$	0.725 ± 0.295 1.335 ± 0.315	1.000 ± 0.233 (Zh) 1.000 ± 0.139 $(W^\pm h)$	[49–51]
	$h \to ZZ^*$	1.21 ± 0.85 1.635 ± 1.025	1.000 ± 0.786 (Zh) 1.000 ± 0.478 $(W^\pm h)$	[49, 51, 52]
	$h \to WW^*$	1.850 ± 0.438 –	1.000 ± 0.184 (Zh) 1.000 ± 0.138 $(W^\pm h)$	[51, 53]
	$h \to b\bar{b}$	– 1.025 ± 0.175	1.000 ± 0.065 (Zh) 1.000 ± 0.094 $(W^\pm h)$	[49, 51]
Zh CMS	$h \to \tau^+\tau^-$ $h \to b\bar{b}$	1.645 ± 1.485 0.94 ± 0.32	–	[52]
$W^\pm h$ CMS	$h \to \tau^+\tau^-$ $h \to b\bar{b}$	3.08 ± 1.58 1.28 ± 0.41		

Table 2.1. The experimental single Higgs observables measurements from the LHC Run II and projections for the HL-LHC. In all cases we have symmetrised the experimental uncertainties that we use in the fits.

3 Higgs and effective field theories

If the new BSM degrees of freedom are much heavier than the electroweak scale, a general description of potential new physics effects can be formulated in the language of an effective field theory (EFT). One possibility of such a parameterization is the so-called Standard Model EFT (SMEFT), in which new physics effects are given in terms of higher-dimensional operators involving only SM fields and that also respect the SM gauge symmetries. The dominant effects on Higgs physics, electroweak physics and top quark physics stem from dimension-six operators, suppressed by the new physics scale Λ. This approach is justified in the limit in which energy scales $E \ll \Lambda$ are probed.

In the presence of a gap between the electroweak scale and the scale of new physics, Λ, the effect of new particles below the new physics scale can be described by an EFT. In the case of the SMEFT, the SM Lagrangian is extended by a tower of higher-dimensional operators, $\mathcal{O}_i$, built using the SM symmetries and fields (with the Higgs field belonging to an $SU(2)_L$ doublet), and whose interaction strength is controlled by Wilson coefficients, C_i, suppressed by the corresponding inverse power of Λ. In a theory where baryon and lepton number are preserved, the leading order (LO) new physics effects are described by the dimension-six SMEFT Lagrangian,

$$\mathcal{L}_{\text{SMEFT}}^{d=6} = \mathcal{L}_{\text{SM}} + \frac{1}{\Lambda^2} \sum_i C_i \mathcal{O}_i. \tag{3.1}$$

A complete basis of independent dimension-six operators was presented for the first time in [54], the so-called *Warsaw basis*.

Part II

Single Higgs Processes at the LHC

4 Overview of Higgs production at colliders

The precise determination of the Higgs boson properties is one of the main focus of the Large Hadron Collider (LHC) physics programme. Within the current experimental precision, the measurement of the Higgs couplings so far appear to be in agreement with the Standard Model (SM) prediction within an accuracy of, typically, ten percent [55, 56]. In many beyond the SM (BSM) scenarios, however, it is expected that new physics will introduce modifications in the Higgs properties.

The LO amplitude

We recall the projected LO on shell amplitude [57]

$$\mathcal{M}_{LO} = \frac{T_f \alpha_s g_{ht\bar{t}}}{2\sqrt{2}\pi} \mathcal{F}^{(1\ell)} S_\epsilon, \tag{4.1}$$

with the projector

$$\mathbb{P}^{\mu\nu} = g^{\mu\nu} - 2\frac{p_2^\mu p^\nu}{m_h^2}, \tag{4.2}$$

and the 1 loop form factor

$$\begin{aligned} \mathcal{F}^{(1\ell)} &= m_h \sqrt{\tau}\left((1-\tau)H(0,0,x)+2\right), \\ x &= \frac{\tau + 2\sqrt{1-\tau}-2}{\tau}, \end{aligned} \tag{4.3}$$

where $\tau = 4m_t^2/m_h^2$, $H(m,n,x)$ is the harmonic ploylogarithm function (HPL), and

$$S_\epsilon = \Gamma(1+\epsilon)(\mu/m_t)^{2\epsilon}. \tag{4.4}$$

The decay width is therefore given by

$$\Gamma_{LO}(h \to gg) = \frac{\alpha_s^2 G_F m_h^3 m_t^2 \tau}{8\pi^3\sqrt{2}} \left(3(\tau-1)^2 H(0,0,0,0,x) + 2(\tau-1)H(0,0,x) + 2\right) \tag{4.5}$$

With the following definitions

$$\begin{aligned} g_{ht\bar{t}} &= g_{ht\bar{t}}^{SM} = \frac{\sqrt{2}m_t}{v}, \\ v &= \left(G_F\sqrt{2}\right)^{-1/2}, \\ T_f &= \frac{1}{2}. \end{aligned} \tag{4.6}$$

5 Four top operator in Higgs production and decay

In the previous chapters, the SMEFT has been portrayed as a robust and practical parametrisation of NP degrees of freedom for LHC searches, keeping in mind that these degrees of freedom have masses that are higher than the LHC reach. We have seen in chapter 3 the SMEFT parametrisation for dimension-six operators involving the Higgs boson, and discussed some constraints on them. The operator $\mathcal{O}_\phi$ stands out as one of the weakly constrained SMEFT operators involving the Higgs, this is due to the current low experimental sensitivity on the Higgs self-coupling as shown in Figure 2.1. In order to probe the Higgs trilinear sel-coupling directly, one ought to observe Higgs pair production, see Part III. However, it has been proposed that bounds on the Higgs trilinear coupling could still be constructed from single Higgs data, and yield competitive constraints on this coupling than the current Higgs pair searches [58–65], this due the appearance of the Hggs self-coupling in the NLO EW corrections to single Higgs processes, as Figure 5.1 demonstrates an example of such corrections. Using the results

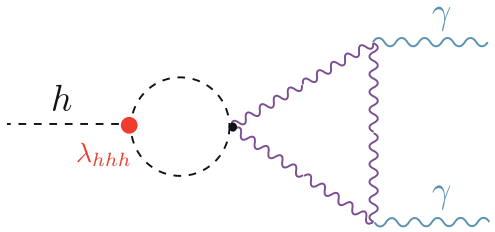

Figure 5.1. NLO EW corrections of single Higgs processes, were the Higgs trilinear self-coupling (the red circle) enters. Here the Higgs decay to two photons is shown as an example.

from the aforementioned references, a global fit with all operators that enter at tree-level in addition to the loop effects from the Higgs self-coupling has been preformed in ref. [66]. Additionally, experimental searches for Higgs trilinear self-coupling have been presented by ATLAS [67] and CMS [52].

The physics of the top quark and the Higgs are deeply intertwined, and when one starts looking at the operators entering at NLO of Higgs processes, and by restricting oneself to pure Higgs or EW operators, one would miss the full picture in a global fit. Namely, the top quark operators. Though many of the top quark operators are

strongly constraint from top observables, a few set of dimension-six operators remain as weakly constraint as the trilinear Higgs self-coupling or more. These operators are four-fermion operators involving the top quark. They would be constrained directly from the production of four tops observation. However, this process has a small cross-section at the LHC of 12 fb [68], which is more or less comparable to the Higgs pair production. Experimental searches for the production of four top quarks has been first made byCMS [69] combining different LHC runs, followed by ATLAS [70], the latter reporting a 4.3σ observation of this processes with cross-section of 24^{+7}_{-6} fb. When the whole third generation quarks is included, one sees the same story with $t\bar{t}b\bar{b}$ contact interaction which require the observation of $t\bar{t}b\bar{b}$ production for a direct constraint, see [71, 72] for experimental searches and [73, 74] for SMEFT fits. It should be noted that for the production of four tops, or two tops two beauty quarks in SMEFT, the contact terms do not interfere with the SM process, and only appear proportional to $\mathcal{O}(1/\Lambda^4)$. This makes the SMEFT global analysis of these operators depend highly on the EFT truncation scheme used, i.e. whether to keep quadratic terms or not.

These four-fermion operators enter in single Higgs processes at NLO, in a similar manner as the Higgs self-coupling. In this chapter, the exact NLO corrections to the Higgs rates, i.e. production and decay, due to these four-fermion operators have been competed, and it was found to be significantly larger or at the same scale as the corrections from C_ϕ. Since the four-fermions operators are weakly constrained they should be included in fits involving Higgs data. We shall demonstrate that, there is a significant correlation amongst the Higgs self-coupling and the four-fermion operators.

As the direct bounds for $t\bar{t}t\bar{t}$ and $t\bar{t}b\bar{b}$ contact interactions are weak, single Higgs data provides competitive bounds of there operators alongside other alternative constraints like top quark pair production [75] and electroweak precision data [76] .

The chapter is structured as follows: in section 5.1 the SMEFT four-fermion operators of the third generation are presented. In section 5.2 the full NLO calculation of Higgs rates due to the four-fermion operators is illustrated. Afterwards, in section 5.3, a fit from Higgs data combining the Higgs trilinear coupling and the four-fermion operators is presented, for both Run-II and HL-LHC, with more collaborate results for the latter is found in **??**. The results are further discussed in section 5.4.

5.1 Four-fermion operators in SMEFT

Before estimating the corrections of the four-fermion operators to Higgs rates, we start by introducing these operators in SMEFT . We are interested here in four-fermion operators of the third generation, that arise at dimension-six level. Using the same convention as the Higgs SMEFT operators in chapter 3, we recall the relearnt part of the SMEFT

Lagrangian [54],

$$\begin{aligned}\Delta\mathcal{L}^{d=6}_{\text{SMEFT}} = &\frac{C_{tt}}{\Lambda^2}(\bar{t}_R\gamma_\mu t_R)(\bar{t}_R\gamma^\mu t_R) + \frac{C^{(1)}_{Qt}}{\Lambda^2}(\overline{Q}_L\gamma_\mu Q_L)(\bar{t}_R\gamma^\mu t_R) + \frac{C^{(8)}_{Qt}}{\Lambda^2}(\overline{Q}_L T^A\gamma_\mu Q_L)(\bar{t}_R T^A\gamma^\mu t_R)\\ &+ \frac{C^{(1)}_{QQ}}{\Lambda^2}(\overline{Q}_L\gamma_\mu Q_L)(\overline{Q}_L\gamma^\mu Q_L) + \frac{C^{(3)}_{QQ}}{\Lambda^2}(\overline{Q}_L\sigma_a\gamma_\mu Q_L)(\overline{Q}_L\sigma_a\gamma^\mu Q_L) \qquad (5.1)\\ &+ \left[\frac{C^{(1)}_{QtQb}}{\Lambda^2}(\overline{Q}_L t_R)i\sigma_2(\overline{Q}^{\mathrm{T}}_L b_R) + \frac{C^{(8)}_{QtQb}}{\Lambda^2}(\overline{Q}_L T^A t_R)i\sigma_2(\overline{Q}^{\mathrm{T}}_L T^A b_R) + \text{h.c.}\right]\\ &+ \frac{C_{bb}}{\Lambda^2}(\bar{b}_R\gamma_\mu b_R)(\bar{b}_R\gamma^\mu b_R) + \frac{C^{(1)}_{tb}}{\Lambda^2}(\bar{t}_R\gamma_\mu t_R)(\bar{b}_R\gamma^\mu b_R) + \frac{C^{(8)}_{tb}}{\Lambda^2}(\bar{t}_R T^A\gamma_\mu t_R)(\bar{b}_R T^A\gamma^\mu b_R)\\ &+ \frac{C^{(1)}_{Qb}}{\Lambda^2}(\overline{Q}_L\gamma_\mu Q_L)(\bar{b}_R\gamma^\mu b_R) + \frac{C^{(8)}_{Qb}}{\Lambda^2}(\overline{Q}_L T^A\gamma_\mu Q_L)(\bar{b}_R T^A\gamma^\mu b_R)\,,\end{aligned}$$

here the notation is slightly modified from the standard Warsaw basis one. The flavour indices were suppressed since only the the third generation is considered throughout this chapter. Adopting the same notation from previous chapters, Q_L denotes the left-handed $SU(2)_L$ doublet quarks while t_R and b_R refer to the right-handed singlets, the rest of the objects in (5.1) follow the same conventions as in chapter 3 . In studies involving SMEFT fits, such as [77] the $SU(3)_C$ singlet and octet left-handed operators $C^{(1),SU(3)}_{QQ}$, $C^{(8)}_{QQ}$ are used instead of the singlet and triplet of $SU(2)_L$ appearing in eq. (5.1). These two conventions are related via the relations

$$\begin{aligned}C^{(1),SU(3)}_{QQ} &= 2C^{(1)}_{QQ} - \frac{2}{3}C^{(3)}_{QQ},\\ C^{(8)}_{QQ} &= 8C^{(3)}_{QQ}.\end{aligned} \qquad (5.2)$$

Additionally, all of these Wilson coefficients are assumed to be real.

From here on, only operators that induce sizeable NLO correction to Higgs processes are taken into account. These operators turns out to be the ones that introduce loop corrections to the top or beauty Yukawa, top or beauty masses and finite corrections from top loops. Such corrections will be proportional to the top mass. On the contrary, corrections from beauty loops are highly suppressed by m_b. Also, operators that have chiral structure that does not enable them to enter in the Yukawa renormalisation group equation (RGE)'s will not be constrained from Higgs data as they would only contribute through small finite terms, as we shall see later. Hence, only four top and the $\mathcal{O}^{(1),(8)}_{QtQb}$ operators will be considered, as they will possess corrections with top quark loops.

5.2 Contribution of four-fermion operators to Higgs production and decay

In this section, we discuss the contribution of the third generation four-fermion operators to various Higgs production mechanisms and Higgs decay channels.

5.2.1 Higgs coupling to gluons and photons

We start by discussing the calculation of the Higgs couplings to gluons and photons. The four-top-quark operators enter these couplings at the two-loop level. The diagrams are shown in Figure 5.2. There are three classes of diagrams: (a) corrections to the top-quark propagator, (b) corrections to the Higgs Yukawa coupling and (c) corrections to the $t\bar{t}g$ and $t\bar{t}\gamma$ vertices. The latter turns out to be zero when the gluons or photons are on-shell. The first and second type of corrections are left-right (LR) transitions hence the only contributions stem from the operators with Wilson coefficients $C_{Qt}^{(1),(8)}$ and $C_{QtQb}^{(1),(8)}$. As can be inferred from the diagrams in Figure 5.2 the result can be expressed as a product of one-loop integrals. We computed the diagrams in two independent calculations making use of different computer algebra tools such as `PackageX` [78], `KIRA` [79], `Fire` [80], `FeynRules` [81] and `FeynArts` [82].[1] We cross-checked the Feynman rules with ref. [83]. For the renormalisation procedure we adopt a mixed on-shell (OS)-$\overline{\text{MS}}$ – scheme as proposed in [84], in which we renormalise the quark masses OS and the Wilson coefficients of the dimension-six operators using the $\overline{\text{MS}}$ scheme. We hence renormalise the top/bottom mass as

$$m_{t/b}^{\text{OS}} = m_{t/b}^{(0)} - \delta m_{t/b}, \tag{5.3}$$

where the counterterms are given by

$$\begin{aligned}\delta m_t =& \frac{1}{16\pi^2}\frac{C_{Qt}^{(1)} + c_F C_{Qt}^{(8)}}{\Lambda^2} m_t^3 \left[\frac{2}{\bar{\epsilon}} + 2\log\left(\frac{\mu_R^2}{m_t^2}\right) + 1\right] \\ &+ \frac{1}{16\pi^2}\frac{(2N_c+1)C_{QtQb}^{(1)} + c_F C_{QtQb}^{(8)}}{\Lambda^2}\left[\frac{1}{\bar{\epsilon}} + \log\left(\frac{\mu_R^2}{m_b^2}\right) + 1\right] m_b^3\,,\end{aligned} \tag{5.4}$$

$$\delta m_b = \frac{1}{16\pi^2}\frac{(2N_c+1)C_{QtQb}^{(1)} + c_F C_{QtQb}^{(8)}}{\Lambda^2}\left[\frac{1}{\bar{\epsilon}} + \log\left(\frac{\mu_R^2}{m_t^2}\right) + 1\right] m_t^3\,, \tag{5.5}$$

with $\bar{\epsilon}^{-1} = \epsilon^{-1} - \gamma_E + \log(4\pi)$, in dimensional regularization with $d = 4 - 2\epsilon$, $N_c = 3$ the number of colors, and $c_F = (N_c^2 - 1)/(2N_c) = 4/3$ the $SU(3)$ quadratic Casimir in the fundamental representation. We note that, for the calculations of the physical processes in this paper, the difference between using the OS or the $\overline{\text{MS}}$ definitions of the

[1] Note that the latter tool needed some manual adjustments to deal with four-fermion operators.

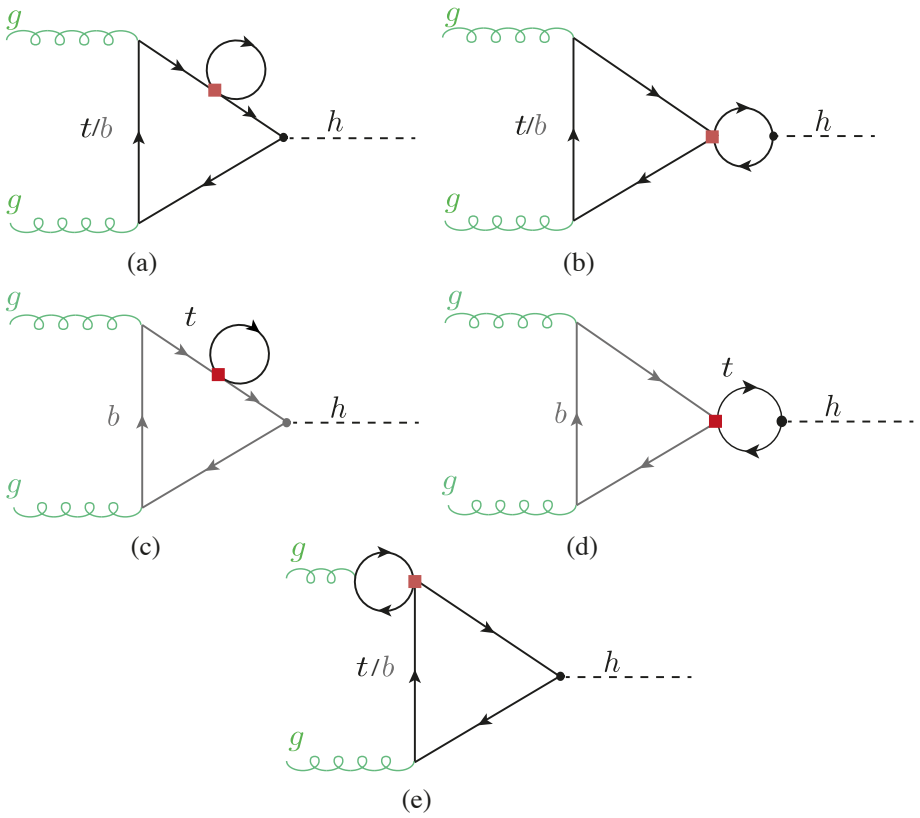

Figure 5.2. Example Feynman diagrams for four-fermion-operator contributions to the Higgs production via gluon fusion. The red box indicates the four-fermion operator.

top and bottom masss in SMEFT results in changes that are formally of $\mathcal{O}(1/\Lambda^4)$.[2] We note though that using a SM running $\overline{\text{MS}}$ bottom mass instead of an OS one makes a relevant difference in the numerical results. In the results presented below we will use the OS bottom mass as an input.

The coefficients of the dimension-six operators are renormalised in the $\overline{\text{MS}}$ scheme. At one-loop level the only operators entering the Higgs to gluon or photon rates that

[2] In the $\overline{\text{MS}}$ scheme the mass counterterms become

$$\delta m_t^{\overline{\text{MS}}} = \frac{1}{8\pi^2}\frac{C_{Qt}^{(1)} + c_F C_{Qt}^{(8)}}{\Lambda^2} m_t^3 \frac{1}{\bar{\epsilon}} + \frac{1}{16\pi^2}\frac{(2N_c+1)C_{QtQb}^{(1)} + c_F C_{QtQb}^{(8)}}{\Lambda^2}\frac{1}{\bar{\epsilon}} m_b^3 \,, \tag{5.6}$$

$$\delta m_b^{\overline{\text{MS}}} = \frac{1}{16\pi^2}\frac{(2N_c+1)C_{QtQb}^{(1)} + c_F C_{QtQb}^{(8)}}{\Lambda^2}\frac{1}{\bar{\epsilon}} m_t^3 \,. \tag{5.7}$$

mix with the four-quark operators are the ones that modify the top or bottom Yukawa couplings: $\mathcal{O}_{t\phi}$ and $\mathcal{O}_{b\phi}$, respectively. The coefficients of these operators are renormalized according to

$$C^{\overline{\text{MS}}}_{t\phi/b\phi} = C^{(0)}_{t\phi/b\phi} + \delta C_{t\phi/b\phi} \qquad \text{with} \qquad \delta C_{t\phi/b\phi} = -\frac{1}{2\bar{\epsilon}}\frac{1}{16\pi^2}\gamma^j_{t\phi/b\phi} C_j. \tag{5.8}$$

The only four-quark Wilson coefficients contributing to $\gamma_{t\phi/b\phi}$ are the ones from $\mathcal{O}^{(1),(8)}_{Qt}$ and $\mathcal{O}^{(1),(8)}_{QtQb}$. The explicit expressions for the relevant one-loop anomalous dimension can be obtained from ref. [85, 86]. The Wilson coefficients $C_{t\phi/b\phi}$ modify the Higgs couplings to top quarks/bottom quarks as follows

$$g_{ht\bar{t}/hb\bar{b}} = \frac{m_{t/b}}{v} - \frac{v^2}{\Lambda^2}\frac{C_{t\phi/b\phi}}{\sqrt{2}}\,. \tag{5.9}$$

Hence, a modification of the Higgs couplings to bottom and top quarks is generated by operator mixing, even if $C_{t\phi/b\phi}$ are zero at Λ.

The modification of the Higgs production rate in gluon fusion (ggF) can be written as

$$\frac{\sigma_{ggF}}{\sigma^{\text{SM}}_{ggF}} = 1 + \frac{\sum_{i=t,b} 2\text{Re}\left(F^i_{\text{LO}} F^*_{\text{NLO}}\right)}{\left|F^t_{\text{LO}} + F^b_{\text{LO}}\right|^2} \tag{5.10}$$

with

$$F^i_{\text{LO}} = -\frac{8m_i^2}{m_h^2}\left[1 - \frac{1}{4}\log^2(x_i)\left(1 - \frac{4m_i^2}{m_h^2}\right)\right] \tag{5.11}$$

where m_h is the Higgs mass, and

$$\begin{aligned} F_{\text{NLO}} =& \frac{1}{4\pi^2\Lambda^2}(C^{(1)}_{Qt} + c_F C^{(8)}_{Qt}) F^t_{\text{LO}} \left[2m_t^2 + \frac{1}{4}(m_h^2 - 4m_t^2)\left(3 + 2\sqrt{1 - \frac{4m_t^2}{m_h^2}}\log(x_t)\right)\right. \\ &\left. + \frac{1}{2}(m_h^2 - 4m_t^2)\log\left(\frac{\mu_R^2}{m_t^2}\right)\right] \\ &+ \frac{1}{32\pi^2\Lambda^2}((2N_c+1)C^{(1)}_{QtQb} + c_F C^{(8)}_{QtQb})\left[F^b_{\text{LO}}\frac{m_t}{m_b}\left(4m_t^2 - 2m_h^2\right.\right. \\ &\left.\left. -(m_h^2 - 4m_t^2)\sqrt{1 - \frac{4m_t^2}{m_h^2}}\log(x_t) - (m_h^2 - 4m_t^2)\log\left(\frac{\mu_R^2}{m_t^2}\right)\right) + (t \leftrightarrow b)\right]. \end{aligned} \tag{5.12}$$

Only top quark loops contribute to the parts proportional to $C^{(1),(8)}_{Qt}$. We have neglected the contributions of the operators with Wilson coefficient $C^{(1),(8)}_{Qb}$ as they would lead only to subleading contributions proportional to m_b^3. The variable x_i for a loop particle

with mass m_i is given by

$$x_i = \frac{-1 + \sqrt{1 - \frac{4m_i^2}{m_h^2}}}{1 + \sqrt{1 - \frac{4m_i^2}{m_h^2}}} \,. \tag{5.13}$$

In analogy to (5.10), we can write the modified decay rates of the Higgs boson to gluons as

$$\frac{\Gamma_{h\to gg}}{\Gamma^{\rm SM}_{h\to gg}} = 1 + \frac{\sum_{i=t,b} 2{\rm Re}\left(F^i_{\rm LO} F^*_{\rm NLO}\right)}{|F^t_{\rm LO} + F^b_{\rm LO}|^2} \tag{5.14}$$

and

$$\frac{\Gamma_{h\to\gamma\gamma}}{\Gamma^{\rm SM}_{h\to\gamma\gamma}} = 1 + \frac{2{\rm Re}\left(F_{{\rm LO},\gamma} F^*_{{\rm NLO},\gamma}\right)}{|F_{{\rm LO},\gamma}|^2}. \tag{5.15}$$

In the latter

$$F_{{\rm LO},\gamma} = N_C\, Q_t^2 F^t_{\rm LO} + N_C\, Q_b^2 F^b_{\rm LO} + F^W_{\rm LO} + F^G_{LO}, \tag{5.16}$$

and $F_{{\rm NLO},\gamma}$ is obtained from $F_{\rm NLO}$ by replacing the LO form factor that appears inside of it by $F^i_{\rm LO} \to N_c\, Q_i^2 F^i_{\rm LO}$, with the charges $Q_t = 2/3$ and $Q_b = -1/3$. The W boson contribution

$$F^W_{\rm LO} = 2\left(1 + 6\frac{m_W^2}{m_h^2}\right) - 6\frac{m_W^2}{m_h^2}\left(1 - 2\frac{m_W^2}{m_h^2}\right)\log^2(x_W), \tag{5.17}$$

with m_W the W mass, and the Goldstone contribution

$$F^G_{\rm LO} = 4\frac{m_W^2}{m_h^2}\left(1 + \frac{m_W^2}{m_h^2}\,\log^2(x_W)\right) . \tag{5.18}$$

The formulae presented above are valid under the assumption that, at the electroweak scale, the four-quark operators are the only new physics contributions in the dimension-six effective Lagrangian. If, on the other hand, one assumes that the four-quark operators are defined at some high scale Λ, e.g. after matching with an specific ultraviolet (UV) model, further (logarithmic) contributions appear during the running to low energies, as a result of the mixing between these four-fermion interactions and those operators that would modify the processes at LO. Those effects can be included via the renormalisation group equation (RGE) for the operators with Wilson coefficient $C_{t\phi}$ and $C_{b\phi}$ [85, 86],

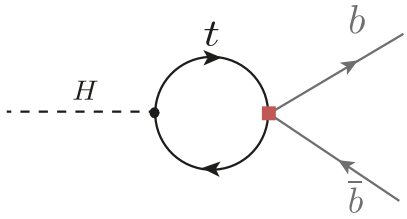

Figure 5.3. Feynman diagram contributing to the NLO $h \to b\bar{b}$ process.

that lead approximatively to

$$\begin{aligned} C_{t\phi}(\mu_R) - C_{t\phi}(\Lambda) =& \frac{1}{16\pi^2 v^2}\left[-2y_t(m_h^2 - 4m_t^2)(C_{Qt}^{(1)} + c_F C_{Qt}^{(8)})\log\left(\frac{\mu_R^2}{\Lambda^2}\right)\right. \\ &\left. + \frac{y_b}{2}(m_h^2 - 4m_b^2)\left((2N_c+1)C_{QtQb}^{(1)} + c_F C_{QtQb}^{(8)}\right)\log\left(\frac{\mu_R^2}{\Lambda^2}\right)\right] \end{aligned} \tag{5.19}$$

and

$$C_{b\phi}(\mu_R) - C_{b\phi}(\Lambda) = \frac{y_t}{32\pi^2 v^2}\left[(m_h^2 - 4m_t^2)\left((2N_c+1)C_{QtQb}^{(1)} + c_F C_{QtQb}^{(8)}\right)\log\left(\frac{\mu_R^2}{\Lambda^2}\right)\right], \tag{5.20}$$

where $y_{t/b} = \sqrt{2}m_{t/b}/v$. Note that the combinations of Wilson coefficients appearing in (5.19)(5.20) are the same as in F_{NLO} in (5.12). Effectively, we can then obtain the result under the assumption that the four-fermion operators are the only non-zero ones at the high scale by replacing in (5.12) $\mu_R \to \Lambda$, noting that we have renormalised the top and bottom quark mass in the OS scheme.

5.2.2 Higgs decay to bottom quarks

The dominant four-fermion contributions to decay channel $h \to b\bar{b}$ come from the operators with Wilson coefficients $C_{QtQb}^{(1),(8)}$. The corresponding diagram at NLO is shown in fig 5.3. Adopting the same renormalisation procedure as outlined in the previous subsection, we obtain the following expression for the correction to the $h \to b\bar{b}$ decay rate in the presence of $\mathcal{O}_{QtQb}^{(1),(8)}$,

$$\begin{aligned} \frac{\Gamma_{h\to b\bar{b}}}{\Gamma_{h\to b\bar{b}}^{\mathrm{SM}}} =& 1 + \frac{1}{16\pi^2}\frac{m_t}{m_b}(m_h^2 - 4m_t^2)\frac{(2N_c+1)C_{QtQb}^{(1)} + c_F C_{QtQb}^{(8)}}{\Lambda^2} \\ &\times\left[2 + \sqrt{1 - \frac{4m_t^2}{m_h^2}}\log(x_t) - \log\left(\frac{m_t^2}{\mu_R^2}\right)\right], \end{aligned} \tag{5.21}$$

which carries an enhancement factor of m_t/m_b and is hence expected to be rather large. Again, we have neglected subdominant contributions suppressed by the bottom mass from the operators $\mathcal{O}_{Qb}^{(1),(8)}$. Including the leading logarithmic running of $C_{b\phi}$ of (5.20) from the high scale Λ to the electroweak scale is achieved by setting in (5.21) $\mu_R \to \Lambda$. The expression in (5.21) agrees with results obtained from the full calculation of the NLO effects in the dimension-six SMEFT, first computed in [87].

This closes the discussion of the main effects that the third-generation four-quark operators can have in the different Higgs decay widths.[3] Note also that these modifications of the Higgs decay rate to photons, gluons and, especially, bottom quarks, affect all the branching ratios (BRs) due to the modification of the Higgs total width, and therefore have an observable effect in all Higgs processes measured at the LHC.

5.2.3 Associated production of a Higgs boson with top quarks

The associated Higgs production with top quarks, $t\bar{t}h$, receives significant NLO corrections from the singlet and octet operators $\mathcal{O}_{Qt}^{(1),(8)}$, while the contributions from $\mathcal{O}_{QtQb}^{(1),(8)}$ remain small. In addition, there are some small contributions from the singlet and triplet left-handed operators, $\mathcal{O}_{QQ}^{(1),(3)}$, and the right-handed four-top operator, $\mathcal{O}_{tt}$, as well. The $t\bar{t}h$ process can be either initiated by gluons, see Figure 5.4, or by a quark anti-quark pair, see Figure 5.5. The triangle and box topologies (shown as (d) and (e) in Figure 5.4 and as (b) in Figure 5.5) are finite. While for Higgs production/decay in/to gluons only certain combinations of singlet/octet operators entered, leading to a degeneracy, this is not the case for $t\bar{t}h$ production, where the gluons no longer need to combine to a colour singlet state. The degeneracy between the singlet and octet operators is mainly broken by the contributions from the triangle diagrams, where, for instance, the difference between the contributions of $\mathcal{O}_{Qt}^{(1)}$ and $\mathcal{O}_{Qt}^{(8)}$ does not follow the same color structure as other diagrams.

We adopt a four-flavour scheme for the computation of the quark-initiated contributions. We note that within a five-flavour scheme operators containing both bottom and top quarks lead to a LO contribution from a direct contact diagram. Nevertheless, this gives an overall negligible correction as the $b\bar{b}$ initiated $t\bar{t}h$ process is suppressed by the small bottom parton distribution functions. The effect of changing the flavour scheme results in an uncertainty of $1-2\%$.

We have computed the NLO corrections using `Madgraph_aMCNLO` [88] (version 3.1.0) with the `SMEFTatNLO v1.0.2` model [75]. The results were cross-checked by an analytic computation[4], based on the reduction of one-loop amplitudes via the method developed

[3] Four-fermion operators also affect the $h \to Z\gamma$ partial width. However, as in the diphoton case, the effect is expected to be small due to the dominance of the W boson loop. Because of this, and given the smallness of the $h \to Z\gamma$ branching ratio and the relatively low precision expected in this channel at the LHC, we neglect the effects of four-fermion interactions in this decay.

[4] The `FORTRAN` code containing this analytical calculation can be provided on request.

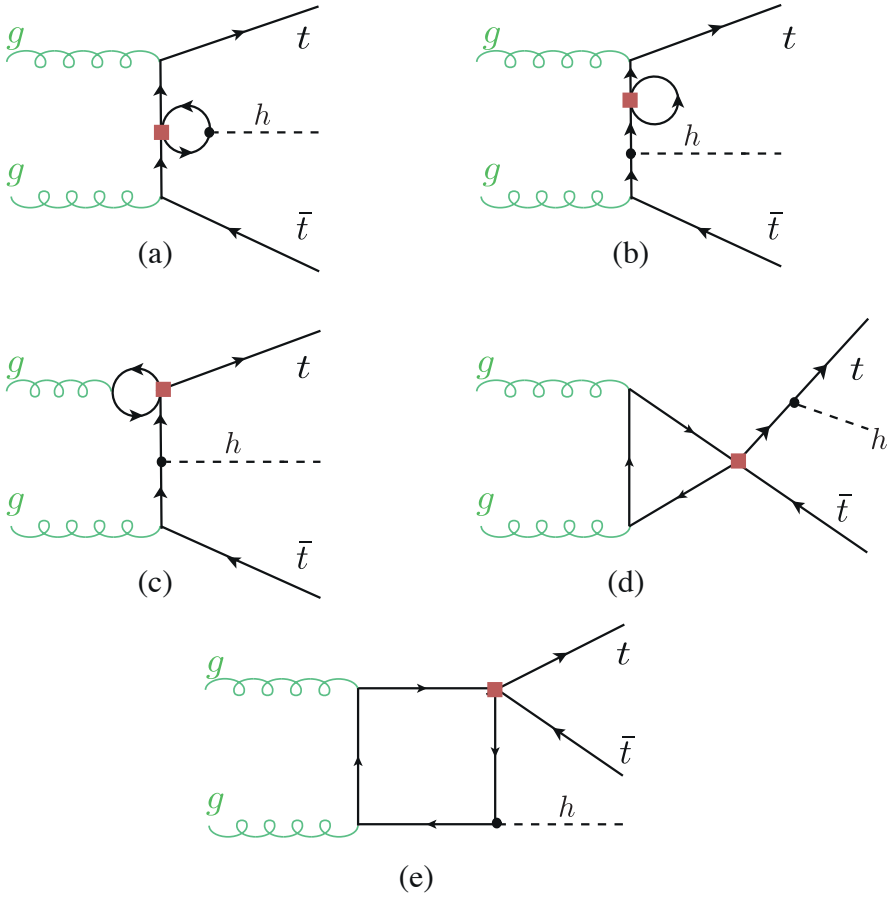

Figure 5.4. Feynman diagrams including the four-fermion loop contributions to the $gg \to t\bar{t}h$ subprocess.

by G. Ossola, C.G. Papadopoulos and R. Pittau (OPP reduction) [89]. The OPP reduction was done using the `CutTools` programme [90]. It reduces the one-loop amplitude into 1,2,3 and 4-point loop functions in four dimensions, keeping spurious terms from the ϵ part of the amplitude. To correct for such terms, one needs to compute the divergent UV counterterm as well as a finite rational terms, denoted R_2 as in Ref. [91].[5] The amplitudes were generated in the same way as for gluon fusion. The UV and R_2 counterterms, that need to be supplemented to `CutTools`, were computed manually following the method detailed in [91]. The UV counterterms are the same as for gluon fusion, in addition to a new one that is needed to be introduced to renormalise diagrams

[5] Another rational term R_1 appears due to the mismatch between the four and d dimensional amplitudes, but this is computed automatically in `CutTools`.

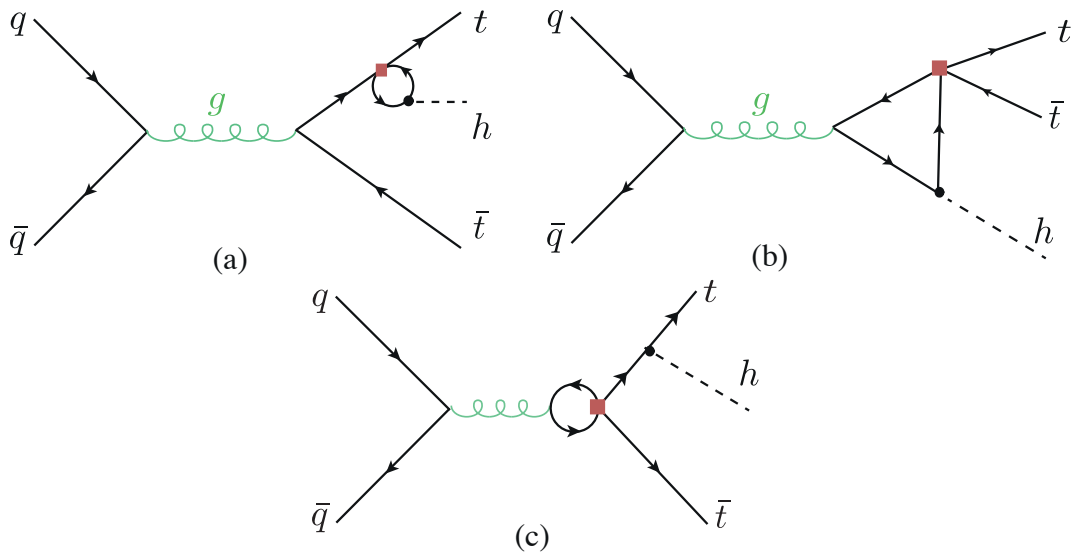

Figure 5.5. Feynman diagrams including the four-fermion loop contributions to the $q\bar{q} \to t\bar{t}h$ subprocess.

of type (c) in Figure 5.4 and Figure 5.5. This is due to the operator mixing of light – heavy four-quark operators with heavy four-quark operators. Effectively, this leads to a counterterm

$$= \frac{ig_s}{12\pi^2\Lambda^2} T^A_{ij} p_g^2 \gamma^\mu \left(C_{tt} P_R + \left(C^{(1)}_{QQ} + C^{(3)}_{QQ} \right) P_L + \frac{C^{(8)}_{Qt}}{4} \right) \left(\frac{1}{\bar{\epsilon}} - 1 \right). \quad (5.22)$$

Since the singlet and octet operators $\mathcal{O}^{(1),(8)}_{QtQb}$ are not implemented in the current version of `SMEFTatNLO`, or in any other loop-capable `UFO` model available, we have modified the `SMEFTatNLO` model to include these operators, by including their Feynman rules and computing the UV and R_2 counterterms needed for the $t\bar{t}h$ calculation. These $\mathcal{O}^{(1),(8)}_{QtQb}$ contributions are included for consistency, as they were relevant and thus included in the calculation of, e.g. $h \to b\bar{b}$. However, as we will argue below, their contribution to $t\bar{t}h$ is rather small. Similarly, other "mixed" bottom-top operators are expected to give also suppressed contributions, compared to those from four-top operators. Therefore we neglect their effects in our calculation.[6]

Again, to connect with specific models that may generate the four-quark operators

[6] Furthermore, we note that such operators are also currently not included in `SMEFTatNLO`. A computation of their contributions, while being beyond the scope of this paper, would require a similar strategy as for the $\mathcal{O}^{(1),(8)}_{QtQb}$ operator.

at the new physics scale Λ, one needs to consider the contributions that come from the running from Λ to low energies, and that mix these operators with those entering in $t\bar{t}h$ at the LO level. For the gluon-initiated subprocess the relevant contributions are from the running of $C_{t\phi}$ in (5.19), while for the quark-initiated subprocess we need to account for the mixing of the third generation four-fermion operators with the ones connecting the third generation with the first two generations. The corresponding corrections can be obtained from the RGEs in refs. [85, 86, 92].

5.2.4 Results

Here we provide semi-analytical expressions for the results of our NLO calculations including the effects of the third generation four-quark operators. These NLO contributions to the single Higgs rates, as a function of the four-heavy-quark Wilson coefficients, are denoted by

$$\delta R(C_i) = R/R^{\mathrm{SM}} - 1, \tag{5.23}$$

where R stands generically for partial width Γ or cross section σ. They are summarised in Table 5.1. The numbers consider only the linear contributions in Λ^{-2}. The respective $\delta R(C_i)$ get a contribution from the computation of the finite corrections to the process and an additional contribution from operator mixing due to RGE running and can hence be split into two parts

$$\delta R(C_i) = \frac{C_i}{\Lambda^2}\left(\delta R_{C_i}^{fin} + \delta R_{C_i}^{log}\log\left(\frac{\mu_R^2}{\Lambda^2}\right)\right). \tag{5.24}$$

We note that the way we write our results corresponds to the finite part of the NLO correction taken at a typical process scale μ_R and a contribution obtained by solving the RGE of the dimension-six Wilson coefficients via the leading log approximation from the high scale Λ to the low scale μ_R. Both the finite part dependence $\delta R_{C_i}^{fin}$ of these corrections on the Wilson coefficient as well as the part proportional to the logarithm $\delta R_{C_i}^{log}$ are reported in table 5.1. Our results can be improved by replacing the part proportional to the coefficients $\delta R_{C_i}^{log}$ by solving the coupled system of RGEs. For $\Lambda = 1$ TeV, and depending on the renormalisation scale of the process, the value of the logarithm in (5.24) ranges between $\sim [-5.5, -2.9]$. With these numerical values in mind and by looking at $\delta R_{C_i}^{log}$ in table 5.1, we see that the finite part of the NLO calculation, i.e. $\delta R_{C_i}^{fin}$, is usually of the same order of magnitude or larger than the leading-log part, with the exception of the $C_{QtQb}^{(1),(8)}$ contributions to the $h \to b\bar{b}$. This underlines the importance of considering the full NLO computation in the determination of the Wilson coefficients for $C_{Qt}^{(1),(8)}$, whereas for $C_{QtQb}^{(1),(8)}$, where the limits are mainly driven by $h \to b\bar{b}$, they turn out to play less important role.

Operator	Process	μ_R	$\delta R_{C_i}^{fin}$ [TeV^2]	$\delta R_{C_i}^{log}$ [TeV^2]
$\mathcal{O}_{Qt}^{(1)}$	ggF	$\frac{m_h}{2}$	$9.91 \cdot 10^{-3}$	$2.76 \cdot 10^{-3}$
	$h \to gg$	m_h	$6.08 \cdot 10^{-3}$	$2.76 \cdot 10^{-3}$
	$h \to \gamma\gamma$		$-1.76 \cdot 10^{-3}$	$-0.80 \cdot 10^{-3}$
	$t\bar{t}h$ 13 TeV	$m_t + \frac{m_h}{2}$	$-4.20 \cdot 10^{-1}$	$-2.78 \cdot 10^{-3}$
	$t\bar{t}h$ 14 TeV		$-4.30 \cdot 10^{-1}$	$-2.78 \cdot 10^{-3}$
$\mathcal{O}_{Qt}^{(8)}$	ggF	$\frac{m_h}{2}$	$1.32 \cdot 10^{-2}$	$3.68 \cdot 10^{-3}$
	$h \to gg$	m_h	$8.11 \cdot 10^{-3}$	$3.68 \cdot 10^{-3}$
	$h \to \gamma\gamma$		$-2.09 \cdot 10^{-3}$	$-1.07 \cdot 10^{-3}$
	$t\bar{t}h$ 13 TeV	$m_t + \frac{m_h}{2}$	$6.53 \cdot 10^{-2}$	$-2.24 \cdot 10^{-3}$
	$t\bar{t}h$ 14 TeV		$7.29 \cdot 10^{-2}$	$-2.24 \cdot 10^{-3}$
$\mathcal{O}_{QtQb}^{(1)}$	ggF	$\frac{m_h}{2}$	$2.84 \cdot 10^{-2}$	$9.21 \cdot 10^{-3}$
	$h \to gg$		$1.57 \cdot 10^{-2}$	$9.21 \cdot 10^{-3}$
	$h \to \gamma\gamma$	m_h	$-1.30 \cdot 10^{-3}$	$-0.78 \cdot 10^{-3}$
	$h \to b\bar{b}$		$9.25 \cdot 10^{-2}$	$1.68 \cdot 10^{-1}$
	$t\bar{t}h$ 13 TeV	$m_t + \frac{m_h}{2}$	$-3.23 \cdot 10^{-6}$	$-9.16 \cdot 10^{-6}$
	$t\bar{t}h$ 14 TeV		$-3.51 \cdot 10^{-6}$	$-9.16 \cdot 10^{-6}$
$\mathcal{O}_{QtQb}^{(8)}$	ggF	$\frac{m_h}{2}$	$5.41 \cdot 10^{-3}$	$1.76 \cdot 10^{-3}$
	$h \to gg$		$2.98 \cdot 10^{-3}$	$1.76 \cdot 10^{-3}$
	$h \to \gamma\gamma$	m_h	$-0.25 \cdot 10^{-3}$	$-0.15 \cdot 10^{-3}$
	$h \to b\bar{b}$		$1.76 \cdot 10^{-2}$	$3.20 \cdot 10^{-2}$
	$t\bar{t}h$ 13 TeV	$m_t + \frac{m_h}{2}$	$4.07 \cdot 10^{-6}$	$-1.74 \cdot 10^{-6}$
	$t\bar{t}h$ 14 TeV		$6.14 \cdot 10^{-6}$	$-1.74 \cdot 10^{-6}$
$\mathcal{O}_{QQ}^{(1)}$	$t\bar{t}h$ 13 TeV	$m_t + \frac{m_h}{2}$	$1.75 \cdot 10^{-3}$	$1.90 \cdot 10^{-3}$
	$t\bar{t}h$ 14 TeV		$2.35 \cdot 10^{-3}$	$1.90 \cdot 10^{-3}$
$\mathcal{O}_{QQ}^{(3)}$	$t\bar{t}h$ 13 TeV	$m_t + \frac{m_h}{2}$	$0.66 \cdot 10^{-3}$	$5.50 \cdot 10^{-3}$
	$t\bar{t}h$ 14 TeV		$0.44 \cdot 10^{-3}$	$5.50 \cdot 10^{-3}$
$\mathcal{O}_{tt}$	$t\bar{t}h$ 13 TeV	$m_t + \frac{m_h}{2}$	$7.50 \cdot 10^{-3}$	$2.01 \cdot 10^{-3}$
	$t\bar{t}h$ 14 TeV		$6.45 \cdot 10^{-3}$	$2.01 \cdot 10^{-3}$

Table 5.1. The NLO corrections from the four heavy-quark SMEFT operators of this study to single Higgs rates. We have separated the contributions into the finite piece $\delta R_{C_i}^{fin}$ and the leading log running of the Wilson coefficients $\delta R_{C_i}^{log}$, see (5.24).

The numerical values were obtained using as input parameters

$$\begin{aligned} &G_F = 1.166378 \cdot 10^{-5}\ \text{GeV}^{-2}\,,\ m_W = 80.379\ \text{GeV}\,,\ m_Z = 91.1876\ \text{GeV}\,, \\ &m_t^{\text{OS}} = 172.5\ \text{GeV}\,,\ m_b^{\text{OS}} = 4.7\ \text{GeV}\,,\ m_h = 125.1\ \text{GeV}\,, \end{aligned} \tag{5.25}$$

and the NNPDF23 set at NLO [93].

Looking at the results, first we note that the operators $\mathcal{O}_{QQ}^{(1),(3)}$ and $\mathcal{O}_{tt}$ only contribute to $t\bar{t}h$ production. In this regard, however, it must be noted that the uncertainties of the renormalisation schemes, the scale uncertainty, the PDF+α_s uncertainty and the one of the flavour schemes of the $t\bar{t}h$ process are $\sim 5\%$. This is larger than the typical effects of $C_{QQ}^{(1),(3)}$ and C_{tt} for $\mathcal{O}(1)$ coefficients. Therefore, all Higgs rates are expected to be relatively insensitive to these interactions unless rather large values of these Wilson coefficients are allowed. Secondly, from the analytic results, we observe that in the NLO corrections to Higgs rates, the Wilson coefficients $C_{QtQb}^{(1)}, C_{QtQb}^{(8)}$ always appear in a linear combination identical to the one seen in the RGE of the Wilson coefficients $C_{t\phi}$ and $C_{b\phi}$, i.e.

$$C_{QtQb}^{+} = (2N_c + 1)C_{QtQb}^{(1)} + c_F C_{QtQb}^{(8)}. \tag{5.26}$$

The exception is the $t\bar{t}h$ process, which has a small finite part contribution that breaks this relation. However, this finite part is suppressed by the bottom quark mass and therefore it is very small. Thus, all single Higgs rates are mostly sensitive to the linear combination in (5.26). We finally note that apart from $\mathcal{O}_{Qt}^{(1),(8)}$ all the other operators produce only small contributions to the $t\bar{t}h$ process. In particular, the top-bottom operators $\mathcal{O}_{QtQb}^{(1),(8)}$ show a suppression with m_b, which also typically results in contributions below the theoretical uncertainties. (We explicitly checked this in our calculation and by setting $m_b = 0$ in the `Madgraph_aMCNLO` simulations.) This is also expected for other "mixed" top-bottom operators, which would contribute via bottom-quark loops and hence would be strongly suppressed, justifying that we did not consider them here.

5.3 Fit to Higgs observables

In this section we will show the results of a combined fit of the four-quark operators of the third generation and the operator that modifies the Higgs potential and hence the Higgs self-coupling. In ref. [59–62, 64] it was proposed to extract the trilinear Higgs self-coupling via its loop effects in single Higgs measurements. Within the assumptions of the SMEFT, a model-independent determination of the triple Higgs self-interaction, λ_3, should be considered within a global analysis considering all effective interactions that enter up to the same order in perturbation theory as λ_3. In particular, apart from the trilinear Higgs self-coupling modification, such a study must include those operators that enter at LO in Higgs production and decay [66]. Furthermore, the sensitivity to the Higgs self-coupling modifications can also be diminished by other operators entering as the trilinear Higgs self-coupling via loop effects, if those operators are not yet strongly constrained experimentally by other processes. Such is the case for some of the four-quark operators considered in this paper. In order to show this, we have performed a combined fit to the operator with Wilson coefficient C_ϕ and the four-fermion operators considered in this study. A full global fit including all new physics effects would require

the combination of Higgs data with that from other processes and is beyond the scope of this paper.

5.3.1 Fit methodology

For each experimentally observed channel with a signal strength $\mu_{\text{Exp}} \equiv \sigma_{\text{Obs}}/\sigma_{\text{SM}}$, one can build a theoretical prediction for this signal strength, $\mu_{\text{Th}} \equiv \sigma_{\text{Th}}/\sigma_{\text{SM}}$, where $\sigma_{\text{Th}} = \sigma_{\text{Prod}} \times \text{BR}$ includes the effects generated by the dimension-six operators. The theory predictions for the signal strengths are then used to build a test statistic in the form of a log-likelihood of a Gaussian distribution

$$\log(L) = -\frac{1}{2}\left[(\vec{\mu}_{\text{Exp}} - \vec{\mu})^T \cdot \mathbf{V}^{-1} \cdot (\vec{\mu}_{\text{Exp}} - \vec{\mu})\right]. \tag{5.27}$$

The covariance matrix $\mathbf{V}$ is constructed from the experimental uncertainties $\delta\mu_{\text{Exp}}$ and correlations[7], as well as the theoretical uncertainties (scale, PDF, α_s, ...).

The log-likelihood of (5.27) was used together with flat priors $\pi(C_i) = const.$ in a Bayesian fit of the Wilson coefficients of interest. A Markov chain Monte Carlo (MCMC) using `pymc3` [94] was used to construct the posterior distribution. We use the `Arviz` Bayesian analysis package [95] to extract the credible intervals (CIs) from the highest density posterior intervals (HDPI) of the posterior distributions, where the intervals covering 95% (68%) of the posterior distribution are considered the 95% (68%) CIs. In the Gaussian limit, these 95% (68%) CIs should be interpreted as equivalent to the 95% (68%) Frequentist Confidence Level (CL) two-sided bounds. To cross-check the MCMC Bayesian fit, a frequentist Pearson's χ^2 fit was performed using `iminuit` [96, 97], where the χ^2 was taken to be

$$\chi^2 = -2\log(L). \tag{5.28}$$

Both fit results agreed on the 95% and 68% CI (or CL) bounds.[8] The code for the fit, experimental input and the analysis can be found in the repository [101].

In the theoretical predictions for the signal strengths, we will assume that the new physics corrections to the cross sections and the decay widths are linearised, i.e.

$$\mu(C_\phi, C_i) = \frac{\sigma_{\text{Prod}}(C_\phi, C_i) \times \text{BR}(C_\phi, C_i)}{\sigma_{\text{Prod,SM}} \times \text{BR}_{\text{SM}}} \approx 1 + \delta\sigma(C_\phi, C_i) + \delta\Gamma(C_\phi, C_i) - \delta\Gamma_h(C_\phi, C_i), \tag{5.29}$$

with $\delta\sigma$, $\delta\Gamma$, $\delta\Gamma_h$ (Γ_h denotes the Higgs total width) being the NLO corrections, relative to the SM prediction as in (5.23), from the dimension-six operators with Wilson coefficients C_ϕ and C_i. Here, C_i stands schematically for $C_{Qt}^{(1)}$, $C_{Qt}^{(8)}$, $C_{QtQb}^{(1)}$, $C_{QtQb}^{(8)}$, $C_{QQ}^{(1)}$, $C_{QQ}^{(3)}$

[7] Correlations amongst channels of $< 10\%$ were ignored.

[8] In order to plot the multidimensional posterior distributions and the forest plots we have used a code based on `corner.py` [98], `pygtc` [99] and `zEpid` [100].

and C_{tt}. As mentioned in the previous section, however, the sensitivity to $C_{QQ}^{(1),(3)}$ and C_{tt} is rather small, typically below the theory uncertainty of the calculation, and we will ignore these Wilson coefficients in the fits presented in this section.

In particular, in (5.29) all the corrections from the four-quark operators to the cross sections and decay widths are fully linearised in $1/\Lambda^2$. Given that current bounds on these operators are rather weak, one may wonder about the uncertainty in our fits associated to the truncation of the EFT. Note that, since the four-quark operators only enter into the virtual corrections at NLO, Higgs production and decay contain only linear terms in $1/\Lambda^2$ in the corresponding Wilson coefficients, i.e. the quadratic terms coming from squaring the amplitudes are technically of next-to-NLO. Hence, the quadratic effects in the signal strengths come from not linearising the corrections to the product $\sigma_{\rm Prod} \times {\rm BR}$. We explicitly checked that, for the fits we presented in the next section, the difference between including the full expression of the signal strength or the linearised version in (5.29) results in differences in the bounds at the $\lesssim 10\%$ level. The results we present for the four-quark operator are, therefore, relatively stable with respect to the truncation of the EFT expansion. For the $\mathcal{O}_\phi$ operator, however, there is an additional contribution to the virtual corrections stemming from the wave function renormalisation of the Higgs field. The correction to a given production cross section or decay width, again denoted generically by R, is given by

$$\delta R_{\lambda_3} \equiv \frac{R_{\rm NLO}(\lambda_3) - R_{\rm NLO}(\lambda_3^{\rm SM})}{R_{\rm LO}} = -2\frac{C_\phi v^4}{\Lambda^2 m_h^2} C_1 + \left(-4\frac{C_\phi v^4}{\Lambda^2 m_h^2} + 4\frac{C_\phi^2 v^8}{m_h^4 \Lambda^4}\right) C_2. \tag{5.30}$$

In (5.30), the coefficient C_1 corresponds to the contribution of the trilinear coupling to the single Higgs processes at one loop, adopting the same notation as [60]. The values of C_1 for the different processes of interest for this paper are given in Appendix **??**. The coefficient C_2 describes universal corrections and is given by

$$C_2 = \frac{\delta Z_h}{1 - \left(1 - \frac{2C_\phi v^4}{\Lambda^2 m_h^2}\right)^2 \delta Z_h}\,, \tag{5.31}$$

where the constant δZ_h is the SM contribution from the Higgs loops to the wave function renormalisation of the Higgs boson,

$$\delta Z_h = -\frac{9}{16}\frac{G_F m_h^2}{\sqrt{2}\pi^2}\left(\frac{2\pi}{3\sqrt{3}} - 1\right). \tag{5.32}$$

The coefficient C_2 thus introduces additional $\mathcal{O}(1/\Lambda^4)$ (and higher order) terms in δR_{λ_3}. In ref. [60] considering the κ formalism the full expression of (5.31) is kept, while we define two different descriptions: one in which we expand δR_{λ_3} up to linear order and an

alternative scheme in which we keep also terms up to $\mathcal{O}(1/\Lambda^4)$ in the EFT expansion. We explicitly checked that keeping the full expression in (5.31) and including terms up to $\mathcal{O}(1/\Lambda^4)$ in C_2 lead to nearly the same results in our fits.

5.3.2 Fit to LHC Run-II data

For the fit we have used inclusive Higgs data from the LHC Run II for centre-of-mass energy of $\sqrt{s} = 13$ TeV and integrated luminosity of $139\,\text{fb}^{-1}$ for ATLAS and $137\,\text{fb}^{-1}$ for CMS. The experimental input is summarised in Table 2.1 in Appendix **??**.

In Figure 5.6 we show the limits of a two-parameter fit for various heavy quark Wilson coefficients C_i, marginalising over C_ϕ. We confront them also with the limits obtained from fits to top data [73, 74, 77, 102–104]. Note that, although our bounds do not come from a global fit, they can be compared with similar results from the the fits to top data that assume that only one operator is "switched on" at a time. In these cases, we find that our new bounds are more stringent or at least comparable to the 95% CI bounds on the C_i operators fit results from top data. We also note that, while the limits from top data show a large uncertainty from the EFT truncation[9], even when only one operator is considered at a time, our NLO results for the four-quark operators are quite stable if one considers quadratic effects, as mentioned above. On the other hand, fig. 5.6 also shows that there is a rather large uncertainty associated to the EFT truncation of the effects of the $\mathcal{O}_\phi$ operator in the wave function renormalization of the Higgs boson. Furthermore, the plot diplays the bounds for two different assumptions for the scale at which the operators are defined. The lines showing δR^{fin} assume that there are only the corresponding four-quark operator and $\mathcal{O}_\phi$ at the electroweak scale[10], while the line corresponding to δR shows the limits assuming that the four-fermion operators (and $\mathcal{O}_\phi$) are the only ones at a scale $\Lambda = 1$ TeV. We can again infere from the fact that the bounds remain the same order of magnitude between δR^{fin} and δR that the inclusion of the finite terms for the operators $\mathcal{O}_{Qt}^{(1),(8)}$ is important if the new physics scale is not extremely high. Instead, for the operators $\mathcal{O}_{QtQb}^{(1),(8)}$ the bounds become much stronger when including the logarithmic piece, so we can conclude that in that case the finite piece is less relevant. In all the fit results that we will present in what follows, we will assume that the Wilson coefficients are always evaluated at the scale $\Lambda = 1$ TeV.

In Figure 5.7 we show the limits on C_ϕ for various two-parameter fits including the two different EFT truncations of δR_{λ_3}. We also show the results from a single parameter fit on C_ϕ. For comparison, we show the ATLAS limits from full LHC run-II Higgs pair production in the final state $b\bar{b}\gamma\gamma$ [105] where we have translated the bounds from

[9] In particular, for the $C_{QtQb}^{(1),(8)}$ operator the references only calculate contributions of order $\mathcal{O}(1/\Lambda^4)$. (The fit considering only linear terms would result in bounds of order $\mathcal{O}(10^4)$.) Hence, in this case, we only quote the quadratic bounds.

[10] We neglect in this case the small running between the scales involved in the different processes included in the fit.

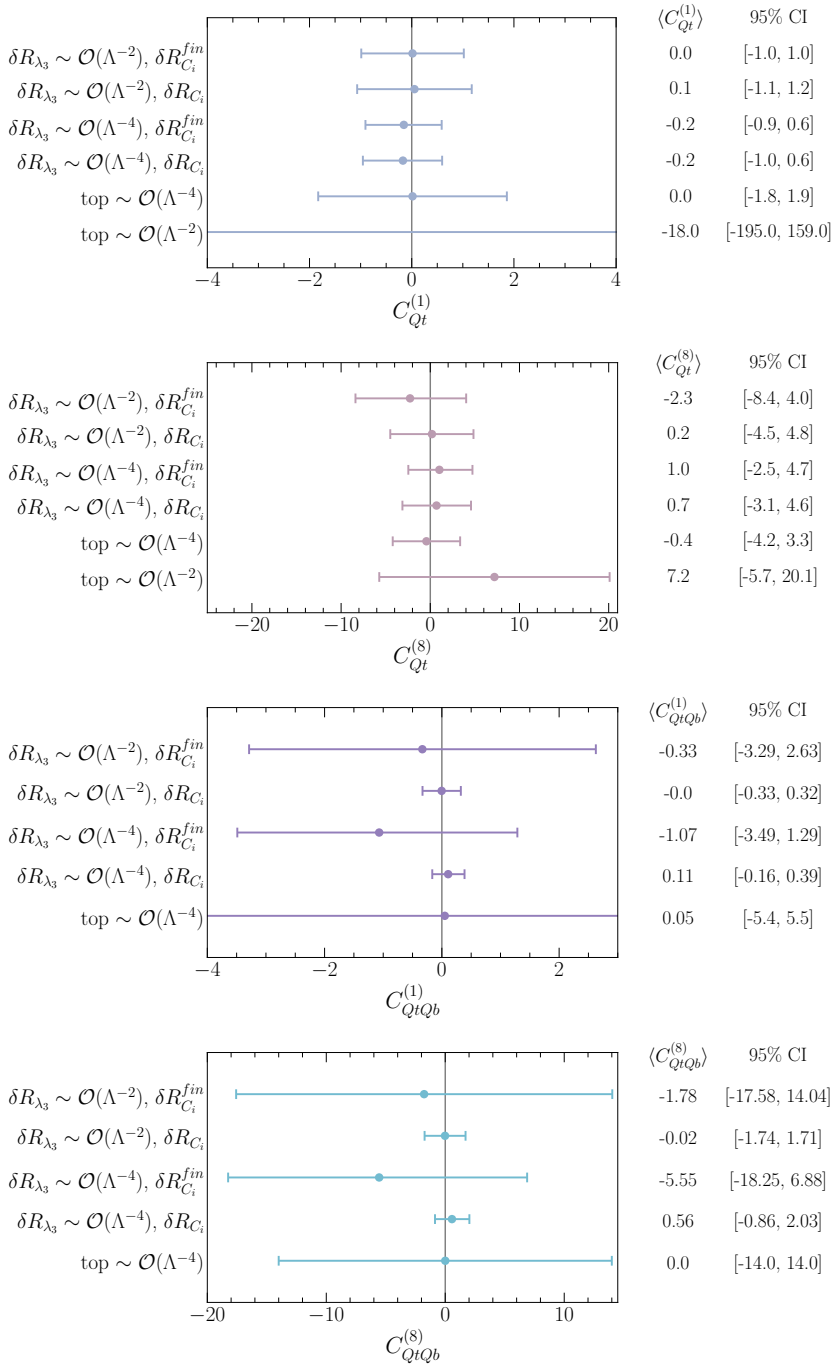

Figure 5.6. Forest plots illustrating the means and 95% CIs of the posteriors built from the four-fermion Wilson coefficients with C_ϕ marginalised. The plots confront also the truncation of the EFT at $\mathcal{O}(1/\Lambda^2)$ and $\mathcal{O}(1/\Lambda^4)$ of δR_{λ_3} as defined in (5.30). The 95% CI bounds stem from Higgs data. The last two rows for each operator show instead the limits obtained by a single parameter fit to top data, linear and quadratic. The top data results are taken from [77] for $C_{Qt}^{(1),(8)}$ and [74] for $C_{QtQb}^{(1),(8)}$.

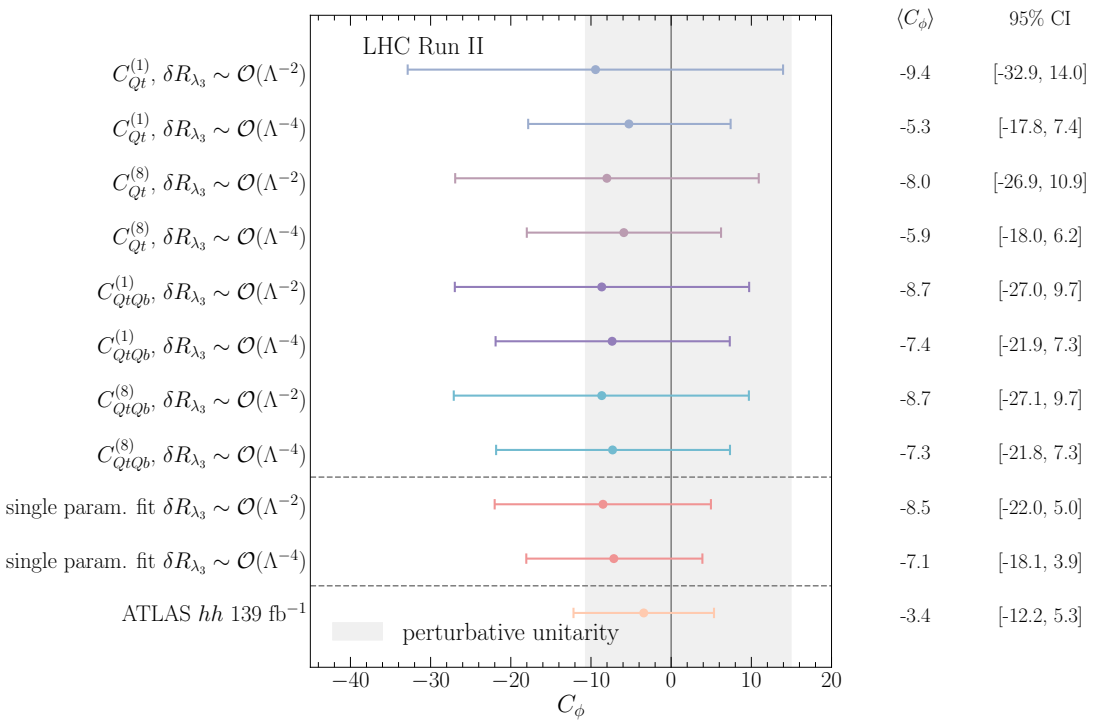

Figure 5.7. A forest plot illustrating the means and 95% CIs of the posteriors built from the C_ϕ in a two-parameter fit with the four-fermion operators marginalised. We compare the fit results for C_ϕ from full run-II Higgs data keeping terms up to $\mathcal{O}(1/\Lambda^2)$ or $\mathcal{O}(1/\Lambda^4)$ in δR_{λ_3}. For comparison, also the 95% CI and means for the single parameter fit for C_ϕ with the same single Higgs data is shown as well as the bounds on C_ϕ from the 139 fb^{-1} search for Higgs pair production [105]. The horizontal grey band illustrates the perturbative unitarity bound [106].

$\kappa_\lambda \equiv \lambda_3/\lambda_3^{\mathrm{SM}}$ to the SMEFT, keeping both linear and quadratic terms. While the limits on C_ϕ from single and double Higgs production are of similar size when keeping terms up to $\mathcal{O}(1/\Lambda^4)$ in the single Higgs fit, the limits from single Higgs become weaker if one keeps only terms up to $\mathcal{O}(1/\Lambda^2)$. In this case, the fit remains questionable leading to limits beyond the perturbative unitarity bound of ref. [106]. Instead, for Higgs pair production is makes only a negligible effect if linear or up to quadratic terms in the EFT expansion are kept for the $C_\phi > 0$ bound, while the bound weakens at linear order in $1/\Lambda^2$ for $C_\phi < 0$ [107]. We also see that the limits on C_ϕ become significantly weaker in a two-parameter fit with the four-quark operators, indicating that in a proper global SMEFT fit also the loop effects of other weakly constrained operators, such as these, need to be accounted for.

5.3.3 Two parameter fits

We present in figs. 5.8 and 5.9 the 68% and 95% highest posterior density contours of the two-parameter posterior distributions and their marginalisation for the two-parameter fits involving C_ϕ and one of the four-heavy quark Wilson coefficients, evaluated at the scale $\Lambda = 1$ TeV. Both linearised and quadratically truncated δR_{λ_3} fits are shown, and we observe that the 95% CI bounds (shown on top of the panels) and correlations depends on the truncation.

One of the important aspects of multivariate studies is the correlation among variables. Apart from the two-parameter fits discussed above, here we also consider a four-parameter fit to C_ϕ plus the three directions in the four heavy-quark operator parameter space that the Higgs rates are mostly sensitive too, i.e. neglecting $C_{QQ}^{(1),(3)}$ and C_{tt}, and trading $C_{QtQb}^{(1)}$ and $C_{QtQb}^{(8)}$ by C_{QtQb}^{+}. When considering two- or four-parameter fits of C_ϕ and the four-heavy-quark Wilson coefficients, we observe a non-trivial correlation patterns amongst these coefficients. Figure 5.10 illustrates these correlation patterns clearly for the four-parameter fit. We observe that the Wilson coefficients $C_{Qt}^{(1),(8)}$ are strongly correlated because, in analogy to $C_{QtQb}^{(1),(8)}$, they only appear in certain linear combination whenever correcting the Yukawa coupling. However, unlike $C_{QtQb}^{(1),(8)}$ they are not completely degenerate because the main part of the NLO correction to $t\bar{t}h$ does not contain the aforementioned linear combination. The four-parameter fit also reveals that the Wilson coefficients $C_{Qt}^{(1),(8)}$ have a large correlation with C_{QtQb}^{+} because all of the four Wilson coefficients appear in a linear combination in the NLO corrections except for $h \to b\bar{b}$ and $t\bar{t}h$. However, this correlation is not as strong due to the large NLO correction of the Higgs decay $h \to b\bar{b}$ from $C_{QtQb}^{(1),(8)}$. Moreover, the correlation between the four-heavy-quark Wilson coefficients and C_ϕ depends on the δR_{λ_3} truncation. In Appendix 5.3.3 we present similar correlation plots for various two-parameter fits, where the same behaviour of the change in the correlation with the inclusion of quadratic terms δR_{λ_3} is found. The correlation in those cases are though generally stronger.

5.3.4 Prospects for HL-LHC

We now turn to examine the potential of the HL-LHC. For this, we use the CMS projections for the single Higgs signal strengths provided in refs. [51, 108] for a centre-of-mass energy of $\sqrt{s} = 14$ TeV and integrated luminosity of $3\,\text{ab}^{-1}$. We use the projections for the S2 scenario explained in [48]. These assume the improvement on the systematics that is expected to be attained by the end of the HL-LHC physics programme, and that theory uncertainties are improved by a factor of two with respect to current values. These projections are assumed to have their central values in the SM prediction with the total uncertainties summarised in table 2.1 in Appendix **??**.[11]

[11] The correlation matrix for the S2 scenario can be found on the webpage [108].

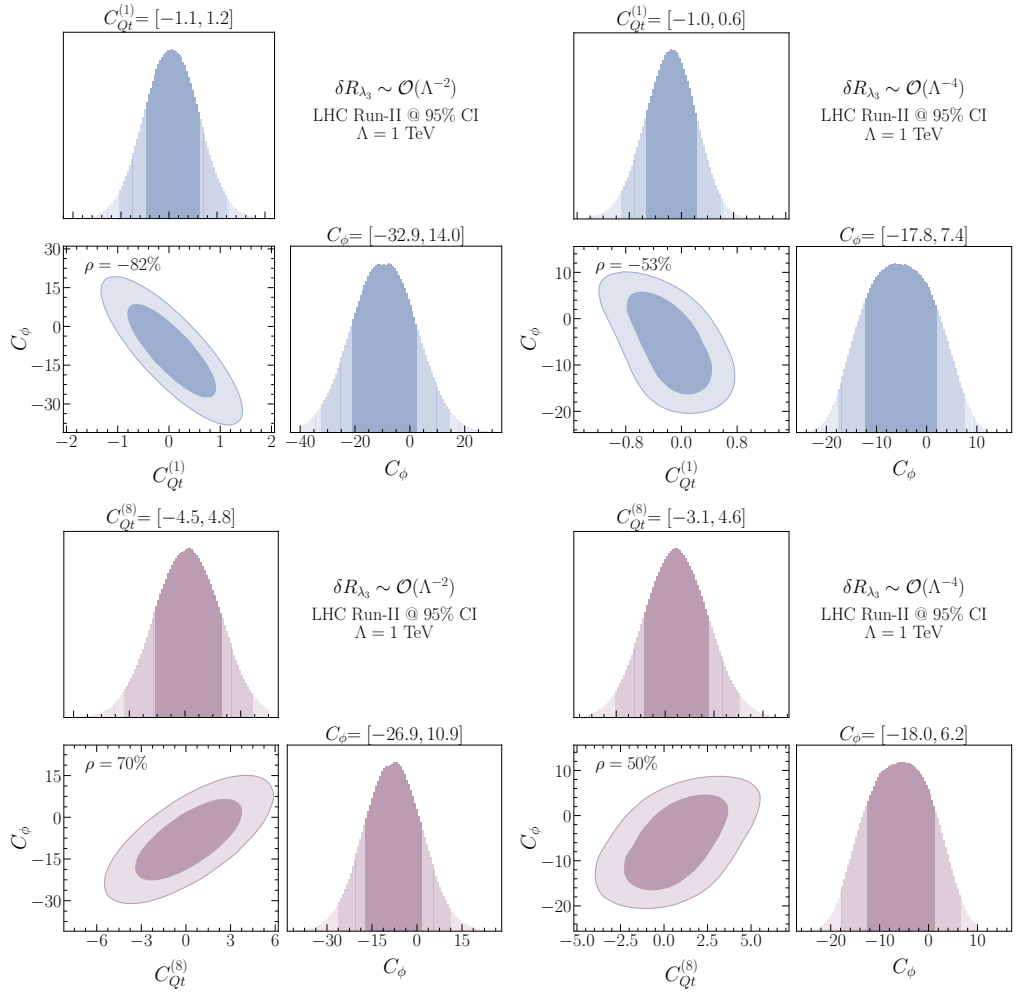

Figure 5.8. The 68% and 95% highest density posterior contours of the posterior distribution of C_ϕ with $C_{Qt}^{(1)}$ (up) and C_ϕ with $C_{Qt}^{(8)}$ (down) with the marginalised one-dimensional posteriors for each of the Wilson coefficients and their 68% and 95% HDPIs (shown above in numbers the 95% CI bounds). The limits correspond to values of the Wilson coefficients evaluated at the scale $\Lambda = 1$ TeV. On the left we used the linear scheme in δR_{λ_3} while on the right we keep up to quadratic terms in δR_{λ_3}.

In Figure 5.11 we confront the results of the fits to Run-2 data with the projections for the HL-LHC for single parameter fits. For the operators $\mathcal{O}_{Qt}^{(1),(8)}$ the constraining power of the HL-LHC is roughly a factor two better as the current bounds we could set from single Higgs data, while for the operators $\mathcal{O}_{QtQb}^{(1),(8)}$ the improvement is a little less.

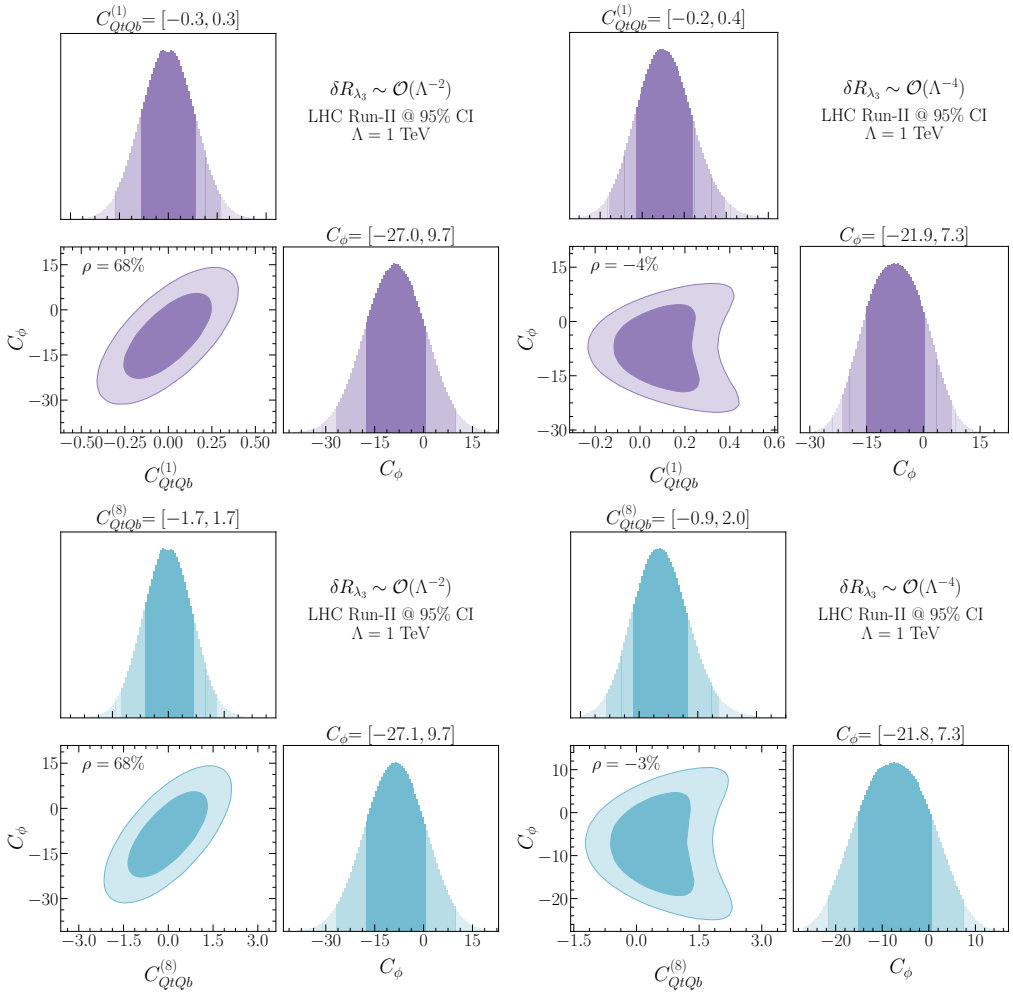

Figure 5.9. The 68% and 95% highest density posterior contours of the posterior distribution of C_ϕ with $C^{(1)}_{QtQb}$ (up) and C_ϕ with $C^{(8)}_{QtQb}$ (down) with the marginalised one-dimensional posteriors for each of the Wilson coefficients. and their 68% and 95% HDPIs (shown above in numbers the 95% CI bounds). The limits correspond to values of the Wilson coefficients evaluated at the scale $\Lambda = 1$ TeV. Similar to $C^{(1),(8)}_{Qt}$, the left plot shows the linearised δR_{λ_3} while the right one shows the quadratic scheme in the trilinear Higgs self-coupling modification. Due to the degeneracy between these Wilson coefficients the posterior contours and their marginalised intervals look very similar for both of them (except for the range they cover).

In Figure 5.13 we show the limits on C_ϕ in a single parameter fit for Run-2 and the projections for the HL-LHC including in δR_{λ_3} up to order $\mathcal{O}(1/\Lambda^2)$ or $\mathcal{O}(1/\Lambda^4)$. While for Run-2 data the inclusion of $\mathcal{O}(1/\Lambda^4)$ made a huge difference, this is less pronounced

for the HL-LHC projections. Our results are very similar to the projections presented in a κ_λ fit in [109]. We confront this also with data from searches for Higgs pair production 139 fb^{-1} [105] and HL-LHC projections [110] on Higgs pair production, showing that Higgs pair production will still allow to set stronger limits on C_ϕ.

5.4 Summary and discussion

In this paper, we have computed the NLO corrections induced by third generation four-quark operators in Higgs observables that are relevant for its production and decay at the LHC. Our results show that such processes are sensitive to the all possible chiral structures for the third generation four-quark operators in the dimension-six SMEFT, but in different degrees. Operators with different chiralities are, for instance, the only ones that can contribute to Higgs production via gluon fusion, and the decay of the Higgs boson to gluons, photons and bottom quarks pairs. The latter are particularly sensitive to the top-bottom operators $\mathcal{O}_{QtQb}^{(1),(8)}$, which then also significantly affect the total decay width. In the associate production of a Higgs boson with a top quark pair, on the other hand, all the third generation four-fermion operators enter. Sensitivity to four-quark operators where all fields have the same chirality, however, is only possible for large values of the Wilson coefficients, in a way that they can generate contributions beyond the size of current theory uncertainties. The $t\bar{t}h$ process is also rather important in setting limits on the four-quark operators $\mathcal{O}_{Qt}^{(1)}$ and $\mathcal{O}_{Qt}^{(8)}$, due to the comparatively large NLO corrections they induce in this process with respect to others. It also breaks a degeneracy among the Wilson coefficients of those two operators, which always appear in a single combination for all other processes.

To illustrate the constraining power of single Higgs processes in bounding these four-quark operators, we performed several simplified fits to these interactions and find that the resulting limits from our fits are, in some cases, comparable or better than similar results obtained from top data [74, 77].

We have also performed a combined fit including the above-mentioned four-quark operators and the operator $\left(\phi^\dagger\phi\right)^3$, that modifies the Higgs potential and the trilinear Higgs self-coupling. Due to the lack of powerful constraints from top data, the inclusion of the four-fermion operators diminishes the power of setting limits on the trilinear Higgs self-coupling from single Higgs observables. From our analysis we conclude that, in the absence of strong direct bounds on the third-generation four-quark operators, these should be included into a global fit on Higgs data, when attempting to obtain model-independent bounds on the trilinear Higgs self-coupling. The results of our calculations are presented such that they can be easily used by the reader in truly global fits including all other interactions entering at the LO. We leave this, as well as the inclusion of differential Higgs data, to future work.

Finally, we also illustrated the increase in constraining power expected during the

high-luminosity phase of the LHC by presenting the HL-LHC projections of the above-mentioned fits.

Moving beyond hadron colliders, it must be noted that the interplay between the Higgs trilinear and four heavy-quark operators in Higgs processes is expected to be less of an issue at future leptonic Higgs factories, such as the FCC-ee [111, 112], ILC [113, 114], CEPC [115, 116] or CLIC [117, 118]. At these machines, the effects of C_ϕ are still "entangled" with those of the four-fermion operators in the Higgs rates, but only through the decay process, i.e. via the contributions to the BRs. However, Higgs production is purely electroweak, namely via Higgs-strahlung (Zh: $e^+e^- \to Zh$) or W boson fusion, and receives no contributions from the four-quark operators at the same order in perturbation theory where C_ϕ modifies these processes, i.e. NLO. Moreover, at any of these future e^+e^- Higgs factories there is the possibility of obtaining a sub-percent determination of the total Zh cross section at e^+e^- colliders, by looking at events recoiling against the Z decay products with a recoil mass around m_h. This observable is therefore completely insensitive to the four-quark operators, while still receiving NLO corrections from C_ϕ. Although, in practice, in a global fit one needs to use data from all the various Higgs rates at two different energies to constrain all possible couplings entering at LO in the Higgs processes and also obtain a precise determination of C_ϕ [119], the previous reasons should facilitate the interpretation of the single-Higgs bounds on the Higgs self-coupling at e^+e^- machines.

We conclude this paper with a few words on the relevance of the results presented here when interpreted from the point of view of specific models of new physics. In particular, one important question is *are there models where one expects large contributions to four-top operators while all other interactions entering in Higgs processes are kept small?* Indeed, large contributions to four-top operators can be expected in various BSM scenarios.[12] For instance, in Composite Higgs Models, in which the top quark couples to the strong dynamics by partial compositeness, one expects on dimensional grounds that some of the four-top quark operators are of order $1/f^2$, where f indicates the scale of strong dynamics [120]. By its own nature, however, Composite Higgs models also predict sizeable contributions to the single Higgs couplings $\sim 1/f^2$. While, in general, sizeable modifications of the Higgs interactions are typically expected in scenarios motivated by "naturalness", this is not necessarily the case in other scenarios. It is indeed possible to think of simple models where modifications of the Higgs self-interactions or contributions to four-quark operators are the only corrections induced by the dimension-six interactions at tree level, see [121]. Thinking, for instance, in terms of scalar extensions of the SM, there are several types of colored scalars whose tree-level effects at low energies can be represented by four-quark operators only, e.g. for complex scalars in the $(6,1)_{\frac{1}{3}}$ and

[12] Generically, models where four-top interactions are much larger than four-fermion operators of the first and second generation can be easily conceived from some UV dynamics coupling mostly to the third generation of quarks hence respecting the Yukawa hierarchies.

$(8,2)_{\frac{1}{2}}$ SM representations (Ω_1 and Φ in the notation of [121]). If these colored states are the only moderately heavy new particles, our results can provide another handle to constrain such extensions. One must be careful, though, as a consistent interpretation of our results for any such models would require to include higher-order corrections in the matching to the SMEFT. At that level, as shown e.g. by the recent results in [122], multiple contributions that modify Higgs processes at LO are generated at the one-loop level, and are therefore equally important as the NLO effects of the (tree-level) generated four-quark operators.[13] In any case, one must note that, even if similar size contributions to single Higgs processes are generated, the four-top or Higgs trilinear effects can provide extra information on the model. For instance, in some of the most common scalar extensions of the SM, with an extra Higgs doublet, $\varphi \sim (1,2)_{\frac{1}{2}}$, tree-level contributions to some of the four-heavy-quark operators discussed in this paper are generated together with modifications on the Higgs trilinear self-coupling. These two effects are independent but they are both correlated with the, also tree level, modifications of the single Higgs couplings. Essentially, the LO effects on Higgs observables are proportional to $\lambda_\varphi y_\varphi^f$, where λ_φ is the scalar interaction strength of the $(\varphi^\dagger\phi)(\phi^\dagger\phi)$ operator and y_φ^f the new scalar Yukawa interaction strength, whereas the NLO effects are proportional to the square of each separate coupling. Hence, these effects might help to resolve (even if only weakly) the flat directions in the model parameter space that would appear in a LO global fit. At the end of the day, for a proper interpretation of the SMEFT results in terms of the widest possible class of BSM models, all the above simply remind us of the importance of being global in SMEFT analyses, to which our work contributes by including effects in Higgs physics that enter at the same order in perturbation theory as modifications of the Higgs self-coupling.

[13] Furthermore, given that some SMEFT interactions induce tree-level contributions to Higgs processes that in the SM are generated at the loop level, e.g. $\mathcal{O}_{\phi G}$ in gluon fusion, a consistent interpretation in terms of new physics models may require to include up to two-loop effects in the matching for such operators, for which there are currently no results or tools available.

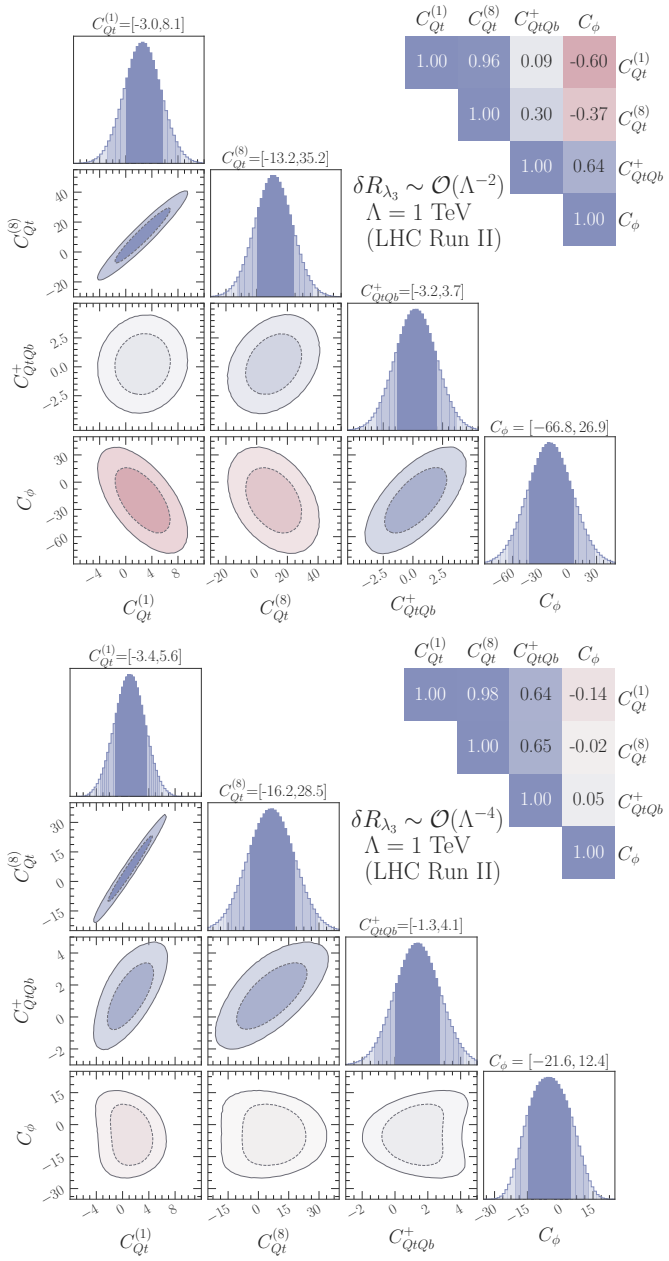

Figure 5.10. The marginalised 68% and 95% HDPI's for the four-parameter fits including the different four-quark Wilson coefficients and C_ϕ. The numbers above the plots show the 95% CI bounds while the correlations are given on the top-right side. These limits correspond to values of the Wilson coefficients evaluated at the scale $\Lambda = 1$ TeV. The upper panel shows the fit including up to $\mathcal{O}(1/\Lambda^2)$ in δR_{λ_3} while the lower one shows the fit with including also $\mathcal{O}(1/\Lambda^4)$.

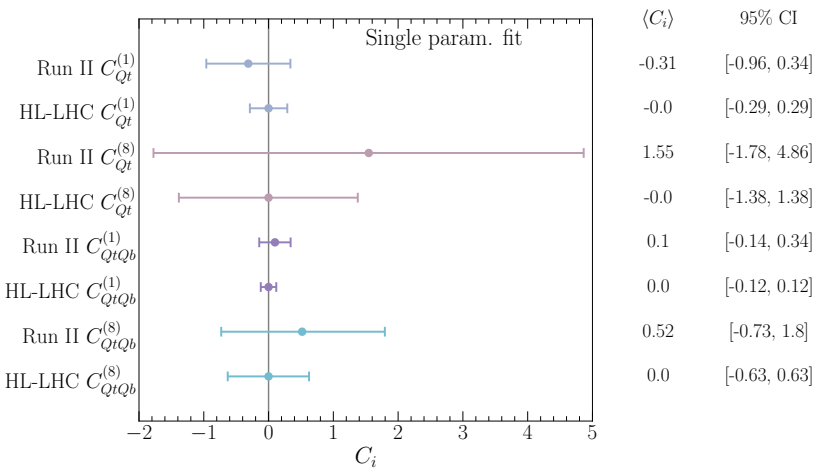

Figure 5.11. Results of a single parameter fit showing the improvement in constraining power of the HL-LHC over the current bounds from Run-2 data. The limits correspond to values of the Wilson coefficients evaluated at the scale $\Lambda = 1$ TeV.

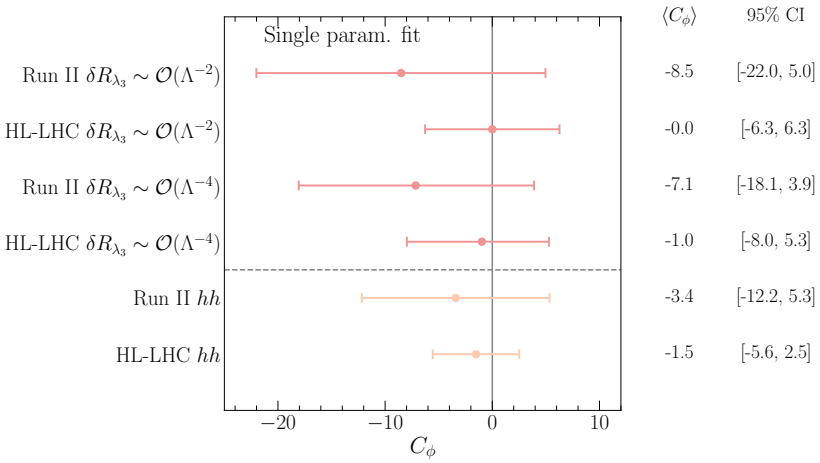

Figure 5.12. A forest plot illustrating the means and 95% CIs of the posteriors built from the C_ϕ in a single-parameter fit, showing also the differences in including terms of $\mathcal{O}(1/\Lambda^2)$ or up to $\mathcal{O}(1/\Lambda^4)$ in the definition of δR_{λ_3}. For comparison, also the limits and projections from searches for Higgs pair production are shown.

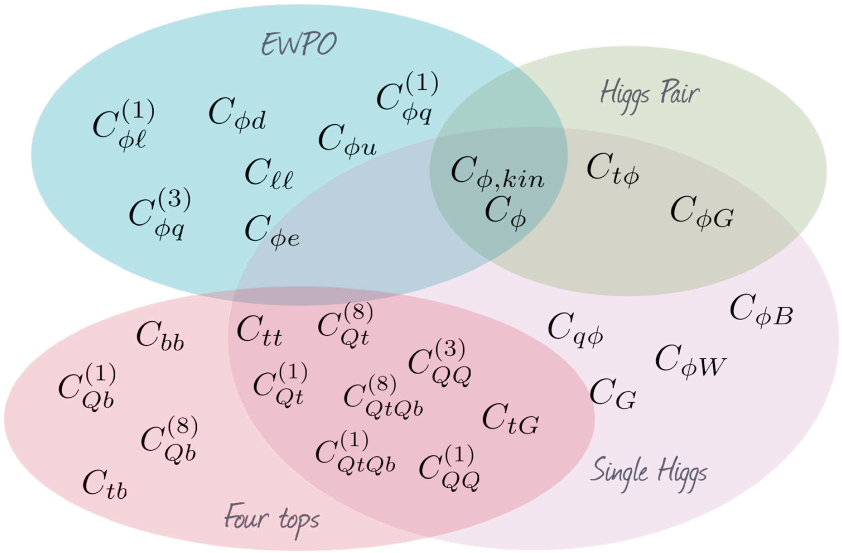

Figure 5.13. A forest plot illustrating the means and 95% CIs of the posteriors built from the C_ϕ in a single-parameter fit, showing also the differences in including terms of $\mathcal{O}(1/\Lambda^2)$ or up to $\mathcal{O}(1/\Lambda^4)$ in the definition of δR_{λ_3}. For comparison, also the limits and projections from searches for Higgs pair production are shown.

6 Virtual two-loop calculation of Zh production via gluon fusion

As we have seen in the previous sections, Higgs couplings to the weak vector bosons, i.e. Z and W is approaching the precision level. Moreover, the associated Higgs production with these bosons is the first channel used to observer the Higgs decaying into beauty quarks $h \to b\bar{b}$ by both ATLAS and CMS [123, 124]. Hence, the Vh Higgs production channels are important channels to look for in the future runs of the LHC for better measurement of the VVh coupling as well as Higgs coupling to the beauty quark. As the statistical and systematic uncertainties coming from the experimental setup of the LHC will be eventually reduced in the future runs, due to higher integrated luminosity, upgraded detectors and improved analysis techniques. There is an exigency to reduce theoretical uncertainties emerging from the perturbative calculations of cross-sections. In order to accomplish that, one should include more terms in the perturbative expansion in the couplings, particularly the strong coupling α_s. In this chapter, we are interested in the channel $pp \to Zh$, which is quark-initiated tree-level process at LO interpreted as **Drell-Yan process** [125, 126]. This process has been computed up to next-to-next-to-leading-order (NNLO) in QCD ($\sim \alpha_s^2$), and at next-to-leading-order (NLO) in the EW interactions ($\sim \alpha^2$) [127].

Despite arising for the first time at NNLO in perturbation theory to the partonic cross-section, the gluon fusion channel $gg \to Zh$ has a non-negligible contribution to the hadronic cross-section $pp \to Zh$, which could reach $> 16\%$ of the total cross-section contribution at 14 TeV [48], see Figure 6.1. The contribution becomes more significant when looking at large invariant mass bins in the differential cross-section. This is due to the significant abundance of gluons at the LHC for large energy faction Q as well as the extra enhancement coming from the top quark initiated contribution near the $t\bar{t}$ threshold [128]. The gluon fusion channel has a higher scale uncertainties than the quark induced one,as one can see from the uncertainty band of Figure 6.1 predominantly coming from the gluon fusion part σ_{gg}. With that in mind, and the absence of gluon fusion channel for Wh channel, the Zh channel has higher theoretical uncertainties. This further motivates NLO calculation of the $gg \to Zh$ channel to higher orders in perturbation theory, such that these uncertainties get reduced. Facilitating the precision measurement of the Zh channel at the future LHC runs, which in term provides better constraints on several observables, such as sign and magnitude of the top Yukawa coupling, dipole operators [129]. Additionally, this channel can receive contributions from new particles

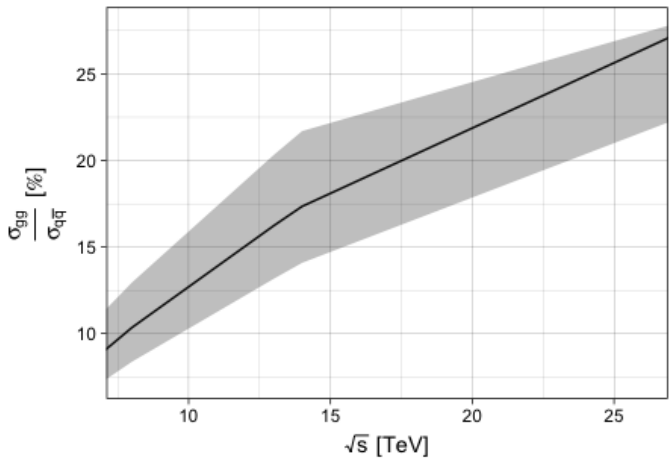

Figure 6.1. The ratio of the LO gluon fusion production cross-section $gg \to Zh$ (σ_{gg}) with respect to the NLO Drell-Yan process $q\bar{q} \to Zh$ cross-section ($\sigma_{q\bar{q}}$) at a pp collider with centre-of-mass energy $\sqrt{s}$. The error band captures the total theoretical uncertainties on both cross-sections dominated by σ_{gg} .

[130], particularly at the large invariant-mass region where the gluon fusion contribution becomes more important. Therefore, better understanding of the SM prediction of the Zh gluon fusion channel is crucial for both the SM precision measurements of Higgs production within the SM and for testing NP in this channel, e.g. new vector-like leptons.

The leading order (LO) contribution to the $gg \to Zh$ amplitude, given by one-loop diagrams, was computed exactly in refs.[131, 132]. However, for the NLO, the virtual corrections contain multi-scale two-loop integrals some of which are still not known analytically (for the box diagram). The first computation of the NLO terms has been done by [133] using an asymptotic expansion in the limit $m_t \to \infty$ and $m_b = 0$, and pointed to a K-factor of about ~ 2. Later, the computation has been improved via soft gluon resummation, and including NLL terms found in ref.[134], the NLL terms has been matched to the fixed NLO computation of [133]. Top quark mass effects to the $gg \to Zh$ process were first implemented using a combination of large-m_t expansion (LME) and Padé approximants [135]. A data-driven approach to extract the gluon fusion dominated non-Drell-Yan part of Zh production using the known relation between Wh and Zh associated production when only the Drell-Yan component of the two processes is considered has been investigated in ref.[136]. The differential distributions of $gg \to Zh$ at NLO was studied in ref.[137] via LO matrix element matching.

More recent studies of the NLO virtual corrections to this process were based on the high-energy (HE) expansion improved by Padé approximants with the LME, which

extended the validity range of the HE expansion [138]. However, this expansion is only valid for in the invariant mass region $\sqrt{\hat{s}} \gtrsim 750\,\text{GeV}$ and $\sqrt{\hat{s}} \lesssim 350\,\text{GeV}$, which only covers $\sim 32\%$ of the hadronic cross section. Additionally, numerical computation of the two-loop virtual corrections, though implemented exactly in [139], are rather slow for practical use in MC simulations. This highlights the importance of an analytical method that can cover the remaining region of the cross-section and can be merged with the HE expansion via Padé approximants. Fortunately, the two-loop corrections to the triangle diagrams can be computed exactly. And the loop integrals appearing in the box correction having no analytic expression can be expanded in small Z (or Higgs) transverse momentum, p_T. This method was first used for Higgs pair production in [140], to compute the NLO virtual corrections to the box diagrams in the forward kinematics. In this chapter, I discuss the method and results of the two-loop calculation of the triangle and p_T expansion of Zh process published in [141].

This chapter is structured as follows : In section 6.1 contains the general notation we have used for the gluon fusion Zh process calculation. Then, in subsection 6.1.1 the transverse momentum expansion method is discussed. Calculation of the LO form-factors in the transverse momentum expansion is illustrated in section 6.2 as a proof of concept for the p_T-expansion technique. Outline of the two-loop calculation is discussed in section 6.3. Finally, in section 6.4, the results of our calculation are shown with concluding remarks at the end.

6.1 General notation

The amplitude $g_a^\mu(p_1)g_b^\nu(p_2) \to Z^\rho(p_3)h(p_4)$ can be written as

$$\mathcal{A} = i\sqrt{2}\frac{m_Z G_F \frac{\alpha_s^0}{4\pi}(\mu_R)}{\pi}\delta_{ab}\epsilon_\mu^a(p_1)\epsilon_\nu^b(p_2)\epsilon_\rho(p_3)\hat{\mathcal{A}}^{\mu\nu\rho}(p_1,p_2,p_3), \tag{6.1}$$

$$\hat{\mathcal{A}}^{\mu\nu\rho}(p_1,p_2,p_3) = \sum_{i=1}^{6}\mathcal{P}_i^{\mu\nu\rho}(p_1,p_2,p_3)\mathcal{A}_i(\hat{s},\hat{t},\hat{u},m_t,m_h,m_Z), \tag{6.2}$$

where μ_R is the renormalisation scale and $\epsilon_\mu^a(p_1)\epsilon_\nu^b(p_2)\epsilon_\rho(p_3)$ are the polarization vectors of the gluons and the Z boson, respectively. It is possible to decompose the amplitude into a maximum of 6 Lorentz structures encapsulated by the tensors $\mathcal{P}_i^{\mu\nu\rho}$. Due to the presence of the γ_5 these projectors are proportional to the Levi-Civita total anti-symmetric tensor $\epsilon^{\alpha\beta\gamma\delta}$. One can choose to an orthogonal basis explicitly shown in section A.1, such that

$$\mathcal{P}_i^{\mu\nu\rho}\mathcal{P}_{j\,\mu\nu\rho} = 0, \quad \text{for } i \neq j \tag{6.3}$$

By this choice one obtains unique form factors corresponding to each projector

$$\mathcal{A}_i(\hat{s},\hat{t},\hat{u},m_t,m_h,m_Z), \tag{6.4}$$

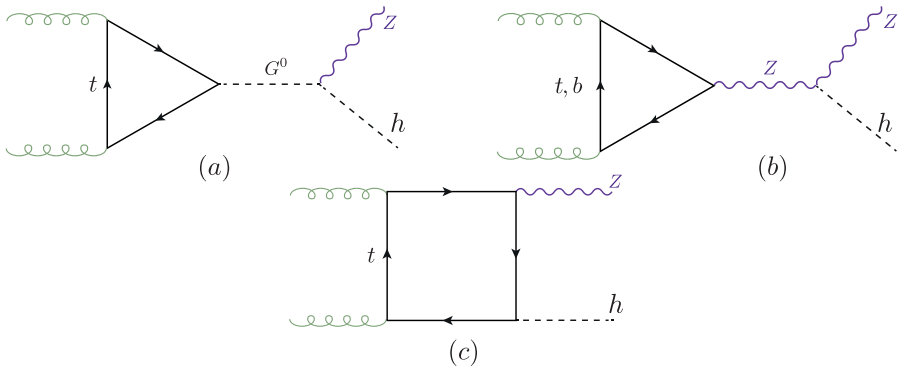

Figure 6.2. Feynman diagrams type for the LO $gg \to Zh$ process. The triangle diagrams in a general ξ gauge involve Z and the neutral Goldstone G^0 propagators.

that are multivariate complex functions of the top (m_t), Higgs (m_h) and Z (m_Z) bosons masses, and of the partonic Mandelstam variables

$$\hat{s} = (p_1 + p_2)^2, \quad \hat{t} = (p_1 + p_3)^2, \quad \hat{u} = (p_2 + p_3)^2, \tag{6.5}$$

where $\hat{s} + \hat{t} + \hat{u} = m_Z^2 + m_h^2$ and all the momenta are considered to be incoming. The form-factors $\mathcal{A}_i$ can be perturbatively expanded in orders of α_s,

$$\mathcal{A}_i = \sum_{k=0} \left(\frac{\alpha_s}{\pi}\right)^k \mathcal{A}_i^{(k)} \tag{6.6}$$

Where $\mathcal{A}_i^{(0)}$ and $\mathcal{A}_i^{(1)}$ are the LO and NLO terms, respectively. Using Fermi's Golden Rule, we can write thee Born partonic cross-section as

$$\hat{\sigma}^{(0)}(\hat{s}) = \frac{m_Z^2 G_F^2 \alpha_s(\mu_R)^2}{64\hat{s}^2(2\pi)^3} \int_{\hat{t}^-}^{\hat{t}^+} d\hat{t} \sum_i \left|\mathcal{A}_i^{(0)}\right|^2, \tag{6.7}$$

where $\hat{t}^{\pm} = [-\hat{s} + m_h^2 + m_Z^2 \pm \sqrt{(\hat{s} - m_h^2 - m_Z^2)^2 - 4m_h^2 m_Z^2}\,]/2$.

The LO has two sets of diagrams, the triangle, and box diagrams shown in Figure 6.2. In (a), the triangle diagrams contains a neutral Goldstone boson G^0, instead in (b) the Z boson is mediated. The interplay between these two diagram types depends on the ξ gauge. Moreover, the Z boson is strictly off-shell, due to Furry's theorem. In the Landau gauge the Z- mediated diagrams will also vanish, this can be seen by considering the subamplitude ggZ^* which in the Landau gauge can be related to the decay of a massive vector boson with mass $\sqrt{\hat{s}}$ into two massless ones, a process that is forbidden by the

Landau-Yang theorem [142, 143]. The triangle diagrams are also proportional to the mass difference between the up and down type quarks. In this calculation, the first and second generation quarks are assumed to be massless, as well as the b quark, hence light quarks loops do not contribute to this process. The same would apply to the box diagrams (c), as they are proportional to the quark Yukawa coupling, and vanish in the massless quarks case. Moreover, triangle diagrams with $b-$ quark loops contribute to $\sim 1\%$ of the total amplitude, computed in the limit $m_b \to 0$.

6.1.1 The transverse momentum expansion

Choosing to expand in small p_T of the Z boson, the first step is expressing p_T in terms of the Mandelstam variables and masses

$$p_T^2 = \frac{\hat{t}\hat{u} - m_Z^2 m_h^2}{\hat{s}}. \tag{6.8}$$

From eq.(6.8), together with the relation between the Mandelstam variables, one finds

$$p_T^2 + \frac{m_h^2 + m_Z^2}{2} \leq \frac{\hat{s}}{4} + \frac{\Delta_m^2}{\hat{s}}, \tag{6.9}$$

where $\Delta_m = (m_h^2 - m_Z^2)/2$. Eq.(6.9) implies $p_T^2/\hat{s} < 1$ that, together with the kinematical constraints $m_h^2/\hat{s} < 1$ and $m_Z^2/\hat{s} < 1$. With these relations in mind, one can expand the amplitudes in terms of small $p_T^2/\hat{s}$, $m_h^2/\hat{s}$ and $m_Z^2/\hat{s}$, which is technically valid throughout the whole phase space, contrary to the LME and HE limits. The caveat for this expansion is that, the amplitude does not depend on p_T explicitly. Instead, one would expand in the reduced Mandelstam variables $t'/s' \ll 1$ or $u'/s' \ll 1$, defined as

$$s' = p_1 \cdot p_2 = \frac{\hat{s}}{2}, \quad t' = p_1 \cdot p_3 = \frac{\hat{t} - m_Z^2}{2}, \quad u' = p_2 \cdot p_3 = \frac{\hat{u} - m_Z^2}{2} \tag{6.10}$$

and satisfy

$$s' + t' + u' = \Delta_m. \tag{6.11}$$

The choice of the expansion parameter t' or u' depends whether one expands in the forward or backwards kinematics. Because the process $gg \to Zh$, has two particles in the final states with different masses, the amplitude is not symmetric under the their exchange. One therefore cannot compute the cross-section by integrating only the forward-expanded amplitude [141], contrary what has been done for the Higgs pair [140]. In order to overcome this issue, one could further examine the projectors in section A.1 and observe that they can be split into symmetric and anti-symmetric parts with respect to the exchange $t' \leftrightarrow u'$. Then, expand the symmetric part in the forward kinematics, like the Higgs pair case. As for the anti-symmetric part, the antisymmetric factor is simply extracted by multiplying the form-factors by $1/(\hat{t} - \hat{u})$, written as $1/(2s' - 4t' - 2\Delta_m)$,

then perform the expansion in the forward kinematics and finally multiply back by $(\hat{t}-\hat{u})$.

In order to implement the p_T-expansion at the Feynman diagrams level we start by splitting the momenta into longitudinal and transverse with respect to the beam direction, by introducing the vector [140],

$$r^\mu = p_1^\mu + p_3^\mu, \tag{6.12}$$

which satisfies

$$r^2 = \hat{t}, \quad r \cdot p_1 = \frac{\hat{t} - m_Z^2}{2}, \quad r \cdot p_2 = -\frac{\hat{t} - m_h^2}{2}, \tag{6.13}$$

and hence can be also written as

$$r^\mu = -\frac{\hat{t} - m_h^2}{\hat{s}} p_1^\mu + \frac{\hat{t} - m_Z^2}{\hat{s}} p_2^\mu + r_\perp^\mu = \frac{t'}{s'}\left(p_2^\mu - p_1^\mu\right) - \frac{\Delta_m}{s'} p_1^\mu + r_\perp^\mu, \tag{6.14}$$

where

$$r_\perp^2 = -p_T^2. \tag{6.15}$$

substituting the definition of p_T from eq.(6.8) one obtains

$$t' = -\frac{s'}{2}\left\{1 - \frac{\Delta_m}{s'} \pm \sqrt{\left(1 - \frac{\Delta_m}{s'}\right)^2 - 2\frac{p_T^2 + m_Z^2}{s'}}\right\} \tag{6.16}$$

implying that the expansion in small p_T (the minus sign case in eq.(6.16)) can be realized at the level of Feynman diagrams, by expanding the propagators in terms of the vector r^μ around $r^\mu \sim 0$ or, equivalently, $p_3^\mu \sim -p_1^\mu$, see eq.(6.14).

6.2 Born cross-section in the p_T-expansion

As a baseline test for the validity and convergence behaviour of the p_T expansion we start by computing the LO amplitude, and consequently the Born partonic cross-section in the p_T expansion then compare it with the exact results found in [131, 132] .
Starting by defining the one-loop functions appearing in the similar calculation of the Born cross-section for $gg \to hh$ in the same expansion carried out in ref. [140]

$$B_0[\hat{s}, m_t^2, m_t^2] \equiv B_0^+, \qquad B_0[-\hat{s}, m_t^2, m_t^2] \equiv B_0^-, \tag{6.17}$$

$$C_0[0, 0, \hat{s}, m_t^2, m_t^2, m_t^2] \equiv C_0^+, \qquad C_0[0, 0, -\hat{s}, m_t^2, m_t^2, m_t^2] \equiv C_0^- \tag{6.18}$$

$$B_0[q^2, m_1^2, m_2^2] = \frac{1}{i\pi^2}\int \frac{d^n k}{\mu^{n-4}} \frac{1}{(k^2 - m_1^2)((k+q)^2 - m_2^2)}, \tag{6.19}$$

$$C_0[q_a^2, q_b^2, (q_a+q_b)^2, m_1^2, m_2^2, m_3^2] = \frac{1}{i\pi^2}\int \frac{d^dk}{\mu^{d-4}} \frac{1}{[k^2-m_1^2][(k+q_a)^2-m_2^2][(k-q_b)^2-m_3^2]} \tag{6.20}$$

are the Passarino-Veltman functions [144], with d the dimension of spacetime and μ the 't Hooft mass. There are only two non-vanishing form-factors at LO, one is symmetric $\mathcal{A}_2$, and the other is antisymmetric $\mathcal{A}_6$, in the p_T-expansion, these form-factors are give by, up to order $\mathcal{O}(p_T^2)$

$$\mathcal{A}_2^{(0,\triangle)} = -\frac{p_T}{\sqrt{2}\,(m_Z^2+p_T^2)}(\hat{s}-\Delta_m)\,m_t^2 C_0^+, \tag{6.21}$$

$$\begin{aligned}
\mathcal{A}_2^{(0,\square)} &= \frac{p_T}{\sqrt{2}\,(m_Z^2+p_T^2)}\Bigg\{ \\
&\left(m_t^2 - m_Z^2\frac{\hat{s}-6m_t^2}{4\hat{s}} - p_T^2\frac{12m_t^4-16m_t^2\hat{s}+\hat{s}^2}{12\hat{s}^2}\right)B_0^+ \\
&- \left(m_t^2 - \Delta_m\frac{m_t^2}{(4m_t^2+\hat{s})} + m_Z^2\frac{24m_t^4-6m_t^2\hat{s}-\hat{s}^2}{4\hat{s}\,(4m_t^2+\hat{s})} - \right. \\
&\qquad \left. p_T^2\frac{48m_t^6-68m_t^4\hat{s}-4m_t^2\hat{s}^2+\hat{s}^3}{12\hat{s}^2\,(4m_t^2+\hat{s})}\right)B_0^- \\
&+ \left(2m_t^2 - \Delta_m + m_Z^2\frac{3m_t^2-\hat{s}}{\hat{s}} + p_T^2\frac{3m_t^2\hat{s}-2m_t^4}{\hat{s}^2}\right)m_t^2\,C_0^- \\
&+ \left(\hat{s}-2m_t^2 + m_Z^2\frac{\hat{s}-3m_t^2}{\hat{s}} + p_T^2\frac{2m_t^4-3m_t^2\hat{s}+\hat{s}^2}{\hat{s}^2}\right)m_t^2\,C_0^+ \\
&+ \log\left(\frac{m_t^2}{\mu^2}\right)\frac{m_t^2}{(4m_t^2+\hat{s})}\left(\Delta_m + 2m_Z^2 + p_T^2\frac{2\hat{s}-2m_t^2}{3\hat{s}}\right) \\
&- \Delta_m\frac{2m_t^2}{(4m_t^2+\hat{s})} + m_Z^2\frac{\hat{s}-12m_t^2}{4\,(4m_t^2+\hat{s})} + p_T^2\frac{8m_t^4-2m_t^2\hat{s}+\hat{s}^2}{4\hat{s}(4m_t^2+\hat{s})}\Bigg\},
\end{aligned} \tag{6.22}$$

and

$$\mathcal{A}_6^{(0,\triangle)} = 0, \tag{6.23}$$

$$\mathcal{A}_6^{(0,\square)} = \frac{\hat{t}-\hat{u}}{\hat{s}^2}\, p_T \left[\frac{m_t^2}{2}\left(B_0^- - B_0^+\right) - \frac{\hat{s}}{4} \right.$$
$$\left. - \frac{2m_t^2+\hat{s}}{2} m_t^2\, C_0^- + \frac{2m_t^2-\hat{s}}{2} m_t^2\, C_0^+ \right], \tag{6.24}$$

where these form-factors were divided into triangle ($\triangle$) and box ($\square$) contributions, and B_0 functions are understood as the finite part of the integrals on the right hand side of eq.(6.19).

Using several truncations of the p_T-expansion, and comparing it to the exact LO result, one can see in Figure 6.3 the exact Born partonic LO cross section (red line) as a function of the invariant mass of the Zj system, M_{Zh}, in comparison to the p_T-expansions. For the numerical evaluation of the cross section here and in the following, we used as SM input parameters

$$m_Z = 91.1876 \text{ GeV}, \quad m_h = 125.1\,\text{GeV}, \quad m_t = 173.21 \text{ GeV},$$
$$m_b = 0 \text{ GeV}, \quad G_F = 1.16637 \text{ GeV}^{-2}, \quad \alpha_s(m_Z) = 0.118.$$

From the ratio plotted in the lower panel of Figure 6.3 , we observe that the $\mathcal{O}(p_T^0)$ expansion is in good agreement with the exact result when $M_{Zh} \lesssim 2m_t$. Inclusion of higher order terms up tp $\mathcal{O}(p_T^6)$ extended the validity of the expansion to reach $M_{Zh} \lesssim 750\,\text{GeV}$. This is the similar behaviour seen in [140] for Higgs pair. Therefore, one would expect the p_T-expanded two-loop virtual correction to be an accurate approximation with the exact (numerical) result for the region of the invariant mass of $M_{Zh} \sim 700-750\,\text{GeV}$. Similar conclusions can be seen more explicitly in Table 6.1, where it is shown that the partonic cross-section at $\mathcal{O}(p_T^4)$ agrees with the full result for $M_{ZH} \lesssim 600\,\text{GeV}$ on the permille level and the agreement further improves when $\mathcal{O}(p_T^6)$ terms are included.

6.3 NLO calculation

The virtual two-loop corrections to $gg \to Zh$ are shown in Figure 6.4, which involve corrections to the triangle topology in (a) and (b). The corrections to the box topology in (c) and a new topology , dented by double triangle in (d). Both two-loop corrections to the triangles, and the double triangle diagrams can be computed exactly analytically. However, the two-loop box diagrams contain master-integrals (MI's) that have no analytic solutions, so far. The two-loop box diagrams will be computed in the p_T-expansion.

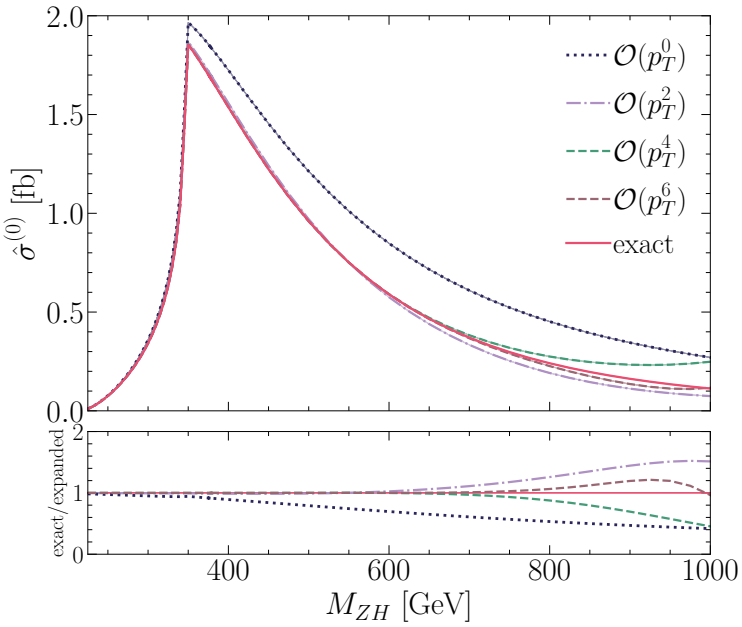

Figure 6.3. The Born partonic cross-section as a function of the invariant mass M_{Zh}. The exact (red line) is plotted together with results at different orders in the p_T-expansion (dashed lines). In the bottom part, the ratio of the full result over the p_T-expanded one at various orders is shown. This plot has been already published in [141]

6.3.1 Renormalisation

The two-loop corrections to the triangle and box diagrams contain both UV and IR divergences. The first emerges from UV divergent sub-diagrams, such as top mass renormalisation and QCD vertex correction. While the lR divergences come from massless loops. In order to remove these divergences, one introduces adequate counter-terms. On the other hand, the double triangle is both UV and IR finite.

We start by the gluon wavefunction renormalisation of the incoming gluons (external legs) such that the amplitude is renormalised by $Z_A^{1/2}$ for each gluon.

$$Z_A = 1 + \frac{\alpha_s^0}{4\pi}\frac{2}{3\epsilon}\left(\frac{\mu_R^2}{m_t^2}\right)^{\epsilon}. \tag{6.25}$$

The on-shell scheme for the top mass renormalisation has been used, in which the bare mass is replaced by the renormalised one $m_0 = Z_m m$ in the propagators this gives the

M_{Zh} [GeV]	$\mathcal{O}(p_T^0)$	$\mathcal{O}(p_T^2)$	$\mathcal{O}(p_T^4)$	$\mathcal{O}(p_T^6)$	full
300	0.3547	0.3393	0.3373	0.3371	0.3371
350	1.9385	1.8413	1.8292	1.8279	1.8278
400	1.6990	1.5347	1.5161	1.5143	1.5142
600	0.8328	0.5653	0.5804	0.5792	0.5794
750	0.5129	0.2482	0.3129	0.2841	0.2919

Table 6.1. The partonic cross section $\hat{\sigma}^{(0)}$ at various orders in p_T and the full computation for several values of M_{Zh}, This table has been already published in [141].

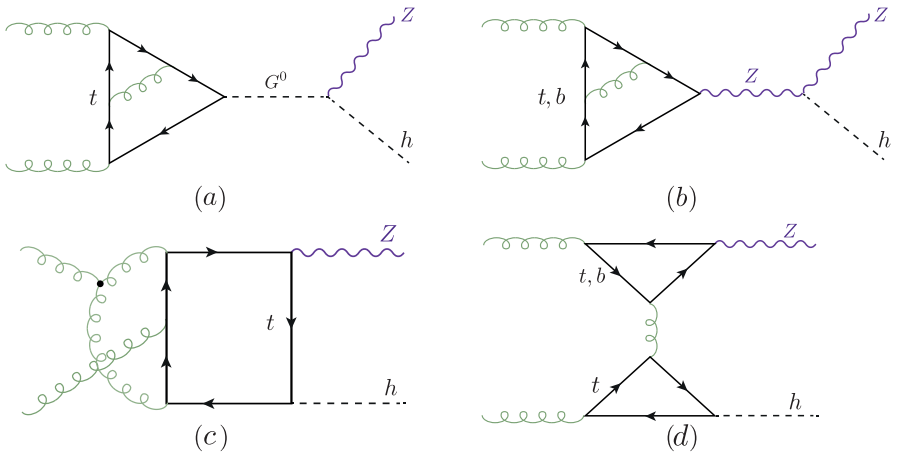

Figure 6.4. Feynman diagrams types for the virtual NLO corrections to the $gg \to Zh$ process.

$\overline{\text{MS}}$ renormalised mass.

$$Z_m = 1 + C_F \frac{3}{\epsilon}. \tag{6.26}$$

In order to convert the mass definition to the on-shell scheme we add the finite renormalisation term

$$Z_m^{OS} = 1 - 2C_F, \tag{6.27}$$

here $C_F = (N_c^2 - 1)/2N_c$ is one of the two Casimir invariants of QCD along with $C_A = N_c$. The $q\bar{q}g$ vertex correction involves a renormalisation of the strong couplings constant α_s which is done via replacing the bare constant α_s^0 with the renormalised one, hence it becomes $\alpha_s^0 = \frac{\mu_R^{2\epsilon}}{S_\epsilon} Z_{\alpha_s} \alpha_s$, where

$$Z_{\alpha_s} = 1 - \frac{\alpha_s}{4\pi} \frac{1}{\epsilon} \left(\beta_0 - \frac{2}{3}\right) \left(\frac{\mu_R^2}{m_t^2}\right)^\epsilon, \tag{6.28}$$

and the constant $\beta_0 = \frac{11}{3} C_A - \frac{2}{3} N_f$, where N_f is the number of "active" flavours. The 5-flavour scheme $N_f = 5$ is adopted here.

The loop integrals were evaluated via dimensional regularisation in $d = 4 - 2\epsilon$ dimensions. Which requires some caution when γ_5 is present in the amplitude. We let γ_5 naively anti-commute with all d-dimensional γ_μ's and then correct that with the finite renormalisation constant known as **Larin counter-term** [145]

$$Z_5 = 1 - 2\, C_F. \tag{6.29}$$

The renormalised amplitude is written as

$$\mathcal{M}(\alpha_s, m, \mu_R) = Z_A \mathcal{M}(\alpha_s^0, m^0). \tag{6.30}$$

Putting all the above substitutions together, we get the renormalised two-loop form-factor:

$$(\mathcal{A}^{(1)})^R = \mathcal{A}^{(1)} - \mathcal{A}^{(0)}_{UV} - \mathcal{A}^{(0)}_{UV,m} + \mathcal{A}^{(0)}_{\text{Larin}} \tag{6.31}$$

$$\begin{aligned} \mathcal{A}^{(0)}_{UV} &= \frac{\alpha_s}{4\pi} \frac{\beta_0}{\epsilon} \left(\frac{\mu_R^2}{\hat{s}}\right)^{-\epsilon} \mathcal{A}^{(0)}. \\ \mathcal{A}^{(0)}_{UV,m} &= \frac{\alpha_s}{4\pi} \left(\frac{3}{\epsilon} - 2\right) C_F \left(\frac{\mu_R^2}{\hat{s}}\right)^{-\epsilon} m^0 \partial_m \mathcal{A}^{(0)}. \end{aligned} \tag{6.32}$$

$$\mathcal{A}^{(0)}_{\text{Larin}} = -\frac{\alpha_s}{4\pi} C_F \mathcal{A}^{(0)}.$$

The following IR-counter-term is used in order to cancel the IR divergences.

$$\mathcal{A}_{IR}^{(0)} = \frac{e^{\gamma_E \epsilon}}{\Gamma(1-\epsilon)} \frac{\alpha_s}{4\pi} \left(\frac{\beta_0}{\epsilon} + \frac{C_A}{\epsilon^2} \right) \left(\frac{\mu_R^2}{\hat{s}} \right)^{2\epsilon} \mathcal{A}^{(0)} \tag{6.33}$$

The one-loop form-factors, need to be expanded up to order $\mathcal{O}(\epsilon^2)$, for the UV and IR counter-terms.

6.3.2 Calculation of the exact virtual corrections

The two-loop calculations of the triangle digrams involves the diagrams of with virtual Z^* and G^0, depending on the gauge of choice. Observations found in ref.[133] shows that due to Landau-Yang theorem in the Landau gauge the diagrams with the Z^* exchange vanishes. Therefore, the part of the top triangle diagrams can be obtained from the decay amplitude of a pseudoscalar boson into two gluons which is known in the literature in the full mass dependence up to NLO terms [146, 147]. On the contrary, in the unitary gauge, the NLO calculation needs to be done with the Z^* exchange diagrams only. The calculations result in apparently different Lorentz structures, that are linked via the Schouten identity

$$q^\alpha \epsilon^{\beta\gamma\delta\phi} + q^\beta \epsilon^{\gamma\delta\phi\alpha} + q^\gamma \epsilon^{\delta\phi\alpha\beta} + q^\gamma \epsilon^{\delta\phi\alpha\beta} + q^\delta \epsilon^{\phi\alpha\beta\gamma} + q^\phi \epsilon^{\alpha\beta\gamma\delta} = 0 \tag{6.34}$$

A cross-check has been preformed in order to ensure that the NLO calculation introduces no new Lorentz structures, and gives the same result in a general R_ξ gauge as the results in [146, 147]. The two-loop calculation has been carried out in R_ξ gauge. The amplitudes have been automatically generated by `FeynArts` [82] and contracted with the projectors as defined in section A.1 using `FeynCalc` [148, 149] and `Package X` [150] and in-house Mathematica routines. The two-loop integrals were reduced to a set of master integrals MI, illustrated graphically in Figure 6.5 using `Kira` [151]. These MI's are either products of one-loop functions (a)-(c), (e),(f),(h) and (l) or can be found in the literature [147, 152]. Their implementation in our calculation has been validated numerically using `SecDec` [153, 154]. The virtual correction for the triangle diagrams can be separated according to their colour factors into

$$\mathcal{A}^{(1)} = C_F \mathcal{A}_{CF}^{(1)} + C_A \mathcal{A}_{CA}^{(1)}, \tag{6.35}$$

The C_A part contains a double pole $\mathcal{O}(1/\epsilon^2)$ and a single pole $\mathcal{O}(1/\epsilon)$, both coming from the IR divergence. Whilst the C_F part contains a UV divergent pole that needs to be cured via mass renormalisation. The poles do not have a dependence on the renormalisation scale μ_R. However, there is a dependence on that scale in the finite part, as well. No new Lorentz structures appeared, and the final result in R_ξ matched the one found in [146, 147] for the Landau gauge. The explicit results are shown in **??**

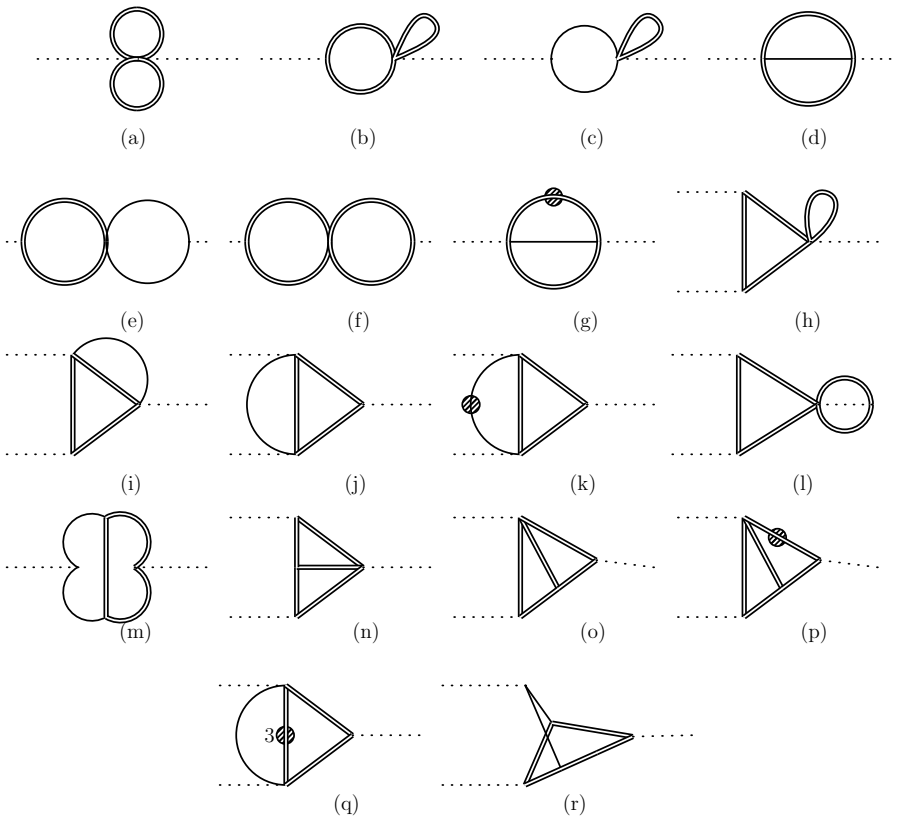

Figure 6.5. The list of two-loop master integrals (MI's) resulting from the reduction of the two-loop triangle corrections, and the product of one-loop MI's appearing in this list also appear in the calculation of the double-triangle diagrams. A single line denotes a massless propagator, while a double line denotes a massive one. The dot denotes a squared propagator, unless the number of the exponent is indicated, here only 3 appears in diagram (q).

The calculation of the double triangle diagrams (d) of Figure 6.4 is fairly straightforward, all of the integrals can be rewritten in terms of products of one-loop functions. All of the Lorentz structures appear in the double triangle except for $\mathcal{P}_6$, analogous to the triangle case. The explicit forms of form-factors corresponding to these structures are presented in **??**. Although we write the amplitude using a different tensorial structure with respect to ref.[138] we have checked, using the relations between the two tensorial structures reported in section A.1, that our result is in agreement with the one presented in ref.[135].

6.3.3 Calculation of the p_T-expanded virtual corrections

The two-loop triangle diagrams can also be interpreted as an expansion in p_T, but this expansion terminates at $\mathcal{O}(p_T^2)$, rather being an infinite series. Hence, in this section we concentrate on the two-loop box diagrams p_T-expansion [1].
Similar to the two-loop triangle diagrams, the box diagrams amplitudes were generated projected through the same pipeline. After the contraction of the epsilon tensors the diagrams were expanded as described in subsection 6.1.1, keeping only $\mathcal{O}(p_T^4)$ terms. They were reduced to MI's using `FIRE` [155] and `LiteRed` [156]. The resulting MI's were identical to the one for Higgs pair production [140]. Nearly all of them are expressed in terms of generalised harmonic polylogarithms with the exception of two elliptic integrals [157, 158]. The renormalisation and IR pole subtraction procedure was carried out like prescribed subsection 6.3.1.
As a control, the two-loop box diagrams were also computed in the LME up to $\mathcal{O}(1/m_t^6)$. Since this expansion should be included within the p_T-expansion. We have retained the LME analytic expression by further expanding the p_T-expanded amplitude in small $\hat{s}/m_t^2$. Providing an additional cross-check for the validity of the p_T-expansion.

6.4 Results and conclusions

The virtual corrections to the gluon fusion Zh production have been implemented in a `FORTRAN` code using `handyG` [159], for the evaluation of generalised harmonic polylogarithms, `Chaplin` [160] for the harmonic polylogarithms appearing in the triangle two-loop functions while the elliptic integrals are evaluated using the routines of ref.[158]. Since the result is analytic, the code is significantly faster than the numerical evaluation of the two-loop amplitude [139], with evalution time of ca. 0.5 min per one phase space point on a personal laptop.
In order to facilitate the comparison of our results with the ones presented in the liter-

[1] The calculation of the box diagrams has been done mainly by my collaborators, the co-authors of [141]

$\hat{s}/m_t^2$	$\hat{t}/m_t^2$	ref.[139]	$\mathcal{O}(p_T^6)$
1.707133657190554	-0.441203767016323	35.429092(6)	35.430479
3.876056604162662	-1.616287256345735	4339.045(1)	4340.754
4.130574250302561	-1.750372271104745	6912.361(3)	6915.797
4.130574250302561	-2.595461551488002	6981.09(2)	6984.20

Table 6.2. Comparison of $\mathcal{V}_{fin}4/(\alpha_s^2\alpha^2)$ with the numerical results of ref.[139]. This plot has been already published in [141].

ature, we define the finite part of the virtual corrections as in ref.[138][2]

$$\mathcal{V}_{fin} = \frac{G_F^2 m_Z^2}{16}\left(\frac{\alpha_s}{\pi}\right)^2\left[\sum_i \left|\mathcal{A}_i^{(0)}\right|^2 \frac{C_A}{2}\left(\pi^2 - \log^2\left(\frac{\mu_R^2}{\hat{s}}\right)\right)\right. \\ \left. +2\sum_i \mathrm{Re}\left[\mathcal{A}_i^{(0)}\left(\mathcal{A}_i^{(1)}\right)^*\right]\right] \tag{6.36}$$

and in the numerical evaluation of eq.(6.36) we fixed $\mu_R = \sqrt{\hat{s}}$. Triangle and LME box toopologies were validated against the results of refs.[135, 138] finding perfect agreement at the form-factor level, i,.e.$\mathcal{A}_i^{(1)}$.

The virtual part of the partonic cross-section from the finite part of the virtual corrections in eq.(6.36) is defined by

$$\Delta\hat{\sigma}_{virt} = \int_{\hat{t}^-}^{\hat{t}^+} d\hat{t}\frac{\alpha_s}{16\pi^2}\frac{1}{\hat{s}^2}\mathcal{V}_{fin} \tag{6.37}$$

This function is used to confront p_T-expanded results. Starting with low M_{Zh} we have compared the p_T-expanded with the LME $\mathcal{V}_{fin}$, finding a good numerical agreement. It is important to note that, at the same order in the expansion, the p_T-expanded terms are more accurate than the LME ones, although computationally more demanding. Additional checks have been done using the numerical evaluation of the NLO amplitude by [139], where they have evaluated the exact two-loop MI's using `pySecDec` [161, 162]. Table 6.2 shows a comparison between our p_T-expanded $\mathcal{V}_{fin}4/(\frac{\alpha_s^0}{4\pi}^2\alpha^2)$ versus the exact numerical result of [139] for several phase space points. As can be seen from the table the relative difference between the two results is less than half a permille.

In Figure 6.6, the dashed lines show the different orders of the expansion. For all parts of the matrix elements the best results available, i.e. both $\mathcal{A}^{(0)}$ were used and the double-triangle contribution are evaluated exactly, while for $\mathcal{A}^{(1)}$ we use the various orders in the p_T-expansion. For comparison, the results are shown were $\mathcal{A}^{(1)}$ is replaced

[2]The definition of the matrix elements here differs by a factor of $\frac{1}{\hat{s}}$ from ref.[138], *cf.* also section A.1.

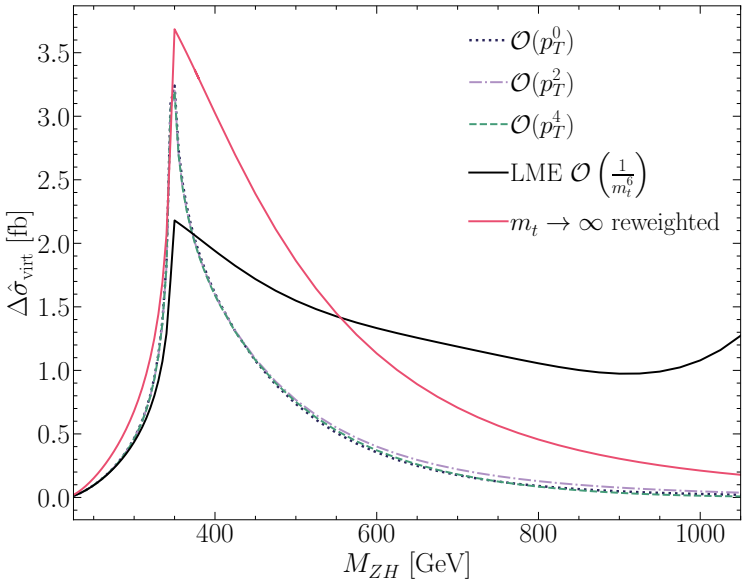

Figure 6.6. $\Delta\hat{\sigma}_{virt}$ defined by eq.(6.37), shown as a function of M_{ZH}. The various orders of the p_T-expansion are plotted as dashed lines, while the black and red continuous lines stand for the LME and reweighted $m_t \to \infty$ results, respectively.This plot has been already published in [141].

by the one computed in LME up to $\mathcal{O}(1/m_t^6)$ (full black line), which as mentioned before is valid up to $M_{ZhH} < 2m_t$. We observe that within the validity of the LME our results agree well with it. Furthermore, the results in the infinite top mass limit reweighted by the full amplitudes squared can be seen as the full red line in the plot, corresponding to the approach of ref.[133], keeping though the double triangle contribution in full top mass dependence. Differently from the LME line, the $m_t \to \infty$ reweighted one shows a behaviour, for $M_{Zh} \gtrsim 400\,\text{GeV}$, similar to the behaviour of the p_T lines. Still, the difference between the reweighted result and the p_T-expanded ones is significant. The p_T-expanded results show very good convergence. The zero order in our expansion agrees extremely well with the higher orders in the expansion, and all the three results are very close up to $M_{Zh} \sim 500\,\text{GeV}$.

The calculation of the virtual two-loop corrections to the $gg \to Zh$ is done using exact results for the triangle and double-triangle topologies, and in the p_T-expansion for the box one. The result of the calculation showed that we get the exact same MI's that was found for Higgs pair production [140] , mostly these MI's are expressed in terms of generalised harmonic polylogarithms with the exception of two elliptic integrals. Using the LO calculation, we have shown the validity of the p_T-expansion covering the invariant mass interval $M_{Zh} \lesssim 750$ GeV which covers $\sim 98\%$ of the total phase space for $13 - 14$

TeV energies.
The p_T-expansion agrees with per mill level with the numerical results found in [139]. However, it allows for fast computation of the amplitude with circa one second per phase space point using a modern laptop with mid-range specifications. Additionally. the integration over the $\hat{t}$ variable in eq.(6.37) converges very well. The flexibility of our analytic results, an application to beyond-the-Standard Model is certainly possible.
Finally, it should be noted that this calculation complements nicely the results obtained in ref.[138] using a high-energy expansion, that according to the authors provides precise results for $p_T \gtrsim 200\,\text{GeV}$. The merging of the two analyses is going to provide a result that covers the whole phase space, can be easily implemented into a Monte Carlo code using Padé approximants, which is currently a work in progress in Cite the new paper here-later

Part III

Higgs Pair at Hadron Colliders

7 Overview of Higgs pair production at colliders

The dominant process for Higgs pair production at the LHC (and hadron colliders in general) is the gluon gluon fusion (ggF) via a heavy quark loop Q, mainly the top and beauty quark, with the latter contributing only to about 1%, see figure 7.1. This process

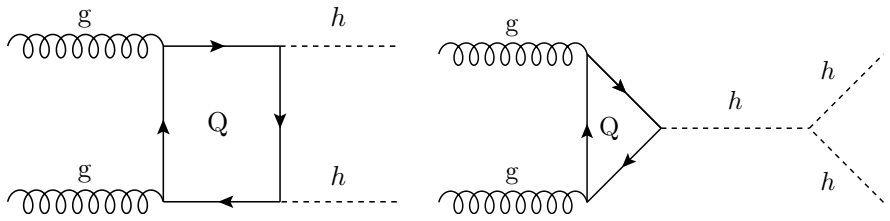

Figure 7.1. Feynman diagrams for the ggF process of Higgs pair production in the SM.

is well-studied at leading order (LO) analytically [163–166]. The next-to-leading QCD order (NLO) was initially computed using infinite top mass limit ($m_t \to \infty$) using the Higgs effective field theory (HEFT) and implemented in the programme `Hpair` [167]. However, this approximation is not suitable for obtaining distributions, and using numerical methods [168–170] the full NLO results were obtained. In [171], parton shower effects were included in the NLO calculations, allowing the use of the NLO in event generators such as Pythia and Powheg. Analytical calculations for the NLO corrections using small Higgs transverse momentum $p_{T,h} \to 0$ yielded a good estimation for the numerical result [140]. The use of Padé approximation obtained also analytical results for the NLO result and a description for the three-loop (NNLO) form factors [172]. The NNLO cross section with top mass effects has been computed numerically in [173].

In this work, we have calculated the $\sqrt{s} = 14$ TeV LO ggF inclusive cross-section and distributions with modified light Yukawa couplings by including the light quark loops and the coupling $hhq\bar{q}$ described in the last diagram in figure 8.2 . The calculation was carried out using a FORTRAN code utilising the `VEGAS` integration algorithm, and NNPDF30 parton distribution functions (PDF's)[174] implemented via `LHAPADF-6` package[175]. For the loop integrals (see Appendix), we have used the Collier library [176] for regularisation of the IR divergent light quark loops, that were assumed massless. A K-factor, for the NNLO correction were used according to the Higgs cross

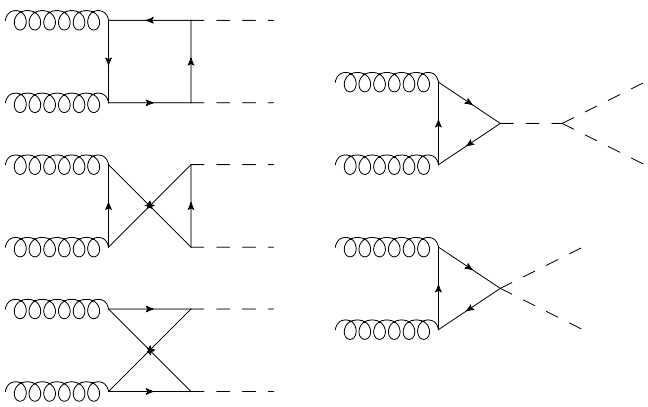

Figure 7.2. The one-loop diagrams calculated in the ggF with modified Yukawa couplings

section working group recommended values [177, 178]:

$$K = \frac{\sigma_{NNLO}}{\sigma_{LO}}, \qquad K_{14\text{TeV}} \approx 1.71. \tag{7.1}$$

Since the cross-section is not expected to change a lot by changing the light Yukawa couplings, we use the same NNLO K-factor for all values of the scalings. The renormalisation μ_R and factorisation μ_F scales of the α_s and PDF running are set to $\mu_0 = 0.5\, M_{hh}$, and $\alpha_s(M_Z) = 0.118$. In our calculations, we did not consider the quark mass running, as the later will be accounted for in the K-factor.

Theoretical systematic uncertainties

There are three main sources of theoretical *systematic* uncertainties:

1. Scale uncertainty: coming form the arbitrariness of scales choice.
2. PDF uncertainties : coming form the uncertainty in the PDF fitting and model.
3. α_s running uncertainty: originating from the initial value (i.e. $\alpha_s(M_Z)$).

In order compute these uncertainties, we follow the recommendations of the Higgs cross-section working group for the value and uncertainty of α_s

$$\alpha_s(M_Z) = 0.1180 \pm 0.0015, \tag{7.2}$$

and the methods described in [179, 180]. for PDF and α_s uncertainties. In order to calculate the scale uncertainties, the cross-section was computed with different μ_R and

	σ [fb]	Scale [fb]	PDF+α_s [fb]	Total [fb]
SM HEFT (LO)	18.10	–	–	–
SM running mass (LO)	16.96	–	–	–
SM (LO)	21.45	$^{+4.29}_{-3.43}$	± 1.46	$^{+4.53}_{-3.73}$
SM (NLO) [181]	33.89	$^{+6.17}_{-4.98}$	$^{+2.37}_{-2.01}$	$^{+6.61}_{-5.37}$
SM (NNLO) [173]	36.69	$^{+0.77}_{-1.83}$	± 1.10 ($g_{hq\bar{q}} = g^{SM}_{hb\bar{b}}$)	$^{+1.66}_{-6.43}$ (incl. m_t uncertainty)
($g_{hq\bar{q}} = g^{SM}_{hb\bar{b}}$) (ggF-LO)	21.84	$^{+4.38}_{-3.51}$	± 1.49	$^{+4.62}_{-3.81}$

Table 7.1. Gluon fusion (ggF) Higgs pair production cross-section with theoretical systematic uncertainties, for infinite top mass limit (SM HEFT), running mass, LO, NLO and NNLO QCD corrections. The NLO and NNLO results are taken from the references cited in the table. We also state the benchmark point ($g_{hq\bar{q}} = g^{SM}_{hb\bar{b}}$) cross section result (all the light Yukawa couplings are scaled to the SM beauty Yukawa)

μ_F values ranging between:

$$\frac{M_{hh}}{4} \leq \mu_R/\mu_F \leq M_{hh} \tag{7.3}$$

The scale uncertainty for the LO total cross-section was found to be $+20\%, -16\%$. Moreover, the PDF+α_s uncertainty was $\pm 6.8\%$.

results

The total cross sections with their uncertainties is shown in table **??**.

7.1 Overview of Light Yukawa searches

There are additional measurements of the light-quark Yukawa couplings that might become relevant at HL-LHC or FCC-hh, a careful study of which is beyond the scope of the current work. Yet we attempt to include a discussion here, so as to provide a comparison with our study and to put it into proper context, or to serve as proposal for further studies.

The channel $pp \to h+j$ has been suggested as a probe for charm Yukawa coupling [182] with charm-tagged jet having a potential bound of $\kappa_c \sim 1$ for the HL-LHC, depending on the charm-tagging scheme. This process could be used for the first and second generations Yukawa couplings by looking at the shapes of kinematic distributions, the most important one being the p_T distribution [183–185]. The expected HL-LHC 95% CL bounds are $\kappa_c \in [-0.6, 3.0]$, $|\kappa_u| \lesssim 170$ and $|\kappa_d| \lesssim 990$. The use of $h + j$ process along with other single Higgs processes have also been suggested as indirect probes for Higgs self coupling [58–62, 64], due to the contribution of the trilinear coupling to NLO

electroweak corrections to these processes. In addition, experimental fits have been carried out for the trilinear coupling from single Higgs observables [67, 186].

It seems that for the HL-LHC, an optimal bound for the trilinear coupling can be obtained by combing both the data from single-Higgs process as well as Higgs pair production [66], with 68% CL bound on $\kappa_\lambda \in [0.1, 2.3]$, compared to the expected bound of $\kappa_\lambda \in [0.0, 2.5] \cup [4.9, 7.4]$ coming from using di-Higgs measurements alone. Moreover, single Higgs processes, namely Zh and $W^\pm h$ production, could also be useful in probing charm-Yukawa coupling using a mixture of b- and c-tagging schemes leveraging the mistagging probability of c-jets as b-jets in b-tagging working points, and vice-versa, in order to break the degeneracy in the signal strength [187]. The use of this technique could probe $\kappa_c \sim 1$ in the FCC-hh. Of course, for the charm-Yukawa coupling, the constraints are set to improve significantly, as there has been recent direct observation of $h \to c\bar{c}$ [188]. Therefore, from here on, we will mainly concentrate on the process with more potential for constraining Yukawa couplings of the first generation quarks.

Rare Higgs decays to mesons, $h \to M + V$, $M = \Upsilon, J/\Psi, \phi \ldots$, were also suggested as a probe for light-quark Yukawa couplings [189–191], and there have been experimental searches for these decays [188, 192] with bounds on the branching ratios, $\mathcal{B}(h \to X, \gamma,\ X = \Upsilon, J/\Psi,) \sim 10^{-4} - 10^{-6}$ at 95% CL. It was shown in Ref. [193], that the charge asymmetry of the process $pp \to hW^+$ vs $pp \to hW^-$ can be used as a probe for light-quark Yukawa couplings as well as to break the degeneracy amongst quark flavours. Moreover, the rare process $pp \to h\gamma$ is also a possible way to distinguish between enhancements of the up- and down-Yukawa couplings [194] where the authors have estimated the bounds on the up-Yukawa coupling of $\kappa_u \sim 2000$ at the HL-LHC. Despite some processes appearing more sensitive than others, one should think of these processes as complementary to each other.

One of the main features of the effective couplings $hhq\bar{q}$ and $hhhq\bar{q}$ emerging from SMEFT operator $\mathcal{O}_{q\phi}$, or the Chiral Lagrangian for that matter, is that these couplings are either free from propagator suppression for $hhq\bar{q}$ or scale with energy for $hhhq\bar{q}$ while being safe from strong unitarity constraints. This feature gives processes with multiple Higgs and/or vector bosons $V = W^\pm, Z$ an advantage in constraining $\mathcal{O}_{q\phi}$. The latter constrains come from the longitudinal degrees of freedom of the gauge bosons which can be understood from the Goldstone boson equivalence theorem. The use of the final state VV as a probe for $\mathcal{O}_{q\phi}$ is difficult due to the large SM background. However, the three-boson final state VVV was shown to give strong projected bounds for light-quark Yukawa couplings for HL-LHC with 95% CL bounds on $\kappa_u \sim 1600$, and $\kappa_d \sim 1100$. A ten fold improvement is expected at FCC-hh [195] with bounds of order $\kappa_d \sim 30$. Higgs pair production has a smaller SM background compared to VV production, but it has a significantly smaller cross section too, even when compared to VVV, as the latter process has already been observed at the LHC [196, 197].

On the contrary, Higgs pair production is inaccessible with the runs I-III of the LHC, but it is potentially accessible at the HL-LHC [198] having a $\sigma \cdot BR \sim 1\text{fb}^{-1}$. However,

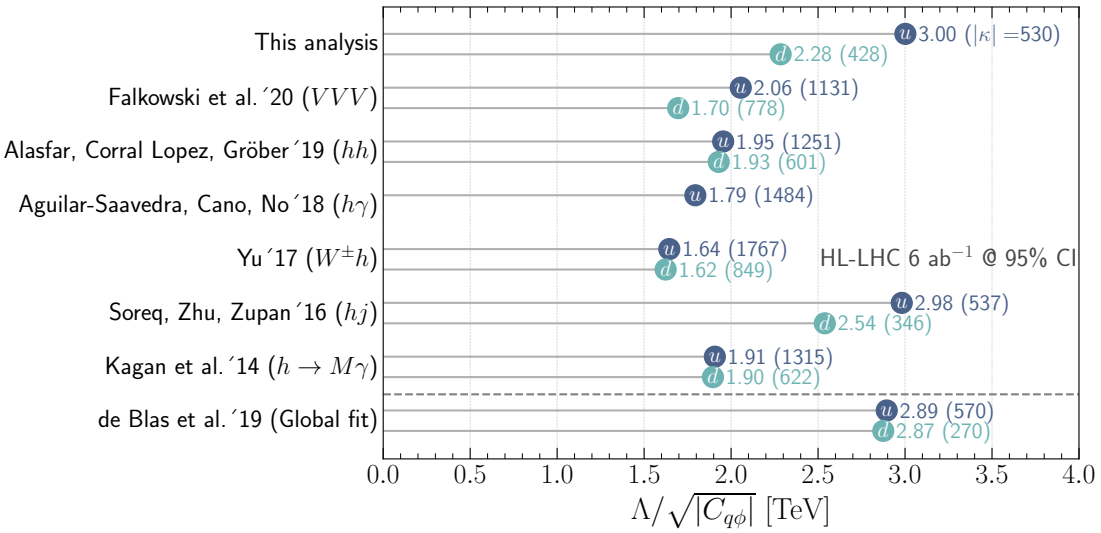

Figure 7.3. Summary of the 95% CI/CL sensitivity bounds on the SMEFT Wilson coefficients $C_{u\phi}$ (blue), and $C_{d\phi}$ (green). The bounds are interpreted in terms of the NP scale Λ that can be reached through the measurements of the Wilson coefficient at the HL-LHC at 6 ab^{-1}, the corresponding κ_q's are shown inside the parentheses. Single parameter fit 95% CI bounds are used from this analysis for comparison with previous studies.

Higgs pair production, particularly the channel $h \to b\bar{b}\gamma\gamma$, is of significant interest as it has unique features. The first being the ability to constrain the trilinear and light-quark Yukawa couplings simultaneously, as we show in this work. Secondly, Higgs pair production could probe non-linear relations between Yukawa interaction and $hhq\bar{q}$ couplings [199, 200]. Lastly, Higgs pair production is expected to be significant enhanced in certain models involving modification of light-quark Yukawa couplings (cf. [201–203])

For future colliders, like the FCC-hh at 100 TeV, in addition to Higgs pair production triple Higgs production might be an interesting channel for constraining the operators with Wilson coefficient $C_{u\phi}$ and $C_{d\phi}$ due to the energy increase of a Feynman diagram coupling the quarks to three Higgs bosons. In this case, a similar study to ours should be performed to see whether also in this case it will be important to do a combined fit on the light quark Yukawa couplings together with the trilinear and quartic Higgs self-couplings.[1]

Finally, we note that there are also non collider signatures for enhanced light-quark Yukawa couplings, manifesting in frequency shifts in atomic clocks from Higgs forces at the atomic level [205].

[1] In [204], it was shown that $\sim \mathcal{O}(1)$ bounds on the quartic Higgs self-coupling can be reached at the FCC-hh.

8 Higgs pair as a probe for light Yukawas

8.1 Introduction

After the Higgs boson discovery the era of precision measurements of Higgs properties has begun. While the Higgs boson couplings to vector bosons and third generation fermions have been measured at the LHC and agree with their Standard Model (SM) prediction at the level of 10% – 20% [55], the situation for the Higgs self-couplings and couplings to first and second generation fermions is quite different. Current bounds on the trilinear Higgs self-coupling range from $-5.0 < \lambda_{hhh}/\lambda_{hhh}^{SM} < 12.0$ [206] and are still above the limits of perturbative unitarity [106] or vacuum stability [207]. The quartic Higgs self-coupling is out of reach of the high-luminosity-LHC (HL-LHC) [198, 208]. Upper limits on the Higgs boson decays to muons are $g_{h\bar{\mu}\mu}/g_{h\bar{\mu}\mu}^{SM} < 1.53$ [55], while current bounds on the Higgs coupling to electrons, $g_{h\bar{e}e}/g_{h\bar{e}e}^{SM} < 611$, are far away from the SM [209].

For the Yukawa couplings to the first and second generation quarks, henceforth denoted as light quark Yukawa couplings, the current best limits are obtained from a global fit to Higgs data [190, 210]. For instance for the HL-LHC, ref. [211] obtained for a projection on the coupling strength modification, $\kappa_i = g_{h\bar{q}_i q_i}/g_{h\bar{q}_i q_i}^{SM}$, where $g_{h\bar{q}_i q_i}$ denotes the $i = u, d, s, c$ Higgs Yukawa coupling to quarks, in a global fit

$$|\kappa_u| < 570\,, \quad |\kappa_d| < 270\,, \quad |\kappa_s| < 13\,, \quad |\kappa_c| < 1.2\,. \tag{8.1}$$

The determination of the light quark Yukawa couplings in a global fit is plagued by the fact that the Higgs boson width can only be measured at the LHC under certain assumptions.[1] The global fit can therefore not be considered to be completely model-independent. A more direct way of constraining the light Yukawa couplings is hence welcome.

Searches for exclusive decays of the Higgs boson to a vector meson and a photon $h \to X\gamma$ with $X = \rho, \omega, \phi, J/\psi$ [2] as a probe of light Yukawa couplings have been proposed in [189] and can be even used to probe flavour-off-diagonal Yukawa couplings [190] for instance in Higgs boson rare decays such as $h \to MW^{\pm}$ or $h \to MZ$, with M denoting generically a scalar or pseudoscalar vector meson. From the experimental side,

[1] The width determination due to on- and off-shell measurements [212, 213] of Higgs boson couplings [214] is for instance made under the assumption that the couplings do not depend on the energy scale [215].

[2] In addition, $h \to \Upsilon\gamma$ allows to probe the bottom Yukawa coupling [216].

ATLAS and CMS have reported upper bounds on the decays $h \to \rho\gamma$, $h \to \phi\gamma$ in [217] and to $h \to J/\psi\gamma$ in [218, 219]. The charm Yukawa coupling can also be constrained to a factor of a few times its SM value at the HL-LHC making use of charm tagging in $pp \to W/Zh$ with subsequent decay of the Higgs boson to $c\bar{c}$ [187] (see [220, 221] for first experimental results) or in $pp \to hc$ [182].

Another possibility for constraining the light quark Yukawa couplings is from Higgs kinematics. If the Higgs boson is produced with an associated jet, the transverse momentum distribution changes with respect to the SM one in the presence of enhanced quark Yukawa couplings of the second and first generation. For the second generation quarks, the main effect stems from log-enhanced contributions due to interference between top and light quark loop diagrams. This allows to set a bound on $\kappa_c \in [-0.6, 3.0]$ at 95% C.L. at the HL-LHC [184]. Instead in the presence of significantly enhanced first generation quark Yukawa couplings the Higgs boson can be directly produced from initial state quarks, which again would alter the Higgs p_T-distribution [183]. For non-collider probes of the light Yukawa couplings see ref. [205].

In this paper, we will study the potential to constrain light quark Yukawa couplings from Higgs pair production. As for Higgs plus jet production, we can make use of kinematical information. We will mainly consider the case in which the modifications of the light Yukawa couplings can be described by a dimension six effective operator, denoted schematically by

$$\mathcal{O}_f = (\phi^\dagger \phi)(\overline{Q}_L \phi q_R)\,. \tag{8.2}$$

The left-handed quark $SU(2)$ doublet has been denoted by Q_L,the right-handed quark $SU(2)$ singlet by q_R, while ϕ is the scalar Higgs doublet field. In the presence of such an operator, both a shift in the Yukawa coupling to one Higgs boson as well as a new coupling of two Higgs bosons to two fermions modifies the Higgs pair production cross section. In the case of the top quark it was shown that such a new coupling can lead to large enhancements of the double Higgs production process [199, 222–224]. For the light quark Yukawa couplings this was shown in [201] under the assumption of universally enhanced light Yukawa couplings. We will consider more general scenarios and will show that indeed such an operator can also be constrained in di-Higgs production for the light generations of quarks. Under the assumption of linearly realised electroweak symmetry breaking we can then obtain a bound on the light quark Yukawa couplings which is competitive with the above mentioned ways of constraining them. We will also investigate how our bounds are modified if we allow for a modification of the trilinear Higgs self-coupling. Furthermore, we will discuss the possibility of charm tagging for di-Higgs final states, which will allow us to set bounds on the second generation quark Yukawa couplings.

The paper is structured as follows: in sect. 8.2 we will introduce our notation and point out under which circumstances scenarios considered in our analysis can be realised. In sect. 8.3 we present how the di-Higgs production process and the Higgs boson decays

are modified in the presence of enhanced light quark Yukawa couplings. In sect. 8.4 we present the results of our analysis both in the presence of enhanced first and second generation Yukawa couplings. We also consider the potential reach of the HL-LHC by employing charm tagging. We conclude in sect. 8.5.

8.2 Effective Field Theory of light Yukawa couplings

Within the SM, the Higgs couplings to quarks are described by the Lagrangian

$$\mathcal{L}_y = -y^u_{ij}\overline{Q}^i_L\tilde{\phi}u^j_R - y^d_{ij}\overline{Q}^i_L\phi d^j_R + h.c.\,, \tag{8.3}$$

with $\tilde{\phi} = i\sigma_2\phi^*$, σ_2 is the second Pauli matrix, ϕ denotes the Higgs doublet, Q^i_L the left-handed $SU(2)$ quark doublet of the i-th generation and u^j_R and d^j_R the right-handed up- and down-type fields of the j-th generation, respectively. Modifications of the SM from high-scale new physics can be described in a model-independent way by means of the SM effective field theory (SMEFT), in terms of higher dimensional operators. In particular, the couplings of the quarks to the fermions are modified by the operator

$$\Delta\mathcal{L}_y = \frac{\phi^\dagger\phi}{\Lambda^2}\left(c^u_{ij}\overline{Q}^i_L\tilde{\phi}u^j_R + c^d_{ij}\overline{Q}^i_L\phi d^j_R + h.c.\right)\,, \tag{8.4}$$

where Λ denotes the cut-off of the effective field theory (EFT). The mass matrices of the up-type and down-type quarks are

$$M^u_{ij} = \frac{v}{\sqrt{2}}\left(y^u_{ij} - \frac{1}{2}c^u_{ij}\frac{v^2}{\Lambda^2}\right)\,, \tag{8.5}$$

$$M^d_{ij} = \frac{v}{\sqrt{2}}\left(y^d_{ij} - \frac{1}{2}c^d_{ij}\frac{v^2}{\Lambda^2}\right)\,. \tag{8.6}$$

They can be diagonalised by means of a bi-unitary transformation

$$m_{q_i} = \left((V^{u/d}_L)^\dagger M^{u/d} V^{u/d}_R\right)_{ii}\,, \tag{8.7}$$

while the CKM matrix is defined as $V_{CKM} = (V^u_L)^\dagger V^d_L$. By defining

$$\tilde{c}^q_{ij} = (V^q_L)^*_{ni}\, c^q_{nm}\, (V^q_R)_{mj}\,, \quad \text{with} \quad q = u, d\,, \tag{8.8}$$

we can write the couplings of one and two Higgs boson to fermions with

$$\mathcal{L} \supset g_{h\bar{q}_iq_j}\bar{q}_iq_jh + g_{h\bar{q}_iq_j}\bar{q}_iq_jh^2 \tag{8.9}$$

as

$$g_{h\bar{q}_i q_j}: \quad \frac{m_{q_i}}{v}\delta_{ij} - \frac{v^2}{\Lambda^2}\frac{\tilde{c}^q_{ij}}{\sqrt{2}}\,, \qquad\qquad g_{hh\bar{q}_i q_j}: \quad -\frac{3}{2\sqrt{2}}\frac{v}{\Lambda^2}\tilde{c}^q_{ij}\,. \tag{8.10}$$

In the following, we will also use for the diagonal couplings alternatively the notation

$$g_{h\bar{q}_i q_i} = \kappa_q g^{\rm SM}_{h\bar{q}_i q_i}\,, \qquad\qquad g_{hh\bar{q}_i q_i} = -\frac{3}{2}\frac{1-\kappa_q}{v} g^{\rm SM}_{h\bar{q}_i q_i}\,, \tag{8.11}$$

in a slight abuse of language of the κ-framework used often in experimental analyses.

Flavour-changing Higgs couplings are strongly constrained from low-energy flavour observables, such as meson-antimeson mixing. The bounds are of order $|\tilde{c}_{uc/ds}| \lesssim 10^{-5}\Lambda^2/v^2$ and $|\tilde{c}_{db/sb}| \lesssim 10^{-4}\Lambda^2/v^2$ [225]. Given that, a common assumption for the Wilson coefficients in eq. (10.1) is that of minimal flavour violation (MFV) [226], where

$$c^u_{ij} = \bar{c}_u\, y^u_{ij}\,, \qquad\qquad c^d_{ij} = \bar{c}_d\, y^d_{ij}\,, \tag{8.12}$$

with flavour universal $\bar{c}_u$ and $\bar{c}_d$. Hence, under the assumption of MFV the Yukawa matrices y_u (y_d) and the Wilson coefficients c^u (c^d) are simultaneously diagonalisable and no flavour changing Higgs interactions with quarks exist. We refrain though from making the assumption of MFV, due to the reason that with the Wilson coefficients being proportional to the Yukawa couplings, we introduce a strong hierarchy into the Higgs couplings to quarks. Since we want to describe modifications of the order of the ones in eq. (8.1) we would need to assume very low values of the new physics scale Λ and/or large Wilson coefficients, rendering the validity of the EFT questionable and in potentially conflict with measurements of the third generation couplings to the Higgs boson.

Instead, we will consider the case in which the $\tilde{c}^q_{ij}$ are diagonal, though not proportional to the Yukawa matrices. This can be realised by appropriate choice of the parameters. For instance, $V^u_{L/R} = \mathbb{1}\,,\ V^d_R = \mathbb{1}\,,$ and $V^d_L = V_{CKM}$, which keeps $\tilde{c}^u$ flavour-diagonal if c^u is chosen flavour-diagonal. Flavour violation then originates only from the CKM matrix. We will refer to this as flavour alignment. However, from a UV-perspective there is no obvious symmetry argument to enforce this at low-energy.

A possible way of keeping $\tilde{c}$ flavour-diagonal with symmetry arguments could be realised for flavour universal $c^{u/d}$ and a left-right symmetry rendering $V_L = V_R$. Then by setting universal $\tilde{c}^{u/d}/\Lambda^2 \approx 1/(3\text{ TeV})^2$ we get for instance a modification of the up-quark coupling to the Higgs boson of a factor of 500, but only a modification of the top Yukawa coupling by 1%, which is still consistent with the current limits on the top Yukawa coupling [227, 228]. Note that doing so for the down-type quarks would of course be more difficult, as it would imply a larger deviation in the bottom quark Yukawa coupling, due to its smaller mass. Alternatively, one can chose $\tilde{c}^f$ flavour-diagonal (or with strongly suppressed flavour-off-diagonal elements) by choosing horizontal symmetries. We refer to [201] for a model with vector-like quarks and strongly enhanced light quark

Yukawa couplings. Another realisation of large first and second generation Yukawa couplings without tree-level flavour-changing neutral currents (FCNCs) has been discussed in [229], and is refereed to as spontaneous flavour violation. The basic idea is to achieve this by breaking the quark family number symmetry via the RH up-type or down-type quark wave function renormalisation, leading to either enhanced up- or down-type quark Yukawa couplings. A concrete realisation of this idea for a two-Higgs doublet model was discussed in [230].

We would also like to stress that from a UV perspective it makes sense to assume that if there is a modification in the light quark Yukawa couplings with respect to the SM, deviations in the di-Higgs production process can be expected, which in the limit of heavy new physics can be traced back to a coupling of two Higgs boson to two fermions. We show this schematically in fig. 8.1 for a heavy new scalar and a heavy new vector-like fermion. The coupling of the SM-like Higgs boson in the models extended by a heavy new Higgs boson or a heavy new vector-like quark as shown in fig. 8.1 is modified due to a mixing with either the new Higgs boson, if it acquires a vacuum expectation value (VEV), or by the mixing between the quark and the new vector-like fermion. For the case of the heavy new scalar, the effective coupling of two SM-like Higgs bosons to fermions in the limit of $m_H \gg E$, with E denoting the energy scale of the process and m_H the Higgs mass of the heavy Higgs boson, can be written as

$$g_{hh\bar{q}q} \to -i\frac{g_{H\bar{q}q}g_{Hhh}}{m_H^2}\,. \tag{8.13}$$

A coupling g_{Hhh} always exist, if both of the Higgs fields acquire a VEV, since a portal term in the Lagrangian, $(\phi^\dagger\phi)(\Phi^\dagger\Phi)$, is always allowed by the symmetries. We denoted here the new Higgs multiplet by Φ with neutral component H.

In the presence of new vector-like quarks that mix with the SM quarks, the coupling of two Higgs bosons to two fermions comes from $\hat{t}/\hat{u}$ channel diagrams. If the mass of the new vector-like quark m_Q is $m_Q \gg E$ one obtains for the coupling[3]

$$g_{hh\bar{q}q} \to -i\frac{g_{h\bar{q}\mathcal{Q}}g_{h\overline{\mathcal{Q}}q}}{m_Q}\,. \tag{8.14}$$

A more explicit consideration of models that realise large light Yukawa couplings is beyond the scope of this paper and we refer to existing work [201, 230].

We finally note that an alternative way of describing model-independent deviations from the SM Higgs couplings is by a non-linear effective Lagrangian (alternatively referred to as electroweak chiral Lagrangian) [231, 232]. While in SMEFT the Higgs boson is assumed to be part of an $SU(2)$ doublet and the expansion is organised in terms of dimensionality of the operator, in the chiral Lagrangian the Higgs boson is assumed to

[3] In Composite Higgs Models with vector-like quarks there is also a contribution from the non-linearities of the model.

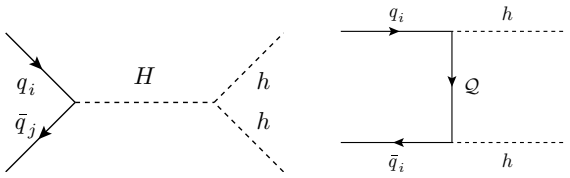

Figure 8.1. Examples of potential UV-complete models leading to a $hhf\overline{f}$ coupling. The left Feynman diagram shows a heavy Higgs H, the right diagram a vector-like quark $\mathcal{Q}$.

be a singlet and the expansion is organised in terms of chiral dimension, where bosonic fields are assigned chiral dimension 0 and derivatives and fermion bi-linears chiral dimension 1. The Lagrangian responsible for a potential modification of the Yukawa couplings can be written as [233]

$$\mathcal{L} = -\frac{v}{\sqrt{2}}(\overline{u}^i_L, \overline{d}^i_L)\Sigma \left(y_{q,ij} + k_{q,ij}\frac{h}{v} + k_{2q,ij}\frac{h^2}{v^2} + ... \right) \begin{pmatrix} u^j_R \\ d^j_R \end{pmatrix} \tag{8.15}$$

with

$$\Sigma = e^{i\sigma^a \pi^a(x)/v}\,, \tag{8.16}$$

in terms of the Pauli matrices σ^a and the Goldstone bosons π^a with $a = 1, 2, 3$. The field Σ transforms linearly under the custodial symmetry $SU(2)_L \times SU(2)_R$. We note again as for the SMEFT that off-diagonal elements of k_q are strongly constrained. Compared to SMEFT the couplings of one or two Higgs boson to fermions are now uncorrelated, leading to different coefficients k_q and k_{2q}. In principle, the coefficients of the light fermion couplings to two Higgs bosons are yet unconstrained and di-Higgs production is *the* place to test if there exists a correlation among those and hence whether a linear or non-linear EFT prescription is to be preferred. While in the following we will mainly concentrate on the case of SMEFT we shall shortly comment also on the case of non-linear EFT.

8.3 Higgs pair production and Higgs decays with modified light Yukawa couplings

In this section we will describe how the Higgs pair production process for modified light quark Yukawa couplings is affected. While in the SM Higgs pair production is dominantly mediated by gluons fusing into a heavy quark loop coupling to the Higgs boson, for large first and second generation quark Yukawa couplings also quark annihilation becomes relevant. For a phenomenological analysis we also need to take into account the Higgs boson decays, which we describe in the last part of the section.

8.3.1 Higgs pair production via gluon fusion

The dominant process for Higgs pair production at the LHC in the SM is the gluon fusion process (ggF) via a heavy quark loop Q, where Q stands mainly for the top quark. The bottom quark contributes with less than 1%. We show the Feynman diagrams for the process in fig. 7.1. The process has been known since long at leading order (LO) in full mass dependence [163–166]. The next-to-leading order (NLO) in the strong coupling constant was initially computed using the infinite top mass limit ($m_t \to \infty$) and reweighted with the full LO results [167]. However, this approximation is only valid up to the top quark threshold. More recently, the NLO QCD corrections have been computed in full top mass dependence, showing that the infinite top mass limit overestimates the full result by 14% [168–170].[4] For distributions, the approximation of infinite top mass is even worse. At next-to-next-to leading order (NNLO) results are available in the infinite top mass limit [236, 237] and by including top mass effects for the double real radiation [173]. First steps towards an inclusion of top mass effects for the virtual corrections (for the triangle only) have been made in [172, 238] and for the light fermion triangle contributions the NNLO has been computed in [239].

For our analysis, we have calculated the $\sqrt{s} = 14$ TeV LO ggF inclusive cross section and distributions with modified light Yukawa couplings by including the light quark loops and the coupling $hhq\bar{q}$ shown in fig. 8.2. The calculation was carried out using a

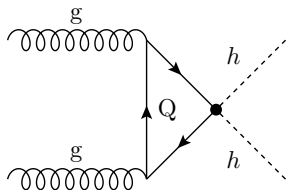

Figure 8.2. The new diagram for ggF emerging from the $hhq\bar{q}$ coupling stemming from an effective dim-6 operator.

private FORTRAN implementation of the LO cross section utilising the `VEGAS` integration algorithm, and NNPDF30 parton distribution functions (PDF's)[174] implemented via the `LHAPDF-6` package [175]. For the one-loop integrals appearing in the form factors of the box and triangle diagrams, we have used the Collier library [176] to ensure numerical stability of the loop integral calculation for massless quarks inside the loops. A K-factor for the NNLO correction was used following the recommendations by the Higgs cross section working group [178]

$$K = \frac{\sigma_{NNLO}}{\sigma_{LO}}, \qquad K_{14\,\text{TeV}} = 1.72. \tag{8.17}$$

[4] The numerical NLO QCD results for the virtual corrections were cross-checked by employing different analytic expansions [140, 234, 235].

For differential distributions in the invariant mass of the Higgs boson pair, M_{hh}, we extract a differential K-factor from [173]. As a reference cross section at NNLO [173] for the analysis in sect. 8.4 we use

$$\sigma^{\mathrm{SM}}_{NNLO} = 36.69^{+1.99}_{-2.57}\ \mathrm{fb}\,. \tag{8.18}$$

The uncertainty stems from the scale choice, the PDF+α_s error and the uncertainty associated to the usage of the infinite top mass limit in parts of the calculation. Since we found that the cross section does not change much once the effects of the modified light Yukawa couplings are included, we use the same NNLO K-factor for all values of the scalings. The renormalisation, μ_R, and factorisation scales, μ_F, are set to $\mu_0 = M_{hh}/2$ as has been pointed out as an optimal choice in ref. [240], and $\alpha_s(M_Z) = 0.118$.

Results

For comparison of the results with modified Yukawa couplings with the SM results, we define as a benchmark point the case where all first and second generation quark Yukawa couplings are scaled to the SM bottom Yukawa coupling, which we will refer to in plots and tables as $g_{hq\bar{q}} = g^{\mathrm{SM}}_{hb\bar{b}}$. This means we scale the Yukawa couplings by $\kappa_q = g_{h\bar{q}q}/g^{\mathrm{SM}}_{h\bar{q}q}$ with

$$\kappa_u = 1879\,, \quad \kappa_d = 889\,, \quad \kappa_s = 44\,, \quad \kappa_c = 3.3\,, \tag{8.19}$$

and use only flavour-diagonal modifications of the quark Yukawa couplings. This benchmark is inspired by ref. [201].

Figure 8.3 shows the di-Higgs invariant mass M_{hh}- and the $p_{T,h}$-distributions for the computed LO process. From the distributions it is evident, that the change of the ggF process in the presence of enhanced light Yukawa couplings is quite small. The reason is that the box contribution which is the major part of the cross section has two fermion coupling insertions and hence is strongly suppressed for all the light quarks with respect to the top quark loop diagrams. The bottom quark contribution to the ggF process in the SM is less than 1% and comes mainly from the triangle diagram, so adding several contributions from similar size does not change the cross section by much. Also the new diagrams (*cf.* fig. 8.2) are suppressed compared to the box diagrams of the top quark. In the presence of enhanced light quark Yukawa couplings the Higgs boson pair can though be directly produced by quark annihilation. We turn to discuss this process in the next part. In the meanwhile we can conclude that for the ggF process we can improve on the LO predictions by using SM K-factors and that the effects of light Yukawa coupling modifications for the ggF process are small for the still allowed modifications.

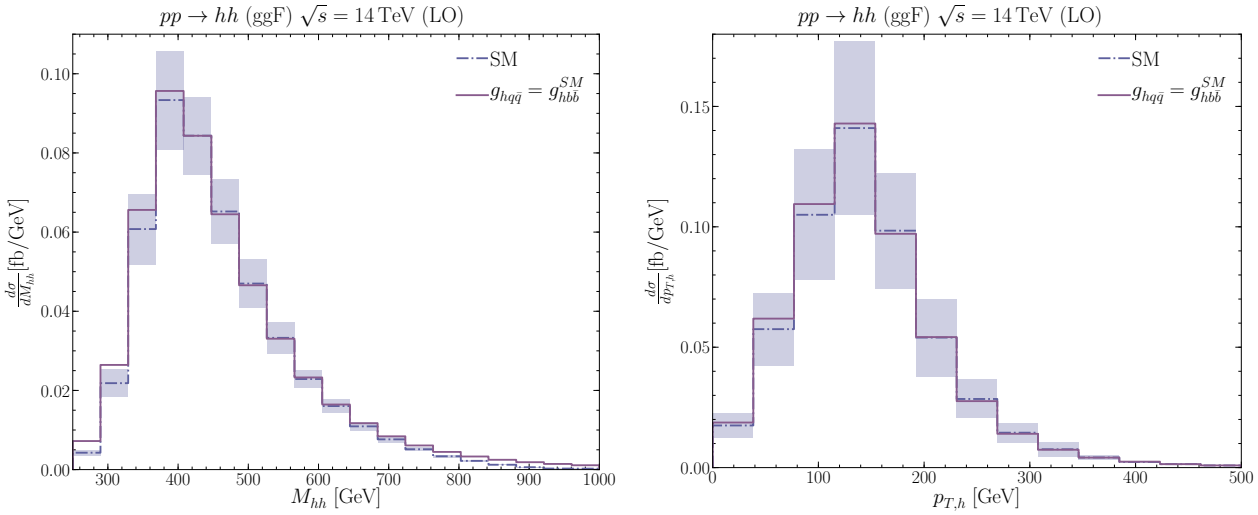

Figure 8.3. *Left:* The di-Higgs invariant mass differential cross section $d\sigma/dM_{hh}$ for the SM at LO and the benchmark point toy. The error boxes denote the total scale, PDF and α_s uncertainties. *Right:* The same but for the Higgs transverse momentum $p_{T,h}$ distribution.

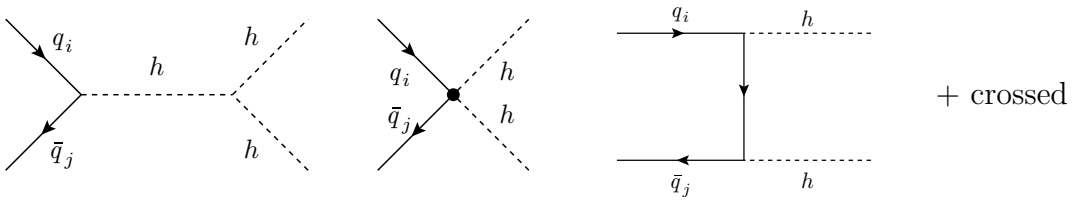

Figure 8.4. Feynman diagrams for the qqA Higgs pair production.

8.3.2 Higgs pair production via quark anti-quark annihilation

If the Yukawa couplings of the light quark generations are sufficiently increased, the Higgs bosons will be produced directly from the constituents of the proton with a sizeable rate. The quark anti-quark annihilation (qqA) process becomes then relevant for Higgs pair production. The qqA process has four Feynman diagrams shown in the fig. 8.4.

The differential cross section given by

$$\frac{d\hat{\sigma}_{q_i\bar{q}_j}}{d\hat{t}} = \frac{1}{16\pi}\frac{1}{12\hat{s}}\left[\left|2g_{hhq_i\bar{q}_j} + \frac{g_{hhh}\, g_{hq_i\bar{q}_j}}{\hat{s} - m_h^2 - im_h\Gamma_h}\right|^2 + \mathcal{O}(g^4_{hq_i\bar{q}_j})\right]. \tag{8.20}$$

We neglect here the $\hat{t}$ and $\hat{u}$ channel diagrams, as their contribution is typically only $\sim 0.1\%$ of the total cross section.

The hadronic cross section is then obtained by

$$\sigma_{\text{hadronic}} = \int_{\tau_0}^{1} d\tau \int_{\hat{t}_-}^{\hat{t}_+} d\hat{t} \sum_{i,j} \frac{d\mathcal{L}^{q_i\bar{q}_j}}{d\tau} \frac{d\hat{\sigma}_{q_i\bar{q}_j}}{d\hat{t}} \,, \tag{8.21}$$

with $\tau_0 = 4\,m_h^2/s$, $\hat{s} = \tau s$ and

$$\hat{t}_\pm = m_h^2 - \frac{\hat{s}(1 \mp \beta)}{2} \qquad \text{and} \qquad \beta = \sqrt{1 - \frac{4m_h^2}{\hat{s}}} \,. \tag{8.22}$$

The parton luminosity is given by

$$\frac{d\mathcal{L}^{q_i\bar{q}_j}}{d\tau} = \int_\tau^1 \frac{dx}{x} \left[f_{q_i}(x/\tau, \mu_F^2) f_{\bar{q}_j}(x, \mu_F^2) + f_{\bar{q}_j}(x/\tau, \mu_F^2) f_{q_i}(x, \mu_F^2) \right] . \tag{8.23}$$

We neglected all the kinematical masses in accordance with the 5-flavour scheme of the PDFs while the coupling of the Higgs boson to the light quarks (for flavour diagonal couplings) is

$$g_{hq_i\bar{q}_j} = \frac{m_q^{\overline{MS}}(\mu_R)}{v} \kappa_q \delta_{ij} \,, \tag{8.24}$$

and analogously for the $g_{hhq_i\bar{q}_j}$ coupling.[5]

NLO QCD correction

Since NLO QCD corrections are sizeable, we will take them into account in our analysis. For this purpose, we will detail here how we obtained them. Since the $\hat{t}$ and $\hat{u}$ channel diagrams are strongly suppressed we can take the NLO QCD corrections over from $b\bar{b} \to h$ in the 5-flavour scheme [241–243][6] by some adjustments taking into account the modified LO cross section and the different kinematics of the process. The Feynman diagrams at NLO QCD are shown in fig. 8.5. For convenience and for making our adjustments explicit we report here the formulae from [246]

$$\sigma(q\bar{q} \to h) = \sigma_{LO} + \Delta\sigma_{q\bar{q}} + \Delta\sigma_{qg} \tag{8.25a}$$

$$\Delta\sigma_{q\bar{q}} = \frac{\alpha_s(\mu_R)}{\pi} \int_{\tau_0}^1 d\tau \sum_q \frac{d\mathcal{L}^{q\bar{q}}}{d\tau} \int_\tau^1 dz\; \hat{\sigma}_{LO}(Q^2 = z\tau s)\; \omega_{q\bar{q}}(z) \tag{8.25b}$$

$$\Delta\sigma_{qg} = \frac{\alpha_s(\mu_R)}{\pi} \int_{\tau_0}^1 d\tau \sum_{q,\bar{q}} \frac{d\mathcal{L}^{qg}}{d\tau} \int_\tau^1 dz\; \hat{\sigma}_{LO}(Q^2 = z\tau s)\; \omega_{qg}(z) \tag{8.25c}$$

[5] We note that there is no inconsistency with such an assumption since in scenarios of modified Yukawa couplings, the masses of the quarks need not to be generated by electroweak symmetry breaking.

[6] Note that the NLO and NNLO QCD corrections for $b\bar{b}hh$ have been given in [244, 245].

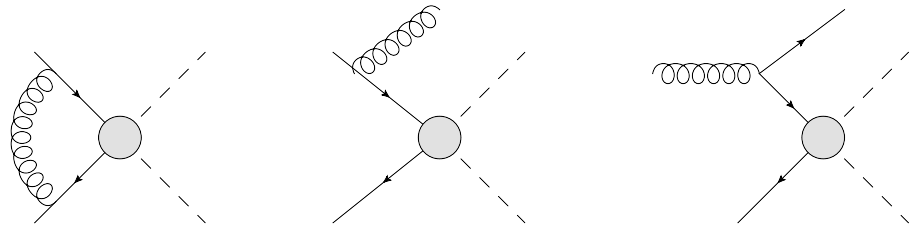

Figure 8.5. Generic form of the QCD corrections of order $\mathcal{O}(\alpha_s)$ to the qqA Higgs pair production.

and

$$\hat{\sigma}_{LO}(Q^2) = \int_{\hat{t}_-}^{\hat{t}_+} \frac{d\hat{\sigma}_{q_i\bar{q}_j}}{d\hat{t}} \tag{8.26}$$

with $z = \tau_0/\tau$, $\sigma_{LO} = \sigma_{\text{hadronic}}$ of eq. (8.21), and the ω factors are given by

$$\begin{aligned}
\omega_{q\bar{q}}(z) &= -P_{qq}(z)\ln\frac{\mu_F^2}{\tau s} + \frac{4}{3}\left\{\left(2\zeta_2 - 1 + \frac{3}{2}\ln\frac{\mu_R^2}{M_{hh}^2}\right)\delta(1-z)\right. && \text{(8.27a)}\\
&+ \left.(1+z^2)\left[2\mathcal{D}_1(z) - \frac{\ln z}{1-z}\right] + 1 - z\right\}, \\
\omega_{qg}(z) &= -\frac{1}{2}P_{qg}(z)\ln\left(\frac{\mu_F^2}{(1-z)^2\tau s}\right) - \frac{1}{8}(1-z)(3-7z), && \text{(8.27b)}
\end{aligned}$$

with $\zeta_2 = \frac{\pi^2}{6}$. The Altarelli Parisi splitting functions $P_{qq}(z)$ and $P_{qg}(z)$ [247–249] are given by

$$P_{qq}(z) = \frac{4}{3}\left[2\mathcal{D}_0(z) - 1 - z + \frac{3}{2}\delta(1-z)\right], \tag{8.28a}$$

$$P_{qg} = \frac{1}{2}\left[z^2 + (1-z)^2\right], \tag{8.28b}$$

and the 'plus' distribution is

$$\mathcal{D}_n(z) := \left(\frac{\ln(1-z)^n}{1-z}\right)_+ . \tag{8.29}$$

We have chosen the renormalisation scale $\mu_R = M_{hh}$ and the factorisation scale $\mu_F = M_{hh}/4$, as central values. We define the NLO K-factor, as

$$K_{NLO} = \frac{\sigma_{NLO}}{\sigma_{LO}} = 1.28 \pm 0.02, \tag{8.30}$$

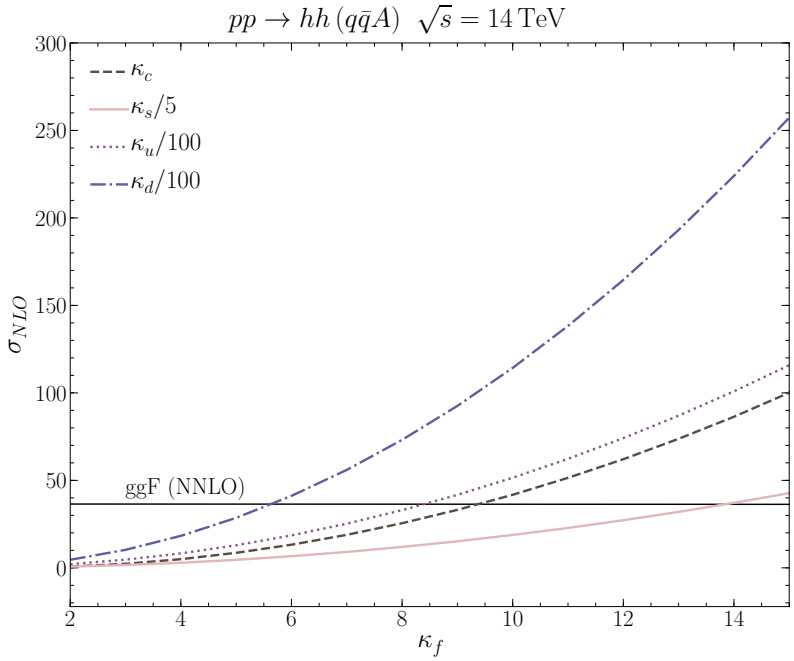

Figure 8.6. The NLO cross section for the qqA process for different scalings of the quark Yukawa couplings. The solid black line shows the NNLO ggF process width rescaled charm Yukawa coupling, whose effect though is unrecognisable in the plot.

with the error denoting the theoretical uncertainty. The K-factor does not depend on the scaling of the couplings, nor the flavour of the initial $q\bar{q}$ since the LO cross section factors out (with exception of the different integration in the real contributions).

Results

While in the SM, the contribution from quark annihilation to a Higgs boson pair is below 0.11 fb at NLO, it scales like $\sim \kappa_q^2 m_q^2/v^4$, dominated by the $hh\bar{q}q$ diagram as can be seen from eq. (8.20), hence showing significant enhancement for enhanced Yukawa couplings. For our benchmark scenario ($g_{hq\bar{q}} = g_{hb\bar{b}}^{\text{SM}}$) we find for the cross section

$$\sigma_{NLO}^{qqA} = 284 \pm 25\ \text{fb}\,, \tag{8.31}$$

and therefore a significantly larger cross section as for the ggF process. In fig. 8.6 we compare the ggF process (black line) for rescaled charm coupling to the Higgs boson(s) with the qqA process for different scalings of the light quark Yukawa couplings (different coloured, dashed, dotted solid and dashed dotted lines). We find that for sufficiently

large scaling of the Yukawa couplings still allowed by current data, qqA can be even the dominant di-Higgs production channel. Note that in the figure we scale the Yukawa couplings for the different quark mass eigenstates differently. For the up and down quark Yukawa coupling the scaling is the same, hence the effect from rescaling the down Yukawa coupling is larger even though the up quark is more abundant in the proton. The plot shows nicely for which values of the coupling modifications the qqA process surpasses ggF.
We would also like to give a qualitative argument for the dominance of qqA for large κ_q. The dominant term for the qqA comes from the $hhq\bar{q}$ vertex diagram, such that the qqA cross section behaves for large values of κ as (assuming that $\sigma_{SM}^{qqA} \sim 0$)

$$(\sigma^{qqA} - \sigma_{SM}^{qqA}) \sim g_{hhq\bar{q}}^2 \sim v^{-4}\, m_q^2\, \kappa_q^2. \tag{8.32}$$

The ggF cross section instead gets contributions from light quark loops from the diagram in fig. 8.2 interfering with top quark loops in the triangle SM diagram, leading to a scaling of

$$(\sigma^{ggF} - \sigma_{SM}^{ggF}) \sim \kappa_q \frac{m_q^2}{v^2\, M_{hh}^2} \ln^2\left(\frac{M_{hh}}{m_q}\right). \tag{8.33}$$

Taking the ratio we get

$$\frac{(\sigma^{qqA} - \sigma_{SM}^{qqA})}{(\sigma^{ggF} - \sigma_{SM}^{ggF})} \sim \frac{\kappa_q}{v^2 \left(\frac{\ln^2\left(\frac{M_{hh}}{m_q}\right)}{M_{hh}^2}\right)}. \tag{8.34}$$

This ratio approaches one (neglecting effects from different PDFs) when

$$\kappa_q^{qqA=ggF} \sim \frac{v^2 \ln^2\left(\frac{M_{hh}}{m_q}\right)}{M_{hh}^2}. \tag{8.35}$$

Using this order of magnitude estimate, we see that the two cross sections are roughly equal if $\kappa_c^{qqA=ggF} \sim 1$, $\kappa_s^{qqA=ggF} \sim 10$ and $\kappa_u^{qqA=ggF} \sim \kappa_d^{qqA=ggF} \sim 10^3$. The actual values of $\kappa_q^{qqA=ggF}$ can be read from fig. 8.6. We observe that $\kappa_q^{qqA=ggF}$ values are not yet excluded, particularly for the first family.

In fig. 8.7 we show the di-Higgs invariant mass normalised differential cross section distributions for the $g_{hq\bar{q}} = g_{hb\bar{b}}^{\mathrm{SM}}$ benchmark point at NLO compared to the NNLO SM ggF cross section extracted from [173]. We notice a considerable shape difference, with shifted peak to the left, and a larger tail. This will allow us later on to use kinematical information to extract the light quark Yukawa couplings.

8.3.3 Higgs decays

The light fermion decay channels will no longer be negligible for enhanced light Yukawa couplings. The decay channels $h \to gg$, $h \to \gamma\gamma$ and $h \to Z\gamma$ containing fermion loops will get modified, but similarly to the production, the modification is $\sim 2\,\kappa_q\,(m_q^2/m_h^2)\,\ln^2(m_q/m_h)$. Thus, the main effect on the Higgs boson branching ratios and width is the 'opening' of the new light fermion channels.
In order to compute the Higgs partial widths and branching ratios (BR) at higher orders in QCD, we have modified the FORTRAN programme `HDECAY` [250, 251] to include the light fermion decay channels and loops in the above-mentioned decays. In the SM, light fermion BRs are of order $\mathcal{O}(10^{-4})$ for $h \to c\bar{c}$, $\mathcal{O}(10^{-6})$ for $h \to s\bar{s}$ and $< \mathcal{O}(10^{-9})$ for the first generation quarks [178]. In our benchmark point ($g_{hq\bar{q}} = g_{hb\bar{b}}^{\mathrm{SM}}$) these would increase to $\sim 18\%$. Correspondingly, the BRs for $h \to b\bar{b}/VV/\tau^+\tau^-$ decrease due to the increased Higgs width in the model.

In fig. 8.8 we show the BRs, denoted by $\mathcal{B}$ in the following, of the Higgs boson pair with the best prospects for discovering Higgs pair production, $hh \to b\bar{b}b\bar{b}$, $hh \to b\bar{b}\gamma\gamma$

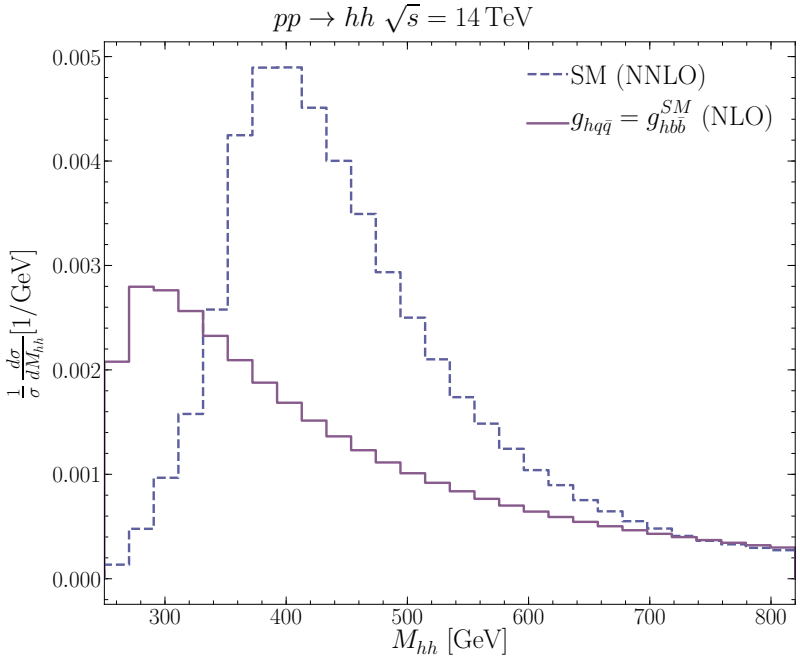

Figure 8.7. The qqA normalised NLO invariant mass differential cross section distribution for the benchmark point ($g_{hq\bar{q}} = g_{hb\bar{b}}^{\mathrm{SM}}$) (solid line) and the NNLO SM ggF cross section obtained from [173] (dashed line).

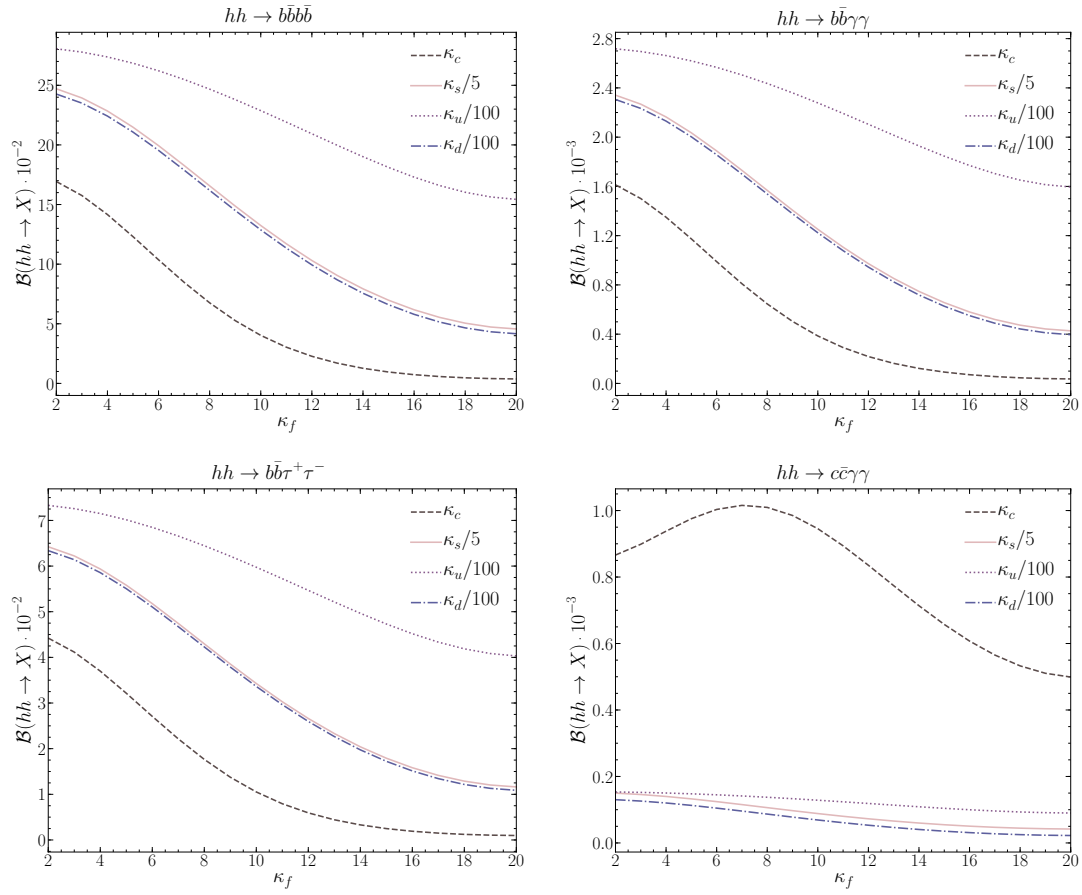

Figure 8.8. Different Higgs pair final states BRs including state-of-the-art QCD corrections as functions of the coupling modification factors κ_f. *Top left*: $hh \to b\bar{b}b\bar{b}$. *Top right*: $hh \to b\bar{b}\gamma\gamma$. *Bottom left*: $hh \to b\bar{b}\tau^+\tau^-$. *Bottom right*: $hh \to c\bar{c}\gamma\gamma$.

and $hh \to b\bar{b}\tau^+\tau^-$ [206], and in addition we show for later purpose also $hh \to c\bar{c}\gamma\gamma$. Once we increase the light quark Yukawa couplings (shown for the different quarks by the different coloured lines) the BRs to $b\bar{b}b\bar{b}$, $b\bar{b}\gamma\gamma$ and $b\bar{b}\tau^+\tau^-$ decrease due to the increased Higgs width. Instead the $\mathcal{B}(hh \to c\bar{c}\gamma\gamma)$ first increases with increasing κ_c, but starts decreasing after reaching a maximum around $\kappa_c \approx 8$, where the $\mathcal{B}(h \to c\bar{c})$ asymptotically reaches 1 while the $\mathcal{B}(h \to \gamma\gamma)$ continues decreasing.

In fig. 8.9 we show the signal strength modifier defined here as

$$\mu_i := \frac{\sigma\, \mathcal{B}_i}{\sigma^{\mathrm{SM}}\, \mathcal{B}_i^{\mathrm{SM}}} \qquad (i = b, c), \tag{8.36}$$

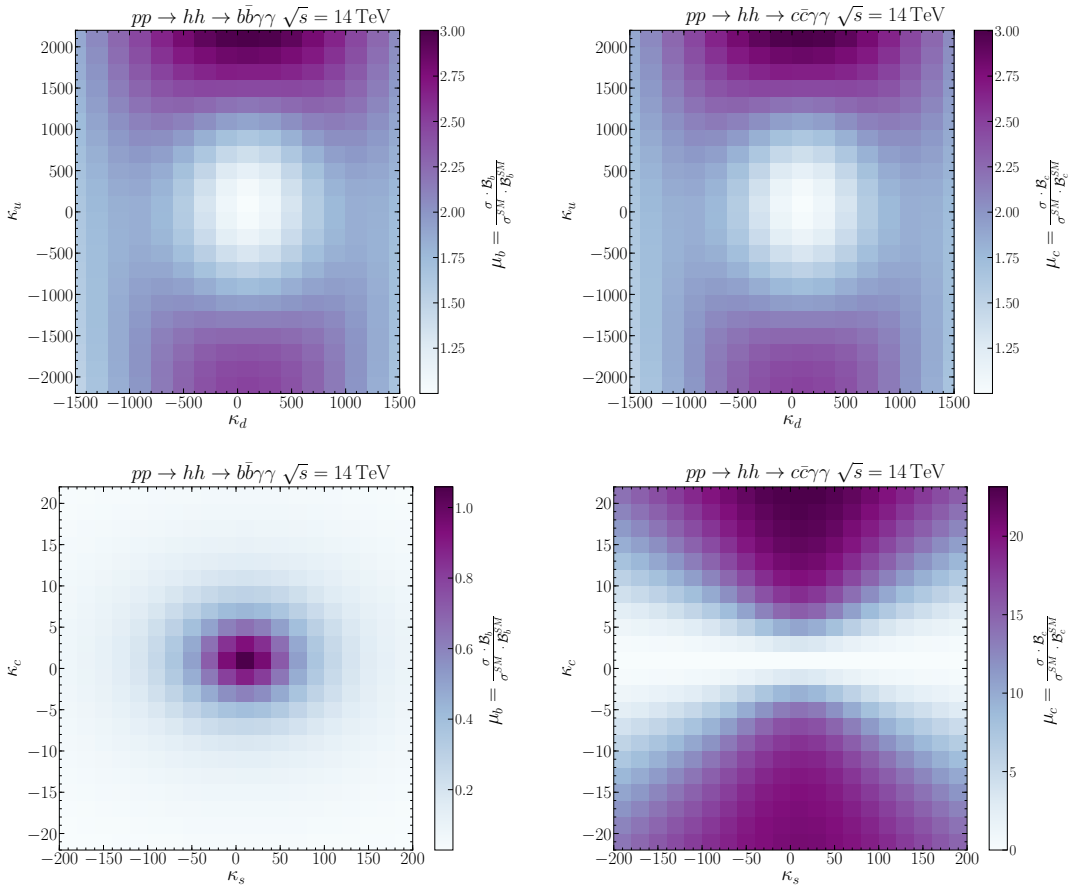

Figure 8.9. Signal strength modifier $\mu = \sigma\,\mathcal{B}(hh \to X)/(\sigma^{SM}\,\mathcal{B}^{SM}(hh \to X))$ fits for bottom quark (left plots) and charm quark (right plots) final states for first (upper row) and second (lower row) generations quark Yukawa modifications.

for final states with bottom (left hand side) and charm quarks (right hand side) for first generation (plots in the upper row) and second generation (plots in the lower row) modified Yukawa couplings. For the first generation, we obtain enhancement of both of the signal strengths μ_c and μ_b, as seen plots in the top of fig. 8.9. The second generation signal strength is instead reduced with respect to the SM for the channels with bottom quarks in the final state $\mu_b := \sigma\,\mathcal{B}_b/\sigma^{\mathrm{SM}}\,\mathcal{B}_b^{\mathrm{SM}}$ when scaling the charm and strange Yukawa couplings, as seen in the lower left plot of fig. 8.9. Nevertheless, when considering channels with charm quarks in the final state the signal strength $\mu_c := \sigma\,\mathcal{B}_c/\sigma^{\mathrm{SM}}\,\mathcal{B}_c^{\mathrm{SM}}$ is enhanced due to both enhancements from the cross section and BRs. The increased cross section in the presence of enhanced light quark Yukawa couplings has to compete

with the decreased BRs for the standard search channels for di-Higgs production. We shall notice however, that while the increase of the cross section comes mainly from the $q\bar{q}hh$ vertex diagram, the decrease of the BRs stems from the increased width which would be in good approximation (for flavour-diagonal couplings)

$$\Gamma_H \approx \Gamma_{\text{SM}} + \sum_{q=c,s,u,d} \frac{g^2_{h\bar{q}_i q_i}}{(g^{\text{SM}}_{h\bar{q}_i q_i})^2} \Gamma_q \,, \tag{8.37}$$

where Γ_q stands generically for the partial width of the Higgs boson decaying to light quarks. In a non-linear EFT as briefly discussed in sect. 8.2, the couplings of one Higgs boson to quarks and two Higgs bosons to quarks are uncorrelated. So an increase of the cross section for hh production in the presence of modified light quark Yukawa couplings does not need to go hand in hand with a decrease of the BRs in the final states with bottom quarks (or at least the decrease could be in-proportional).

8.4 Phenomenological analysis

In this section we will investigate whether enhanced light quark Yukawa couplings can be measured in Higgs pair production. As we have seen in the previous section, we can get an enhancement in the signal strengths for first generation quarks from the enhanced cross sections while BRs in the standard di-Higgs search channels decrease. We have also seen that final states with charm quarks might be worth studying further for enhanced second generation Yukawa couplings. Here in this section, we will perform a phenomenological analysis to see if the HL-LHC has potential to constrain the light quark Yukawa couplings in di-Higgs channels. The first part of the section is devoted to the analysis strategy, before we discuss the bounds from final states with bottom quarks. We will be focussing in particular on the $b\bar{b}\gamma\gamma$ final state as it holds promising prospects [181, 252–256] despite the low BR of 0.27% in the SM for the Higgs boson pair. At the end of the section we take a closer look at the $c\bar{c}\gamma\gamma$ final state, which is in particular interesting for enhanced charm Yukawa couplings.

For our phenomenological analysis we do not assume that the efficiency is constant for the new physics hypothesis with respect to the SM efficiency. Hence, we use the full definition of the signal strength μ as the ratio of the number of events measured or expected given the new physics hypothesis over the number of events expected by the SM (null) hypothesis

$$\mu = \frac{N_{expec}}{N^{SM}_{expec}}. \tag{8.38}$$

The number of expected events N_{expec} at a hadron collider with integrated luminosity L and selection efficiency ϵ_{SEL} in the narrow width approximation for a process $pp \to R$

with subsequent decay of $R \to X$ is given by the formula

$$N_{expec} = \sigma(pp \to R)\, \mathcal{B}(R \to X)\, L\, \epsilon_{\text{SEL}}. \tag{8.39}$$

The selection efficiency can be written in terms of several factors by

$$\epsilon_{\text{SEL}} = \epsilon_{\text{Acc}} \cdot \epsilon_{\text{Rec}} \cdot \epsilon_{\text{Trig}} \cdot \epsilon_{\text{cut}}, \tag{8.40}$$

with ϵ_{Acc} being the detector acceptance efficiency, ϵ_{Rec} the efficiency from reconstruction, ϵ_{Trig} the trigger efficiency and ϵ_{cut} the efficiency obtained from the applied kinematical cuts on the signal. For the ATLAS and CMS experiments, the acceptance for the Higgs pair production is close to 100% due to the complete coverage of the pseudorapidity range of $2.5 < |\eta| < 5$, so we use $\epsilon_{\text{Acc}} = 1$. The other efficiencies will be discussed in more detail in subsect. 8.4.2.

8.4.1 Event generation

The parton showering and hadronisation of the process $pp \to hh \to b\bar{b}\gamma\gamma$ has been simulated using `Pythia` 6.4 [257] with the settings detailed in appendix **??**. The cross section of the Higgs pair production (ggF and qqA both at LO multiplied by a K-factor as described in subsect. 8.3.1 and 8.3.2) is fed to `Pythia` which decays the two Higgs bosons and then performs the parton showering. We have accounted for the correct BRs by using the values obtained as described in subsect. 8.3.3 from `HDECAY`. We have turned on initial and final state QCD and QED radiation and multiple interactions.
The generated events were written to a ROOT file via `RootTuple` tool [258] for further analysis.

8.4.2 Analysis strategy

The analysis strategy follows the one performed in [252] allowing us to use their backgrounds. Note that the analysis was based on the SM simulated events, meaning that the significances could be potentially improved performing a dedicated new physics analysis. In order to satisfy the minimal reconstruction requirements of the LHC we select only events with

$$p_T(\gamma/j) > 25\,\text{GeV}\,, \quad |\eta(\gamma/j)| < 2.5\,. \tag{8.41}$$

Moreover, we veto events with hard leptons

$$p_T(\ell) > 20\,\text{GeV}, \quad |\eta(\ell)| < 2.5\,, \tag{8.42}$$

corresponding of an expected $\epsilon_{\text{Trig}} = 0.9$. Jets were clustered using `fastjet` [259] with the anti-kt algorithm with a radius parameter of $R = 0.5$.

cut	ϵ_{cut}	$\delta\epsilon_{\text{cut}}$
p_T cuts in eq. (8.43)	0.35	0.07
ΔR cuts in eq. (8.44)	0.69	0.21
total	0.16	0.05

Table 8.1. The cuts used in the analysis with their efficiency ϵ_{cut} and uncertainties on these efficiencies $\delta\epsilon_{\text{cut}} = \sqrt{\epsilon(1-\epsilon)\,N}$, where N is the total number of events. The analysis was performed on 100K SM simulated events.

We have used a b-tagging efficiency of $\epsilon_b = 0.7$ [7]. The contamination probability of $\epsilon_{j\to b} < 1\%$ is found to be consistent with ATLAS and CMS performance [261–263]. For the photon reconstruction efficiency we used $\epsilon_\gamma = 0.8$ as reported by ATLAS and CMS in [263, 264]. The selection cuts we used are the same ones as in [252], starting with the cuts of the transverse momentum p_T of the photons and b-tagged jets. The two hardest photons/b-tagged jets, with transverse momentum $p_{T>}$, and the softer ones with $p_{T<}$ are selected to satisfy

$$p_{T>}(b/\gamma) > 50\,\text{GeV}, \quad \text{and} \quad p_{T<}(b/\gamma) > 30\,\text{GeV}\,. \tag{8.43}$$

In order to ensure well-separation of the photons and b-jets, we require the following cuts on the jet radius,

$$\Delta R(b,b) < 2, \quad \Delta R(\gamma,\gamma) < 2, \quad \Delta R(b,\gamma) > 1.5\,. \tag{8.44}$$

While the majority of the signal lies within this region, these cuts significantly reduce the backgrounds.

We choose a wide $m_{\gamma\gamma}$ window (see eq. (8.45)) corresponding to 2-3 times the photon resolution of ATLAS and CMS [263, 264] which does not cause any significant loss. As for the Higgs mass window reconstructed from 2 b-jets $m_{b\bar{b}}$, the mass window chosen in eq. (8.45) corresponds to the given b-tagging efficiency. The mass windows used are then

$$105\,\text{GeV} < m_{b\bar{b}} < 145\,\text{GeV}, \quad 123\,\text{GeV} < m_{\gamma\gamma} < 130\,\text{GeV}\,. \tag{8.45}$$

The selection cuts are summarised in table 8.1 with their corresponding efficiency. In table 8.2 we summarise all the efficiencies used in the analysis.

The major backgrounds for the considered final state are the $b\bar{b}\gamma\gamma$ continuum background, $\gamma\gamma jj$ with two mistagged jets, $t\bar{t}h$, Zh and $b\bar{b}h$ in the order of importance after the cuts in eq. (8.43). The number of background events (surviving the cuts) is taken from [252]. The backgrounds are illustrated in the fig. **??** in which we show the number of events for the SM Higgs pair signal in light blue and the most relevant backgrounds

[7] We have explicitly cross checked the number by doing a mass-drop tagger analysis [260].

Type	efficiency
ϵ_{Acc}	~ 1
ϵ_{Rec}	0.31
ϵ_{Trig}	0.90
ϵ_{Cut}	0.16
total	0.044

Table 8.2. Values of the efficiencies calculated/used in this analysis.

in other colors. It should be noted that the background $h(\to \gamma\gamma)Z(\to b\bar{b})$ is modified in the presence of enhanced light quark Yukawa couplings. We checked though explicitly that scaling the Yukawa couplings to the values of our benchmark point only changes the NLO cross section by less than 1%, making this effect negligible. The analysis was carried out for varying values of κ_f for the different flavours. Due to the change in the kinematical distributions (cf. fig. **??**) resulting from the PDFs of the different flavours, the efficiencies depend on the flavour of the quarks. For $\kappa_f \gg 1$ the κ_f dependence factors out of the cross section such that for the values considered in the analysis of the distributions no dependence on the concrete value of κ_f is seen. The flavour-specific efficiency ratio ϵ_f is given by

$$\epsilon_f = \frac{\sigma_{ggF}\,\epsilon_{ggF} + \sigma_{q\bar{q}}\,\epsilon_{qq}}{\sigma_{gg} + \sigma_{q\bar{q}}}\,, \tag{8.46}$$

with σ_{ggF} being the gluon fusion cross section, $\sigma_{q\bar{q}}$ the quark annihilation cross section and $\epsilon_{ggF} = 0.044$. We give the values for the qqA efficiency ϵ_{qq} in table 8.3.

In fig. **??** we show for the SM and for our benchmark point $g_{hq\bar{q}} = g^{\text{SM}}_{hb\bar{b}}$ the M_{hh} distribution. The lower panels in the plot show the efficiencies. These plots illustrate how the efficiency depends on the shape of the distribution, and hence the flavour f that is scaled by κ_f.

$\delta\kappa$	ϵ_{qq}
κ_u	0.050
κ_d	0.049
κ_u & κ_d	0.053
κ_c	0.034
κ_s	0.037
κ_c & κ_s	0.039

Table 8.3. The dependence of ϵ_{qq} on the flavour of the Yukawa couplings' scalings.

8.4.3 Statistical analysis

We have used the likelihood ratio test statistic q_μ in order to estimate the HL-LHC sensitivity, and set projected limits on the scalings of the light Yukawa couplings. A (log)–likelihood was constructed from the signal and background events in each bin of the histogram in fig. **??**,

$$-\ln \mathscr{L}(\mu) = \sum_{i\in \text{bins}} (N_{bi} + \mu\, N_{si}) - n_i\, \ln(N_{bi} + \mu\, N_{si}), \tag{8.47}$$

with N_{bi} and N_{si} being the number of background and signal events in the ith M_{hh} distribution, respectively. In order to include the theoretical uncertainties on the expected number of signal events, the above likelihood was extended by a gaussian distribution for N_{si} in which the mean equals to the central value of the bin values and standard deviation σ equals to its theoretical uncertainty. The signal strength μ was then estimated by minimising $-\ln \mathscr{L}(\mu)$ to obtain the estimator for $\hat{\mu}$ by injecting SM signal + background events n_i. The test statistic is then given by

$$q_\mu = 2(\ln \mathscr{L}(\mu) - \ln \mathscr{L}(\hat{\mu})), \tag{8.48}$$

following the procedure described in [265].

In order to set bounds on the scalings, we have fitted the signal strength inclusively by a function depending on the scaling of the Yukawa couplings

$$\mu(\kappa_1, \kappa_2) = \left\{ \frac{1}{Z} \left[A_0 \left(\kappa_1^2 \frac{m_{q1}^2}{M_{hh}^2} \ln^2\left(\frac{M_{hh}}{m_{q1}}\right)\right) + A_1 \left(\kappa_2^2 \frac{m_{q2}^2}{M_{hh}^2} \ln^2\left(\frac{M_{hh}}{m_{q2}}\right)\right)\right] + B_2 \right\} \epsilon_f, \tag{8.49}$$

with

$$Z = \frac{\kappa_1^2\, m_{q1}^2 + \kappa_2^2\, m_{q2}^2 + B_0}{m_{q1}^2 + m_{q2}^2 + B_1} \tag{8.50}$$

and m_{q1} and m_{q2} denoting the $\overline{\text{MS}}$ masses of the quarks.

Taking $M_{hh} \approx 300$ GeV, we could perform a fit for the signal strength for each of the quark generations scalings separately. Note that one could of course also extend the model to include the dependence of the signal strength on four Yukawa coupling modifications, taking into account the correlation between them when fitting the likelihood in eq. (8.47).

The expected HL-LHC sensitivity for the signal strength at 95% (68 %) CL is found to be $\mu = 2.1(1.6)$.

8.4.4 Results for the $b\bar{b}\gamma\gamma$ final state

We have performed a scan on the first generation Yukawa coupling scalings κ_u and κ_d in order to obtain exclusion limits, derived from the likelihood contours shown in fig. 8.10. The individual κ_q expected upper bounds at 68% and 95% CL are obtained by profiling the likelihood over the other first generation κ_q. Doing so, we obtain the following upper bounds for HL-LHC

$$-571 < \kappa_d < 575, \ (68\% \text{ CL}), \qquad -853 < \kappa_d < 856, \ (95\% \text{ CL}), \tag{8.51}$$

and

$$-1192 < \kappa_u < 1170, \ (68\% \text{ CL}), \qquad -1771 < \kappa_u < 1750, \ (95\% \text{ CL}). \tag{8.52}$$

Note that these bounds are not directly comparable to the standard κ formalism bounds since we relate with κ the Yukawa couplings $g_{hq\bar{q}}$ and the new coupling $g_{hhq\bar{q}}$. For the second generation quarks we were not able to obtain similar bounds due to the reduction of μ/μ_{SM} with increasing κ_s and κ_c away from the SM, which stems from the

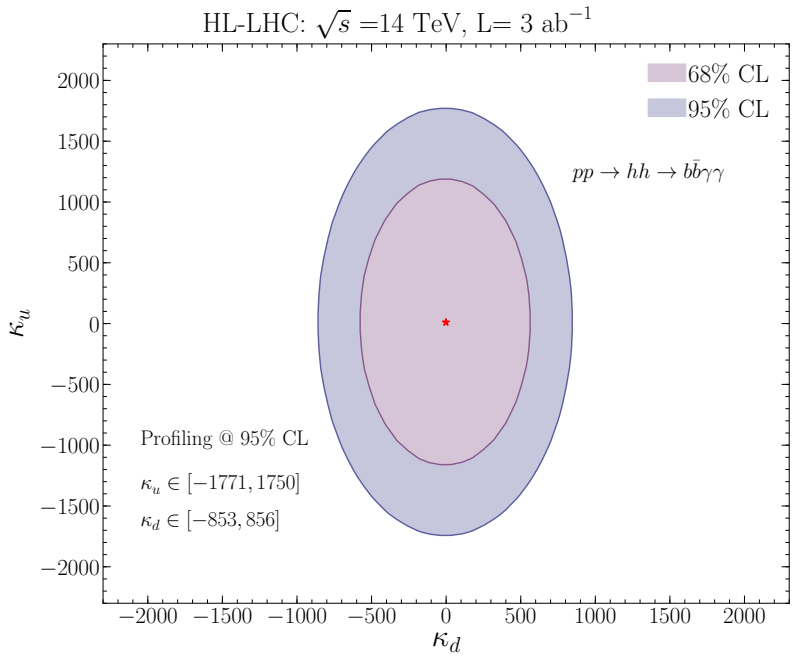

Figure 8.10. The expected sensitivity likelihood contours at 68% and 95% CL of the HL-LHC for the first generation Yukawa coupling scalings.

decrease of the branching ratio $\mathcal{B}(hh \to b\bar{b}\gamma\gamma)$ as new decay channels open, while the cross section is not as much enhanced as for up and down quarks due to the charm and strange quark being less abundant in the proton. This leads to signal strength modifiers $\mu/\mu_{\rm SM} < 1$ (*cf.* fig. 8.9). We will analyse the second generation Yukawa couplings instead for the final state $hh \to c\bar{c}\gamma\gamma$, in which we observe significant enhancement of the relative signal strength modifier $\mu/\mu_{\rm SM}$ (*cf.* fig. 8.9). Before turning to a different final state though, we will reanalyse the $b\bar{b}\gamma\gamma$ final state under the point of view of a non-linear effective field theory, hence leaving the couplings $g_{hq\bar{q}}$ and $g_{hhq\bar{q}}$ independent.

Results for non-linear EFT

We will consider in this part a non-linear EFT as introduced in eq. (8.15). By expanding in the chiral modes, taking the 0th mode and the flavour diagonal terms, we get

$$-\mathcal{L} = \bar{q}_L \frac{m_q}{v}\left(v + c_q h + \frac{c_{qq}}{v}h^2 + \dots\right) q_R + h.c, \tag{8.53}$$

where we rescaled the coefficients k_q and k_{2q} of eq. (8.15) as $k_{q,ii} = \sqrt{2}c_q m_q/v$ and $k_{2q,ii} = \sqrt{2}c_{qq}m_q/v^2$. Unlike the linear EFT, the Wilson coefficients c_q and c_{qq} are independent of each other. Using the previous analysis, it is possible to set bounds on these coefficients separately, as seen in fig. 8.11. We observe that without the $hh\bar{q}q$ interaction, one cannot set bounds on any of the light Yukawa couplings from Higgs pair production. We remark though that in case any deviation in the light Yukawa couplings is observed, the di-Higgs channel can distinguish whether electroweak symmetry breaking is realised linearly or non-linearly.

8.4.5 Charm-tagging and second generation bounds

In order to set bounds on the second generation Yukawa couplings, we use the method developed in [210, 266] that re-analyses final states with b-quarks based on the mistagging of c-jets as b-jets in associated VH production. The analysis relies on the current CMS [267] and ATLAS [268] working points for b-tagging, as illustrated in the table 8.4. The signal strength estimator when considering the mistagging probability of b-jets to c-jets (i.e. c-jet contamination of b-tagged jets) $\epsilon_{b\to c}$ is

$$\hat{\mu} = \frac{\sigma_{hh}\,\mathcal{B}_b\;\epsilon_{b1}\,\epsilon_{b2}\,\epsilon_f + \sigma_{hh}\,\mathcal{B}_c\,\epsilon_{b\to c,1}\,\epsilon_{b\to c,2}\,\epsilon_f}{\sigma_{hh}^{\rm SM}\,\mathcal{B}_b^{\rm SM}\,\epsilon_{b1}\,\epsilon_{b2}}, \tag{8.54}$$

with ϵ_f being the efficiency ratio in eq. (8.46). The above expression simplifies to

$$\hat{\mu} = \mu_b\,\epsilon_f + 0.05 \cdot \left(\epsilon_{c/b}^{b\text{-tag}}\right)^2 \epsilon_f \cdot \mu_c\,, \tag{8.55}$$

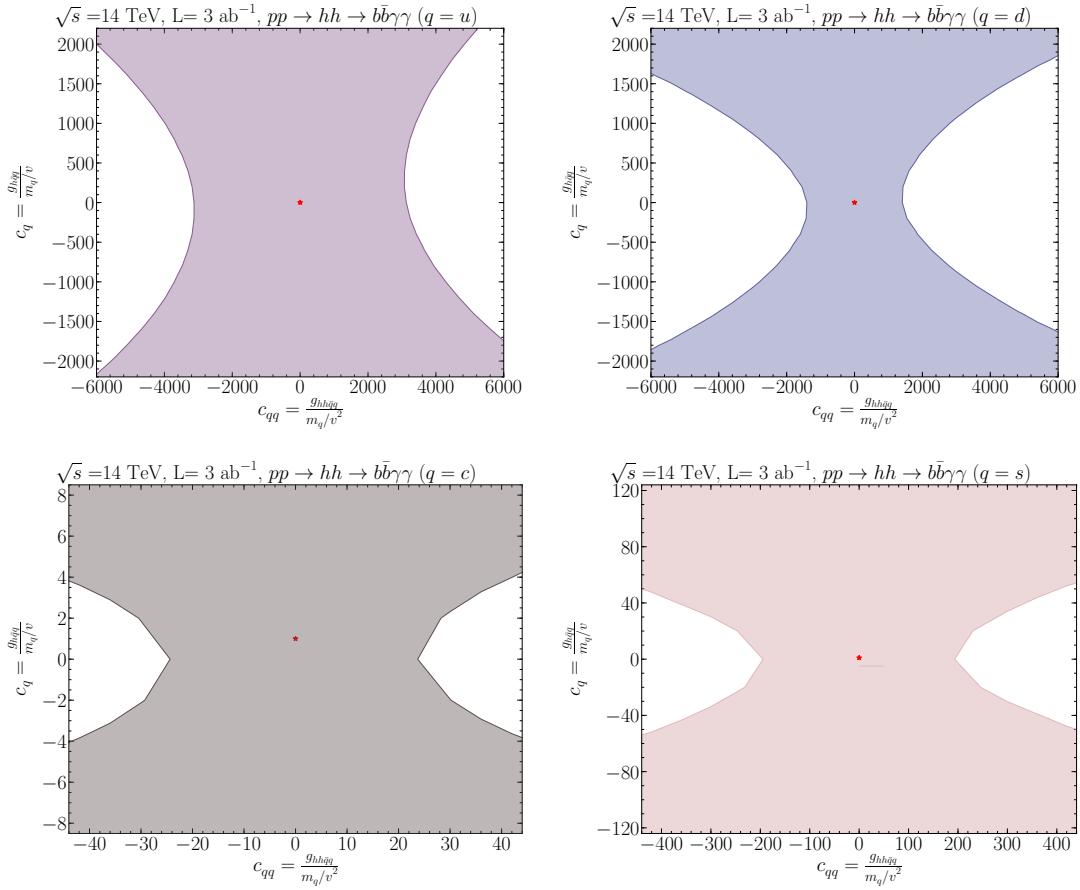

Figure 8.11. 95% CL likelihood contours for the non-linear EFT Wilson coefficients c_{qq} and c_q for up (*upper left*), down (*upper right*), charm (*lower left*) and strange quarks (*lower right*).

for $\mathcal{B}_c^{\mathrm{SM}}/\mathcal{B}_b^{\mathrm{SM}} \approx 0.05$. The signal strength modifier of the $b\bar{b}\gamma\gamma$ final state is denoted by μ_b and the one of the $c\bar{c}\gamma\gamma$ final state by μ_c. The ratio of tagging efficiencies is defined as

$$\left(\epsilon_{c/b}^{b\text{-tag}}\right)^2 = \frac{\epsilon_{b\to c,1}\epsilon_{b\to c,2}}{\epsilon_{b1}\epsilon_{b2}}\,. \tag{8.56}$$

One b-tagging working point could only constrain either μ_b or μ_c. In order to resolve the flat direction several b-tagging working points $\left(\epsilon_{c/b}^{b\text{-tag}}\right)^2$ are needed. This is illustrated in fig. 8.12, where the working points fitting contours are combined using Fisher's method [269]. We thus obtain an upper projected limit on the charm final state signal

Detector	Cuts (1st, 2nd) b-jets	$\epsilon_{c/b}^{\text{b-tag 2}}$
CMS	Med1-Med1	0.18
CMS	Med1-Loose	0.23
ATLAS	Med-Med	$8.2 \cdot 10^{-2}$
ATLAS	Tight-Tight	$5.9 \cdot 10^{-3}$

Table 8.4. The b-tagging working points used in the analysis, for CMS [267] and ATLAS [268].

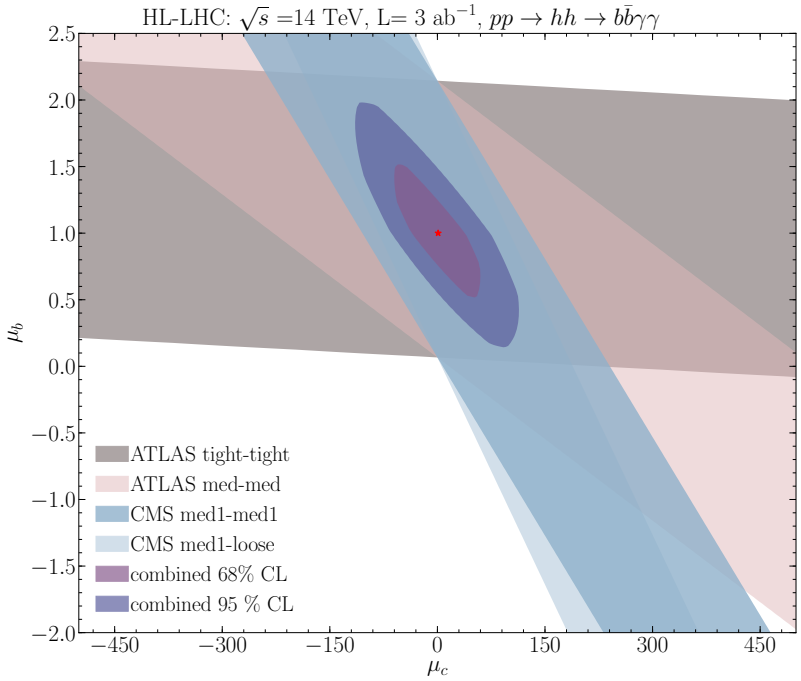

Figure 8.12. The 95 % CL contours of μ_b vs μ_c, obtained from fitting of the signal strength for several CMS and ATLAS b-tagging working points. Their combination with the 68% and 95% CL upper limits on μ_b and μ_c are shown.

strength after profiling over μ_b,

$$\mu_c(\text{up}) = 36.6\ (68\%\ \text{CL})\,, \qquad \mu_c(\text{up}) = 74.8\ (95\%\ \text{CL})\,. \tag{8.57}$$

However, the obtained sensitivity is not sufficient to set any better limits at 95% CL than the existing ones (or projected ones in other channels) for the Yukawa coupling modifiers κ_c, and κ_s. Instead, we can improve on them by introducing c-tagging working

c-tagging working point	ϵ_c	$\epsilon_{c\to b}$	μ_c(up) 95% CL
c-tag I [270, 271]	19%	13%	10.1
c-tag II [272, 273]	30%	20%	8.2
c-tag III [272, 273]	50%	20%	3.8

Table 8.5. The c-tagging working points with the expected 95% CL upper limit (sensitivity) of μ_c obtained after profiling over μ_b.

points $(\epsilon_{c/b}^{c\text{-tag}})^2$

$$\left(\epsilon_{c/b}^{c\text{-tag}}\right)^2 = \frac{\epsilon_{c1}\epsilon_{c2}}{\epsilon_{c\to b,1}\epsilon_{c\to b,2}}\,, \tag{8.58}$$

mixed with the b-tagging ones. We denoted the contamination of c-jets with b-jets by $\epsilon_{c\to b}$. For mixed tagging, the signal strength estimator becomes

$$\hat{\mu} = \frac{\sigma_{hh}\,\mathcal{B}_b\,\epsilon_{b1}\,\epsilon_{b2}\,\epsilon_f + \sigma_{hh}\,\mathcal{B}_c\,\epsilon_{c1}\,\epsilon_{c2}\,\epsilon_f}{\sigma_{hh}^{\rm SM}\,\mathcal{B}_b^{\rm SM}\,\epsilon_{b1}\,\epsilon_{b2} + \sigma_{hh}^{\rm SM}\,\mathcal{B}_c^{\rm SM}\,\epsilon_{c1}\,\epsilon_{c2}}\,, \tag{8.59}$$

where now ϵ_b is either ϵ_b or $\epsilon_{c\to b}$ and ϵ_c either ϵ_c or $\epsilon_{b\to c}$. This simplifies to

$$\hat{\mu} = \frac{\mu_b + 0.05\,\epsilon_{c/b}^2\,\mu_c}{1 + 0.05\,\epsilon_{c/b}^2}\,\epsilon_f\,. \tag{8.60}$$

The working point $\epsilon_{c/b}^2$ could be the b-tagging or c-tagging working point. Assuming that c-tagging and b-tagging are uncorrelated, and working with the methods discussed in [187, 210], i.e. combining the ATLAS medium cuts (med.) for b-tagging with the c-tagging working points in order to break the degeneracy, we could improve the 95% CL sensitivity on μ_c. We start by the c-tagging working point used by the ATLAS collaboration in Run I searches for top squarks decays to charm and neutralino [270, 271], which we refer to as c-tagging I. Further c-tagging working points from the HL-LHC upgrade are used: with the expected insertable B-layer (IBL) sub-detector that is to be installed during the ATLAS HL-LHC upgrade [272, 273], the new c-tagging II and III points, as illustrated in table 8.5, can be identified. In fig. **??** we used them to obtain in combination with the ATLAS med b-tagging expected 95% CL upper limits on μ_c for the HL-LHC from an analysis of the final state $b\bar{b}\gamma\gamma$. Fitting signal strengths with varying κ_c, κ_s for charm and bottom final states (*cf.* eq. (8.49)) for constructing the likelihood $\mathscr{L}(\kappa_c, \kappa_s)$, we can set limits from the anticipated charm tagging working points as shown in fig. 8.13. These projected limits are an improvement compared to the current direct bound and prospects for HL-LHC, particularly for charm quark Yukawa modifications [187, 210]. Again, it should be kept in mind that the bounds on κ_q do not just correspond to the scaling of the Yukawa coupling, but also to the new coupling

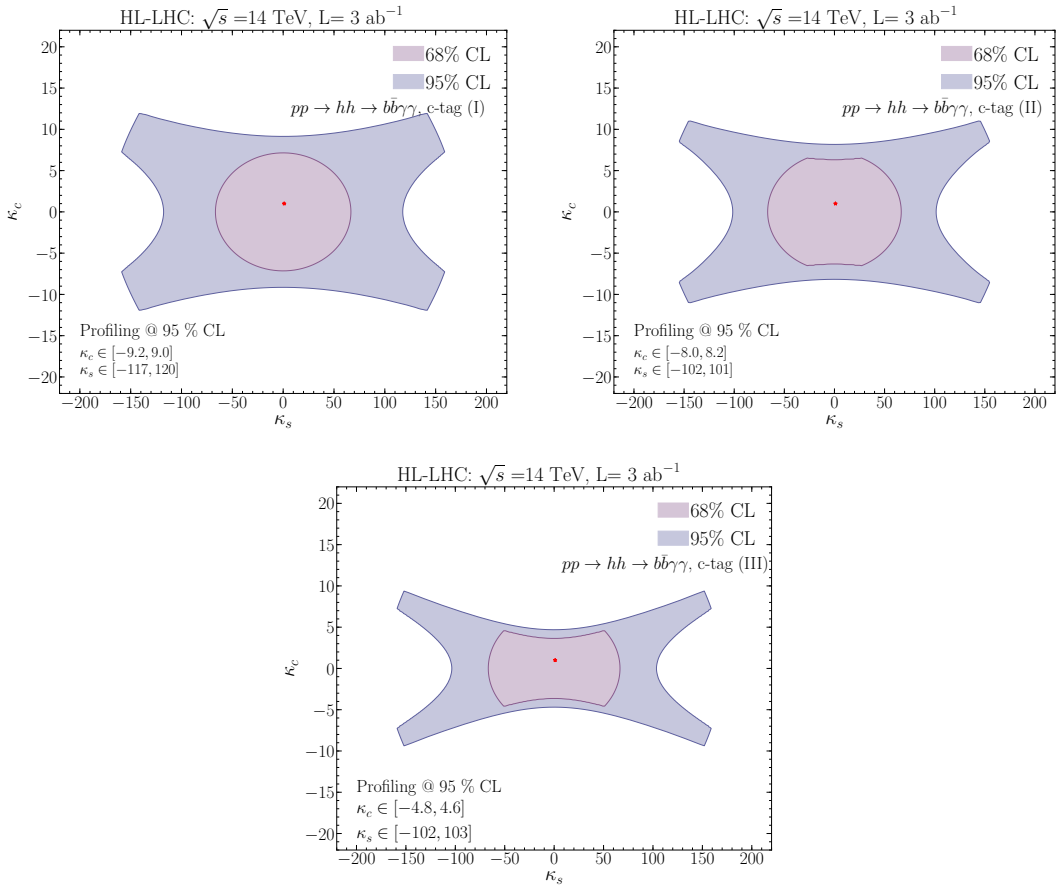

Figure 8.13. The expected sensitivity likelihood contours at 68% CL and 95% CL for an integrated luminosity $L = 3000$ fb^{-1} for modified second generation quark Yukawa couplings, using the c-tagging I (*upper pannel, left*), II (*upper pannel, right*) and III (*lower pannel*) working points.

$g_{hhq\bar{q}}$ arising in SMEFT.

8.5 Conclusion

The couplings to the first and second generation fermions remain among the less well measured couplings of the Higgs boson. In this paper we investigated the possibility of measuring light quark Yukawa couplings in Higgs pair production. For enhanced Yukawa couplings of the first generation quarks, we found that limits can be set when considering quark annihilation with subsequent decay of the Higgs boson pair to $b\bar{b}\gamma\gamma$. In an effective theory description with dimension 6 operators that modify the quark

Yukawa couplings, there exists also a coupling of two Higgs bosons to two fermions. This coupling increases the Higgs pair production cross section and hence allows to set bounds on the light quark Yukawa coupling modifications. For the HL-LHC we found a sensitivity of $|\kappa_u| \lesssim 1170$ and $|\kappa_d| \lesssim 850$, *cf.* fig. 8.10, which is comparable to the sensitivity of other channels that can directly probe the light quark Yukawa couplings though being weaker than the results from a global fit. Further improvements could be possible with a more dedicated analysis. We note though that the bounds we find stem mostly due to the diagram involving the coupling of two Higgs bosons to two quarks, as we showed explicitly also by considering a non-linear effective theory in which the coupling of one and two Higgs boson to fermions are uncorrelated. This channel can hence also be used to distinguish between a linear vs non-linear Higgs EFT hypothesis in the light quark sector. The LHC experiments should hence consider the Higgs pair production process in addition to other channels for probing the light quark Yukawa couplings.

For the second generation quarks we found that at the HL-LHC in the di-Higgs channel we will be able to set competitive bounds on the charm Yukawa coupling if final states with tagged charm quarks are considered. We were in particularly considering the final state $c\bar{c}\gamma\gamma$, in which we found a sensitivity of $|\kappa_c| \lesssim 5$ and $|\kappa_s| \lesssim 100$, *cf.* fig. 8.13, where the first prospective limit is comparable to the prospects from charm tagging in the Vh channel [187].

9 Optimised search for Higgs pair via Interpretable machine learning

9.1 Introduction

The primary objectives of this work are as follows:

- We show some well motivated BSM scenarios where light-quark Yukawas can be enhanced simultaneously with the Higgs trilinear coupling.
- We perform an interpretable machine learning analysis based on boosted decision trees and Shapley values, a measure derived from Coalition Game Theory to extract signal significance to get a better handle on the measurement of light-quark Yukawas.
- We perform simultaneous fits for several combinations of light-quark Yukawa couplings and the Higgs trilinear coupling.

We show in section 8.2 the relevant EFT operators for the di-Higgs processes, discuss flavor bounds and minimal flavor violation (MFV). Then we introduce in section 10.2 the concept of aligned flavor violation (AFV), and various "concrete" examples realising large enhancement to light yukawa while evading flavor bounds. We then study the leading contributing channels with simulation details explained in section 9.2. Further we discuss in section 9.3 the multivariate analysis and interpretable machine learning approach we adopt. We present prospected results in section 9.4 at the HL-LHC and FCC. In section 9.5 we summarize our main findings.

In the general framework of SMEFT, additional assumptions on UV-motivated flavor structure avoids stringent low energy FCNC and EDM bounds, making collider probe on the Yukawa and related Wilson coefficients competitive and relevant. See a recent overview of Yukawa coupling bounds from flavor and collider Higgs data, in the SMEFT framework given certain flavor structure. [274]

The single Higgs production and decay channels as measured currently already provide indirect bounds on the light quark Yukawa couplings from global fit. The main sensitivity comes from enhancement to the production when $q\bar{q}$ fusion of the Higgs become comparable to ggF channel when the corresponding light-quark Yukawa is sufficiently enhanced. Secondly, there is additional overall "dilution" factor from the modified Higgs

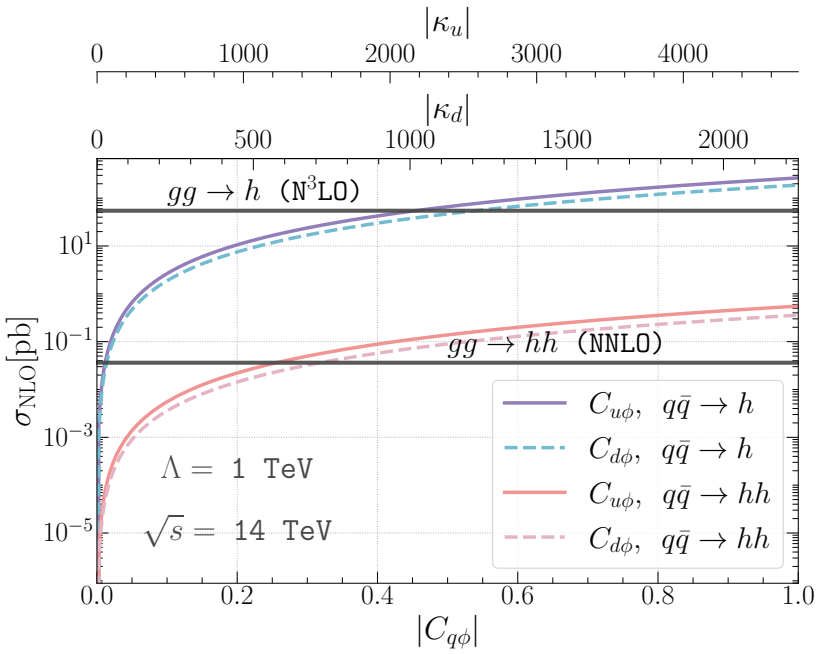

Figure 9.1. *The production cross-section of single Higgs and di-Higgs at* 14 *TeV from the quark anti-quark annihilation $q\bar{q}A$ as a function of the Wilson coefficients $C_{u\phi}$ and $C_{d\phi}$ versus the SM gluon fusion cross-sections (the horizontal solid line for $gg \to h$ and the dashed-dotted one for $gg \to hh$). One can observe that for values of $C_{u\phi} = 0.22\,(0.43)$ and $C_{d\phi} = 0.26\,(0.47)$ the $q\bar{q}A$ channel becomes the dominant di-Higgs (single Higgs) production channel. The UV scale is set to $\Lambda = 1$ TeV.*

total width, for a final state of a specific (non-"light-jet") decay channel. In the case of di-Higgs, the $q\bar{q}hh$ contact interaction become important for the di-Higgs production, and could become dominant production channel over the SM gluon fusion channel through loop. The sensitivity thus achieved to the corresponding light-quark Yukawa in the SMEFT framework is better compared to that from single Higgs inclusive observable, and could even be competitive to single Higgs differential studies, as will be shown from our study.

9.1.1 Considerations of experimental constraints

For the 2HDM model, there are three main scenarios from the experimental searches point of view, in which one can obtain enhancements to light-quark Yukawa couplings. In the first scenario, the heavy Higgs H has a small mass $m_H < 2$ TeV. Experimental resonance searches rules out this scenario where the resonant Higgs pair production is enhanced significantly due to the decay $H \to hh$, as the trilinear Hhh coupling scales

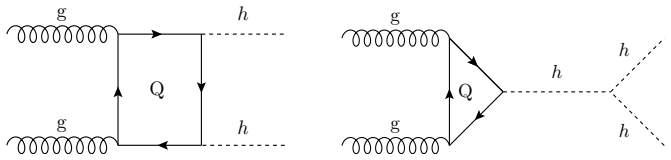

Figure 9.2. *The cross-section of the ggF channel can be decomposed into three subprocesses based on its dependence on the trilinear coupling λ. The triangle topology depends on λ^2, the box one does not depend on it and the interference amongst the latter two is linear in λ.*

as [203]

$$g_{Hhh} \approx \frac{m_H^2}{v^2} \cos(\beta - \alpha). \tag{9.1}$$

In the second scenario, we have a heavier H but a large $Hq\bar{q}$ coupling. Here, the dijet resonance searches from $H \to jj$ decay, provides the strongest constraints. Lastly, when we consider a heavy H and $Hq\bar{q}$ not excluded by di-jet searches we lie within the EFT limit and non-resonant Higgs pair production discussed in this paper gives us the dominant constraints.

In the 2HDM with AFV or SFV, there is an interplay between light quark Yukawa and the Higgs trilinear self-coupling. This comes from the alignment parameters α and β, as we see in equations (10.25) and (10.26). For example, when the mass of H is allowed to be very large $m_H > 4$ TeV, enhancement to light-quark Yukawa couplings would be completely constrained from the bound on the Higgs self-coupling provided the 2HDM potential is tuned to avoid triviality and perturbativity bounds.

From the discussion in this section we see that several models are present in the literature that are able to accommodate for large deviations of the light-quark Yukawa couplings from their SM values while avoiding excessive contributions to FCNCs that are well measured and particularly limiting for models with additional flavour structures due to the implementation of AFV or SFV. The primary new physics deviation, complementary to direct searches, in the presented models will show up in the modification of the light quark Yukawa couplings. Armed with this knowledge, we motivate a study of how light-quark Yukawa couplings can be constrained at future experiments from Higgs pair production.

9.2 Events simulation for HL-LHC and FCC-hh

We consider the final state $b\bar{b}\gamma\gamma$, as this channel has the most potential for Higgs pair searches [48]. It has the "clean" $h \to \gamma\gamma$ decay, but also the other Higgs decay to b-quark pair is a channel with large branching ratio $\sim 58\%$ and b-tagging capabilities for ATLAS and CMS are continuously improving.

To be able to study the effects of enhanced light-quark Yukawa couplings or Higgs

Channel	LO σ [fb]	NLO K-fact	$6\,\text{ab}^{-1}$ [#evt @ NLO]
y_b^2	0.0648	1.5	583
$y_b y_t$	-0.00829	1.9	-95
y_t^2	0.123	2.5	1,840
Zh	0.0827	1.3	645
$\sum b\bar{b}h$	0.262	-	2,970
$b\bar{b}\gamma\gamma$	12.9	1.5	116,000
$t\bar{t}h$	1.156	1.2	6,938

Table 9.1. *SM cross-section for the main background processes at 14 TeV with $6\,ab^{-1}$ data at the HL-LHC, and the number of events after the basic cuts as defined in Equation 9.3. For $b\bar{b}h$ production, the Higgs boson is decayed to a pair of photons. The total production of Higgs associated with $b\bar{b}$ is denoted by $\sum b\bar{b}h$ and is the sum of the top four channels.*

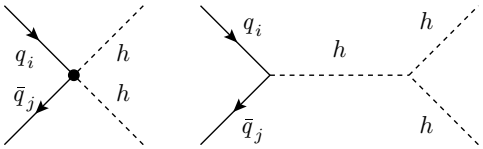

Figure 9.3. *The dominant Feynman diagrams for the quark anti-quark annihilation ($q\bar{q}A$) production of Higgs pair, via the SMEFT operator $\mathcal{O}_{q\phi}$.*

trilinear coupling, we need to simulate events for HL-LHC and FCC-hh which we use to train a machine learning model to identify the signal from the background. We consider the $b\bar{b}h$, $t\bar{t}h$, $b\bar{b}\gamma\gamma$ processes as the main sources of background for the hh signal. For the $b\bar{b}h$ processes, the contributions proportional to y_b^2, $y_b y_t$ and y_t^2 are simulated separately with y_b running effects. The details of the simulation can be found in Ref. [275]. The $Zh, Z \to b\bar{b}$ events are generated at leading order (LO), then scaled to NLO by K-factors, defined as the ratio of higher order cross section over its LO counterpart. The K-factors were taken from $t\bar{t}h$ [276], $b\bar{b}\gamma\gamma$ [277], Zh [278] and the remaining part of the $b\bar{b}h$ processes from [279]. The Higgs particles are further decayed to $\gamma\gamma$ following the Higgs cross-section working group recommendations [280]. The parton-level results are showered using `Pythia 8.3` [281] and a detector simulation is done using `Delphes 3` [282]. To be inclusive and to explore the capabilities and importance of the full detector coverage, no generator-level cuts were applied on these processes except for the $b\bar{b}\gamma\gamma$ processes to avoid divergences. These minimal generator-level cuts for $b\bar{b}\gamma\gamma$ are

$$\text{generator level cuts:} \quad \begin{aligned} & Xp_T^b > 20 \text{ GeV}, \\ & \eta_\gamma < 4.2,\ \Delta R_{b\gamma} > 0.2, \\ & 100 < m_{\gamma\gamma}\,(\text{GeV}) < 150. \end{aligned} \tag{9.2}$$

Channel	LO σ [fb]	K-fact.	Order	$6\,\mathrm{ab}^{-1}$ [#evt @ order]
hh^{ggF}_{tri}	$7.288 \cdot 10^{-3}$	2.28	NNLO	96
hh^{ggF}_{box}	0.054	1.98		680
hh^{ggF}_{int}	-0.036	2.15		-460
$u\bar{u}\mathrm{A}$ $(C_{d\phi} = 0.1)$	2.753	1.29	NLO	28
$d\bar{d}\mathrm{A}$ $(C_{u\phi} = 0.1)$	4.270	1.30		43

Table 9.2. The LO cross-section for di-Higgs production at the HL-LHC for $6\,\mathrm{ab}^{-1}$ of data multiplied by the $hh \to b\bar{b}\gamma\gamma$ branching ratio, K-factors (taken from [283] for the gluon channels and [200] for the quark channels) and the number of events after the basic cuts for the separated gluon fusion (ggF) and quark annihilation ($q\bar{q}$A) at $\sqrt{s} = 14$ TeV.

Here Xp_T implies a minimum p_T cut for at least one b-jet. After the showering and detector simulation, further basic selection cuts were applied to select events with

$$\text{basic cuts:} \quad \begin{aligned} & n_{\mathrm{eff}}^{bjet} \geq 1,\ n_{eff}^{\gamma jet} \geq 2, \\ & p_T^{bjet} > 30\ \mathrm{GeV},\ p_T^{\gamma jet} > 5\ \mathrm{GeV}, \\ & \eta_{bjet,\gamma jet} < 4,\ 110\ \mathrm{GeV} < m_{\gamma_1\gamma_2} < 140\ \mathrm{GeV}, \end{aligned} \tag{9.3}$$

and $n_{eff}^{b/\gamma jet}$ representing the number of b/γ-jets that pass the basic selection. The cross-section, K-factors, number of events with $6\mathrm{ab}^{-1}$ luminosity at 14 TeV are given in Table 9.1.

While the backgrounds are generated using `MadGraph_aMC@NLO` [88], the hh signal is separated into two main channels. The first is the gluon-fusion (ggF) channel which is the dominant channel in the SM and which can be further decomposed into three subprocesses based on their dependence on the Higgs trilinear self-interaction, λ, as seen in Figure 9.2. Amongst these subprocesses, the first is the amplitude squared of the contribution from the triangle diagram. It is proportional to λ^2. The second is the squared amplitude of the contribution from the box diagram that does not depend on the trilinear coupling. The third is the contribution from the interference between the triangle and box diagrams, which is proportional to λ. Using this separation allows us to remove the dependence of the total K-factor for hh production on rescaling of the trilinear Higgs coupling [171]. The individual K-factors for each of the subprocesses are independent of the rescaling of the trilinear Higgs coupling making our analysis computationally much simpler. The ggF process is generated using the `HH` production program implemented in `POWHEG` [171, 284, 285], which has been modified to separate the individual contributions from the three diagrams. The cross-section for these individual contributions and the corresponding K-factors can be found in Table 9.2.

The other main process, the quark anti-quark annihilation ($q\bar{q}$A), is strongly sup-

pressed in the SM for first generation quarks since the SM Yukawa couplings are proportional to the mass of the considered quark flavour. However, since this channel is a tree-level process, with sufficient large enhancement factors of the light quark Yukawa coupling, it becomes dominant as shown in Figure 9.1. The $q\bar{q}$A cross section scales like $\tilde{C}^2_{q\phi}/\Lambda^4$, while the gluon fusion production cross-section remains almost unchanged. Therefore, for constraining enhancements of the light-quark Yukawa, we consider this channel as the signal and the ggF channel as part of the background. The $q\bar{q}$A process is generated with `MadGraph_aMC@NLO` with a UFO model created with `FeynRules` [81]. Samples for both up- and down-quark initiated $q\bar{q}$A processes is generated. For all the hh signals, the samples are generated at LO and later scaled by the NLO K-factors given in Table 9.2. The K-factors are obtained from ref. [286] for the gluon fusion process in EFT and adapted from [241–243] as described in [200] for the $q\bar{q}$A channel. Moreover, the two Higgs bosons are decayed to $b\bar{b}$ and $\gamma\gamma$ respectively, with `Pythia 8.3` and then showered. The same detector simulation and basic cuts as for the background are then performed. In addition, the same sets of parton distribution function (`NNPDF31_nlo_as_0118_nf_4`) are used for the signal and the background, implemented via `LHAPDF` [175]. The calculation of the Higgs full width and branching ratios is done using a modified version of `Hdecay` [250, 251] to include the new SMEFT operators $\mathcal{O}_{q\phi}$. It should be noted, that in both di-Higgs production and decay calculation, the light-quark masses are set to zero. However, when converting between SMEFT and κ-formalism, the $\overline{\text{MS}}$ quark masses are used, in accordance to the PDG.

For FCC-hh, almost everything is done similarly after setting the energy to 100 TeV and the luminosity to 30 ab^{-1}. Since we do not have all K-factors available at a collider energy of 100 TeV we rescaled the LO samples by the same ones as for HL-LHC. We note that we explicitly checked that at least within the SM, for Higgs pair production via gluon fusion the difference is of $\mathcal{O}(1\%)$ [287] and hence small.

9.3 Exploring higher dimensional kinematic distributions

After detector simulation and jet definition, we have a final state of two photon jets and at least one b-jet, where the two photons reconstruct back to a real scalar Higgs mass for all the $b\bar{b}h$ channels. We first define and evaluate a comprehensive set of kinematic observables as the following:

- $p_T^{b_1}$, $p_T^{b_2}$, $p_T^{\gamma_1}$, $p_T^{\gamma\gamma}$,
- $\eta_{b_{j1}}$, $\eta_{b_{j2}}$, η_{γ_1}, $\eta_{\gamma\gamma}$,
- n_{bjet}, n_{jet}, $\Delta R^{b\gamma}_{\text{min}}$, $\Delta\varphi^{bb}_{\text{min}}$,
- $m_{\gamma\gamma}$, m_{bb}, m_{b_1h}, $m_{b\bar{b}h}$, H_T.

$p_T^{b/\gamma_{1,2}}$ and $\eta^{b/\gamma_{1,2}}$ are the p_T and rapidity for the tagged leading and sub-leading b/γ-jets

(in our definition the subleading b-jet could be a null four-vector since we require one b-jet inclusive), n_{bj} is the number of tagged and passed b-jets. $\Delta R^{b\gamma}_{\text{min}}$ and $\Delta\varphi^{bb}_{\text{min}}$ are the minimum R-distance and φ-angle between a tagged b-jet and a photon jet. The remaining variables are the invariant masses and H_T is the scalar sum of the transverse mass of the system. We shall show in what follows, that it is not necessary to be very selective about the kinematic variables one chooses to use in the analysis. What is necessary is that all possibly useful kinematic variables are included. As can be seen from the list above, some of the variables seem to be interdependent and, probably, highly correlated. The beauty of using interpretable machine learning is that a hierarchy of importance for the variables will be built during the analysis using an over-complete basis of collider observables from which the most important ones can be chosen to fine tune the analysis.

9.3.1 Interpretable machine learning

Rule-based machine learning algorithms have for long been used as the gold standard for signal to background discrimination in a wide variety of particle physics analyses. They are known to outperform neural networks in terms of simplicity of implementation, computational resources required and accuracy in modelling the underlying distributions.[1] In addition, rule-based algorithms, such as decision trees, are more transparent as far as the signal vs. background separation is concerned. Placing emphasis on interpretability in multivariate analyses, we chose to work with Boosted Decision Trees (BDT). However, interpretability of a machine learning algorithm requires more than just a choice of an interpretable model. The conditions are:

- A variable set that is easily interpretable in terms of the dynamics being studied.
- A machine learning algorithm that is more transparent and not a complete black box.
- A method for interpreting the model and attribute variable importance to understand how the algorithm models the underlying distributions.

Choosing to work with BDTs just satisfies the second condition. We work with the BDT algorithm implemented in XGBoost [289], a publicly available scalable end-to-end boosting system for decision trees. We follow the normal procedures for training and testing the BDT with simulated data. To satisfy the first condition we chose to work with high level kinematic variables that are representative of the process instead of working with four-vectors. The disadvantage of working with kinematic variable is that a complete set cannot be defined for a particular process unlike the four-vectors associated with the process. So, in principle, a large number of kinematic variables can

[1] Nevertheless, we tested a deep neural network built with Tensorflow [288] and found no improvement in the classification accuracy.

be formulated and used in a multivariate analysis. While the number is never too large for any implementation of BDTs, having a large set of variables clouds the understanding of which ones are important for orchestrating the signal separation from the background. This is where the third point listed above is important. Variable importance attribution is a way to "short-list" only those variable that play an important role in predictive power of the classification (or regression) problem. There are several measures of variable importance used in machine learning like Gini or permutation based measures [290, 291], local explanations with surrogate models [292] etc., to name a few. However, these suffer from inconsistencies or fail to provide a global explanation of the model [293].

To build a mathematically consistent procedure for variable importance attribution we use Shapley values [294] from Coalition Game Theory. Formulated by Shapley in the mid-20^{th} century, Shapley values formulate an axiomatic prescription for fairly distributing the payoff of a game amongst the players in a n-player cooperative game. When applied to machine learning, Shapley values tell us how important the presence of a variable is in determining a certain category (like signal or background) when compared to its absence from the multivariate problem being addressed. The process naturally and mathematically lends itself to studying the correlations between different variables since all possible combinations of variables can be taken out of the game to check the outcome.[2] A more detailed discussion of the application of Shapley values to signal vs. background classification problems for particle physics can be found in Refs. [275, 296, 297]. In this work we follow the same basic procedure as discussed in Ref. [275]. The importance of a variable in determining the outcome of a classification will be quantified by the mean of the absolute Shapley value, $\overline{|S_v|}$, larger values signifying higher importance. We will use the SHAP (SHapley Additive exPlanations) [293] package implemented in python based on Shapley values calculated exactly using tree-explainers [298, 299].

9.4 The hh channel at future hadron colliders

We would like to study the bounds on three specific couplings in this work. The first one being the Higgs trilinear coupling quantified by C_ϕ defined in Equation 10.1 and the other two being the deformation of the first-family SM Yukawa coupling to the up and down quark defined as $C_{u\phi}$ and $C_{d\phi}$ in Equation 10.12 with $i = j = 1$. We will not consider modifications of the second generation of quarks as their effects in di-Higgs production would be suppressed by the small parton distribution functions and are hence expected to be more pronounced using other methods for constraining them. For ease of interpretation we will also present our results in terms of κ_λ, κ_u and κ_d which are simply the rescaling of the SM trilinear coupling and the light-quark Yukawa couplings of the up and down quarks, respectively.

[2] More clarity on Shapley values and interpretable machine learning in general, along with their application can be found in Interpretable Machine Learning by Christoph Molnar [295].

In the BDT analysis we combine the $b\bar{b}h, (h \to \gamma\gamma)$ and $t\bar{t}H, (h \to \gamma\gamma)$ channels into one category calling it $Q\overline{Q}h$ while the other (continuum) background channel, $b\bar{b}\gamma\gamma$, is treated as a separate category. For any analysis involving C_ϕ, we need three separate categories for the triangle, box and interference terms of the ggF hh production which we shall refer to as $hh^{gg\text{F}}_{\text{tri}}$, $hh^{gg\text{F}}_{\text{box}}$ and $hh^{gg\text{F}}_{\text{int}}$, respectively. The $q\bar{q}$A channels stands for two other categories, one each for probing the Wilson coefficients $C_{u\phi}$ and $C_{d\phi}$, respectively. However, the $q\bar{q}$A channels are not the only channels sensitive to $C_{u\phi}$ and $C_{d\phi}$. In fact the decay $h \to \gamma\gamma$, the production of the Higgs in the ggF channel and the width of the Higgs are modified by the size of $C_{u\phi}$ and $C_{d\phi}$ [200]. Hence, these as well need to be taken into account. In what follows, we will refer to the two $q\bar{q}$A channels as $u\bar{u}$A and $d\bar{d}$A explicitly.

As we progress through the analysis we study the modification of one, two and three Wilson coefficients at a time. To extract just C_ϕ from the data we need to perform a five channel classification (two signal and three background modes including the $hh^{gg\text{F}}_{\text{box}}$ contribution that is insensitive to modifications of C_ϕ). To extract either $C_{u\phi}$ or $C_{d\phi}$ we have to perform a four channel classification taking the ggF channel as a single background mode. To extract C_ϕ and one of $C_{u\phi}$ or $C_{d\phi}$ we need to perform a six channel classification. Lastly, to extract all three Wilson coefficients we will need a seven channel classification. All the codes and data necessary to reproduce the results we got from this interpretable machine learning framework are made available at a `Github` repository: https://github.com/talismanbrandi/IML-diHiggs.git.

To set the stage, we will define our measure of significance and how we estimate it. We first construct a confusion matrix from the predictions of the trained BDT. This is a $n \times n$ matrix, for n channels. The sum of the elements in the i^{th} row, $\sum_j N_{ij}$, gives the actual number of events produced in channel i that would be generated in a pseudo-experiment with the projected luminosity corresponding to the actual experiment. The sum of the j^{th} column, $\sum_i N_{ij}$, gives the number of events from channel j predicted (including correct classifications and misclassifications) by the BDT in this pseudo-experiment. Hence the (i, j) element of the matrix gives the number of events of the i^{th} class that is classified as belonging to the j^{th} class with $i \neq j$ signifying a misclassification. The significance of the j^{th} channel given by $S/\sqrt{S+B}$, S being signal and B being background, can be defined as

$$\mathcal{Z}_j = \frac{|N_{jj}|}{\sqrt{\sum_i N_{ij}}}, \tag{9.4}$$

where i is the row index and j is the column index.

The fact that machine learning algorithms can far outperform cut-and-count analyses is a bygone conclusion. Preliminary estimates of the HL-LHC reach for SM di-Higgs production can be found in [48] and range from 4σ to 4.5σ signal significance combining several channels and both the ATLAS and CMS measurements. The $b\bar{b}\gamma\gamma$ final state alone allows for a $\sim 2.7\sigma$ measurement. In [300] a more refined machine learning pro-

cedure using Bayesian Optimization has been suggested and it has been shown that, indeed, the measurement of a di-Higgs signal can be further improved over preliminary estimates made by ATLAS and CMS using the $b\bar{b}\gamma\gamma$ final state alone. A sensitivity of about 5σ can be achieved using their procedure with the caveat that they use $S/\sqrt{B}$ as the definition of significance with very low number of signal and background events. As an exercise we repeated the BDT analysis with our framework and estimated a $\sim 3.4\sigma$ signal significance for SM di-Higgs production, which is similar to the estimate made in [300] without using any optimization.

A better portrayal of the advantages gained by using a multivariate analysis can be made by comparing the constraints set on $C_{u\phi}$, or κ_u, and $C_{d\phi}$, or κ_d, from a cut-and-count (CC) analysis and a multivariate (MV) analysis allowing for the variation of only one Wilson coefficient at a time. The projected 1σ bounds at HL-LHC for $6\,\text{ab}^{-1}$ of luminosity for a CC are given in [200] and compare to our results as follows

$$\begin{aligned} C_{u\phi}^{MV}\left(\kappa_u^{MV}\right) &= [-0.09, 0.10]\ ([-466, 454]), \quad C_{u\phi}^{CC}(\kappa_u^{CC}) = [-0.18, 0.17]\ ([-841, 820]), \\ C_{d\phi}^{MV}(\kappa_d^{MV}) &= [-0.16, 0.16]\ ([-360, 360]), \quad C_{d\phi}^{CC}(\kappa_d^{CC}) = [-0.18, 0.18]\ ([-405, 405]). \end{aligned} \tag{9.5}$$

From this we clearly see a factor of $\sim$2 improvement in the bounds on $C_{u\phi}$ and $\mathcal{O}(10\%)$ improvement in the determination of $C_{d\phi}$. The projected bounds on these operators at FCC-hh with $30\,\text{ab}^{-1}$ of data using our framework are

$$\begin{aligned} C_{u\phi}^{MV}\left(\kappa_u^{MV}\right) &= [-0.012, 0.011]\ ([-57.8, 54.7])\,, \\ C_{d\phi}^{MV}(\kappa_d^{MV}) &= [-0.012, 0.012]\ ([-26.3, 28.4])\,. \end{aligned} \tag{9.6}$$

These projected bounds for FCC-hh are an order of magnitude better than those for HL-LHC. In addition, the bounds on $C_{u\phi}$ and $C_{d\phi}$ are numerically the same displaying a much greater improvement in the bounds on $C_{d\phi}$ than on $C_{u\phi}$ at the higher energy collider.

9.4.1 Constraints on C_ϕ at the HL-LHC and FCC-hh

First, we will show the projections of the limits that can be set on C_ϕ (or equivalently, κ_λ) from HL-LHC and FCC-hh. In Table 9.3 we provide the output of the BDT classification for 6 ab^{-1} of data collected at HL-LHC and in Table 9.4 we provide the same for 30 ab^{-1} of data at FCC-hh. It can be seen from these matrices that while the $b\bar{b}\gamma\gamma$ QCD-QED channel is the dominant background, the BDT performs better in separating it from the signal channels than separating $Q\overline{Q}h$. This is due to the kinematic similarities between the signal and the $Q\overline{Q}h$ background.

In Figure 9.4 we present the constraints on C_ϕ (or κ_λ) that can be set from HL-LHC

Predicted no. of events at HL-LHC

Actual no. of events						
Channel	$hh^{gg\mathrm{F}}_{\mathrm{tri}}$	$hh^{gg\mathrm{F}}_{\mathrm{tri}}$	$hh^{gg\mathrm{F}}_{\mathrm{box}}$	$Q\overline{Q}h$	$b\bar{b}\gamma\gamma$	total
$hh^{gg\mathrm{F}}_{\mathrm{tri}}$	28	14	18	38	10	108
$hh^{gg\mathrm{F}}_{\mathrm{int}}$	89	80	129	178	41	517
$hh^{gg\mathrm{F}}_{\mathrm{box}}$	77	105	266	265	50	763
$Q\overline{Q}h$	177	98	191	5,457	1,835	7,758
$b\bar{b}\gamma\gamma$	1,743	845	1,074	30,849	287,280	321,791
$\mathcal{Z}_j$	0.61	2.37	6.49	28.45	534.1	

Table 9.3. *Trained BDT classification (confusion matrix) of the five channel used to extract constraints on C_ϕ (or κ_λ) at HL-LHC with 6 ab^{-1} luminosity (ATLAS+CMS), assuming SM signal injection. The right-most column gives the total number of events expected in each channel in the SM and the bottom-most row gives the signal significance.*

Predicted no. of events at FCC-hh

Actual no. of events						
Channel	$hh^{gg\mathrm{F}}_{\mathrm{tri}}$	$hh^{gg\mathrm{F}}_{\mathrm{tri}}$	$hh^{gg\mathrm{F}}_{\mathrm{box}}$	$Q\overline{Q}h$	$b\bar{b}\gamma\gamma$	total
$hh^{gg\mathrm{F}}_{\mathrm{tri}}$	3,579	1,303	2,372	4,697	337	12,288
$hh^{gg\mathrm{F}}_{\mathrm{int}}$	13,602	7,300	17,075	24,716	1523	64,216
$hh^{gg\mathrm{F}}_{\mathrm{box}}$	14,534	11,416	35,988	415,26	1,996	105,460
$Q\overline{Q}h$	29,611	12,355	23,279	1,238,266	214,564	1,518,075
$b\bar{b}\gamma\gamma$	45,574	22,290	26,213	150,935	227,142	24,317,657
$\mathcal{Z}_j$	10.95	31.22	111.1	737.7	4,743	

Table 9.4. *Trained BDT classification (confusion matrix) of the five channel used to extract constraints on C_ϕ (or κ_λ) at FCC-hh with 30 ab^{-1} luminosity, assuming SM signal injection. The right-most column gives the total number of events expected in each channel in the SM and the bottom-most row gives the signal significance.*

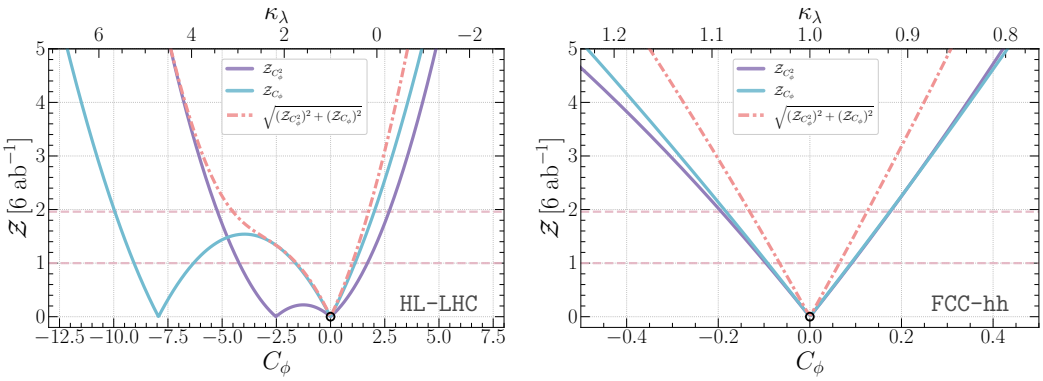

Figure 9.4. *Bounds on C_ϕ (or κ_λ) at the HL-LHC (left panel) and the FCC-hh (right panel). The solid blue lines are the constraints coming from the hh^{ggF}_{int} contribution which scales linearly with the modified coupling and the solid purple line is that from the hh^{ggF}_{tri} contribution that scales quadratically with the modified coupling. The red dashed line is the combination of the quadratic and linear channel. The horizontal light red dashed lines marks the 68% and 95% confidence intervals.*

in the left panel and FCC-hh in the right panel. The hh^{ggF}_{box} topology is not modified by C_ϕ and serves as a background to the measurement of C_ϕ. We separate the constraints from the hh^{ggF}_{tri}, which is quadratic in C_ϕ from the hh^{ggF}_{int} which is linear in C_ϕ. The combination of the two is given by the red dot-dashed line and is asymmetric around the best fit point, for SM signal injection, $C_\phi = 0$ ($\kappa_\lambda = 1$). The projected 1σ bound on C_ϕ is $[-1.57, 1.00]$ at HL-LHC. There is a vast improvement projected for the FCC-hh which is not only due to increased luminosity but also due to the measurement being at a higher energy. The projected 1σ bound is $C_\phi = [-0.066, 0.064]$. The latter corresponds to a 3% bound on κ_λ.

9.4.2 Two and three parameter constraints on C_ϕ, $C_{u\phi}$ and $C_{d\phi}$

The primary focus of this work is to move beyond just looking at constraints on C_ϕ from di-Higgs production and to shed light on how simultaneous modifications of the light-quark Yukawa couplings due to non-zero contributions from $C_{u\phi}$ and $C_{d\phi}$ can change the constraints on C_ϕ. The modifications of the light-quark Yukawa couplings manifest themselves in two different ways. Firstly, non-zero $C_{u\phi}$ and $C_{d\phi}$ open up the $q\bar{q} \to hh$ production mode through a point interaction (see Figure 9.3) thus changing the production cross-section of the di-Higgs channel. This increase in the production cross-section sets the tightest constraints on $C_{u\phi}$ and $C_{d\phi}$ from di-Higgs production. Secondly, the modification of the light-quark Yukawa couplings also modify the branching fraction of $h \to \gamma\gamma$ and the width of the Higgs. The latter modifies the channels that are

Operators	$C_{u\phi}$	$C_{d\phi}$	C_ϕ	κ_u	κ_d	κ_λ
HL-LHC 14 TeV $6\,\text{ab}^{-1}$						
$\mathcal{O}_\phi$	–	–	[-1.57, 1.00]	–	–	[0.53, 1.73]
$\mathcal{O}_{u\phi}$	[-0.09, 0.10]	–	–	[-477, 431]	–	–
$\mathcal{O}_{d\phi}$	–	[-0.16, 0.16]	–	–	[-360, 360]	–
$\mathcal{O}_{u\phi}$ & $\mathcal{O}_\phi$	[-0.087, 0.091]	–	[-2.42, 0.79]	[-434, 417]	–	[0.63, 2.13]
$\mathcal{O}_{d\phi}$ & $\mathcal{O}_\phi$	–	[-0.17, 0.17]	[-2.73, 0.77]	–	[-381, 379]	[0.63, 2.27]
$\mathcal{O}_{u\phi}$ & $\mathcal{O}_{d\phi}$	[-0.065, 0.069]	[-0.12, 0.12]	–	[-331, 312]	[-268, 272]	–
All	[-0.077, 0.084]	[-0.160, 0.162]	[-2.77, 0.43]	[-400, 369]	[-362, 359]	[0.79, 2.30]
FCC-hh 100 TeV $30\,\text{ab}^{-1}$						
$\mathcal{O}_\phi$	–	–	[-0.066, 0.064]	–	–	[0.97, 1.03]
$\mathcal{O}_{u\phi}$	[-0.012, 0.011]	–	–	[-57.8, 54.7]	–	–
$\mathcal{O}_{d\phi}$	–	[-0.012, 0.011]	–	–	[-26.3, 28.4]	–
$\mathcal{O}_{u\phi}$ & $\mathcal{O}_\phi$	[-0.010, 0.011]	–	[-0.091, 0.042]	[-52, 49]	–	[0.98, 1.04]
$\mathcal{O}_{d\phi}$ & $\mathcal{O}_\phi$	–	[-0.010, 0.012]	[-0.092, 0.041]	–	[-24, 26]	[0.98, 1.04]
$\mathcal{O}_{u\phi}$ & $\mathcal{O}_{d\phi}$	[-0.008, 0.009]	[-0.008, 0.009]	–	[-42, 39]	[-19,19]	–
All	[-0.009, 0.010]	[-0.009, 0.010]	[-0.105 0.023]	[-47, 44]	[-21, 21]	[0.99, 1.05]

Table 9.5. *The 1σ bounds on $C_{u\phi}$, $C_{d\phi}$ and C_ϕ from one-, two- and three-parameter fits for HL-LHC with $6\,\text{ab}^{-1}$ of data and FCC-hh with $30\,\text{ab}^{-1}$ of data. The corresponding bounds on the rescaling of the effective couplings, κ_u, κ_d and κ_λ are presented on the right side of the table.*

also sensitive to C_ϕ, thus modifying the constraints that can be set on C_ϕ from future measurements. Such constraints are the subdominant ones on $C_{u\phi}$ and $C_{d\phi}$ but they are necessary for a holistic picture.

In the two parameter fits, we consider three possible scenarios. Firstly, one can assume that the trilinear Higgs coupling is not modified and only the light-quark Yukawa couplings are. Two other possibilities are the simultaneous modification of the C_ϕ and one of $C_{u\phi}$ and $C_{d\phi}$. These are the three constraints that we show in Figure 9.5. As before, the constraints have been obtained by training the BDT to separate the relevant signal channels from the background, the signal used being the one corresponding to the pair of Wilson coefficients that we intend to constrain. The confusion matrices for all the three cases can be found in the `Github` repository for this analysis. The left panels of Figure 9.5 show the projected constraints for HL-LHC and right panels for the FCC-hh.

Comparing with the constraints on C_ϕ given in subsection 9.4.1 and Figure 9.4, it can be seen from the top and middle left panels of Figure 9.5 that, indeed, the constraints on C_ϕ are diluted when the light-quark Yukawa couplings are allowed to vary. This effect is somewhat more prominent for $C_{d\phi}$ than for $C_{u\phi}$ and stems from the fact that away from $C_{u\phi,d\phi} = 0$ larger negative values of C_ϕ are allowed by the crescent shaped curves in Figure 9.5. For $C_{d\phi}$ vs. C_ϕ the 3σ region is unbounded in the domain $|C_{d\phi}| \gtrsim 0.6$. The bounds on $C_{u\phi}$ and $C_{d\phi}$ from the fit with two-parameters including C_ϕ remain the same as the bounds on these Wilson coefficient from the single parameter $C_{u\phi,d\phi}$ fits.

We summarize the results in Table 9.5.

It should be noted that the two-parameter fit for $C_{u\phi}$ and $C_{d\phi}$ provide a stronger bound on the two parameters than the fit done individually. While this might be a bit counter-intuitive considering constraints from fits tend to deteriorate with the increasing number of parameters, we found that is not the case here. The reason is that the two-parameter fit is performed with the predictions made by the BDT trained with simulated events for both $u\bar{u}$A and $d\bar{d}$A. Between these two channels, each form the background for the other when separating them through a confusion matrix. Since the training also give the proportion of mistagged events, both the signal and the backgrounds are modified by the Wilson coefficients leading to a greater deformation of the likelihood in a favourable direction such that the constraints on the Wilson coefficients in the two-parameter fit is better than for the case in which they were separated from other $b\bar{b}\gamma\gamma$ backgrounds individually.

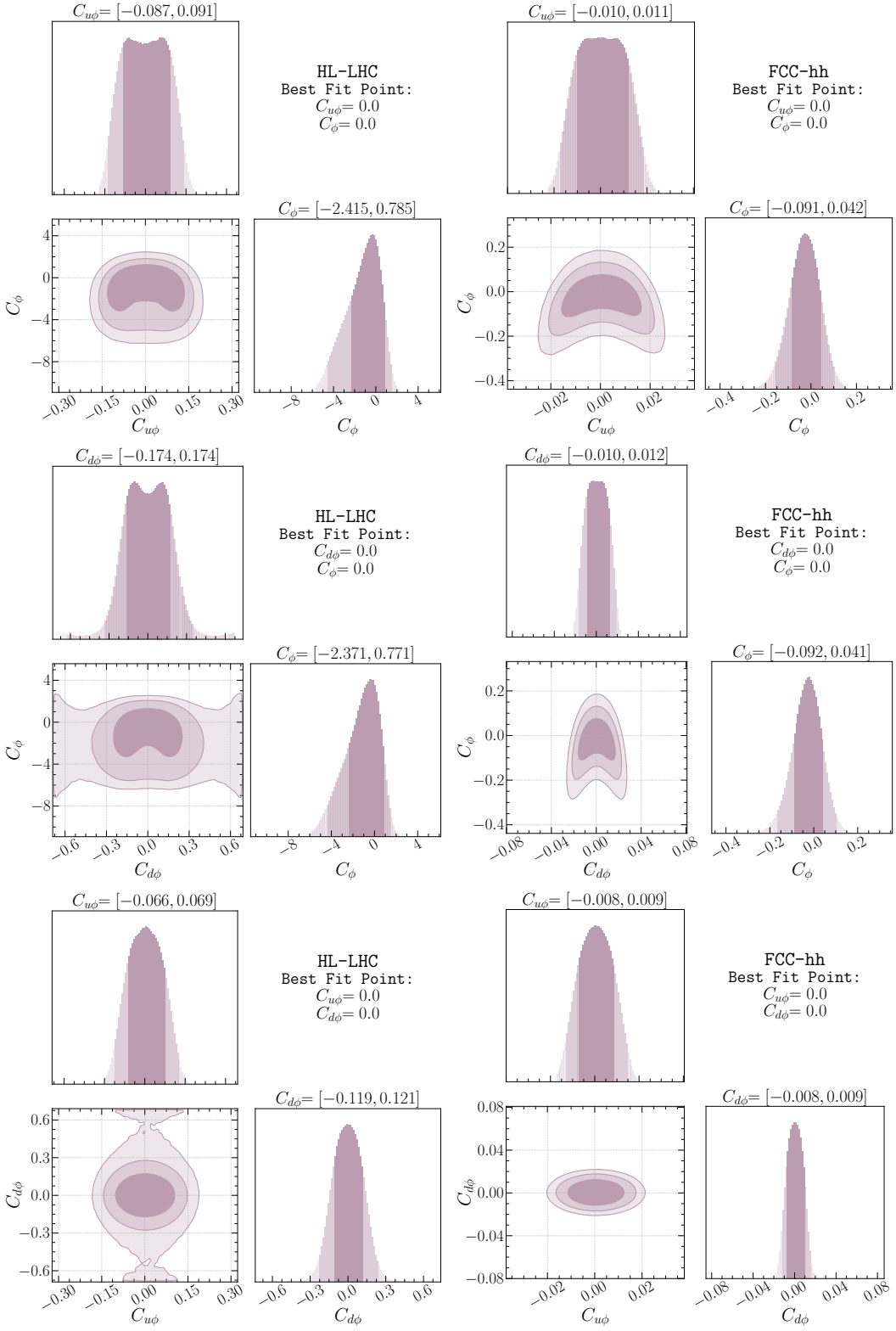

Figure 9.5. *Constraints on pairs of Wilson coefficients for C_ϕ, $C_{u\phi}$ and $C_{d\phi}$, The panels of the left are for HL-LHC with 6 ab^{-1} of luminosity and the ones on the right are for FCC-hh with 30 ab^{-1} of luminosity.*

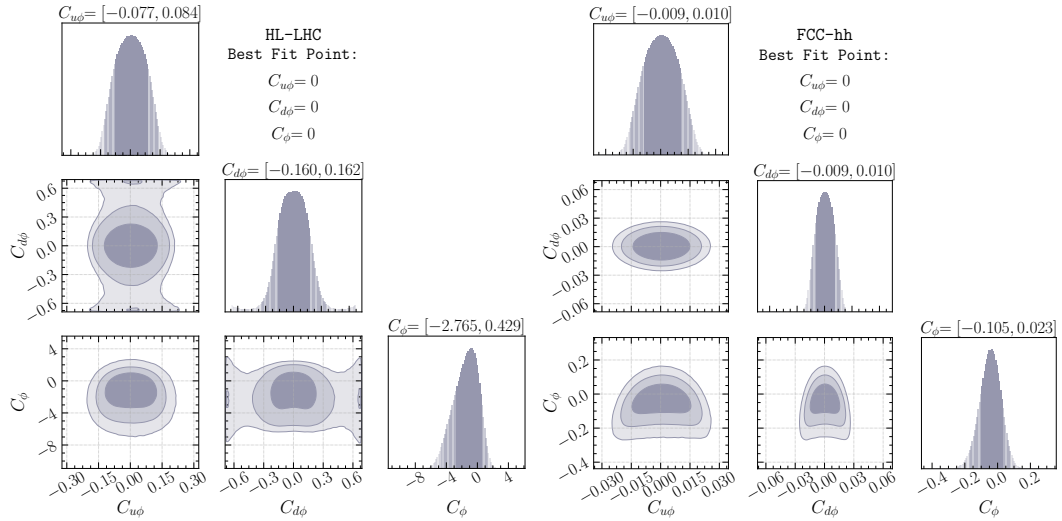

Figure 9.6. *Three parameter fits with $C_{u\phi}$, $C_{d\phi}$ and C_ϕ, 6ab^{-1} of luminosity at 14 TeV for HL-LHC (left panel) and 30ab^{-1} of luminosity at 100 TeV for FCC-hh (right panel).*

Finally, we perform a combined three-parameter fit including $C_{u\phi}$, $C_{d\phi}$ and C_ϕ, with the results shown in Figure 9.6. For the same reason as explained before, the bounds on $C_{u\phi}$ and $C_{d\phi}$ are somewhat better than the two-parameter fits of these operators individually with C_ϕ. The HL-LHC and FCC-hh projected bounds on C_ϕ remain nearly the same as those from the corresponding two-parameter fits. In Table 9.5 we also provide the bounds on κ_u, κ_d and κ_λ for comparison.

9.4.3 Interpretation of Shapley values

Finally, we want to demonstrate the interpretability of the machine learning framework we use and discuss the physics that allows for the separation of the signal channels from the background channels. The advantage of using an interpretable multivariate framework is that one can easily understand which of the kinematic variables are important for orchestrating this separation in a manner that significantly improves upon a cut-and-count analysis. As described previously, we use a measure derived from Shapley values, $\overline{|S_v|}$, to understand the importance of each kinematic variable and, henceforth, understand the differences in kinematic shapes that seperate the signal from the background.

To give a feeling of what the values of S_v mean, let us examine a single event. Assuming we have trained the BDT with n kinematic variables, each event with $n \times m$ Shapley values associated with it, m being the number of channels (signal and background channels). For a particular channel, j and kinematic variable, i, S_v can be positive or negative. A positive value implies that it is more likely that the event belongs to channel j accord-

ing to the value of the kinematic variable i. Conversely, a negative value implies that the event is less likely to belong to channel j given the value of the kinematic variable i. So regardless of whether S_v is positive or negative it helps in the sorting of events into various channels. Hence, $\overline{|S_v|}$ for a particular variable represents the strength of the variable to distinguish between channels. When summed over all channels this gives an overall picture of how good a discriminant a kinematic variable is for the processes involved. This is what is shown in Figure 9.7 which we will now elaborate upon.

To begin with, we take a look at the $\overline{|S_v|}$ computed for the five channel analysis performed for separating hh^{ggF}_{tri} and hh^{ggF}_{int} channels from hh^{ggF}_{box}, $Q\overline{Q}h$ and $b\bar{b}\gamma\gamma$ QCD-QED background. In Figure 9.7 we see the hierarchy plots for HL-LHC (top left panel) and FCC-hh (top right panel) generated from the predictions made by the BDT for this five channel analysis. For both the colliders, H_T is the most important variable that is bringing about separation of the hh^{ggF}_{tri} and hh^{ggF}_{int} channels from the dominating $b\bar{b}\gamma\gamma$ QCD-QED background. The second most important variable is $m_{\gamma\gamma}$. The importance of $m_{\gamma\gamma}$ accentuates the separation of the background by a greater degree at FCC-hh than at HL-LHC.

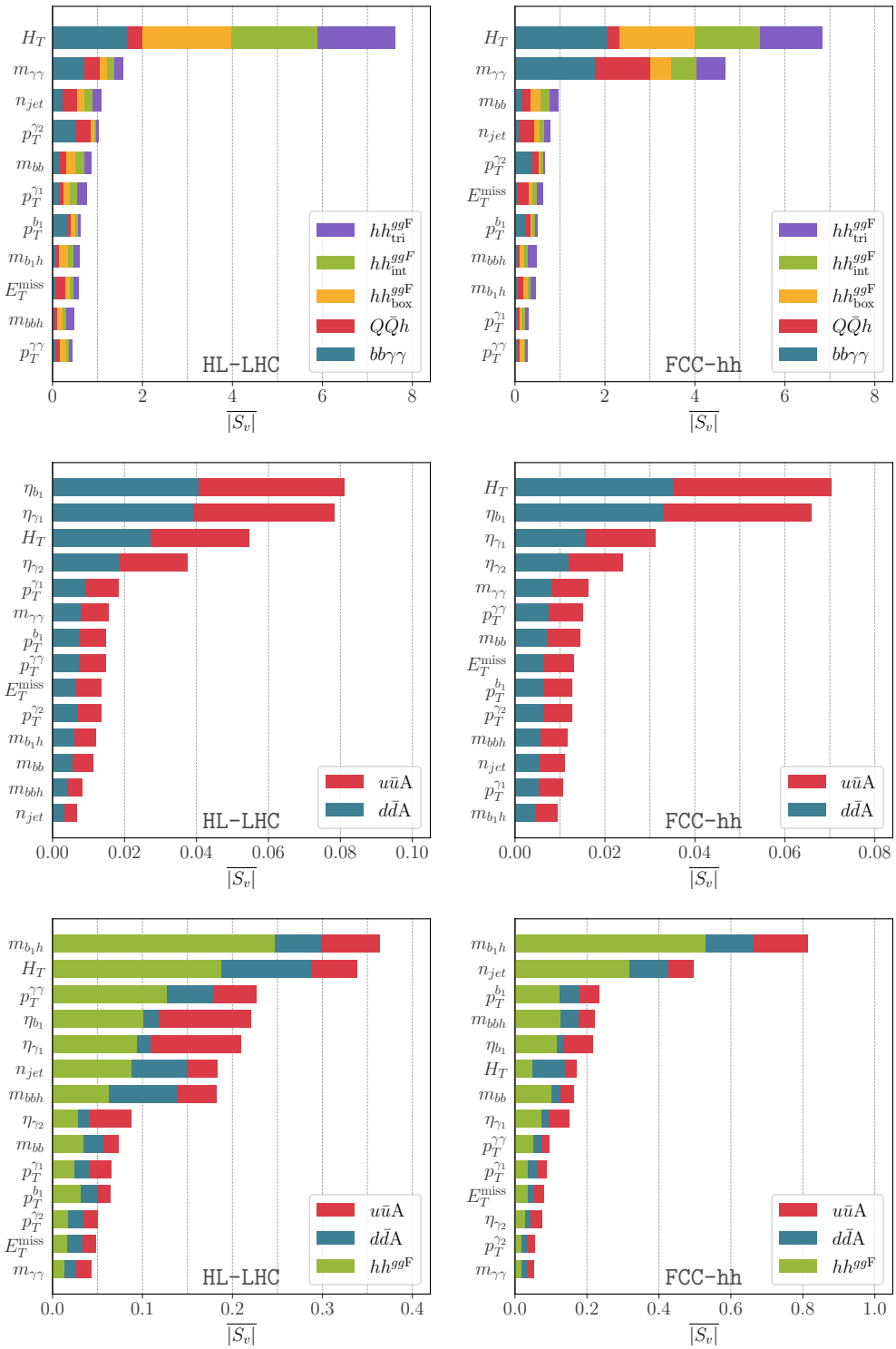

Figure 9.7. *Top panels: The hierarchy of variables important for the separation of hh^{ggF}_{tri} from hh^{ggF}_{int} events from hh^{ggF}_{box}, $Q\overline{Q}h$ and $b\bar{b}\gamma\gamma$ QCD-QED background at HL-LHC (left panel) and FCC-hh (right panel). Middle panels: The hierarchy of variables important for the separation of $u\bar{u}A$ from $d\bar{d}A$ events at HL-LHC (left panel) and FCC-hh (right panel). Lower panels: The hierarchy of variables important for the separation of hh^{ggF}, $u\bar{u}A$ and $d\bar{d}A$ events at HL-LHC (left panel) and FCC-hh (right panel). The higher the value of $|\overline{S_v}|$ is, the more important the kinematic variable is in separating the different channels.*

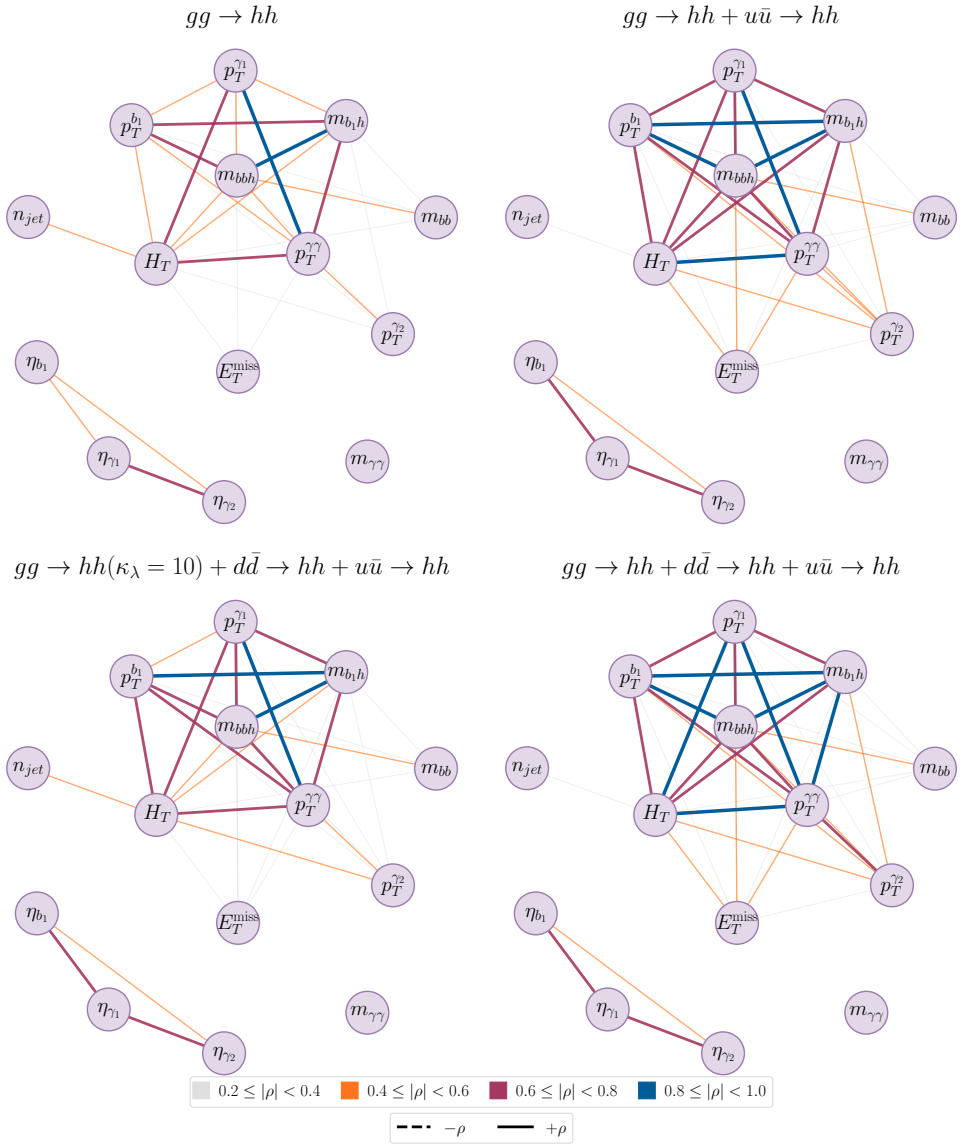

Figure 9.8. *Network diagrams visualization of correlations (ρ) amongst the kinematic variables used in the analysis. Top left: Only the gluon-gluon fusion channel. Top right: The ggF channel along with the $u\bar{u}$A channel with $\kappa_u = 1600$. Bottom right: The $d\bar{d}$A channel with $\kappa_d = 800$ added to the channels in the top right panel. Bottom left: The same channels as in the bottom right panel but with $\kappa_\lambda = 10$.*

For the separation between the two $q\bar{q}$A channels the story is very different. From the middle panels of Figure 9.7 we see that the separation of $u\bar{u}$A and $d\bar{d}$A is truly a multivariate problem. Not surprisingly, the picture is very different for HL-LHC and

FCC-hh. The differences between the two channels are driven by the differences in the parton distribution functions (PDF) of the up and down quarks. Since the PDF for the quarks change significantly from 14 TeV to 100 TeV, the variables that effect the separation of the two channels also change. Thus $\overline{|S_v|}$ give us a true picture of how distributions of several kinematic variables determine the separation of different channels that are mostly similar. When comparing the abscissa of the top two panels with the middle two panels one will also notice that $\overline{|S_v|}$ assumes much smaller values in the separation of $u\bar{u}$A and $d\bar{d}$A. This clearly shows that the two channels are distributed quite identically and are difficult to separate.

Lastly, in the bottom panels of Figure 9.7 we show the variables that are important in separating the $q\bar{q}$A channels from the ggh Higgs pair production channel. The invariant mass of the leading $b-$jet and h, $m_{b_1 h}$ is the most important variable at both HL-LHC and FCC-hh. However the hierarchy of variables below $m_{b_1 h}$ are quite different for HL-LHC and FCC-hh. Both H_T and $p_T^{\gamma\gamma}$ are far less important at FCC-hh than at HL-LHC. This displays the clear advantage that machine learning algorithms have over a cut-and-count analysis where separate cut strategies would have to be built for the two colliders leading to two separate analysis that can, instead, be done with the same framework when using machine learning.

The correlation plots in Figure 9.8 show how the linear correlations amongst the variables evolve when different channels are added. The top left panel are events sampled from the ggF distribution. One can already see a clustering in some of the variables related to momenta and invariant mass. The other cluster is of the pseudorapidity of the particles in the final state. This correlation structure evolves when one adds the $u\bar{u}$A channel when E_T^{miss} gets connected to the upper cluster in the top right panel. The correlation is now stronger between η_{γ_1} and η_{b_1} and several correlations in the upper cluster are much stronger too. The change in the correlations continue as one keeps adding channels as can be seen from the bottom right and bottom left panels. It is the capture of this change in the correlations (and higher-order correlations) that enhances the capabilities of the machine learning algorithms to distinguish between the various channels. While $m_{\gamma\gamma}$ by its shape alone allows for the separation between $b\bar{b}\gamma\gamma$ and the other channels, the correlations between the other kinematic variables aid in the separation of the channels with one or two Higgs in the final state.

9.5 Summary

In this work we walk through an analysis of how kinematic shapes can be used to glean information about the nuances of various production modes with the same final states but deformed differentially by the existence of degrees of freedom beyond the Standard Model. We show that this information can be extracted by using an interpretable machine learning framework which is not only very effective separating these differences

in kinematic shapes, but also yields itself to interpretations in terms of physics that is know and well understood. The example we chose is Higgs pair production in the $b\bar{b}\gamma\gamma$ final state. We emphasized that probing Higgs pair production is an important next step for an understanding of the model underlying the fundamental interactions of particles and hence a potential gateway to new physics. We show that even beyond the trilinear Higgs couplings, the light-quark Yukawa couplings can be probed through this production mode. In fact, the $q\bar{q}$A channel opens up only in the presence of BSM physics and well motivated models of new dynamics bring about the simultaneous modification of the trilinear Higgs coupling and the light-quark Yukawa couplings. Indeed, we motivated our study by showing that in different frameworks large modifications of the light quark Yukawa couplings can be obtained. Knowing the difficulty of measuring these couplings we propose an interpretable machine learning framework that significantly outperforms traditional cut-based analyses.

As opposed to using black-box models, the interpretable framework allows us to gain physics insights into how signal and background separation can be brought into effect, pointing to kinematic variables like H_T and $m_{\gamma\gamma}$ as being important variables that instrument this separation. As a result we find enhanced sensitivities to C_ϕ or κ_λ that quantify the modification to the Higgs trilinear coupling. Furthermore, we see that the measurement of the light-quark Yukawa couplings is aided by using the methods we advocate bringing about far greater sensitivities than would be possible with a cut-based analysis at the HL-LHC and the FCC-hh. The advantage of using an interpretable framework using Shapley values is that it provides added confidence to the robustness of the multivariate analyses that we perform using simulated data.

The salient results of this work are:

- The modification of the Higgs trilinear coupling can be measures at $\mathcal{O}(1)$ precision at the HL-LHC and at $\mathcal{O}(1\%)$ precision at the FCC-hh.
- The rescaling of the light-quark Yukawa couplings, κ_u and κ_d, can be measured to $\mathcal{O}(100)$ at the HL-LHC and $\mathcal{O}(10)$ at FCC-hh. This translated to $C_{u\phi}$ and $C_{d\phi}$ constrained at $\mathcal{O}(10\%)$ at the HL-LHC and $\mathcal{O}(1\%)$ at FCC-hh.
- The measurement of C_ϕ, or κ_λ, is significantly diluted once the light-quark Yukawa couplings are allowed to vary. Hence, in a joint fit, the bounds on C_ϕ are much weaker.
- There are theoretical models that motivate the simultaneous modification of the trilinear Higgs coupling and the light-quark Yukawa couplings. Hence, the dilution of the bounds on C_ϕ due to the presence of NP in the light-quark Yukawa sector should be taken into consideration in future phenomenological extraction of C_ϕ.
- The bounds obtained with the interpretable machine learning framework that we use not only outperforms cut-based analyses by far, but also allows for physics

insights into kinematic distributions of the various channels that helps distinguish them in an experiment.

In conclusion, we stress that the interplay between the Yukawa sector and the Higgs trilinear coupling is non-trivial and requires careful consideration. Future experiments at the HL-LHC and FCC-hh will bring significant improvements in the sensitivities to C_ϕ, $C_{u\phi}$ and $C_{d\phi}$ through the Higgs pair production channel. In particular, the bounds on the light-quark Yukawa couplings from Higgs pair production can possibly be the most stringent bounds amongst all other experimental probes of the light quark Yukawa couplings.

9.6 Discussion of theoretical and systematic uncertainties

In this section we present an estimate of the systematic uncertainties that can affect the measurements discussed in this work at the HL-LHC. We do not present these estimates for the FCC-hh for lack of sufficient information or the ability to project such uncertainties far into the future. We use two scenarios for systematic uncertainties: the first is a 8.2% uncertainty which corresponds to the current systematic uncertainty that ATLAS has reported for their Run-II search for Higgs pair production [301]. The second scenarios is the ATLAS HL-LHC baseline systematic uncertainty of 5.3% reported in [302]. For LHC run-II, statistical uncertainties remain the dominant part of the uncertainty budget for di-Higgs analysis. Regarding the systematic uncertainties, experimental sources remain the dominant part in comparison to the theoretical ones. The story flips for the HL-LHC where the main source of uncertainties is expected to be coming from theoretical uncertainties. The current theoretical uncertainty estimate of the SM gluon fusion process at NNLO is $^{+6\%}_{-23\%}$ for $\sqrt{s} = 14$ TeV and $^{+4\%}_{-21\%}$ for $\sqrt{s} = 100$TeV [303]. The largest part of the uncertainty stems from the uncertainty due to the renormalization scheme choice of the top quark mass. This uncertainty can, for the moment, only be estimated at NLO since no full mass dependent results at NNLO are available. Moreover, the top quark mass renormalization scheme uncertainty is not included in the estimated HL-LHC (nor LHC Run II) uncertainties schemes that we have considered.

In Figure 9.9 we show the significance $\mathcal{Z}$ for the three Wilson coefficient, C_ϕ, $C_{u\phi}$ and $C_{d\phi}$, at the HL-LHC from single parameter fits with no systematic uncertainties (black), LHC Run-II (violet) and HL-LHC baseline (blue) systematic uncertainties ansatze. We observe that for the current Run-II ansatz, the bounds for all three Wilson coefficients is diluted by 100% or more. As for the HL-LHC baseline, the bounds are diluted by $\sim 70\%$. However, it should be noted, that both systematic uncertainties scenarios are rather conservative. It is likely that the HL-LHC detector upgrade and new theoretical developments in higher-order corrections to di-Higgs cross-section will reduce the systematic uncertainties from the baseline.

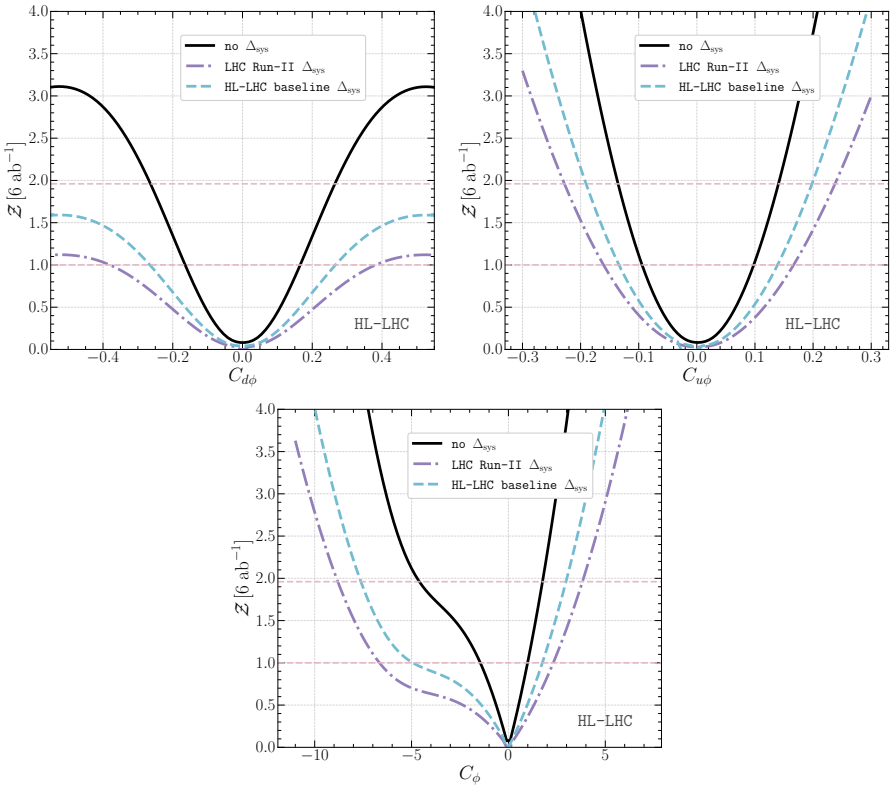

Figure 9.9. *The significance $\mathcal{Z}$ from a single parameter fit for $C_{d\phi}$ (upper left panel) , $C_{u\phi}$ (upper right panel) and C_{ϕ} (lower center panel) for the HL-LHC with no systematic uncertainties (black) and two ansätze for systematic uncertainties. The first is the current Run-II 8.2% in violet and the HL-LHC baseline 5.3% estimated by ATLAS in blue, including theoretical uncertainties without top mass renormalisation scheme.*

9.7 Light-quark Yukawa and Self Coupling at Future Lepton Colliders

Future high energy lepton colliders [113, 116, 304] offer further alternative and clean signals for measurement of Higgs properties. For example, Higgs decays to "un-tagged" light jets including u, d, s quarks can be further disentangled from $H \to gg$ using event shape analysis [305] and can reach a sensitivity of $\kappa_d \approx 90$ and $\kappa_u \approx 192$ at 250 GeV with 5ab^{-1} data compared with a sensitivity of $\kappa_d \approx 470$ and $\kappa_u \approx 900$ at the 6ab^{-1} HL-LHC [183, 306].

The sensitivity to Higgs self-coupling comes indirectly for center of mass energy below 250 GeV from the precision measurement of the Zh production channel ($\delta\kappa_\lambda$ (1σ) 0.4 at 250 GeV), and at 500 GeV directly from the Zhh channel ($\delta\kappa_\lambda$ (1σ) 0.27 at 500 GeV),

Collider	$\lvert\kappa_u\rvert$	$\lvert\kappa_d\rvert$	$\delta\kappa_\lambda$ (1σ)
240GeV 5ab^{-1} (CECP/FCC)	192 [305]	90 [305]	100% (Indirect[119])
350 GeV 1.5 ab^{-1} (FCCee)	310[211]	140[211]	40% (Indirect[119])
500 GeV 4 ab^{-1} (ILC)	330[211]	160[211]	27% [113]
1 TeV 8 ab^{-1} (ILC)	–	–	10% [211]
3 TeV 1 ab^{-1} (CLIC)	430[211]	200[211]	10% [211]
10 TeV 10 ab^{-1} (Muon)	–	–	3% [211]

Table 9.6. *Prospective light-quark Yukawa and Higgs self-coupling sensitivities at future lepton colliders. The light-quark Yukawa bounds are 95% CL, while the self-coupling bounds are* 1σ *or 68% CL sensitivity reach.*

and from vector boson fusion like production to $hh\nu\nu$ when 1 TeV or higher energy scales are available ($\delta\kappa_\lambda$ (1σ) 10% at 1 TeV). The prospective sensitivity depends on the collider setup, mainly the integrated luminosity and polarization of initial lepton beams. Given the updated prospects of future machine designs [211], we list a short summary in Table 9.6 of the expected sensitivities on the individual parameters in the κ framework. These numbers are all assuming one-parameter fits in κ or (translated from) SMEFT framework. No simultaneous fit including both κ_q and κ_λ (or using the corresponding SMEFT operators) have been performed yet.

Part IV

Flavour physics

10 Higgs and flavour

10.1 Effective Field Theory for Higgs pair production

The potential deformations of the SM in a model-independent manner can be accomplished by means of an EFT description parametrising new physics (NP) with higher-dimensional operators suppressed by some large energy scale Λ. A complete basis for the higher-dimensional operators has been given in Refs. [54, 307]. In this work we are interested in probing the Higgs trilinear and light-quark Yukawa couplings. Starting with the dimension-six operators modifying the Higgs self-couplings, we see that they are given by

$$\mathcal{L} \supset \frac{C_{\phi\Box}}{\Lambda^2}(\phi^\dagger\phi)\Box(\phi^\dagger\phi) + \frac{C_{\phi D}}{\Lambda^2}(\phi^\dagger D_\mu\phi)^*(\phi^\dagger D^\mu\phi) + \frac{C_\phi}{\Lambda^2}|\phi^\dagger\phi|^3. \tag{10.1}$$

where ϕ denotes the Higgs-doublet which, in the unitary gauge, can be written as $\phi = 1/\sqrt{2}(0, v+h)^T$. It is common to quote the constraints on the Higgs couplings in terms of rescaling to the SM coupling prediction, typically denoted by κ:

$$\kappa = \frac{g_h}{g_h^{\mathrm{SM}}}\,. \tag{10.2}$$

If the new physics contributions do not generate new Lorentz structures there is a possible translation between the Wilson coefficients in the SMEFT Warsaw basis discussed above, and the κ formalism usually used by experimentalists. In particular, taking the rescaling of the trilinear coupling, κ_λ, the translation is given by

$$\kappa_\lambda = 1 - \frac{v^4}{m_h^2}\frac{C_\phi}{\Lambda^2} + 3c_{\phi,\mathrm{kin}}, \tag{10.3}$$

where $c_{\phi,\mathrm{kin}}$ is given by

$$c_{\phi,\mathrm{kin}} = \left(C_{\phi\Box} - \frac{1}{4}C_{\phi D}\right)\frac{v^2}{\Lambda^2}. \tag{10.4}$$

The latter Wilson coefficients modify all the Higgs couplings, and are strongly constrained by electroweak precision observables (e.g. the T parameter constrains $C_{\phi D}$).Therefore, we set $c_{\phi,\mathrm{kin}} = 0$ from now on.

Before discussing the SMEFT operators modifying the coupling between the Higgs boson and light quarks, we start by a review of the SM couplings between them, i.e. the

Yukawa interaction

$$-\mathcal{L}_y = y^u_{ij}\overline{q}^i_L\tilde{\phi}u^j_R + y^d_{ij}\overline{q}^i_L\phi d^j_R + h.c.\,, \tag{10.5}$$

Here, q^i_L is the left-handed $SU(2)$ quark doublet of the i^{th} generation and u^j_R and d^j_R, the right-handed up- and down-type fields of the j^{th} generation, respectively, and $\tilde{\phi} = i\sigma_2\phi^*$. The 3×3 Yukawa matrices are the SM **spurions** that break the flavour symmetry of the SM $U(3)_{Q_L} \otimes U(3)_{u_R} \otimes U(3)_{d_R}$ to the baryon number and the gauged hypercharge groups, i.e. $U(1)_B \otimes U(1)_Y$. In the ground state, the the Lagrangian (10.5) gives the quark masses. Thus, defining a diagonal *mass basis* as opposed to a generic *interaction basis* that eq (10.5) is written in it. The transformation of the yukawa matricies $y^{u/d}$ from generic flavour basis to the mass basis $Y^{u/d} = \text{diag}(y^{u/d}_1, y^{u/d}_2, y^{u/d}_3)$ is performed by means of a bi-unitary transformation. To illustrate this we show the singular-value decomposition of the Yukawa matrices

$$\begin{aligned}(y^u)_{ij} &= (\mathcal{U}^u_L)_{li}(Y^u)_{ll}(\mathcal{U}^u_R)^\dagger_{lj},\\ (y^d)_{ij} &= (\mathcal{U}^d_R)^\dagger_{li}(Y^d)_{ll}(\mathcal{U}^d_L)_{lj}.\end{aligned} \tag{10.6}$$

This decomposition is not unique and only defined upto a $U(1)^5$ and a $U(1)_B$ phases. However, this transformation freedom does not hold for CKM matrix, defined as

$$V_{CKM} = (\mathcal{U}^u_L)^T(\mathcal{U}^d_L)^*, \tag{10.7}$$

where we can only rotate by $U(1)_B$. This manifests in Flavour-changing charged currents at tree-level. But no Flavour-changing neutral currents (FCNC) are allowed at tree-level in the SM. Additionally, the loop-induced FCNC's are CKM suppressed
In a similar manner, the SMEFT introduces new flavour spurions via the dimension-six operators

$$\mathcal{L} \supset \frac{\phi^\dagger\phi}{\Lambda^2}\left((C_{u\phi})_{ij}\overline{q}^i_L\tilde{\phi}u^j_R + (C_{d\phi})_{ij}\overline{q}^i_L\phi d^j_R + h.c.\right)\,, \tag{10.8}$$

The mass matrices of the up- and down-type quarks are obtained from the Yukawa and the new SMEFT coupling

$$\begin{aligned}M^u_{ij} =& \frac{v}{\sqrt{2}}\left(y^u_{ij} - \frac{1}{2}(C_{u\phi})_{ij}\frac{v^2}{\Lambda^2}\right)\,,\\ M^d_{ij} =& \frac{v}{\sqrt{2}}\left(y^d_{ij} - \frac{1}{2}(C_{d\phi})_{ij}\frac{v^2}{\Lambda^2}\right)\,.\end{aligned} \tag{10.9}$$

The Wilson coefficients' matrices $C_{q\phi}$ need not to be simultaneously diagonalisable with the SM Yukawa's y^q. However, we need to have a diagonal mass basis like the SM ones,

here we will be having new set of bi-unitary transformations $\mathcal{V}_{L/R}^{u/d}$ such that we could write $C_{q\phi}$ in terms of the mass basis ones $\tilde{C}_{q\phi}$ in a similar ways to eq (10.6)

$$\begin{aligned}(C_{u\phi})_{ij} &= (\mathcal{V}_L^u)_{li}(\tilde{C}_{u\phi})_{lm}(\mathcal{V}_R^u)^\dagger_{mj},\\ (C_{d\phi})_{ij} &= (\mathcal{V}_R^d)^\dagger_{li}(\tilde{C}_{d\phi})_{lm}(\mathcal{V}_L^d)_{mj}.\end{aligned} \tag{10.10}$$

where $\mathcal{V}_{L/R}^{u/d}$ are only guaranteed to diagonalise the mass matrices $M_{ij}^{u/d}$ in general [1].
The couplings of one and two Higgs boson to fermions can be defined as (in the mass basis)

$$\mathcal{L} \supset g_{h\bar{q}_i q_j}\bar{q}_i q_j h + g_{h\bar{q}_i q_j}\bar{q}_i q_j h^2\,, \tag{10.11}$$

with

$$g_{h\bar{q}_i q_j} := \frac{m_{q_i}}{v}\delta_{ij} - \frac{v^2}{\Lambda^2}\frac{(\tilde{C}_{q\phi})_{ij}}{\sqrt{2}}\,, \qquad g_{hh\bar{q}_i q_j} := -\frac{3}{2\sqrt{2}}\frac{v}{\Lambda^2}(\tilde{C}_{q\phi})_{ij}\,. \tag{10.12}$$

A similar relation exists for the rescalings of the quark Yukawa couplings κ_q

$$\kappa_q = 1 - \frac{v^3}{\sqrt{2}m_q}\frac{C_{q\phi}}{\Lambda^2}. \tag{10.13}$$

However, one should be careful while interpreting results quoted in terms of Wilson coefficients in the SMEFT framework extracted from di-Higgs, multi-Higgs or multi-vector bosons searches, as these results include couplings that are not present in the SM. For example, the $hhq\bar{q}$ coupling, though being linearly related to the quark Yukawa coupling $hq\bar{q}$, is not a rescaling of any SM Higgs coupling. With this in mind, one can strictly remain within a linear EFT and link the rescaling of the quark Yukawa, κ_q, to the $hhq\bar{q}$ coupling through

$$g_{hhq\bar{q}}^{\text{linear}-\text{EFT}} = -\frac{3}{2}\frac{1-\kappa_q}{v}\, g_{hq\bar{q}}^{\text{SM}}. \tag{10.14}$$

This relation will no longer hold once a non-linear EFT is used. Hence, the κ-formalism, in a strict sense, is not applicable to multi-Higgs studies.
Here, we see that the new Wilson coefficients introduce tree-level FCNC, or even if a tree-level ones are suppressed the loop-levels ones will not have the SM CKM suppression. Generically, such a construction leads to flavour-changing neutral currents (FCNCs) which are strongly constrained from low-energy measurements of flavour observables. The bounds are of order $|(\tilde{C}_{u\phi,d\phi})_{12}| \lesssim 10^{-5}\Lambda^2/v^2$ and $|(\tilde{C}_{u\phi,d\phi})_{13}| \lesssim 10^{-4}\Lambda^2/v^2$ and stem from $\Delta F = 2$ transitions [225, 308]. Given that FCNCs need to be suppressed,

[1] The CKM matrix with this extended flavour sector will not longer guaranteed to be unitary, however unitarity violation will be typically of order m_q^2/Λ^2.

a popular way of realising this is by imposing minimal flavour violation (MFV) [226], where all sources of flavour violation are proportional to the SM Yukawa couplings

$$(C_{u\phi})_{ij} = \overline{a}_u\, y^u_{ij} + \overline{b}_u (y_u y_u^\dagger)(y_u)_{ij} + \overline{c}_u (y_d y_d^\dagger)(y_u)_{ij} + \dots\,,$$
$$(C_{d\phi})_{ij} = \overline{a}_d\, y^d_{ij} + \overline{b}_d (y_d y_d^\dagger)(y_d)_{ij} + \overline{c}_d (y_u y_u^\dagger)(y_d)_{ij} + \dots\,. \tag{10.15}$$

Here $\overline{a}, \overline{b}$ and $\overline{c}$ are generic flavour universal $\mathcal{O}(1)$ coefficients
The assumption of MFV introduces a strong hierarchy amongst the Higgs couplings to quarks, due to the proportionality of the Wilson coefficients to the Yukawa couplings. Since we want to explore rather large modifications of the light-quark Yukawa couplings, in MFV models very low values of the NP scale Λ and/or large Wilson coefficients need to be assumed, rendering the validity of the EFT questionable. Furthermore, this would potentially generate conflict with measurements of the third generation couplings to the Higgs boson. Hence, we refrain from assuming MFV and instead assume *flavour alignment*. We will discuss in the next section how this can be concretely realized. Moreover, we choose setting $\Lambda = 1\,\text{TeV}$ throughout the reminder of this paper, staying well within the SMEFT validity region and in order to simplify the presentation of the results.

10.2 Models of flavour alignment and large light-quark Yukawa couplings

A systematic generalisation of flavour alignment is provided by aligned flavour violation (AFV) [229, 230]. In order to introduce more flavour violation in than (MFV), AFV introduces more spurions, with the constraint that these spurions are invariant under the $U(1)^5$ transfirmations mentioned above. This leaves only the CKM matrix transforming non-trivially under the $U(1)^5$. In AFV, it is possible to write these spurions, for example, the extra couplings to up-type and down-type quarks, k_u and k_d respectively, as an expansion in the CKM matrix V_{CKM}, known as the alignment expansion

$$k_u = \mathcal{V}_L^u \left(K_{0,u} + K_{1,u} V_{CKM}^* K_{2,u} V_{CKM}^T K_{3,u} + \mathcal{O}(V_{CKM}^4)\right) (\mathcal{V}_R^u)^\dagger, \tag{10.16}$$
$$(k_d)^\dagger = \mathcal{V}_L^d \left(K_{0,d} + K_{1,d} V_{CKM}^T K_{2,d} V_{CKM}^* K_{3,d} + \mathcal{O}(V_{CKM}^4)\right) (\mathcal{V}_R^d)^\dagger, \tag{10.17}$$

where $K_{a,u}$ and $K_{a,d}$ are complex 3×3 diagonal matrices, that are arbitrarily flavour invariant, and the transformation matrices are similar to the ones appearing in eq (10.10), they are a generalisation to the SM bi-unitary transformations. The AFV condition necessitates that the alignment coefficients $K_{a,q}$ to be diagonal, such that the expansion is invariant under the $U(1)^5$ transformation. We have omitted generation indices here for readability.

applying AFV to the SMEFT case is rather straightforward, in a generic flavour basis we have.

$$(k_q)_{ij} = \frac{(C_{q\phi})_{ij}}{\Lambda^2}. \tag{10.18}$$

This formalism is stable under renormalisation group (RGE) evolution as only the matrices $K_{i,d}$ will contribute to the RGE and flavour alignment is maintained.

10.2.1 Model realizations

It should be noted that from a UV perspective there is no well-motivated symmetry argument for the realization of AFV, given the fact that the $U(1)^5$ symmetry is only an auxiliary group used when redefining the quark mass eigenstates. Concrete realisations in UV models are rather fine-tuned and other mechanisms might be required for the realisation of flavour alignment.

Flavour alignment can be realized in various models, for instance SUSY [309, 310], two or multi-Higgs doublet models [311, 312] and models with vector-like quarks (VLQ) [201]. In the latter, FCNCs are avoided by imposing horizontal flavour symmetries leading to AFV. The mixing between the SM quarks and the VLQ's $Q \sim (\mathbf{3}_{SU(3)_C}, \mathbf{2}_{SU(2)_L}, 1/6_Y)$, $U \sim (\mathbf{3}, \mathbf{1}, 2/3)$ and $D \sim (\mathbf{3}, \mathbf{1}, -1/3)$ is given by the Lagrangian

$$\begin{aligned}\mathcal{L} = &- \lambda_{Qu}\overline{Q}_L\tilde{\phi}u_R - \lambda_{Qd}\overline{Q}_L\phi d_R - \lambda_{Uq}\overline{q}_L\tilde{\phi}U_R - \lambda_{Dq}\overline{q}_L\phi D_R \\ &- \lambda_{QD}\overline{Q}_L\phi D_R - \lambda_{UQ}\overline{Q}_L\tilde{\phi}U_R + h.c.\end{aligned} \tag{10.19}$$

The matrices λ are the new spurions in this mode, and they do not need to be diagonal, but they are, by virtue of a horizontal symmetry and particular charge assignment, can be made to obey the AFV assumptions. If all the new VLQ's have the same mass scale M, we could write the enhancement of the light quarks-Higgs coupling $\delta g_{hq\overline{q}}$ in terms of these matrices

$$\delta g_{h\bar{u}u} \approx \frac{v^2}{m_Q^2}(\lambda_{Uq}\lambda_{UQ}\lambda_{Qu}) \quad \text{and} \quad \delta g_{h\bar{d}d} \approx \frac{v^2}{M^2}(\lambda_{Dq}\lambda_{DQ}\lambda_{Qd}), \tag{10.20}$$

here, the flavour indices are also dropped. While the exact proposal of [201] foresees Yukawa couplings of the first and second generation quarks up to the value of the bottom quark Yukawa coupling, it requires masses of the VLQs of around 1.5 TeV. For less significant enhancements, the scale of the VLQs could reach > 2 TeV and hence be well within the EFT limit and in accordance with bounds from direct searches of VLQs. The VLQs would also modify Higgs production in gluon fusion and the loop-induced Higgs decays. The contributions would scale like

$$\frac{\alpha_s}{\pi}\frac{\lambda_{QU}}{m_Q^2}\phi^\dagger\phi G^{\mu\nu}G_{\mu\nu} \tag{10.21}$$

which with $\mathcal{O}(1)$ λ_{QU} is suppressed strongly compared to the top quark contributions. The VLQs can in principle contribute to flavour observables through loop contributions, where they would couple with the charged currents. The mixing can be fine-tuned such that the loop contributions of the VLQs in flavour observables can be strongly suppressed.

Another concrete realisation of models with large light quark Yukawa couplings has been provided by the framework of spontaneous flavour violation (SFV) [229], where the tuning necessary in general AFV is avoided by promoting the flavour violating spurions to the wavefunctions of the quark [229]. The wavefunction renormalisation constants come from tree-level diagrams involving interaction between the SM quarks, new set of VLQs and scalars. Unlike general AFV, large deviations from their SM values are possible only for either up-type or down-type Yukawa couplings but not both in the SFV framework. Also, it requires the introduction of a discrete symmetry in order to prevent the VLQ from interacting with the SM degrees of freedom directly. A UV-complete model with SFV has been proposed in Refs. [203, 230] based on a two-Higgs doublet model. Deviations in light quark Yukawa coupling can be achieved by having a second Higgs doublet coupling to fermions via flavour diagonal matrices $K_{0,q}$ $(q = u, d)$ as defined in (10.17). In particular in order to have only the first/second generation deviating from its SM value the corresponding diagonal element in $K_{0,q}$ is supposed to be non-zero. These matrices are then not proportional to the SM Yukawa couplings. SFV is realized either only in the down or only in the up sector, assuming that the flavour mixing that generates the CKM matrix correspondingly stems from the other sector. Assuming that the mass eigenstates of the two Higgs neutral states are

$$h = \sin(\beta - \alpha)h_1 + \cos(\beta - \alpha)h_2 \tag{10.22}$$

$$H = -\cos(\beta - \alpha)h_1 + \sin(\beta - \alpha)h_2 \tag{10.23}$$

where h_1 and h_2 are the CP-even neutral interaction eigenstates, the large Yukawa couplings of h_2 appear in $g_{h\bar{q}_i q_i}$, the Yukawa coupling of the SM-like Higgs boson, via the mixing of h_1 and h_2 with the mixing angle $\beta - \alpha$. Working in the Higgs basis in which h_1 takes a vacuum expectation value, the couplings of the Higgs boson to quarks $g_{hq_i\bar{q}_i}$ then become

$$g_{h\overline{q}_i q_i} = \frac{m_{q_i}}{v}\sin(\beta - \alpha) + (K_q)_{ii}\cos(\beta - \alpha)\,. \tag{10.24}$$

where $(K_q)_{ii}$ is the ith matrix element of the matrices $K_{0,d}$ or $K_{0,u}$ appearing in eq (10.17), and the q indicates either up or down-type quarks. Note that the new matrix K_q is simultaneously diagonalisable with the SM Yukawa. Clearly, the deviation of the Higgs to quark couplings become more pronounced away from the alignment limit $\cos(\beta-\alpha) \to 0$. This automatically leads to a deviation in the Higgs couplings, for instance, to vector bosons proportional to $\cos(\beta-\alpha)$ but not potentially enhanced by large K_q's as in case of

the Higgs couplings to light quarks. We note that while there is freedom to chose values for K_q's in the diagonal, a potential $\mathcal{O}(1)$ choice would lead to much larger modification factors for first and second generation as for the third generation where the first term in eq. (10.24) would dominate. Large K_q's lead also to large couplings of the second Higgs doublet with light quarks

$$g_{Hq_i\overline{q_i}} \approx (K_q)_{ii} \sin(\beta - \alpha) \,. \tag{10.25}$$

We note that if we want to achieve large deviations to light quarks, the alignment parameter given by

$$\cos(\beta - \alpha) = -\lambda_6 \frac{v^2}{m_H^2} \left[1 + \mathcal{O}(v^4/m_H^4)\right], \tag{10.26}$$

where m_H denotes the heavy Higgs mass and λ_6 is the 2HDM potential parameter of the operator $\phi_1^\dagger \phi_1 \phi_1^\dagger \phi_2$, cannot be too small. This implies that the heavy Higgs boson cannot be too heavy if requiring perturbative λ_6. Given this, the model is constrained from heavy Higgs boson searches as well as meson mixing due to diagrams involving heavy charged Higgs bosons.

11 Flavour anomalies and Electroweak precision tests

11.1 Introduction

In the era of the Large Hadron Collider (LHC) an intense program aimed at probing the Standard Model (SM) at the TeV scale has been established. At the same time, one of the most valuable sources for the study of new physics (NP) above the electroweak (EW) scale is provided by indirect tests of the SM via the so-called the EW precision observables (EWPO). These include, in particular, the very precise measurements at the Z pole performed at the Large Electron-Positron (LEP) collider and the Stanford Linear Collider (SLC). In corroboration with the Higgs-boson discovery and the experimental information collected at LHC and Tevatron, they provide strong constraints on theories beyond the SM (BSM) that lead to important deformations of the standard EW sector [76, 313–321]. Intriguingly, the interplay between the TeV region under scrutiny at the LHC and the NP probes represented by EW precision tests may be of fundamental importance for the study of the *B-physics anomalies* [322–329].

The outcome of LHCb and Belle analyses in the study of semileptonic B decays points to the possible presence of NP in the measured ratios $R_{K^{(*)}} \equiv Br(B \to K^{(*)}\mu^+\mu^-)/Br(B \to K^{(*)}e^+e^-)$ at low dilepton mass [330–333]. The averaged experimental values deviate from unity at the $\sim 2.5\sigma$ level, hinting at lepton universality violation (LUV). A statistically significant inference of LUV in $b \to s\ell\ell$ ($\ell = e, \mu$) transitions can be translated into a strong case for the evidence of BSM physics [334–336].

The interpretation of these experimental results as an imprint of heavy new dynamics has primarily been assessed in a model-independent fashion via the language of effective field theories (EFT) in [337–341] and more recently revisited in refs. [327, 328, 342–346]. Furthermore, the NP picture depicted by these global analyses could also accommodate a set of tensions related to the well-measured muonic channel of these B decays, in particular, to the angular analysis of $B \to K^*\mu^+\mu^-$ [347, 348]. These measurements have very recently been updated by the LHCb collaboration [349].

The set of tensions not related to LUV tests would specifically connect NP effects to muon-flavoured couplings. However, long-distant effects present in the amplitude of these processes [350–354] – involving hadronic contributions that are theoretically difficult to handle [355–358] – make such a conclusion debatable, see, e.g. [359, 360]. From this point of view, the LUV information extracted from ratios of branching ratios

and from observables like the ones considered in [361–364] remain the most promising avenue in the future for a more precise assessment of the overall tension seen in $b \to s\ell\ell$ measurements [365]. Eventually, while a tighter upper limit has been recently obtained by LHCb on the branching ratio of $B_s \to e^+e^-$ [366], the combined experimental average for the $Br(B_s \to \mu^+\mu^-)$ [367–369] also shows some tension with the SM prediction [370] as can be seen from the findings in [327, 328].

A broader discussion on B-physics anomalies should also include the LUV information stemming from another class of rare B decays, namely $b \to c$ semileptonic transitions [371–374]. Indeed, a combined resolution of $R_{K^{(*)}}$ anomalies with the long-standing deviations observed in $R_{D^{(*)}} \equiv Br(B \to D^{(*)}\tau\nu)/Br(B \to D^{(*)}\ell\nu)$ originally found at Babar [375] and subsequently measured at Belle [376] and LHCb [377], has triggered a lot of interest in the theory community. In particular, in order for NP effects to simultaneously account for a $\sim 20\%$ deviation in tree-level charged-weak decays and in loop-level flavour-changing neutral currents (FCNC), models with a highly non-trivial flavour structure are required [378–387], often being at the edge of flavour physics constraints [388, 389] and collider bounds [390, 391]. So far, model building has been mainly put forward in the direction of UV-completing low-energy leptoquark benchmarks identified, for instance, in refs. [325, 326, 329, 392, 393].

It is important to acknowledge that the most up-to-date measurements of $R_{D^{(*)}}$ from the Belle collaboration – obtained by fully reconstructing the τ particle via the hadronic [394] and, more notably, leptonic [395] decay modes – turns out to be in good agreement with the SM [396–399]. This fact may cast some doubt on the effective role one should really attribute to $b \to c$ transitions in the interpretation of the depicted *B-physics crisis*.

Therefore, in light of the recent results from Belle and LHCb, it is timely for us to focus again on the $b \to s\ell\ell$ conundrum and reassess the solutions to B-physics anomalies that can be realized at one loop without any new source of flavour violation. The simplest resolution of these anomalies has been proposed in ref. [400], extending the SM with a single new Abelian gauge group, together with the presence of top- and muon-partners, resulting in a top-philic Z' boson capable of evading present collider constraints [401] and responsible for the required LUV signatures.

Such a minimal model actually falls into a larger category pointed out in ref. [324] through the language of the Standard Model Effective Field Theory (SMEFT), and subsequently elaborated upon in greater detail in the phenomenological study of ref. [402].

At the basis of this class of proposals, the notable attempt is twofold:

i) Addressing the deviations in these FCNC processes with NP effects entering at one-loop level, as for SM amplitudes. This reduces the original multi-TeV domain of NP for B anomalies [403] to energies closer to present and future collider reach.

ii) Avoiding the introduction of new sources of flavour violation beyond the SM Yukawa couplings, relaxing in this way, any restrictive flavour probe of NP in

a fashion similar to what is predicted in Minimal Flavour Violation (MFV) [226, 404, 405].

The aforementioned proposal shows a strong tension with Z-pole precision observables [402, 406]. In ref. [327] it has been shown that even in the presence of large hadronic effects in the amplitude of $B \to K^* \mu^+ \mu^-$, a tension of at the 3σ level at least would persist between B data and EWPO for muonic LUV effects, and an even stronger tension would be found in the case of LUV scenarios involving electron couplings.

This fact has been brought to light recently [407] to abandon *ii)*, and reformulate the original proposal addressing B anomalies at one loop adding specific BSM sources of flavour violation in order to reconcile B data with EW precision tests in this context. However, as briefly advertised in ref. [327], an important caveat of this EW tension versus B anomalies concerns the assumption of no tree-level NP contributions to EWPO.

In this work, we attempt, for the first time, to provide a broad exploration of the possible cross-talk of NP in the EW sector and in the flavour playground for $b \to s\ell\ell$ transitions. Firstly, we revisit the standard EW analysis in the presence of leading-log one-loop contributions from the renormalization group equations (RGE) evolution of the operators in the SMEFT [85, 86]. Then, we perform a joint fit to the comprehensive experimental set that includes EWPO in conjugation with the state-of-the-art measurements of semileptonic B decays. Our EFT analysis targets heavy new dynamics that contributes to $b \to s\ell\ell$ at the loop level only through SMEFT RGE, involving the SM Yukawa couplings as the only sources of flavour violation in the resolution of B anomalies.

Within our study, we systematically review novel correlations among gauge-invariant dimension-six operators that help us shed new light on the one-loop solutions to B anomalies. Continuing in the spirit of the previous work done by some of us [327, 340, 356, 359, 408–410], we shall furnish our results in both a conservative and optimistic approach to the non-perturbative hadronic contributions which can significantly affect the conclusions on the NP effects at hand.

On the basis of the SMEFT picture obtained from our combined inspection of EW and flavour data, we proceed to refine simple UV models already considered in the literature [324, 400, 401]. We corner the interesting parameter space of this refined class of models where EWPO are respected while B anomalies can be addressed at one loop without introducing new sources of flavour violation. Eventually, we go on to discuss the complementary probes offered by collider searches.

The paper is organized as follows: in section 11.2 we review the ingredients of our EFT analysis; in section 11.3 we detail the strategy adopted for our combined EW+flavour fit in the SMEFT, the results from which are collected in section 11.4; in section 11.5 we discuss the most economic viable Z' model in relation to our EFT results and also mention possible alternative leptoquark scenarios. Our conclusions are summarized in section 11.6.

11.2 Theoretical preamble

Previous global analyses of $b \to s\ell\ell$ anomalies have highlighted the appearance of new dynamics at a scale of $\mathcal{O}(10)$ TeV for $\mathcal{O}(1)$ effective couplings encoding NP effects at the tree level [337–341]. The mass gap with the weak scale, characterized by the Higgs vacuum expectation value (VEV) $v \approx 246$ GeV, justifies the BSM translation of these results in the gauge-invariant formalism of the SMEFT [54, 411]. At dimension six, in an operator product expansion in inverse powers of the NP scale Λ, and working in the Warsaw basis [54], the operators of interest for the explanation of these B anomalies are [324, 327, 328]:

$$\begin{aligned} O_{\ell\ell 23}^{LQ^{(1)}} &= \overline{L}_\ell \gamma_\mu L_\ell \, \overline{Q}_2 \gamma^\mu Q_3 \ , \\ O_{\ell\ell 23}^{LQ^{(3)}} &= \overline{L}_\ell \gamma_\mu \tau^A L_\ell \, \overline{Q}_2 \gamma^\mu \tau^A Q_3 \ , \\ O_{23\ell\ell}^{Qe} &= \overline{Q}_2 \gamma_\mu Q_3 \, \overline{e}_\ell \gamma^\mu e_\ell \ , \\ O_{\ell\ell 23}^{Ld} &= \overline{L}_\ell \gamma_\mu L \, \overline{d}_2 \gamma^\mu d_3 \ , \\ O_{\ell\ell 23}^{ed} &= \overline{d}_2 \gamma_\mu d_3 \, \overline{e}_\ell \gamma^\mu e_\ell \ , \end{aligned} \tag{11.1}$$

where weak doublets are represented in upper case, $SU(2)_{\rm L}$ singlets in lower case, and Pauli matrices τ^A characterize $SU(2)_{\rm L}$ triplet currents. Within available light-cone sum-rule results on long-distance effects in $B \to K^* \mu^+ \mu^-$ [350, 354], data point to the presence of both the operators with $b \to s$ left-handed and right-handed currents with muonic flavour ($\ell = 2$) in eq. (11.1) [327, 342–344]. However, it is important to observe that:

- The current statistical significance for the need of right-handed $b \to s$ couplings remain small, hinted only by the ratio $R_{K^*}/R_K \neq 1$ at the 1σ level [327, 341]. Hence, the present B anomalies can be essentially addressed by $O_{2223}^{LQ^{(1,3)}}$ and O_{2322}^{Qe}.
- Within a conservative approach to hadronic uncertainties [355–357], the preference for muonic NP effects in global analyses gets mitigated to a large extent and electro-phillic scenarios become viable too [340]; moreover, the fully left-handed operator(s)[1] $O_{\ell\ell 23}^{LQ^{(1,3)}}$ offers the minimal model-independent resolution to $b \to s$ anomalies [327].

Interestingly, with a leading expansion in the top-quark Yukawa coupling of the RGE computed in [85, 86], the Wilson coefficients associated to O_{2223}^{LQ} and O_{2322}^{Qe} can be generated at one loop by two distinct sets of dimension-six operators [324] that can lead to LUV effects in $b \to s\ell\ell$ amplitudes without flavour violation in the quark current. A

[1] The most promising observables that will allow to genuinely disentangle NP effects in the future in the fully left-handed operator $O_{\ell\ell 23}^{LQ^{(3)}}$ from the ones of $O_{\ell\ell 23}^{LQ^{(1)}}$, are $B \to K^{(*)} \nu\overline{\nu}$ decays [412–414].

first set involves operators built of Higgs and leptonic currents:

$$\begin{aligned} O_{\ell\ell}^{HL^{(1)}} &= (H^\dagger i\overleftrightarrow{D}_\mu H)(\overline{L}_\ell\gamma^\mu L_\ell)\,, \\ O_{\ell\ell}^{HL^{(3)}} &= (H^\dagger i\overleftrightarrow{D}^A_\mu H)(\overline{L}_\ell\gamma^\mu\tau^A L_\ell)\,, \\ O_{\ell\ell}^{He} &= (H^\dagger i\overleftrightarrow{D}_\mu H)(\overline{e}_\ell\gamma^\mu e_\ell)\,. \end{aligned} \tag{11.2}$$

A second one corresponds to semileptonic four-fermion (SL-4F) operators with right-handed top-quark currents:

$$\begin{aligned} O_{\ell\ell 33}^{Lu} &= (\overline{L}_\ell\gamma_\mu L_\ell)(\overline{u}_3\gamma^\mu u_3)\,, \\ O_{\ell\ell 33}^{eu} &= (\overline{e}_\ell\gamma_\mu e_\ell)(\overline{u}_3\gamma^\mu u_3)\,. \end{aligned} \tag{11.3}$$

Solving the RGE in a leading-logarithmic approximation, the matching conditions for the left-handed quark-current operators in eq. (11.1) at the scale $\mu_{\rm EW}\sim v$ are:[2]

$$\begin{aligned} C_{\ell\ell 23}^{LQ^{(1)}} &= V_{ts}^*V_{tb}\left(\frac{y_t}{4\pi}\right)^2\log\left(\frac{\Lambda}{\mu_{\rm EW}}\right)\left(C_{\ell\ell 33}^{Lu}-C_{\ell\ell}^{HL^{(1)}}\right)\,, \\ C_{\ell\ell 23}^{LQ^{(3)}} &= V_{ts}^*V_{tb}\left(\frac{y_t}{4\pi}\right)^2\log\left(\frac{\Lambda}{\mu_{\rm EW}}\right)C_{\ell\ell}^{HL^{(3)}}\,, \\ C_{23\ell\ell}^{Qe} &= V_{ts}^*V_{tb}\left(\frac{y_t}{4\pi}\right)^2\log\left(\frac{\Lambda}{\mu_{\rm EW}}\right)\left(C_{\ell\ell 33}^{eu}-C_{\ell\ell}^{He}\right)\,. \end{aligned} \tag{11.4}$$

In terms of vectorial and axial currents typically discussed in the context of the weak effective theory at low energies [417–419], the operators in eq. (11.4) are matched to

$$\begin{aligned} O_{9V,\ell} &= \frac{\alpha_e}{8\pi}(\overline{s}\gamma_\mu(1-\gamma_5)b)(\overline{\ell}\gamma^\mu\ell)\,, \\ O_{10A,\ell} &= \frac{\alpha_e}{8\pi}(\overline{s}\gamma_\mu(1-\gamma_5)b)(\overline{\ell}\gamma^\mu\gamma_5\ell)\,, \end{aligned} \tag{11.5}$$

so that the matching conditions at the scale $\mu_{\rm EW}$ for the set of operators in eq. (11.2) - (11.3) follow:

$$\begin{aligned} C_{9,\ell}^{\rm NP} &= \frac{\pi v^2}{\alpha_e\Lambda^2}\left(\frac{y_t}{4\pi}\right)^2\log\left(\frac{\Lambda}{\mu_{\rm EW}}\right)\left(C_{\ell\ell}^{HL^{(3)}}-C_{\ell\ell}^{HL^{(1)}}-C_{\ell\ell}^{He}+C_{\ell\ell 33}^{Lu}+C_{\ell\ell 33}^{eu}\right)\,, \\ C_{10,\ell}^{\rm NP} &= \frac{\pi v^2}{\alpha_e\Lambda^2}\left(\frac{y_t}{4\pi}\right)^2\log\left(\frac{\Lambda}{\mu_{\rm EW}}\right)\left(C_{\ell\ell}^{HL^{(1)}}-C_{\ell\ell}^{HL^{(3)}}-C_{\ell\ell}^{He}-C_{\ell\ell 33}^{Lu}+C_{\ell\ell 33}^{eu}\right) \end{aligned} \tag{11.6}$$

[2] In this work, for one-loop effects, we assume the NP scale to be $\Lambda = 1$ TeV. We also set $\mu_{\rm EW} = m_t \simeq v/\sqrt{2}$ to minimize the matching-scale dependence with the inclusion of next-to-leading corrections [415, 416].

where $\alpha_e \equiv e^2/(4\pi)$, e being the electric charge, and the overall normalization in the weak Hamiltonian follows the standard conventions adopted in refs. [327, 340, 356].

As anticipated in the Introduction, the set of operators of interest for the study of $R_{K^{(*)}}$ in eq. (11.4) is also probed by EW precision data. Indeed, operators involving the Higgs field and lepton bilinears in the SMEFT induce modifications to EW-boson couplings that have been precisely measured at LEP/SLC, providing also an important test bed for lepton universality [316, 406]. Modifications of the Z couplings to the leptons can be induced also at loop level through the top-loop contribution [76]. In the leading-log approximation and at the leading order in the top Yukawa coupling, LUV effects can be generated by:

$$\begin{aligned} \Delta g^{\ell\ell}_{Z,L}\Big|_{\rm LUV} &= -\frac{1}{2}\left(C^{HL^{(1)}}_{\ell\ell} + C^{HL^{(3)}}_{\ell\ell}\right)\frac{v^2}{\Lambda^2} - 3\left(\frac{y_t\, v}{4\pi\Lambda}\right)^2 \log\left(\frac{\Lambda}{\mu_{\rm EW}}\right) C^{Lu}_{\ell\ell 33}\ , \\ \Delta g^{\ell\ell}_{Z,R}\Big|_{\rm LUV} &= -\frac{1}{2}C^{He}_{\ell\ell}\frac{v^2}{\Lambda^2} - 3\left(\frac{y_t\, v}{4\pi\Lambda}\right)^2 \log\left(\frac{\Lambda}{\mu_{\rm EW}}\right) C^{eu}_{\ell\ell 33}\ , \end{aligned} \tag{11.7}$$

where $\Delta g^{\ell\ell}_{Z,L(R)} \equiv g^{\ell\ell}_{Z,L(R)} - g^{\ell\ell,{\rm SM}}_{Z,L(R)}$ is the deviation with respect to the left-handed (right-handed) leptonic couplings to the Z boson in the SM theory.

Motivated by the previous observations, we would like to perform an EFT analysis of new physics models that can explain the flavour anomalies in the above-mentioned fashion, but exploring more generally the interplay of such SM extensions with EWPO. For that purpose, we consider an EFT analysis of new physics with the following assumptions:

- The solution to the flavour anomalies is obtained via radiative effects, such as those described in eq. (11.6).
- Such NP can also contribute to EWPO at tree-level, in a flavour non-universal way.
- Other effects that could enter in the previous observables via renormalization group (RG) mixing are either small or can be constrained better via other processes.

As we will see in section 11.5, and can also be deduced using the results in [121], it is not difficult to construct minimal BSM models where the previous conditions are satisfied. From an EFT point of view, fulfilling these considerations requires the enlarging of the set of operators considered in eq. (11.2) and also including the corresponding dimension-

six interactions modifying the neutral and charged quark currents:

$$\begin{aligned} O_{qq}^{HQ^{(1)}} &= (H^\dagger i\overleftrightarrow{D}_\mu H)(\overline{Q}_q\gamma^\mu Q_q)\,, \\ O_{qq}^{HQ^{(3)}} &= (H^\dagger i\overleftrightarrow{D}^A_\mu H)(\overline{Q}_q\gamma^\mu \tau^A Q_q)\,, \\ O_{qq}^{Hu} &= (H^\dagger i\overleftrightarrow{D}_\mu H)(\overline{u}_q\gamma^\mu u_q)\,, \\ O_{qq}^{Hd} &= (H^\dagger i\overleftrightarrow{D}_\mu H)(\overline{d}_q\gamma^\mu d_q)\,, \end{aligned} \tag{11.8}$$

where $q = 1, 2, 3$ identifies quark generations.[3] In this regard, we note that EWPO cannot separate in a clean way contributions from the first family quarks, in particular in the d sector. Therefore, and analogously to what was done in ref. [420], we identify deviations in the couplings of the EW bosons to the first and second family of the quarks via $C_{11}^{HQ^{(1,3)}} = C_{22}^{HQ^{(1,3)}}$, $C_{11}^{Hu} = C_{22}^{Hu}$, and $C_{11}^{Hd} = C_{22}^{Hd}$. This implicit $U(2)^3$ symmetry in the quark sector would in general also help to mitigate large contributions to FCNC. Note that, even in this situation, not all the Wilson coefficients related to eq. (11.8) can be well constrained with the EWPO. This is the case for the Wilson coefficient of O_{33}^{Hu}, which modifies the right-handed top quark coupling to the Z. This cannot be probed at tree level by Z-pole measurements.

Introducing eq. (11.8) also modifies the EW couplings of the Z to all fermions at the one-loop level, and in particular the leptonic couplings, $g_{Z,L(R)}^{\ell\ell}$. These are, however, flavour-universal effects. In our study, we propagate the leading y_t effects of this kind, coming from the RG mixing with $O_{33}^{HQ^{(1)}}$. As we will see, given the comparatively weaker bound on the Wilson coefficient of that operator compared to the leptonic ones, these effects can be sizeable in the fit. It must be noted that, at the same order in the perturbative expansions we are considering, similar effects from O_{33}^{Hu} could also have a non-negligible phenomenological impact. However, as explained before, C_{33}^{Hu} cannot be directly bound in the EWPO fit. Hence, to avoid flat directions in our EFT analysis, we assume the RGE boundary condition $C_{33}^{Hu} = 0$ to hold true. Excluding $\mathcal{O}_{33}^{Hu}$ and taking into account the aforementioned assumptions in the quark sector, eq. (11.8) adds a total of 7 new degrees of freedom into our EFT analysis.

Finally, for completeness, we also consider the effects of the four-lepton operator:

$$O_{1221}^{LL} = (\overline{L}_1\gamma^\mu L_2)(\overline{L}_2\gamma_\mu L_1)\,, \tag{11.9}$$

which contributes to the muon decay amplitude, and therefore alters the extraction of the value of the Fermi constant, G_F, which is one of the inputs of the SM EW sector.

[3] In our SMEFT analysis we require these quark operators to be diagonal in a basis that is aligned, as much as possible, with the down-quark physical basis. This will be convenient to avoid possible dangerous tree-level FCNC effects [389]. Similarly, we also assume lepton-flavour alignment with the charged-lepton mass basis.

The operators in eqs. (11.2), (11.8) and (11.9), with the assumptions mentioned before, saturate all the 17 degrees of freedom, i.e. combinations of operators, that can be constrained in a fit to EWPO in the dimension-six SMEFT framework [4], while keeping flavour changing neutral currents in the light quark sector under control. Together with the 4 four-fermion operators from eq. (11.3), this completes a total of 21 operators, which we include in the fit setup described in the next section.

11.3 Analysis strategy

We now proceed to discuss in more detail our EFT analysis. Our aim is to pin down the picture that should address the present B anomalies via one-loop SM RGE effects of flavour-conserving dimension-six operators, and respect at the same time the constraints from EW precision. We can achieve this goal with a comprehensive global analysis that aims at combining EWPO and $b \to s\ell\ell$ data.[5]

We perform a Bayesian analysis on the most recent set of $b \to s\ell\ell$ measurements together with the state-of-the-art theoretical information already implemented and described in ref. [327]. We include in our study EW physics following what originally done in ref. [314] and, more recently, in ref. [316]. In particular, we adopt the list of observables reported in Table 1 of this reference, and allow for lepton non-universal contributions from heavy BSM physics in EWPO [406, 420] within the framework described in section 11.2.

For this purpose we adopt the publicly available `HEPfit` [424] package, a Markov Chain Monte Carlo (MCMC) framework built using the Bayesian Analysis Toolkit [425].[6] In our analyses we vary $\mathcal{O}(100)$ parameters including nuisance parameters. The data that we use for the fits can be categorized as follows:

- The set of EWPO including the Z-pole measurements from LEP/SLD, the measurements of the W properties at LEP-II, as well as several related inputs from the Tevatron and LHC measurements of the properties of the EW bosons [11, 13, 426–

[4] In this regard, we should mention that at dimension six, in the Warsaw basis, EW observables are also affected by two more operators not discussed so far: $O_{HWB} = (H^\dagger \tau^A H) W^A_{\mu\nu} B^{\mu\nu}$ and $O_{HD} = \left|H^\dagger D_\mu H\right|^2$. Contrary to the set in eqs. (11.2) and (11.8), these operators only induce oblique, and therefore flavour-universal, corrections in EW observables. Given our focus on LUV effects, we assume for O_{HWB} and O_{HD} that the corresponding Wilson coefficients are not generated by the NP at the scale Λ.

[5] See ref. [421] for another recent analysis where $b \to s\ell\ell$ data and EW measurements have been combined, with the different scope of resolving tensions in the determination of the Cabibbo angle [422, 423].

[6] All code and configuration files can be made available upon request.

430]. The following lists the bulk of the EWPO included in the fits:

$$M_H,\ m_t,\ \alpha_S(M_Z),\ \Delta\alpha^{(5)}_{\rm had}(M_Z),$$
$$M_Z,\ \Gamma_Z,\ R_{e,\mu,\tau},\ \sigma_{\rm had},\ A_{FB}^{e,\mu,\tau},\ A_{e,\mu,\tau},\ A_{e,\tau}(P_\tau),\ R_{c,b},\ A_{FB}^{c,b},\ A_{s,c,b},\ R_{u+c},$$
$$M_W, \Gamma_W,\ {\rm BR}_{W\to e\nu,\mu\nu,\tau\nu},\ \Gamma_{W\to cs}/\Gamma_{W\to ud+cs},\ |V_{tb}|\,;$$

- The angular distribution of $B \to K^{(*)}\ell^+\ell^-$ decays for both μ and e final states in the large-recoil region.[7] These include data from ATLAS [431], Belle [363], CMS [432, 433] and LHCb [349, 434]; we also include the branching fractions from LHCb [435], and of $B \to K^*\gamma$[8] for which we use the HFLAV average [437];
- Branching ratios for $B^{(+)} \to K^{(+)}\mu^+\mu^-$ decays in the large-recoil region measured by LHCb [438];
- The angular distribution of $B_s \to \phi\mu^+\mu^-$ [439] and the branching ratio of the decay $B_s \to \phi\gamma$ [440], measured by LHCb;
- The lepton universality violating ratios R_K [332] and R_{K^*} [331] from LHCb and Belle [333];
- Branching ratio of $B_{(s)} \to \mu^+\mu^-$ measured by LHCb [368], CMS [367], and ATLAS [369]; we also use the upper limit on $B_s \to e^+e^-$ decay reported recently by LHCb [366].

For the $B \to K^*\ell^+\ell^-$ channel, as in previous works [327, 340, 359, 408–410], we consider two different scenarios for hadronic contributions stemming from long-distance effects [350, 351, 355]. We take into account a conservative approach (Phenomenological Data Driven or PDD) as originally proposed in [356], and refined in ref. [359], and a more optimistic approach based on the results in [350] (Phenomenological Model Driven or PMD). For the PDD model, a quite generic model of hadronic contributions is simultaneously fitted to $b \to s\ell\ell$ data together with the effects coming from NP. Within this approach, a net assessment of the presence of BSM physics is only possible via observables sensitive to LUV effects. See the discussion in ref. [327] for more details. For the PMD approach we use the dispersion relations specified in [350] to constrain the hadronic contributions in the entire large-recoil region considered in the analysis. This leads to much smaller hadronic effects in the $B \to K^*\ell^+\ell^-$ amplitudes [408], which significantly affects NP results of global analysis [327].

[7] We do not consider in this work low-recoil data, plagued by broad charmonium resonances, implying very large hadronic uncertainties. For analogous reasoning, we do not attempt to study here the baryon rare decay $\Lambda_b \to \Lambda\,\mu^+\mu^-$ as well.

[8] NP effects from dipole operators are strongly constrained as extensively investigated in ref. [436]. However, radiative exclusive B decays still provide relevant information about hadronic effects [359].

We have characterized our study by considering several different scenarios for the SMEFT fit. In particular, we would like to clarify the sets of data and operators used in each of these fit scenarios, which are organized as follows:

- **EW**: In this fit we simultaneously vary the Wilson coefficients of the *17 operators* in eqs. (11.2), (11.8), and (11.9), as presented in section 11.2. This fit includes EW precision measurements only, and it is performed under the assumptions listed in section 11.2.
- **EW (SL-4F Only)**: This refers to a fit done with the Wilson coefficients of the *SL-4F operators* involving the right-handed top current, reported in eq. (11.3). This scenario incorporates the assumption that BSM enters the modifications of the Z couplings to muons and electrons through top-quark loops only.
- **EW & Flavour**: In these fits we vary the Wilson coefficients of all the *21 operators* given in eq. (11.2), (11.8), and eq. (11.9), together with eq. (11.3). We use all the EW data and include all the flavour observables listed at the beginning of this section. This scenario comes in two varieties, PDD and PMD, as explained above.
- **Flavour**: These fits exclusively include the Wilson coefficients of the *4 operators* (both electrons and muons) appearing in eq. (11.3), and are done including only flavour data, i.e. excluding EW measurements. Results are again distinguished for the PDD and PMD cases.

11.4 Results from the SMEFT

11.4.1 Analysis of EW and $b \to s\ell\ell$ data

As a first step in our analysis, we reproduced the outcome of the EW fit originally obtained in ref. [406] using `HEPfit`. Then, we expanded upon the standard EW results through the study of the **EW** scenario introduced in the previous section, yielding constraints on the Wilson coefficients of the SMEFT operators involving, in particular, dimension-six operators with a Higgs-doublet current, and including also leading-loop effects under the working hypotheses stated in section 11.2. The subset of these operators containing leptonic currents can give rise to non-universal modifications of EW gauge-boson couplings. Assuming NP integrated out at the heavy scale $\Lambda > v$, these operators also contribute via RGE flow to $b \to s\ell\ell$ observables at one loop, see eq. (11.4).

On the left side of Figure 11.1, we show in orange the bounds from the **EW** fit on the Wilson coefficients of the operators with leptonic currents in terms of mean and standard deviation of the marginalized posterior probability density function. We observe compatibility with the SM within the 2σ level. Note that EW data strongly correlate the operators under consideration among themselves, as can be seen in the correlation matrix presented in Figure 11.2.

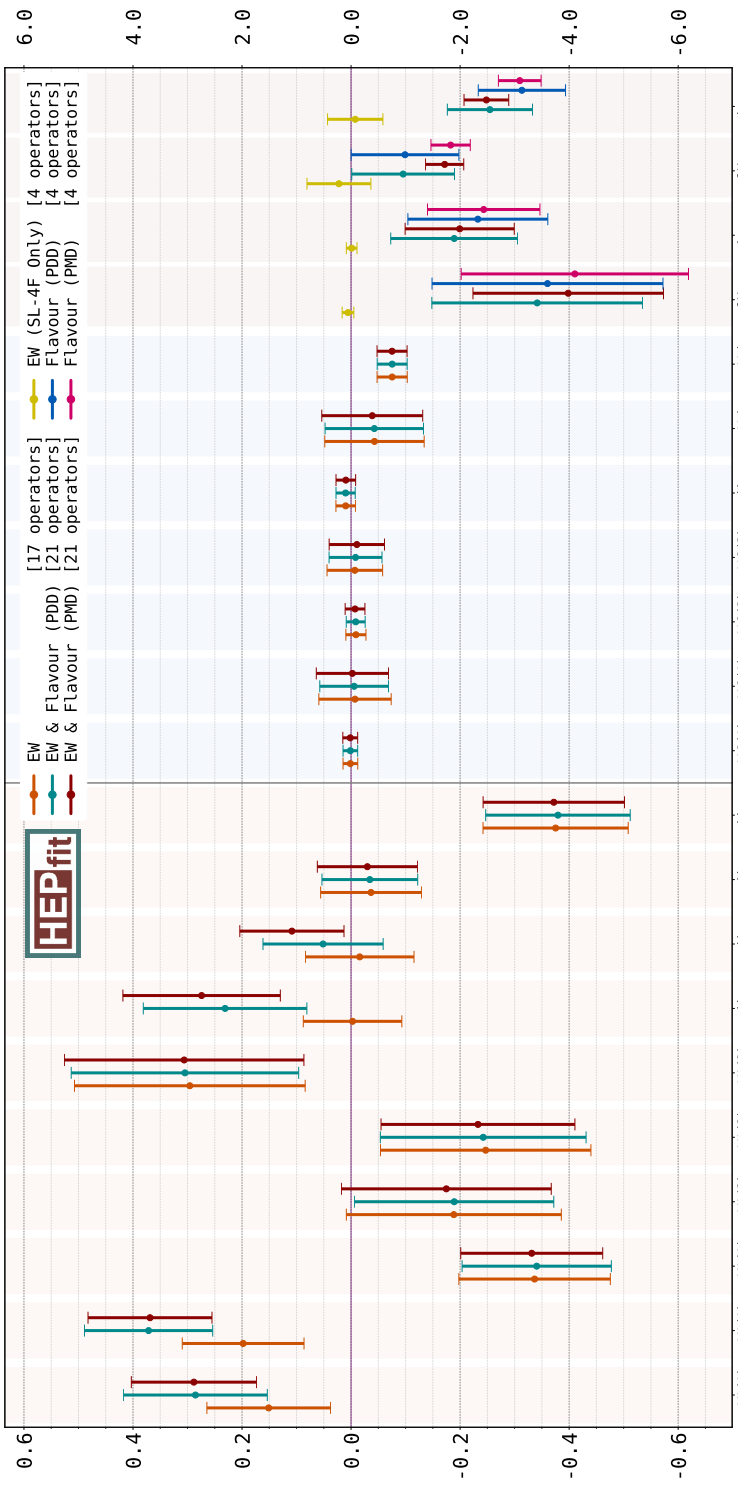

Figure 11.1. Mean and standard deviation of the marginalized posterior distributions for each of the Wilson coefficients (in TeV^{-2}) considered in the different fits described in section 11.3. Note that each fit assumes a different set of non-zero operators: EW – 17 operators presented in eqs. (11.2), (11.8) and (11.9); EW(SL-4F Only) – four-fermion operators in eq.(11.3); Flavour (PDD) and (PMD) are the fits with the operators in eq.(11.3), where (PDD) and (PMD) refer to the various assumptions on the hadronic long-distance effects in the flavour sector; EW & Flavour (PDD) and (PMD) stand for the fits including the 21 operators in eqs. (11.2), (11.3), (11.8) and (11.9). (Note the different scaling in the axes quantifying the size of the bounds presented in each half of the figure.)

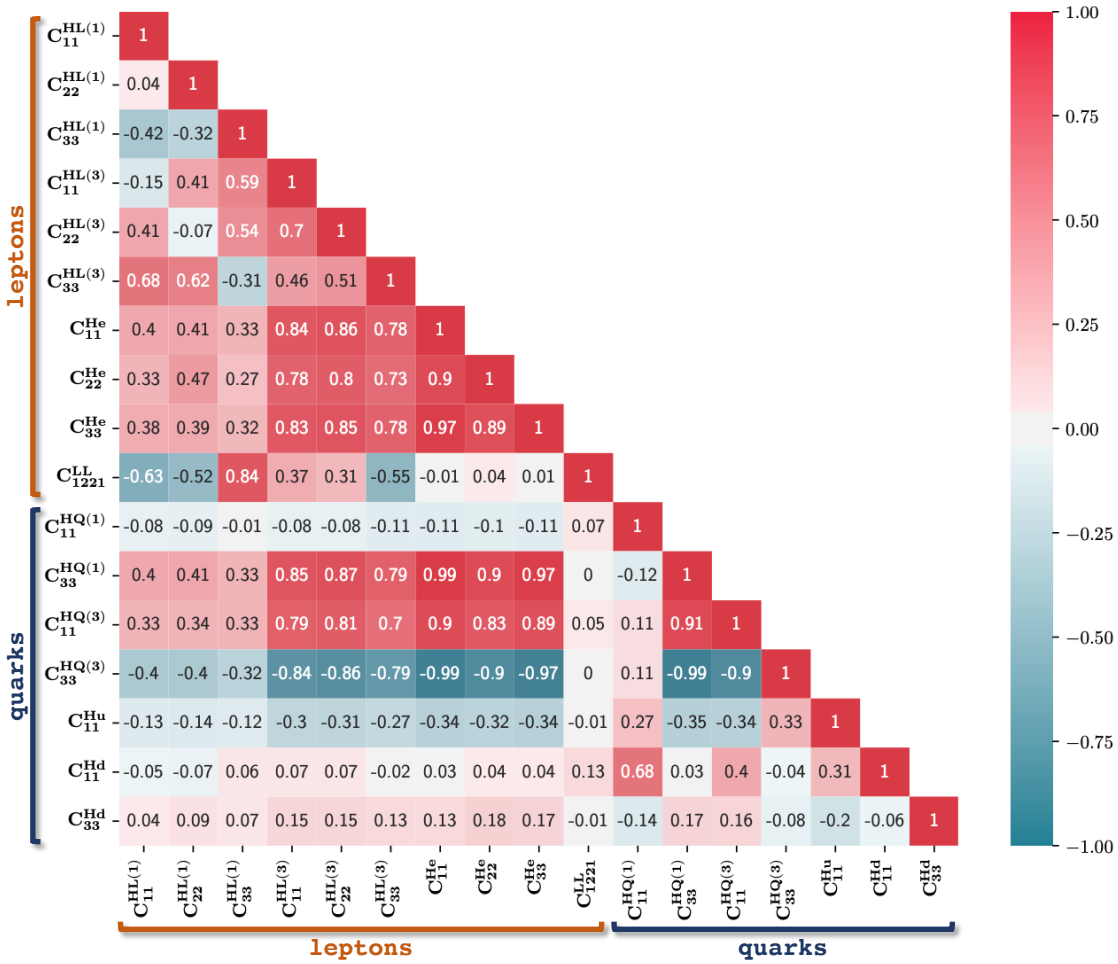

Figure 11.2. *The correlation matrix extracted from the SMEFT analysis of the set of independent operators in eqs. (11.2), (11.8), (11.9) in the **EW** scenario introduced in section 11.3. The two distinct groups of Wilson coefficients associated to leptonic and quark interactions are remarked as "leptons" and "quarks", respectively.*

where away from the photon pole, $R^{\rm SM}_{K^{(*)}}$ are predicted to be unity at percent level [336]. In particular, the strong correlation between the operators with quarks and leptons is introduced by the non-negligible one-loop universal contribution of the operator $\mathcal{O}_{33}^{HQ^{(1)}}$ to all the EW couplings, as anticipated at the end of section 11.4. With the direct bound on $C_{33}^{HQ^{(1)}}$ being relatively weak compared to the limits on the leptonic operators, such effects in the leptonic couplings can be sizable.

This leads to a relaxation of the naive bounds on $C_{\ell\ell}^{HL^{(1)}}$, $C_{\ell\ell}^{HL^{(3)}}$ and $C_{\ell\ell}^{He}$ that one would obtain in a tree-level analysis. To illustrate this, we present in section 11.7 a comparison with the results from such a tree level analysis of the EW fit. The results in

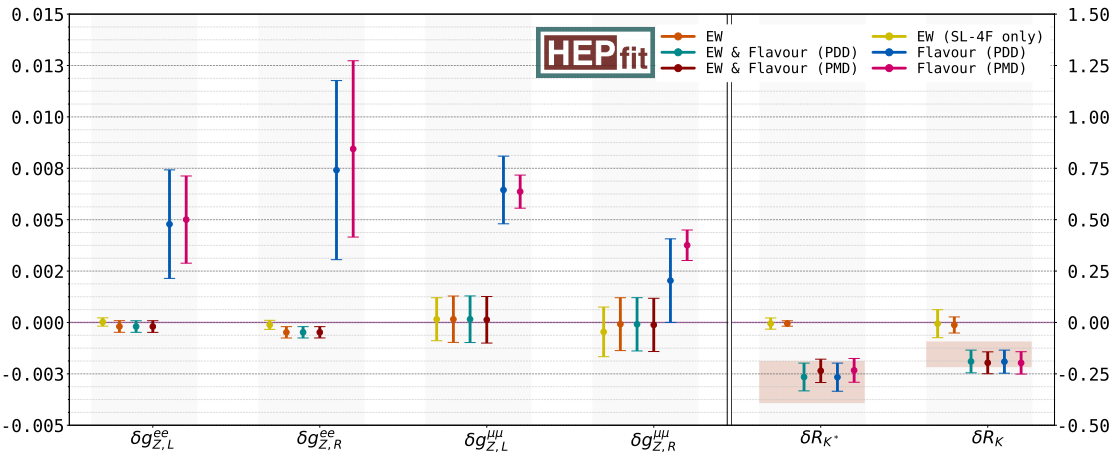

Figure 11.3. *Mean and standard deviation of the marginalized posterior of the key set of observables for this work, in relation to the tension between $b \to s\ell\ell$ anomalies and LEP/SLD measurements. In particular, the left panel shows the deviations in the effective $Z\ell\ell$ couplings, normalized by SM values. The right panel, on the other hand, shows the deviation from the nominal SM values of the lepton universality violating ratios, see eq. (11.10), with the red boxes indicating the region selected by the experimental measurements of $R_{K,(K^*)}$.*

Figure 11.2 can then be compared to those in Figure 11.8 where, as it is apparent, there is a substantial decoupling between the dimension-six operators made of Higgs doublets and quark bilinears from the leptonic ones.

The impact of these operators on the key observables for the present discussion is reported in Figure 11.3. There, we collect mean and standard deviation on the shift in the Z coupling to light leptons (normalized to the corresponding SM value),and on the effect on $R_{K^{(*)}}$ in the dilepton-mass range $[1.0, 6.0]$ GeV^2:

$$\delta g^{ee(\mu\mu)}_{Z,L(R)} \equiv g^{ee(\mu\mu)}_{Z,L(R)} / g^{ee(\mu\mu),\mathrm{SM}}_{Z,L(R)} - 1 \ , \ \delta R_{K^{(*)}} \equiv R_{K^{(*)}} - R^{\mathrm{SM}}_{K^{(*)}} \ , \tag{11.10}$$

Note that EW measurements tightly constrain NP effects modifying the EW gauge boson couplings to electrons, and also forbid deviations beyond the per-mille level in the case of couplings to muons. This translates into strong bounds on the Wilson coefficients $C_{\ell\ell}^{HL^{(1,3)},He}$. Hence, the one-loop contribution to $R_{K^{(*)}}$ from $O_{\ell\ell}^{HL^{(1,3)},He}$ comes out to be tiny. We can then move our attention to the **EW (SL-4F Only)** scenario, reported in yellow in Figure 11.1 and Figure 11.3, and find a similar conclusion. Indeed, EW data once again strongly constrain the NP Wilson coefficients related to $O_{\ell\ell 33}^{eu,Lu}$ – the SL-4F operators – implying all the four NP Wilson coefficients to be compatible with 0. However, note that unlike the previous case, $C_{\ell\ell 33}^{Lu,eu}$ only contribute at one loop to $\delta g^{\ell\ell}_{Z,L(R)}$ and $\delta R_{K^{(*)}}$ in eq. (11.10). Consequently, the resulting impact on $b \to s\ell\ell$ flavour observables can be larger than the one in the **EW** scenario. As depicted in Figure 11.3,

however, there is still an overall tension between EWPO bounds (in yellow) and the experimental measurements of R_K and R_{K^*} (indicated by the shaded red boxes in the right side of the figure) at the 3σ level.

To frame this tension from a different perspective, let us now focus on the set of flavour measurements as previously done in ref. [327]. In Figure 11.1 we also show the constraints on the four Wilson coefficients of eq. (11.3) coming from $b \to s\ell\ell$ data, in what we dubbed as the **Flavour** scenario. We present the PMD case, corresponding to an optimistic approach to QCD power corrections, in pink, while the more conservative PDD case is shown in blue. We observe that in both cases a muonic solution to B anomalies stands out, with C^{Lu}_{2233} different from 0 at more than 3σ in the PDD case, and at roughly 6σ in the PMD one.

We stress that the difference between the results obtained in the PMD and in the PDD case is substantially driven by the angular analysis of $B \to K^*\mu\mu$. In particular, only within the PDD approach the fully left-handed solution to B anomalies, $C_{9,\ell} = -C_{10,\ell}$, is favoured by data (signalled here by the Wilson coefficient of $O^{eu}_{\ell\ell 33}$ being compatible with 0 at 1σ, see the results in blue in Figure 11.1). In addition, an electron resolution of B anomalies is, once again, viable only within PDD [327, 340].

In the **Flavour** scenario one can also predict the induced shift in the Z-boson couplings according to eq. (11.7), and these are shown in Figure 11.3. As can be seen, $\delta g^{\ell\ell}_{Z,L,R}$ would receive large contributions at one loop from $O^{Lu,eu}_{\ell\ell 33}$ in correspondence to the one-loop MFV-like resolution of B anomalies. Such contribution would be, however, now in tension with the results from EW precision tests. In particular, as a reflection of the main role played by O^{Lu}_{2233} in the **Flavour** fit to the four NP Wilson coefficients considered, $g^{\mu\mu}_{Z,L}$ shows the most important deviation from the SM value. Also, the prediction of $g^{\mu\mu}_{Z,L(R)}$ becomes indirectly sensitive to the underlying treatment of hadronic uncertainties adopted for the study of $b \to s$ data. Therefore, we observe that within the PMD approach, the inconsistency between what is needed to address B anomalies and what is required by EW measurements is even more severe than the 3σ established in the **EW (SL-4F Only)** scenario, and imprinted also in the **Flavour** fit with the PDD approach. In fact, we stress once again that adopting light-cone sum-rule results [350] for the long-distant effects in $B \to K^*\ell\ell$ decay, the tension between B anomalies and EW data reaches the 6σ level.

So, how do we reach a consensus between $b \to s\ell\ell$ measurements and EWPO? Succinctly, an obvious solution which satisfies these constraints is a class of models where $R_{K^{(*)}}$ anomalies are addressed at tree level and where modifications to Z-lepton-lepton vertices are at the same time suppressed. However, these models would not offer a solution to B anomalies of the MFV type envisaged so far, namely they would rely on the existence of sizeable new sources of flavour violation. At this point, we would like to emphasize that a combined fit of EW and flavour observables offers a new insight into this matter: it highlights strong correlations between the dimension-six operators

$O_{\ell\ell 33}^{Lu(eu)}$ and $O_{\ell\ell}^{HL^{(1)}(He)}$ as is evident from Figure 11.4. This figure presents a pictorial representation of the correlations between the leptonic operators included in the different fits.

Apart from the fits introduced in the previous section, for illustration purposes we also show in Figure 11.4 the correlations obtained in a variant of the **EW** fit including also the four-fermion operators $O_{\ell\ell 33}^{Lu(eu)}$, labelled as **EW (including SL-4F operators)**. This is shown in the upper-right corner of the figure. As can be seen in that panel, and one could deduce from the relations in eq. (11.7), in a pure EW fit adding the four-fermion operators would simply introduce 4 flat directions. These are illustrated by the links connecting the $C_{\ell\ell 33}^{eu}$ ($C_{\ell\ell 33}^{Lu}$) and $C_{\ell\ell}^{He}$ ($C_{\ell\ell}^{HL^{(1)}}$) operators, corresponding to 100% anti-correlation. Such flat directions are lifted upon the introduction of the flavour measurements of R_K and R_{K^*}, as can be seen in the lower panels of Figure 11.4 for the **EW & Flavour** fits. Even then, due again to relations in eq. (11.4) and (11.7) and the comparatively different precision of the EW and flavour measurements, sizable correlations remain.

In Figure 11.1 the imprint of these correlations is a shift of central values and an increase on the bounds on the corresponding Wilson coefficients, with red and green bars representing the outcome of the fit in the **EW & Flavour** scenario within the **PMD** and **PDD** approaches, respectively. The interplay between $O_{\ell\ell 33}^{Lu(eu)}$ and $O_{\ell\ell}^{HL^{(1)}(He)}$ is evident when comparing the reported red and green bounds versus the orange EW constraints on $C_{\ell\ell}^{HL^{(1)}(He)}$, and the yellow ones for $C_{\ell\ell 33}^{Lu(eu)}$. Consequently, as clearly depicted in Figure 11.3, looking at the red and green ranges reported for the **EW & Flavour** scenario, $R_{K^{(*)}}$ puzzles are solved with EW precision being respected. It is important to emphasize that, despite the significant correlation between quark and lepton operators introduced by the one-loop effects of $C_{33}^{HQ^{(1)}}$, quark operators play no significant role in reconciling the EWPO constraints with the solution to B anomalies. This will become clearer in the next section, but can be easily understood from the fact that, as mentioned before, quark and lepton constraints are somewhat uncorrelated in the tree-level EW fit, and the fact that the one-loop corrections effect induced by $C_{33}^{HQ^{(1)}}$ are flavour universal.

11.4.2 A minimal EFT picture

Finally, let us draw what would be the minimal picture for NP out of the general analysis obtained with the 21 operators considered in the **EW & Flavour** scenario. Indeed, a simpler picture will serve as a guideline for the UV models discussed in section 11.5. As mentioned before, given the hadronic uncertainties at hand, the most economic explanation addressing in particular $R_{K^{(*)}}$ anomalies resides in the NP contribution from the fully left-handed operator, $O_{\ell\ell 23}^{LQ}$. In the present context this operator is generated at one loop by $O_{\ell\ell 33}^{Lu}$, according to eq. (11.4).

Then, in Figure 11.5 we show in orange the overall constraint from $b \to s\ell\ell$ data

on $C^{Lu}_{\ell\ell 33}$ within the most conservative approach to long-distance effects, i.e. the PDD one. In particular, in the left (right) panel we report the constraint on the muonic (electronic) scenario. In the same figure, we highlight with the vertical gray band the bound derived from the full correlated set of EWPO on the same operator. From the comparison of the orange and gray single-operator bounds, the tension between flavour and EW measurements is manifest at the 3σ level in the left panel of Figure 11.5. It gets even more pronounced in the right panel due to the precise probe of NP that EW gauge-boson couplings to electrons provide. In the same Figure 11.5, we also show with the horizontal gray band the result of the EWPO constraints applied this time on the NP contribution coming exclusively from the operator $C^{HL^{(1)}}_{\ell\ell}$. Note that this operator would also contribute to $R_{K^{(*)}}$ at one loop, but the size needed would be $\mathcal{O}(1)$ and it is out of scale in the vertical axis of the plot.

Most importantly, in the same figure we display in (dashed) magenta the $1(2)\sigma$ contour where EW data are reconciled with the one-loop MFV explanation of B anomalies when a combined fit of the NP contributions from these two operators is performed. Therefore, heavy BSM degrees of freedom that, once integrated out, generate sizeable contributions both to the Wilson coefficient of $O^{HL^{(1)}}_{\ell\ell}$ and of $C^{Lu}_{\ell\ell 33}$ are the key aspect of this scenario that addresses B anomalies without requiring sources of flavour violation beyond SM ones.

Finally, note that the role played here by $O^{Lu}_{\ell\ell 33}$ could be shared, in part, with $O^{eu}_{\ell\ell 33}$, depending on how much departure is actually required from the fully left-handed solution to B anomalies. As already noted, this fact critically depends on the information stemming from $B \to K^*\mu\mu$ [327]. On general grounds, to relieve the bounds from EWPO, the presence of $O^{eu}_{\ell\ell 33}$ would also necessitate sizeable NP effects from $O^{He}_{\ell\ell}$.

As a last comment of this section we would also like to highlight that in the class of models considered the prediction for the LUV observable R_K is always close to the one for R_{K^*}: any hint of NP coming from $R_{K^*}/R_K \neq 1$ [334, 335, 341, 441] would not be addressed within the NP models considered here, mainly involving the operators in eq. (11.2) and (11.3). In the following sections we will put our focus on the economic EFT scenario captured in Figure 11.5 to build up simple UV scenarios realizing the EFT picture here delineated.

11.5 Directions for UV models

In this section we discuss how the lesson derived from the SMEFT picture illustrated, in particular, in Figure 11.5, can be realized in a minimal extension of the SM. Here, we explicitly show how models involving a new Z' gauge boson around the TeV scale provide the most economic example of the correlations advertised in the previous section. This can be achieved if we have a Z' coupled both to top and lepton SM fields. These couplings can be obtained introducing vector-like top and muon/electron partners reasonably close

to the EW scale [400, 401], making this class of models potentially interesting also from the point of view of naturalness in the Higgs sector. Finally, we will also briefly comment on possible alternative scenarios that can be obtained with leptoquarks.

11.5.1 Z′ with vector-like partners

Let us start with the baseline presented originally in ref. [400]. A simple extension of the SM, able to address B anomalies, and that does not introduce any explicit new source of flavour violation, can be conceived as follows:

- The SM gauge group, $SU(3)_c \otimes SU(2)_L \otimes U(1)_Y$, is extended by a new Abelian gauge group, $U(1)_X$, under which SM fields are neutral;
- There is a new complex scalar field $\mathcal{S}$ that spontaneously breaks $U(1)_X$, giving a mass to the gauge boson X_μ equal to $m_{Z'} = g_X \langle \mathcal{S} \rangle$;
- A coloured vector-like top partner, $\mathcal{T}$, properly charged under $U(1)_X$ and $U(1)_Y$ can mix with the right-handed top-quark field u_3 via a Yukawa interaction with $\mathcal{S}$;
- A vector-like muonic partner, $\mathcal{M}$, doublet of $SU(2)_L$ and charged under $U(1)_{X,Y}$, can mix with the muonic doublet L_2 via another Yukawa coupling of $\mathcal{S}$;
- The couplings controlling the kinetic-mixing term, $X_{\mu\nu}B^{\mu\nu}$, and the quadratic scalar mixing, $\mathcal{S}^\dagger \mathcal{S} H^\dagger H$, are set to be phenomenologically negligible.[9]

Then, the UV model is completely characterized by eight new parameters: the gauge coupling g_X, the mass $\mu_\mathcal{S}$ and quartic $\lambda_\mathcal{S}$ of the renormalizable potential of $\mathcal{S}$, the new Yukawa couplings $Y_{\mathcal{T},\mathcal{M}}$, here taken to be real, and the vector-like mass-term parameters $M_{\mathcal{T},\mathcal{M}}$. In particular, the Lagrangian of the model contains the following terms:

$$M_\mathcal{T} \overline{\mathcal{T}_R} \mathcal{T}_L + M_\mathcal{M} \overline{\mathcal{M}}_R \mathcal{M}_L + Y_t \overline{u}_3 \tilde{H}^\dagger Q_3 + Y_\mathcal{T} \overline{u}_3 \mathcal{T}_L \mathcal{S} + Y_\mu \overline{e}_2 H^\dagger L_2 + Y_\mathcal{M} \overline{\mathcal{M}}_R L_2 \mathcal{S} + \text{h.c.} \,, \tag{11.11}$$

that characterize the mixing pattern of SM fields and vector-like partners.[10] Symmetry breaking of $U(1)_X$ is triggered by $\langle \mathcal{S} \rangle^2 = -\mu_\mathcal{S}^2/(2\lambda_\mathcal{S}) \equiv \eta^2 \neq 0$, that implies the following

[9] Using naive dimensional analysis, both kinetic and scalar quadratic mixing should appear beyond the tree level suppressed at least by a loop factor and the corresponding SM-partner rotation angles.

[10] Note that upon an opposite $U(1)_X$ charge assignment for the vector-like fermionic partners than the one implicitly assumed, one should replace in eq. (11.11) $\mathcal{S}$ with $S^\dagger$.

fermionic mixing patterns:

$$\text{top sector:} \quad \left(\begin{array}{cc} \overline{u}_3 & \overline{\mathcal{T}}_R \end{array} \right) \begin{pmatrix} \frac{Y_t\, v}{\sqrt{2}} & \frac{Y_{\mathcal{T}}\eta}{\sqrt{2}} \\ 0 & M_{\mathcal{T}} \end{pmatrix} \left(\begin{array}{c} U_3 \\ \mathcal{T}_L \end{array} \right) + \text{h.c.}\,, \tag{11.12}$$

$$\text{muon sector:} \quad \left(\begin{array}{cc} \overline{e}_2 & \overline{\mathcal{M}}_R \end{array} \right) \begin{pmatrix} \frac{Y_\mu v}{\sqrt{2}} & 0 \\ \frac{Y_{\mathcal{M}}\eta}{\sqrt{2}} & M_{\mathcal{M}} \end{pmatrix} \left(\begin{array}{c} E_2 \\ \mathcal{M}_L \end{array} \right) + \text{h.c.}\,,$$

where U_i (E_i) indicates the Q_i-component (L_i-component) with weak isospin 1/2 (-1/2). Using the determinant and trace of the squared mass matrices, one can easily show that the eigenvalues $m_{t,\mathcal{T}}$ and $m_{\mu,\mathcal{M}}$ must satisfy [400]:

$$\begin{aligned} m_{t,\mu}\, m_{\mathcal{T},\mathcal{M}} &= \frac{1}{\sqrt{2}} Y_{t,\mu} v M_{\mathcal{T},\mathcal{M}}\,, \\ m_{t,\mu}^2 + m_{\mathcal{T},\mathcal{M}}^2 &= M_{\mathcal{T},\mathcal{M}}^2 + \frac{1}{2}(Y_{t,\mu}\, v)^2 + \frac{1}{2}(Y_{\mathcal{T},\mathcal{M}}\, \eta)^2\,, \end{aligned} \tag{11.13}$$

that in the decoupling limit clearly yield: $m_{t,\mu} \simeq Y_{t,\mu} v/\sqrt{2}$, $m_{\mathcal{T},\mathcal{M}} \simeq M_{\mathcal{T},\mathcal{M}}$.

Defining for the top sector the rotation matrix from the interaction to the mass basis following the convention:

$$\left(\begin{array}{c} t_{R(L)} \\ \mathcal{T}'_{R(L)} \end{array} \right) = \begin{pmatrix} \cos\theta^t_{R(L)} & -\sin\theta^t_{R(L)} \\ \sin\theta^t_{R(L)} & \cos\theta^t_{R(L)} \end{pmatrix} \left(\begin{array}{c} u_3(U_3) \\ \mathcal{T}_{R(L)} \end{array} \right)\,, \tag{11.14}$$

and doing similarly for the muonic sector, the mixing angles between SM fields, t and μ, and their partner mass eigenstates, $\mathcal{T}'$ and $\mathcal{M}'$, can be conveniently expressed in terms of the dimensionless ratios $\xi_{\mathcal{T},\mathcal{M}}$ and $\varepsilon_{t,\mu}$:

$$\begin{aligned} &\tan 2\theta^t_R = \tfrac{2\xi_{\mathcal{T}}}{\xi^2_{\mathcal{T}} - \varepsilon^2_t - 1}\,, \quad \tan 2\theta^t_L = \tfrac{2\varepsilon_t}{\xi^2_{\mathcal{T}} - \varepsilon^2_t + 1}\,, \text{ with } \varepsilon_t \equiv \tfrac{Y_t v}{Y_{\mathcal{T}}\eta},\ \xi_{\mathcal{T}} \equiv \tfrac{\sqrt{2} M_{\mathcal{T}}}{\eta Y_{\mathcal{T}}}\,; \\ &\tan 2\theta^\mu_R = \tfrac{2\varepsilon_\mu}{\xi^2_{\mathcal{M}} - \varepsilon^2_\mu + 1}\,, \tan 2\theta^\mu_L = \tfrac{2\xi_{\mathcal{M}}}{\xi^2_{\mathcal{M}} - \varepsilon^2_\mu - 1}\,, \text{ with } \varepsilon_\mu \equiv \tfrac{Y_\mu v}{Y_{\mathcal{M}}\eta},\ \xi_{\mathcal{M}} \equiv \tfrac{\sqrt{2} M_{\mathcal{M}}}{\eta Y_{\mathcal{M}}}\,. \end{aligned} \tag{11.15}$$

In a perturbative expansion in $\varepsilon_{t,\mu}$, eq. (11.15) clearly shows that the mixing in the top sector proceeds mainly through $\tan\theta^t_R \simeq 1/\xi_{\mathcal{T}}$, while in the muonic sector one has $\tan\theta^\mu_L \simeq 1/\xi_{\mathcal{M}}$ and very tiny $\tan\theta^\mu_R$.

Hence, for $\varepsilon_{t,\mu}/\xi_{\mathcal{T},\mathcal{M}} = Y_{t,\mu} v/\sqrt{2} M_{\mathcal{T},\mathcal{M}} < 1$, the leading couplings of the Z' boson to the SM fields correspond to right-handed tops and to left-handed muons as well as

neutrinos according to:[11]

$$g_{Z' t_R} = g_X \sin^2\theta_R^t = \frac{g_X}{1+\xi_{\mathcal{T}}^2} + \mathcal{O}\left(\varepsilon_t^2/\xi_{\mathcal{T}}^2\right) , \tag{11.16}$$

$$g_{Z' \mu_L(\nu)} = g_X \sin^2\theta_L^\mu = \frac{g_X}{1+\xi_{\mathcal{M}}^2} + \mathcal{O}\left(\varepsilon_\mu^2/\xi_{\mathcal{M}}^2\right) , \tag{11.17}$$

with $g_{Z' t_{L(\mu_R)}}$ being non-negligible only at order $\varepsilon_{t(\mu)}^2/\xi_{\mathcal{T}(\mathcal{M})}^2$. Consequently, integrating out the Z' relevantly generates the operator O_{2233}^{Lu} with Wilson coefficient:

$$C_{2233}^{Lu} = -\frac{g_{Z' t_R} g_{Z' \mu_L}}{m_{Z'}^2} \simeq -\frac{1}{(1+\xi_{\mathcal{T}}^2)(1+\xi_{\mathcal{M}}^2)\,\eta^2} , \tag{11.18}$$

together with four-fermion operators built of t_R or μ_L, ν fields that can be potentially probed at collider and by experimental signatures like ν-trident production.

From eq. (11.18) it is clear that in order to have $|C_{2233}^{Lu}| \sim 2$ TeV^{-2} as highlighted in Figure 11.5, one needs to rely on a relatively low symmetry-breaking scale $\eta \lesssim$ TeV;[12] for $m_{Z'} \sim$ TeV this implies $g_X \gtrsim 1$. In Figure 11.6 we show the 1σ region corresponding to the explanation of B anomalies via eq. (11.18) in the parameter space $\xi_{\mathcal{T},\mathcal{M}}$, fixing the gauge coupling $g_X = m_{Z'}/\eta$ for a tentative Z' gauge boson at the TeV scale and the VEV of the new scalar field $\mathcal{S}$ set to $\eta = 250$ GeV and $\eta = 500$ GeV in the left and right panel, respectively. In the same plot, we re-interpret in our scenario the most relevant collider constraints originally identified in ref. [402].

For small values of $\xi_{\mathcal{M}}$, the measurement of neutrino-trident production performed in [442] is effective, and its constraint is reported at the 2σ level with the orange vertical band. Under the reasonable assumption that the Z' boson is mainly produced at tree level in association with the $t\bar{t}$ pair, in the blue region we show the 95% high-p_T constraint stemming from the recasting of the $pp \to \mu^-\mu^+ t\bar{t}$ search at ATLAS [443], while in cyan we report the expected constraint on the model from the 4-tops analysis of CMS [444], see ref. [402] for further details. From the same work, we also adopt the expected collider constraints for future projected luminosity corresponding to 300 fb^{-1}, shown with dashed lines. Note that these projections become of fundamental importance when it comes to probe the interesting 1σ region connected to B anomalies. In particular, the right panel in Figure 11.6 captures the benchmark for a promising discovery at the High-Luminosity LHC.

Finally, in the same figure, fixing the partner Yukawa coupling to $\mathcal{O}(1)$ values as reported in the two panels, we mark in gray the region corresponding to the bound on the mass of the vector-like partner expected from collider, taken to be $m_{\mathcal{T}} = 1.4$ TeV

[11] In what follows, for $\eta \sim \mathcal{O}(v)$ we will have $\xi_T \sim \mathcal{O}(1)$; consequently, $\varepsilon_t \sim \mathcal{O}(v/M_{\mathcal{T}})$.

[12] Note that even for masses as low as $\mu_{\mathcal{S}} \sim \mathcal{O}(v)$, for $\eta \simeq v$ and $\lambda_{\mathcal{S}} \sim \mathcal{O}(1)$, the interactions of $\mathcal{S}$ do not alter the phenomenology discussed here since the largest $\mathcal{S}$-generated effects are still suppressed as $\mathcal{O}(\varepsilon_t^2/\xi_{\mathcal{T}}^2)$.

from the search at ATLAS in ref. [445], and $m_{\mathcal{M}} = 0.8$ TeV from the CMS analysis of ref. [446].

As already discussed, the scenario depicted in Figure 11.6 remains viable under the lens of EW precision as long as we also have some heavy new dynamics yielding at the EW scale an imprint of $O_{22}^{HL^{(1)}}$ consistently with the correlation obtained in the left panel of Figure 11.5.

A simple way to obtain such NP contribution would be to consider the joint effect that the leptonic mixing of the vector-like partner would have together with the kinetic mixing of the Z', so far neglected. The Z-Z' mixing could also originate from charging the new scalar field $\mathcal{S}$ under both Abelian gauge groups, introducing a small misalignment with the standard hypercharge $U(1)_Y$ in the UV. However, the required mixing of the Z' would end up mediating light-quark pair annihilation into muons: the typical size of the Wilson coefficient of this four-fermion operator would be $\mathcal{O}(g_Y^2/m_{Z'}^2)$, in net tension with the di-muon bound from ATLAS [443], probing NP scales as high as 20 - 40 TeV for $\mathcal{O}(1)$ (dimensionless) couplings. Hence, we rule out here this possibility.

Interestingly, it is still possible to generate $O_{22}^{HL^{(1)}}$ without relying on the Z-Z' mixing, but rather invoking the presence in the UV theory of additional new vector-like leptonic states [447, 448]. These ones may be phenomenologically interesting in relation to the problem of the origin of neutrino masses as well as for the prediction of the anomalous magnetic moment $(g-2)_\mu$ [449], and may give peculiar multi-lepton signatures at colliders [450, 451].

In the most economic scenario, we may consider the presence in the UV theory of a pair of new vector-like muonic partners: a singlet of $SU(2)_L$, S_Y, and a triplet of $SU(2)_L$, T_Y, where in both cases the subscript Y denotes the hypercharge of the fermion. These fields would have their own mass terms controlled by the parameters M_{S_Y,T_Y}, and interact with the SM doublet L_2 via the Yukawa couplings $\mathcal{Y}_{S_Y,T_Y}$ according to:

$$\mathcal{Y}_{S_0}\overline{S}_{0,R}\tilde{H}^\dagger L_2 + \mathcal{Y}_{T_0}\overline{T}^A_{0,R}\tau^A\tilde{H}^\dagger L_2 + \text{h.c.}\ , \tag{11.19}$$

where we have reported the case of vector-like muonic partners with hypercharge $Y = 0$. We assume the new Yukawa couplings to be real. Another possibility of interest may be the one of replacing in eq. (11.19) $\tilde{H} = i\tau^2 H^*$ with the Higgs doublet, H, and involve then the pair of vector-like partners with hypercharge $Y = 1$.

Integrating out these vector-like states from the theory would generate contributions related to $\mathcal{O}^{HL^{(1,3)}}$ [448, 449] of the form:

$$\begin{aligned} C_{22}^{HL^{(1)}} &= \frac{\mathcal{Y}_{S_0}^2}{4M_{S_0}^2} - \frac{\mathcal{Y}_{S_1}^2}{4M_{S_1}^2} + \frac{3\mathcal{Y}_{T_0}^2}{4M_{T_0}^2} - \frac{3\mathcal{Y}_{T_1}^2}{4M_{T_1}^2}\ , \\ C_{22}^{HL^{(3)}} &= -\frac{\mathcal{Y}_{S_0}^2}{4M_{S_0}^2} - \frac{\mathcal{Y}_{S_1}^2}{4M_{S_1}^2} + \frac{\mathcal{Y}_{T_0}^2}{4M_{T_0}^2} + \frac{\mathcal{Y}_{T_1}^2}{4M_{T_1}^2}\ . \end{aligned} \tag{11.20}$$

Clearly, in order to have $C_{22}^{HL^{(1)}} \sim 0.1$ and negligible $C_{22}^{HL^{(3)}}$[13], one would need to rely on a tuning of the $Y = 0$ triplet Wilson coefficient with one of the contributions coming from the singlet vector-like muonic partner. However, once generated at the NP scale $\Lambda \sim \mathcal{O}(M_{T_0}) \gg v$, we observe that the relation established between the triplet and singlet contributions to $O^{HL^{(1,3)}}$ would be stable under the RG flow of the SMEFT.

A final comment is needed for the electron scenario reported in the right panel of Figure 11.5, that involves opposite signs for the Wilson coefficients of O^{Lu} and $O^{HL^{(1)}}$ discussed so far. For the former, we note that the sign highlighted in the matching in eq. (11.18) follows from having assumed the same sign for the charge of the vector-like top and muon partners under $U(1)_X$. Hence, assuming the vector-like electron partner to have the opposite $U(1)_X$ charge of the top-partner one would be sufficient to accomplish $C_{1133}^{Lu} > 0$. (Of course, this would also imply a distinct use in eq. (11.11) of $\mathcal{S}$ and $\mathcal{S}^\dagger$ couplings in the Yukawa terms of the vector-like partners involved to keep the theory invariant under $U(1)_X$.) For what concerns the generation of $C_{11}^{HL^{(1)}} < 0$, according to eq. (11.20) one needs to correlate once again the contribution stemming from S_0, or from S_1, with the effect coming from a $SU(2)_L$ triplet, that now needs to be identified with T_1, namely the triplet of hypercharge $Y = 1$.

Eventually, we wish also to comment on the possible role of the O^{eu} operator, so far neglected in this discussion, but of potential relevance more in general. In fact, as mentioned earlier, the presence of O^{eu} would be particularly needed in the case where hadronic corrections entering in the amplitude of $B \to K^* \ell\ell$ would be of the size originally estimated in [350]. In that case, a solution to flavour anomalies would be preferred in the muonic channel with NP Wilson coefficient C_{2233}^{eu} also substantially deviating from 0, as already discussed in subsection 11.4.1. Then, one would need to involve also the operator C_{22}^{He} to relieve possible tensions with EW precision. In a general picture, the required NP effects from $O_{11,22}^{He}$ can be obtained integrating out heavy vector-like $SU(2)_L$ leptonic doublets.

11.5.2 Leptoquark scenarios

An alternative way to reproduce the minimal EFT scenario of Figure 11.5 would be via *leptoquarks* (LQ), particles generically predicted in grand unified theories (GUTs) [452, 453]. Notoriously, LQ-induced dimension-six operators could be potentially dangerous as they would lead to proton decay at tree level, forcing to push their scale up to the GUT scale. However, the outcome may drastically change in models where the couplings of the LQs would be non-universal with respect to lepton and/or quark flavours. In such a case their mass could be much lower than what typically expected in GUTs and their

[13] We have indeed verified that a scenario involving at the same time C^{Lu} and $C^{HL^{(1,3)}}$ would not alter what already highlighted in Figure 11.5, with the best-fit value for $|C^{HL^{(3)}}|$ turning out to be of $\mathcal{O}(10^{-2})$.

signatures may actually be probed at present colliders. Interestingly, such LQs are candidates that could explain the lepton flavour universality violation – even at the loop level here considered [402, 407] – hinted in the recent LHCb and Belle data. However, this would imply generically a rather non-trivial flavour structure in the theory [454]. For a comprehensive survey of LQ models, see for instance [121, 393, 455–457].

Here, we limit ourselves to the case of toy models that specifically generate the operators of interest, namely $C^{Lu}_{\ell\ell 33}$ and $C^{eu}_{\ell\ell 33}$, for $\ell = 1$ (electron) or $\ell = 2$ (muon). In these peculiar LQ models we then assume that couplings between right-handed top quarks and light leptons are the only ones that actually matter for TeV phenomenology.

In Table 11.1 we list the vector and scalar LQs that constitute the potential LQ candidates able to generate the solutions for $b \to s\ell\ell$ anomalies at one loop under scrutiny.

Vector LQ: $\mathcal{V}^\mu$	$SU(3)_c \otimes SU(2)_L \otimes U(1)_Y$	Comments
$\overline{L}_\ell \gamma_\mu (\tau^A) Q_3 \, \mathcal{V}^{\mu(A)}$	$(\overline{\mathbf{3}}, \mathbf{1} \text{ or } \mathbf{3}, -2/3)$	not of interest
$(\mathcal{V}^\mu)^\dagger \, \overline{e}^c_\ell \gamma_\mu Q_3$	$(\overline{\mathbf{3}}, \mathbf{2}, 5/6)$	not of interest
$\overline{L}^c_\ell \gamma_\mu u_3 \, i\tau^2 \, \mathcal{V}^\mu$	$(\overline{\mathbf{3}}, \mathbf{2}, -1/6)$	generates $C^{Lu}_{\ell\ell 33} > 0$
$\overline{e}_\ell \gamma_\mu u_3 \, \mathcal{V}^\mu$	$(\overline{\mathbf{3}}, \mathbf{1}, -5/3)$	generates $C^{eu}_{\ell\ell 33} < 0$
Scalar LQ: $\mathcal{S}$		
$\overline{L}_\ell (\tau^A)(i\tau^2) \, Q^c_3 \, \mathcal{S}^{\dagger(A)}$	$(\overline{\mathbf{3}}, \mathbf{1} \text{ or } \mathbf{3}, 1/3)$	not of interest
$\overline{e}_\ell Q_3 \, i\tau^2 \mathcal{S}$	$(\overline{\mathbf{3}}, \mathbf{2}, -7/6)$	not of interest
$\overline{L}_\ell u_3 \, \mathcal{S}$	$(\overline{\mathbf{3}}, \mathbf{2}, -7/6)$	generates $C^{Lu}_{\ell\ell 33} < 0$
$\overline{e}^c_\ell u_3 \, \mathcal{S}$	$(\overline{\mathbf{3}}, \mathbf{1}, 1/3)$	generates $C^{eu}_{\ell\ell 33} > 0$

Table 11.1. Scalar and vector LQ interactions under scrutiny: LQs of interest for our analysis have to generate the dimension-six operators $O^{Lu,eu}_{\ell\ell 33}$.

Looking back at Figure 11.5, from the table above we recognize as the most economic LQ scenario for the resolution of B anomalies at one loop, the case of the vector LQ $\mathcal{V}^\mu \sim (\overline{\mathbf{3}}, \mathbf{2}, -1/6)$ for LUV effects originating from electron couplings, and the scalar $\mathcal{S} \sim (\overline{\mathbf{3}}, \mathbf{2}, -7/6)$ for the ones associated to muons. The interaction terms of interest are:

$$\mathcal{L}_{\mathcal{V}\bar{f}f} = \tilde{\lambda}_{te} \, \overline{L}^c_1 \gamma_\mu u_3 \, i\tau^2 \mathcal{V}^\mu + \text{h.c.} \quad , \quad \mathcal{L}_{\mathcal{S}\bar{f}f} = \lambda_{t\mu} \, \overline{L}_2 u_3 \mathcal{S} + \text{h.c.}, \tag{11.21}$$

leading to the corresponding matching condition:

$$C^{Lu}_{1133} = +\frac{|\tilde{\lambda}_{te}|^2}{M^2_{\mathcal{V}}} \quad , \quad C^{Lu}_{2233} = -\frac{|\lambda_{t\mu}|^2}{2M^2_{\mathcal{S}}} \, . \tag{11.22}$$

In Figure 11.7 we report in (lighter) magenta the underlying $1(2)\sigma$ region where B anomalies are addressed in concordance with the minimal EFT picture of Figure 11.5.

In the same plot, we also show a conservative estimate of the present LHC constraint on the mass of the LQ states considered, based on the dedicated collider study of ref. [458].

We conclude noting that from the point of view of realizing the economic EFT result in Figure 11.5, these leptoquark models should again be supplied by the combination of a singlet and a triplet $SU(2)_L$ muon/electron partners. Otherwise, in these models the leading contribution to $C_{\ell\ell}^{HL^{(1)}}$ would appear only at the loop level, in net distinction with the Z' scenario, where the Z-Z' mixing could be a priori exploited.

11.6 Summary

In this work we have revisited the analysis of $b \to s\ell\ell$ anomalies looking for NP solutions that generate these FCNC processes at one loop and do not involve any new source of flavour violation beyond the SM ones. To this end, we have performed a broad analysis with dimension-six operators in the SMEFT, combining the experimental data on B-physics with measurements of EWPO. The general outcome of our study is summarized in Figure 11.1 and, supported with Figure 11.3, shows that a resolution of B anomalies of the MFV nature can be made fully compatible with EW precision.

From the SMEFT results derived we have then proceeded to identifying a minimal EFT scenario as captured in Figure 11.5, that served as a simple guidance for SM UV completions. In this regard, we have explored in some detail the top-phillic and muon/electron-phillic Z', interesting for direct searches at collider as highlighted in Figure 11.6. We have also commented on the viable leptoquark scenarios, collected in Table 11.1. For both Z' and leptoquark solutions we have found that additional contributions were necessary in order to maintain Z coupling measurements under control: in particular, we have shown that a correlated pair of vector-like leptons, a $SU(2)_L$ singlet and a triplet, can realize the minimal EFT scenario depicted on Figure 11.5. We observe that the existence of these particles may be independently motivated by the heavy new dynamics underlying the origin of neutrino masses and/or by a tentative explanation of the $(g-2)_\mu$ anomaly [449].

We conclude by noting that the measurement of B decays at the scale of a few GeV is expected to reach a precision regime with the completion of the future runs at LHC and SuperKEKB. Hence, better measurements of the LUV observables and angular distributions of $b \to s\ell\ell$ will be available in the next few years from Belle II [365] and LHCb [459]. These will add a fundamental verification of the current interpretation of B anomalies and of the direction in our search for NP signatures. Along these lines, should these signals of LUV persist, their interplay with EW precision measurements could be further tested at future e^+e^- colliders. In particular, circular e^+e^- colliders running at the Z pole, such as the FCC-ee [460, 461] or CEPC [116], could test deviations in the lepton universality of neutral weak currents with more than one order of magnitude improvement in precision compared to current data. At linear colliders, like the ILC [113]

or CLIC [118], where there is no proposed run at the Z pole, it would still be possible to obtain a significant improvement in the measurements of EWPO via radiative return to the Z [462]. Furthermore, the high-energy regime achievable at linear colliders would allow, after crossing the $t\bar{t}$ threshold, to directly test the effects of the interactions $O_{1133}^{Lu,eu}$ via $e^+e^- \to t\bar{t}$. For the muon case, on the other hand, to test $O_{2233}^{Lu,eu}$ one would still need to rely on more complicated signals, such as $t\bar{t}\mu^+\mu^-$, which would be in any case cleaner than at the LHC. (However, ideal optimal tests of these 4-fermion operators in 2-to-2 scattering processes would require a high-energy muon collider.) All of these could represent valuable additions from a "flavour" perspective in the interpretation of EW (and Higgs) measurements at these future machines within the EFT framework [211, 420].

11.7 Discussions on EW fits

Here we revisit the constraints set by EWPO on the parameter space of the SMEFT. We make minimal flavour assumptions and include all quark and lepton operators described in the **EW** fit presented in section 11.3. Measurements of EWPO have been extensively studied in the literature [314, 315, 317, 319, 406, 463–468] within the SMEFT framework. The purpose here is to provide further details on the correlation between quark and lepton sectors constrained by EWPO, illustrating some of the effects when going beyond the tree-level analysis.

The experimental inputs are the same considered for the **EW** fit in section 11.3, and include, in particular, the full set measurements taken at LEP/SLD at the Z pole, as well as the measurements of the W boson obtained at LEP II, the Tevatron and the LHC (e.g. mass, width, branching ratios as well as the determination of $|V_{tb}|$ at the LHC [14]). For these fits we use the `HEPfit`package [424] as for the rest of the work.

We first consider the case of the **EW** fit at the tree level. In this case, the results of the fit reveal that while there is sizable correlation between the left-handed leptonic operators, as well as between the different quark operators, both sector are however decoupled to a good extent in the fit as can be seen from Figure 11.8.

For the main fits presented in section 11.4, however, we also consider the leading logarithmically enhanced contributions at one-loop level via RG running. For our purposes, and considering the size of the bounds on the different operators from the EW fit, the most important contribution comes from $C_{33}^{HQ^{(1)}}$. This induces an universal contribution that propagates into all EWPO. As a result of this, and similar to what was seen between

[14] The extraction of $|V_{tb}|$ could be, a priori, affected by other SMEFT effects entering in single-top production, e.g. 4-fermion operators. Such effects are neglected in our analysis. The only effect of this input in the EW fits in this paper is to lift a flat direction that would otherwise appear between $C_{33}^{HQ^{(1)}}$ and $C_{33}^{HQ^{(3)}}$, had we excluded this measurement. Even with this input, these two coefficients are nearly 100% correlated, as can be seen in Figure 11.8.

the leptonic operators and the 4-fermion operators due to their interplay in eqs. (11.7), a non-trivial pattern of correlations between the lepton and quark operator sectors in the **EW** fit arises, as shown in Figure 11.2. Similar to the change in the bounds on the leptonic operators in the **EW+Flavour** fit once we included the RG effects of the four-fermion operators, the bounds on the leptonic operators also relax in the EW fit once we include the RG effects from $C_{33}^{HQ^{(1)}}$. This is shown in Figure 11.9. However, unlike in the **EW+Flavour** fit, such effects do not induce a significant shift in the central values of the Wilson coefficients, which is simply due to the fact that the data selects $C_{33}^{HQ^{(1)}}$ to be centered around zero.

As can be seen in Figure 11.9, the relaxation of the bounds can be in some cases rather dramatic, which brings about the question of what could be the impact of further effects not included in our analysis. We estimated that including the main RG effects for all the other operators in the EW fit amounts to changes of at most $\sim 25\%$. One should also note that finite terms involving the Wilson coefficients of the quark coupling may become relevant at this point. As can be deduced from the full NLO results presented in [468], these are not expected to significantly change the picture. In any case, the overall conclusions on this paper regarding the reconciliation between EW data and B anomalies hold true.

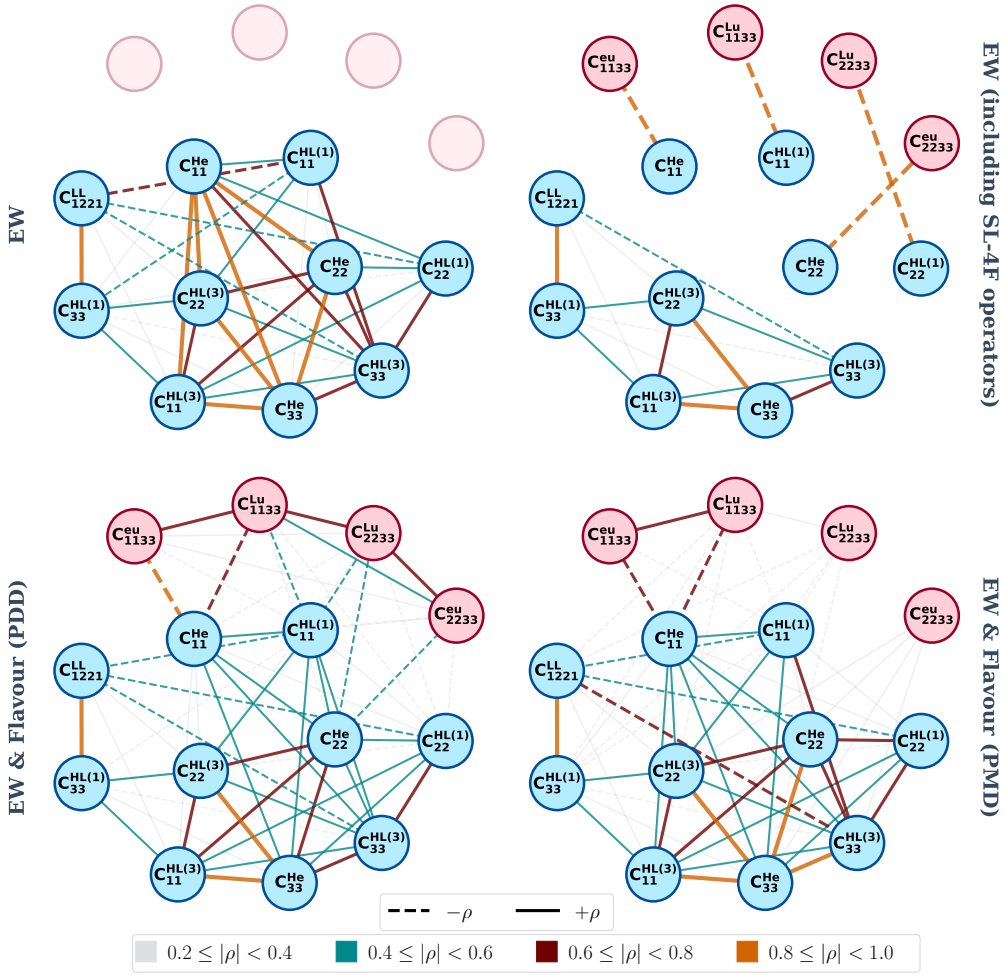

Figure 11.4. *Correlations among dimension-six operators involving leptonic currents in different scenarios. In the upper side we show the* ***EW*** *fit (upper-left panel), and the scenario where in the same setup the SL-4F operators are also included (upper-right panel), highlighting the anti-correlation among the set of Wilson coefficients* $C_{\ell\ell}^{HL^{(1)}}$, $C_{\ell\ell}^{He}$ *and* $C_{\ell\ell 33}^{Lu,eu}$. *In the lower-side panels we show how* $b \to s\ell\ell$ *measurements break these degeneracies, showing the* ***Flavour*** *fit for the PDD case (lower-left panel), and the PMD one (lower-right panel).*

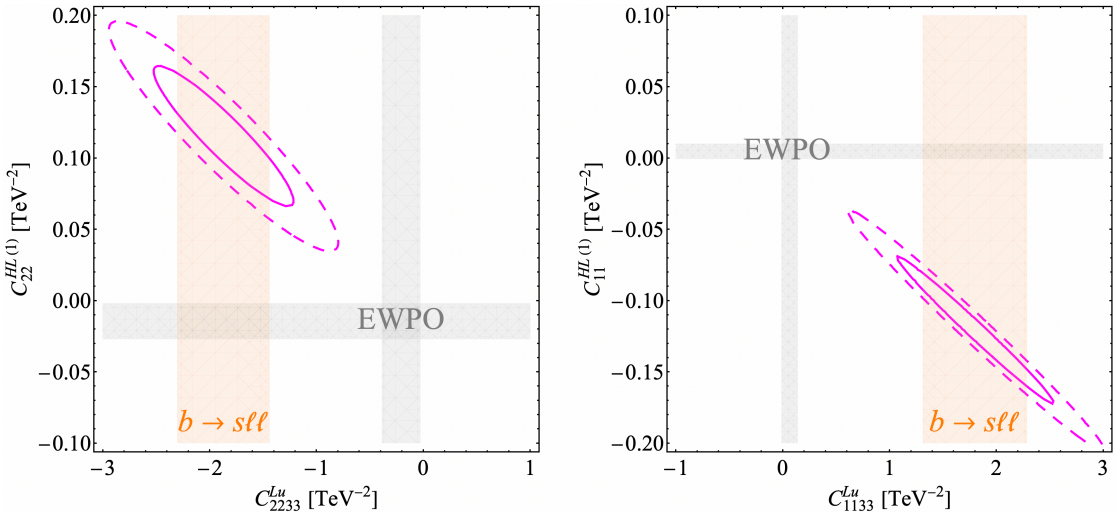

Figure 11.5. *The most economic EFT picture where B anomalies can be reconciled at one loop with EWPO. In (dashed) magenta the 1(2)σ correlation between the Wilson coefficients of the operators responsible of addressing B anomalies without any source of flavour violation beyond the Yukawa couplings of the SM. The minimal scenario involves LUV effects in the (electron) muon sector as highlighted by the 1σ orange band in the (right) left panel, originated from* $b \to s\ell\ell$ *data analyzed with a conservative approach to hadronic uncertainties. In same figure, the 1σ region allowed by EWPO within a single-operator analysis, horizontal and vertical grey bands.*

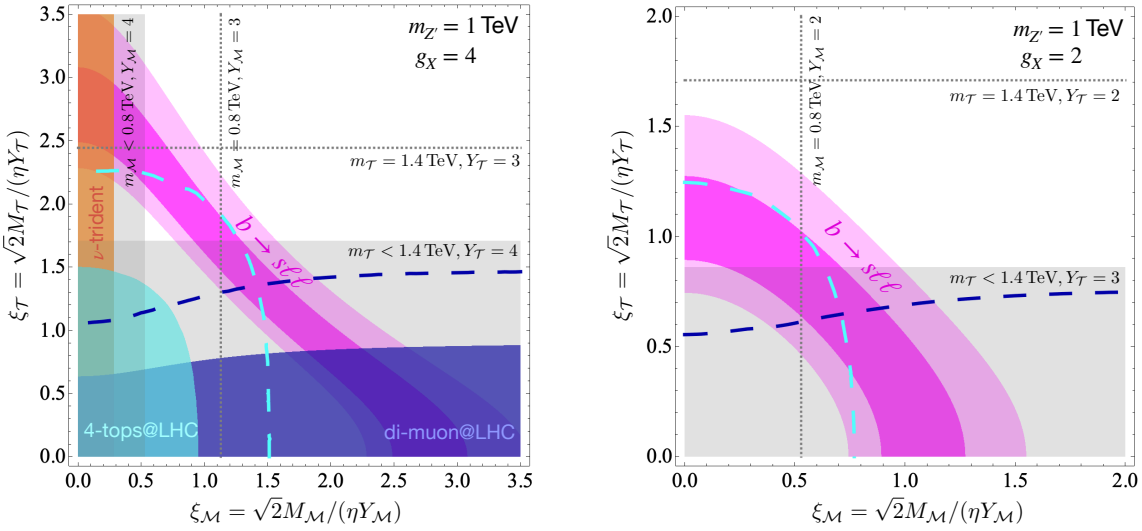

Figure 11.6. *68% (95%) probability region in (lighter) magenta for the minimal Z' model that addresses B anomalies in the parameter space identified by eq. (11.18), with $\eta = m_{Z'}/4$ (left panel), and $\eta = m_{Z'}/2$ (right panel), for $m_{Z'} = 1$ TeV. Relevant LHC constraints are reported in blue and cyan regions according to the analysis originally performed in ref. [402], together with the corresponding collider projections at 300 fb^{-1}. Finally, the gray regions underlie the parameter space where the mass of the vector-like partner lies below current collider limits for a fixed Yukawa coupling as explicitly reported, while dashed lines show the corresponding shift of the limit due to a smaller value of the same type of Yukawa coupling.*

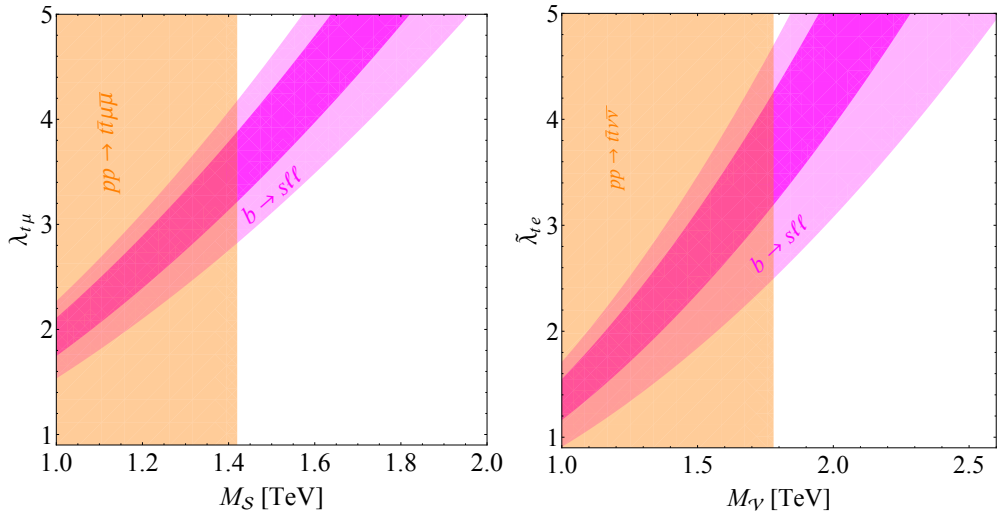

Figure 11.7. 68% (95%) probability region in magenta for the LQ candidates addressing $b \to s\ell\ell$ anomalies at one loop. The scalar (vector) LQ corresponds to a solution with LUV effects related to muon (electron) couplings. A conservative bound on the corresponding LQ mass is reported according to the analysis of ref. [458].

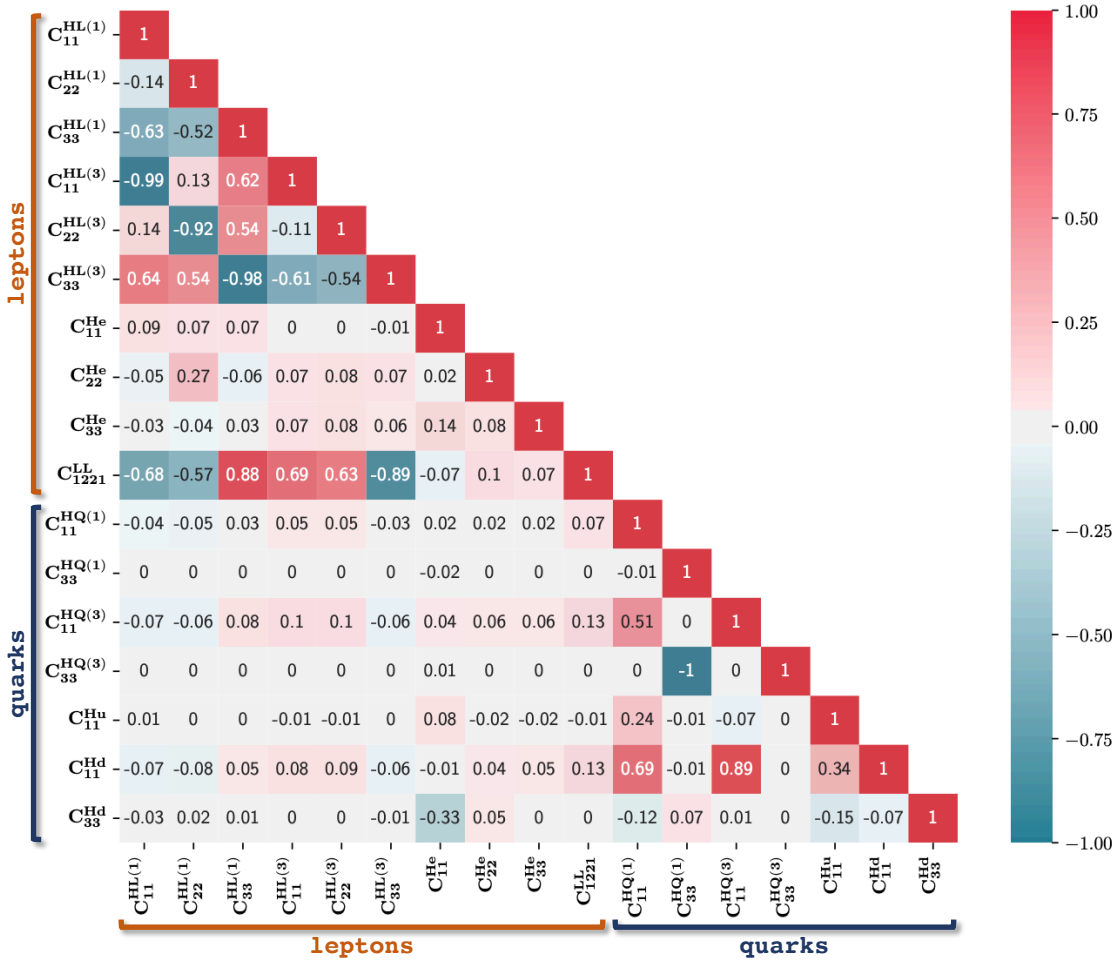

Figure 11.8. *The correlation matrix extracted from the SMEFT analysis of the set of independent operators in eqs. (11.2), (11.8), (11.9), including only their effects at tree-level. The two distinct groups of correlated Wilson coefficients associated to leptonic and quark interactions are remarked as "leptons" and "quarks", respectively. Note that, compared to Figure 11.2, in this tree-level analysis there is a significant decorrelation between the constraints on quarks and lepton operators.*

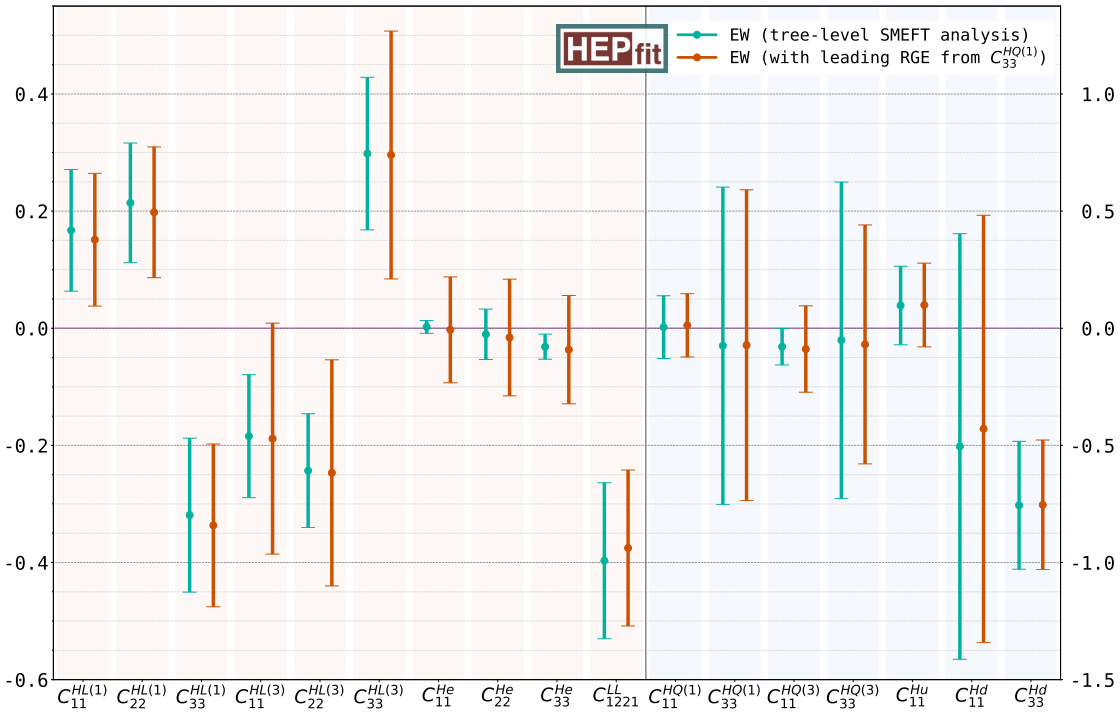

Figure 11.9. *Comparison of the mean and standard deviation of the marginalized posterior for the Wilson coefficients (in TeV^{-2}) of the operators included in the* **EW** *fit under two different approximations: in green the results from a pure tree-level analysis; in orange we show the result including the dominant log-enhanced one-loop terms. See text for details.*

A Details of Zh calculation

A.1 Orthogonal Projectors in $gg \to ZH$

In this appendix I present the explicit expressions of the projectors $\mathcal{P}_i^{\mu\nu\rho}$ appearing in eq.(6.2). The projectors are all normalized to 1. They are:

$$\begin{aligned}
\mathcal{P}_1^{\mu\nu\rho} &= \frac{m_Z}{\sqrt{2}s'p_T^2}\Big[p_1^\nu\epsilon^{\mu\rho p_1 p_2} - p_2^\mu\epsilon^{\nu\rho p_1 p_2} + q_t^\mu\epsilon^{\nu\rho p_2 p_3} && \text{(A.1)}\\
&+ q_u^\nu\epsilon^{\mu\rho p_1 p_3} + s'\epsilon^{\mu\nu\rho p_2} - s'\epsilon^{\mu\nu\rho p_1}\Big], && \text{(A.2)}\\
\mathcal{P}_2^{\mu\nu\rho} &= \frac{1}{\sqrt{2}s'p_T}\Big[q_u^\nu\epsilon^{\mu\rho p_1 p_3} + q_t^\mu\epsilon^{\nu\rho p_2 p_3}\Big], && \text{(A.3)}\\
\mathcal{P}_3^{\mu\nu\rho} &= \frac{\sqrt{3}}{2s'p_T}\Big[s'\epsilon^{\mu\nu\rho p_1} + s'\epsilon^{\mu\nu\rho p_2} - p_1^\nu\epsilon^{\mu\rho p_1 p_2} - p_2^\mu\epsilon^{\nu\rho p_1 p_2}\\
&+ (q_u^\nu\epsilon^{\mu\rho p_1 p_3} - q_t^\mu\epsilon^{\nu\rho p_2 p_3})\left(\frac{1}{3} + \frac{m_Z^2}{p_T^2}\right)\\
&+ \frac{m_Z^2}{p_T^2}(q_t^\mu\epsilon^{\nu\rho p_2 p_1} - q_u^\nu\epsilon^{\mu\rho p_1 p_2})\Big], && \text{(A.4)}\\
\mathcal{P}_4^{\mu\nu\rho} &= \frac{m_Z}{\sqrt{2}s'p_T^2}\Big[q_t^\mu(\epsilon^{\nu\rho p_2 p_1} - \epsilon^{\nu\rho p_2 p_3}) - q_u^\nu(\epsilon^{\mu\rho p_1 p_2} - \epsilon^{\mu\rho p_1 p_3})\Big], && \text{(A.5)}\\
\mathcal{P}_5^{\mu\nu\rho} &= \frac{1}{\sqrt{6}s'p_T}\Big[q_t^\mu\epsilon^{\nu\rho p_2 p_3} - q_u^\nu\epsilon^{\mu\rho p_1 p_3}\Big], && \text{(A.6)}\\
\mathcal{P}_6^{\mu\nu\rho} &= \frac{1}{s'p_T}\Big[g^{\mu\nu}\epsilon^{\rho p_1 p_2 p_3} + s'\epsilon^{\mu\nu\rho p_3} + p_1^\nu\epsilon^{\mu\rho p_2 p_3} - p_2^\mu\epsilon^{\nu\rho p_1 p_3} - \frac{s'}{2}\epsilon^{\mu\nu\rho p_2}\\
&+ \frac{1}{2}\left(p_1^\nu\epsilon^{\mu\rho p_1 p_2} + p_2^\mu\epsilon^{\nu\rho p_1 p_2} + q_u^\nu\epsilon^{\mu\rho p_1 p_3} - q_t^\mu\epsilon^{\nu\rho p_2 p_3} - s'\epsilon^{\mu\nu\rho p_1}\right)\\
&+ \frac{m_Z^2}{2p_T^2}(q_t^\mu\epsilon^{\nu\rho p_2 p_1} - q_u^\nu\epsilon^{\mu\rho p_1 p_2} + q_u^\nu\epsilon^{\mu\rho p_1 p_3} - q_t^\mu\epsilon^{\nu\rho p_2 p_3})\Big], && \text{(A.7)}
\end{aligned}$$

where we defined $q_t^\mu = (p_3^\mu - \frac{t'}{s'}p_2^\mu)$ and $q_u^\nu = (p_3^\nu - \frac{u'}{s'}p_1^\nu)$ and we used the shorthand notation $\epsilon^{\mu\nu\rho p_2} \equiv \epsilon^{\mu\nu\rho\sigma}p_{2\sigma}$.

Using these projectors we obtained the relations between the form factors $\mathcal{A}_i$ defined

in in eq.(6.2) and those defined in section 2 of ref.[138]:

$$\mathcal{A}_1 = \frac{p_T^2}{2\sqrt{2}m_Z(p_T^2+m_Z^2)}\Big[(t'+u')F_{12}^+ - (t'-u')F_{12}^-\Big], \tag{A.8}$$

$$\begin{aligned}\mathcal{A}_2 = &-\frac{p_T}{2\sqrt{2}(p_T^2+m_Z^2)}\Big[(t'+u')F_{12}^+ - (t'-u')F_{12}^- \\ &- \frac{p_T^2+m_Z^2}{2s'}((t'+u')F_3^+ - (t'-u')F_3^-)\Big],\end{aligned} \tag{A.9}$$

$$\begin{aligned}\mathcal{A}_3 = &\frac{p_T}{2\sqrt{3}(p_T^2+m_Z^2)}\Big[(t'+u')F_{12}^- - (t'-u')F_{12}^+ \\ &+ (p_T^2+m_Z^2)(F_2^- + F_4)\Big],\end{aligned} \tag{A.10}$$

$$\begin{aligned}\mathcal{A}_4 = &-\frac{m_Z}{2\sqrt{2}(p_T^2+m_Z^2)}\Big[(t'+u')F_{12}^- - (t'-u')F_{12}^+ \\ &+ (p_T^2+m_Z^2)\left((1-\frac{p_T^2}{m_Z^2})F_2^- + 2F_4\right)\Big],\end{aligned} \tag{A.11}$$

$$\begin{aligned}\mathcal{A}_5 = &\frac{p_T}{2\sqrt{6}(p_T^2+m_Z^2)}\Big[(t'+u')F_{12}^- - (t'-u')F_{12}^+ \\ &+ (p_T^2+m_Z^2)\left(4(F_2^- + F_4) + \frac{3}{2s'}\left((t'+u')F_3^- - (t'-u')F_3^+\right)\right)\Big],\end{aligned} \tag{A.12}$$

$$\mathcal{A}_6 = \frac{p_T}{2}F_4. \tag{A.13}$$

A.2 Two-loop Results

The NLO amplitude can be written in terms of three contributions, namely the two-loop 1PI triangle, the two-loop 1PI box and the reducible double-triangle diagrams,

$$\mathcal{A}_i^{(1)} = \mathcal{A}_i^{(1,\triangle)} + \mathcal{A}_i^{(1,\square)} + \mathcal{A}_i^{(1,\bowtie)}\ . \tag{A.14}$$

In this section, the exact analytic results for the triangle and double triangle topologies are presented.

The two-loop triangle results are

$$\mathcal{A}_1^{(1,\triangle)} = \frac{p_T^2\ (\hat{s}-\Delta_m)}{4\sqrt{2}m_Z}\frac{\mathcal{K}_t^{(2l)}}{(p_T^2+m_Z^2)}, \tag{A.15}$$

$$\mathcal{A}_2^{(1,\triangle)} = -\frac{p_T\ (\hat{s}-\Delta_m)}{4\sqrt{2}}\frac{\mathcal{K}_t^{(2l)}}{(p_T^2+m_Z^2)}, \tag{A.16}$$

$$\mathcal{A}_3^{(1,\triangle)} = \frac{p_T\ (\hat{t}-\hat{u})}{4\sqrt{3}}\frac{\mathcal{K}_t^{(2l)}}{(p_T^2+m_Z^2)}, \tag{A.17}$$

$$\mathcal{A}_4^{(1,\triangle)} = -\frac{m_Z\ (\hat{t}-\hat{u})}{4\sqrt{2}}\frac{\mathcal{K}_t^{(2l)}}{(p_T^2+m_Z^2)}, \tag{A.18}$$

$$\mathcal{A}_5^{(1,\triangle)} = -\frac{p_T\ (\hat{t}-\hat{u})}{4\sqrt{6}}\frac{\mathcal{K}_t^{(2l)}}{(p_T^2+m_Z^2)}, \tag{A.19}$$

$$\mathcal{A}_6^{(1,\triangle)} = 0, \tag{A.20}$$

where the $\mathcal{K}_t^{(2l)}$ function is defined in eq.(4.11) of ref.[147]. While the double-triangle for-factors are found to be.

$$\mathcal{A}_1^{(1,\bowtie)} = -\frac{m_t^2 p_T^2}{4\sqrt{2}\ m_Z\left(m_Z^2+p_T^2\right)^2}\left[F_t(\hat{t})\left(G_t(\hat{t},\hat{u})-G_b(\hat{t},\hat{u})\right)+(\hat{t}\leftrightarrow\hat{u})\right], \tag{A.21}$$

$$\mathcal{A}_2^{(1,\bowtie)} = \frac{m_t^2 p_T}{4\sqrt{2}\left(m_Z^2+p_T^2\right)^2}\left[F_t(\hat{t})\left(G_t(\hat{t},\hat{u})-G_b(\hat{t},\hat{u})\right)+(\hat{t}\leftrightarrow\hat{u})\right], \tag{A.22}$$

$$\mathcal{A}_3^{(1,\bowtie)} = \frac{m_t^2 p_T}{4\sqrt{3}\ \hat{s}\left(m_Z^2+p_T^2\right)^2}\left[\left(m_h^2-\hat{t}\right)F_t(\hat{t})\left(G_t(\hat{t},\hat{u})-G_b(\hat{t},\hat{u})\right)-(\hat{t}\leftrightarrow\hat{u})\right], \tag{A.23}$$

$$\mathcal{A}_4^{(1,\bowtie)} = -\frac{m_t^2}{4\sqrt{2}\ m_Z\hat{s}^2\left(m_Z^2+p_T^2\right)^2}\Big[\Big(m_Z^2\left(m_h^2-\hat{t}\right)^2 - \hat{t}\left(m_Z^2-\hat{u}\right)^2\Big)F_t(\hat{t})\left(G_t(\hat{t},\hat{u})-G_b(\hat{t},\hat{u})\right)-(\hat{t}\leftrightarrow\hat{u})\Big], \tag{A.24}$$

$$\mathcal{A}_5^{(1,\bowtie)} = -\frac{m_t^2 p_T}{4\sqrt{6}\ \hat{s}\left(m_Z^2+p_T^2\right)^2}\Big[\left(4m_Z^2-\hat{s}-4\hat{u}\right)F_t(\hat{t})\left(G_t(\hat{t},\hat{u})-G_b(\hat{t},\hat{u})\right) - (\hat{t}\leftrightarrow\hat{u})\Big], \tag{A.25}$$

$$\mathcal{A}_6^{(1,\bowtie)} = 0, \tag{A.26}$$

where

$$\begin{aligned} F_t(\hat{t}) &= \frac{1}{\left(m_h^2-\hat{t}\right)^2}\Bigg[2\hat{t}\Big(B_0\left(\hat{t},m_t^2,m_t^2\right)-B_0\left(m_h^2,m_t^2,m_t^2\right)\Big) \\ &+ \left(m_h^2-\hat{t}\right)\left(\left(m_h^2-4m_t^2-\hat{t}\right)C_0\left(0,m_h^2,\hat{t},m_t^2,m_t^2,m_t^2\right)-2\right)\Bigg], \end{aligned} \tag{A.27}$$

$$\begin{aligned} G_x(\hat{t},\hat{u}) &= \left(m_Z^2-\hat{u}\right)\Bigg[m_Z^2\Big(B_0\left(\hat{t},m_x^2,m_x^2\right)-B_0\left(m_Z^2,m_x^2,m_x^2\right)\Big) \\ &+ \left(\hat{t}-m_Z^2\right)\left(2m_x^2C_0\left(0,\hat{t},m_Z^2,m_x^2,m_x^2,m_x^2\right)+1\right)\Bigg]. \end{aligned} \tag{A.28}$$

Bibliography

[1] R. A. Minlos, *Introduction to mathematical statistical physics*. No. 19. American Mathematical Soc., 2000.

[2] M. Gell-Mann, "The eightfold way: A theory of strong interaction symmetry,". https://www.osti.gov/biblio/4008239.

[3] C. N. Yang and R. L. Mills, "Conservation of isotopic spin and isotopic gauge invariance," *Phys. Rev.* **96** (Oct, 1954) 191–195. https://link.aps.org/doi/10.1103/PhysRev.96.191.

[4] **Particle Data Group** Collaboration, P. Zyla *et al.*, "Review of Particle Physics," *PTEP* **2020** no. 8, (2020) 083C01.

[5] D. S. Freed, "Lectures on topological quantum field theory," 1993.

[6] R. Dijkgraaf and E. Witten, "Topological gauge theories and group cohomology," *Communications in Mathematical Physics* **129** no. 2, (1990) 393–429.

[7] A. Salam and J. C. Ward, "On a gauge theory of elementary interactions," *Il Nuovo Cimento (1955-1965)* **19** no. 1, (1961) 165–170. https://doi.org/10.1007/BF02812723.

[8] A. Salam and J. C. Ward, "Weak and electromagnetic interactions," *Il Nuovo Cimento (1955-1965)* **11** no. 4, (1959) 568–577. https://doi.org/10.1007/BF02726525.

[9] S. Weinberg, "A model of leptons," *Phys. Rev. Lett.* **19** (Nov, 1967) 1264–1266. https://link.aps.org/doi/10.1103/PhysRevLett.19.1264.

[10] F. Capozzi, E. Lisi, A. Marrone, D. Montanino, and A. Palazzo, "Neutrino masses and mixings: Status of known and unknown 3ν parameters," *Nucl. Phys. B* **908** (2016) 218–234, arXiv:1601.07777 [hep-ph].

[11] **ALEPH, DELPHI, L3, OPAL, SLD, LEP Electroweak Working Group, SLD Electroweak Group, SLD Heavy Flavour Group** Collaboration, S. Schael *et al.*, "Precision electroweak measurements on the Z resonance," *Phys. Rept.* **427** (2006) 257–454, arXiv:hep-ex/0509008.

[12] **SLD** Collaboration, K. Abe *et al.*, "First direct measurement of the parity violating coupling of the Z0 to the s quark," *Phys. Rev. Lett.* **85** (2000) 5059–5063, arXiv:hep-ex/0006019.

[13] **CDF, D0** Collaboration, T. E. W. Group, "2012 Update of the Combination of CDF and D0 Results for the Mass of the W Boson," arXiv:1204.0042 [hep-ex].

[14] **ALEPH, DELPHI, L3, OPAL, LEP Electroweak** Collaboration, S. Schael *et al.*, "Electroweak Measurements in Electron-Positron Collisions at W-Boson-Pair Energies at LEP," *Phys. Rept.* **532** (2013) 119–244, arXiv:1302.3415 [hep-ex].

[15] **DØ** Collaboration, V. M. Abazov *et al.*, "Measurement of $\sin^2\theta^{\ell}_{\text{eff}}$ and Z-light quark couplings using the forward-backward charge asymmetry in $p\overline{p} \to Z/\gamma^* \to e^+e^-$ events with $\mathcal{L} = 5.0$ fb^{-1} at $\sqrt{s} = 1.96$ TeV," *Phys. Rev. D* **84** (2011) 012007, arXiv:1104.4590 [hep-ex].

[16] **CMS** Collaboration, V. Khachatryan *et al.*, "Measurement of the t-channel single-top-quark production cross section and of the $| V_{tb} |$ CKM matrix element in pp collisions at $\sqrt{s}$= 8 TeV," *JHEP* **06** (2014) 090, arXiv:1403.7366 [hep-ex].

[17] **ATLAS** Collaboration, M. Aaboud *et al.*, "Measurement of the W-boson mass in pp collisions at $\sqrt{s} = 7$ TeV with the ATLAS detector," *Eur. Phys. J. C* **78** no. 2, (2018) 110, arXiv:1701.07240 [hep-ex]. [Erratum: Eur.Phys.J.C 78, 898 (2018)].

[18] Y. Nambu, "Quasi-particles and gauge invariance in the theory of superconductivity," *Phys. Rev.* **117** (Feb, 1960) 648–663. https://link.aps.org/doi/10.1103/PhysRev.117.648.

[19] J. Goldstone, "Field theories with superconductor solutions," *Il Nuovo Cimento (1955-1965)* **19** no. 1, (1961) 154–164.

[20] J. Goldstone, A. Salam, and S. Weinberg, "Broken symmetries," *Phys. Rev.* **127** (Aug, 1962) 965–970. https://link.aps.org/doi/10.1103/PhysRev.127.965.

[21] P. W. Anderson, "Plasmons, gauge invariance, and mass," *Phys. Rev.* **130** (Apr, 1963) 439–442. https://link.aps.org/doi/10.1103/PhysRev.130.439.

[22] F. Englert and R. Brout, "Broken symmetry and the mass of gauge vector mesons," *Phys. Rev. Lett.* **13** (Aug, 1964) 321–323. https://link.aps.org/doi/10.1103/PhysRevLett.13.321.

[23] P. W. Higgs, "Broken symmetries and the masses of gauge bosons," *Phys. Rev. Lett.* **13** (Oct, 1964) 508–509. https://link.aps.org/doi/10.1103/PhysRevLett.13.508.

[24] G. S. Guralnik, C. R. Hagen, and T. W. B. Kibble, "Global conservation laws and massless particles," *Phys. Rev. Lett.* **13** (Nov, 1964) 585–587. https://link.aps.org/doi/10.1103/PhysRevLett.13.585.

[25] G. S. Guralnik, "The History of the Guralnik, Hagen and Kibble development of the Theory of Spontaneous Symmetry Breaking and Gauge Particles," *Int. J. Mod. Phys. A* **24** (2009) 2601–2627, arXiv:0907.3466 [physics.hist-ph].

[26] **CMS** Collaboration, S. Chatrchyan *et al.*, "Observation of a New Boson at a Mass of 125 GeV with the CMS Experiment at the LHC," *Phys. Lett. B* **716** (2012) 30–61, arXiv:1207.7235 [hep-ex].

[27] **ATLAS** Collaboration, G. Aad *et al.*, "Observation of a new particle in the search for the Standard Model Higgs boson with the ATLAS detector at the LHC," *Phys. Lett. B* **716** (2012) 1–29, arXiv:1207.7214 [hep-ex].

[28] N. Cabibbo, "Unitary symmetry and leptonic decays," *Phys. Rev. Lett.* **10** (Jun, 1963) 531–533. https://link.aps.org/doi/10.1103/PhysRevLett.10.531.

[29] M. Kobayashi and T. Maskawa, "CP-Violation in the Renormalizable Theory of Weak Interaction," *Progress of Theoretical Physics* **49** no. 2, (02, 1973) 652–657, https://academic.oup.com/ptp/article-pdf/49/2/652/5257692/49-2-652.pdf. https://doi.org/10.1143/PTP.49.652.

[30] R. E. Behrends, R. J. Finkelstein, and A. Sirlin, "Radiative corrections to decay processes," *Phys. Rev.* **101** (Jan, 1956) 866–873. https://link.aps.org/doi/10.1103/PhysRev.101.866.

[31] T. Kinoshita and A. Sirlin, "Radiative corrections to fermi interactions," *Phys. Rev.* **113** (Mar, 1959) 1652–1660. https://link.aps.org/doi/10.1103/PhysRev.113.1652.

[32] I. Mohammad and A. Donnachie, "Radiative Corrections to Radiative Muon Decay,".

[33] T. van Ritbergen and R. G. Stuart, "Complete 2-loop quantum electrodynamic contributions to the muon lifetime in the fermi model," *Phys. Rev. Lett.* **82** (Jan, 1999) 488–491. https://link.aps.org/doi/10.1103/PhysRevLett.82.488.

[34] D. Ross and M. Veltman, "Neutral currents and the higgs mechanism," *Nuclear Physics B* **95** no. 1, (1975) 135–147. https://www.sciencedirect.com/science/article/pii/055032137590485X.

[35] A. Djouadi, "The Anatomy of electro-weak symmetry breaking. I: The Higgs boson in the standard model," *Phys. Rept.* **457** (2008) 1–216, arXiv:hep-ph/0503172.

[36] M. J. Dugan, H. Georgi, and D. B. Kaplan, "Anatomy of a composite higgs model," *Nuclear Physics* **254** (1985) 299–326.

[37] C. T. Hill and E. H. Simmons, "Strong Dynamics and Electroweak Symmetry Breaking," *Phys. Rept.* **381** (2003) 235–402, arXiv:hep-ph/0203079. [Erratum: Phys.Rept. 390, 553–554 (2004)].

[38] M. Schwartz, *Quantum Field Theory and the Standard Model*. Quantum Field Theory and the Standard Model. Cambridge University Press, 2014. https://books.google.nl/books?id=HbdEAgAAQBAJ.

[39] M. Peskin and D. Schroeder, *An Introduction To Quantum Field Theory*. Frontiers in Physics. Avalon Publishing, 1995. https://books.google.de/books?id=EVeNNcslvX0C.

[40] M. Einhorn, D. Jones, and M. Veltman, "Heavy particles and the rho parameter in the standard model," *Nuclear Physics B* **191** no. 1, (1981) 146–172. https://www.sciencedirect.com/science/article/pii/0550321381902923.

[41] M. E. Peskin and T. Takeuchi, "New constraint on a strongly interacting higgs sector," *Phys. Rev. Lett.* **65** (Aug, 1990) 964–967. https://link.aps.org/doi/10.1103/PhysRevLett.65.964.

[42] M. E. Peskin and T. Takeuchi, "Estimation of oblique electroweak corrections," 1991.

[43] M. Golden and L. Randall, "Radiative corrections to electroweak parameters in technicolor theories," *Nuclear Physics B* **361** no. 1, (1991) 3–23. https://www.sciencedirect.com/science/article/pii/0550321391906144.

[44] B. Holdom and J. Terning, "Large corrections to electroweak parameters in technicolor theories," *Physics Letters B* **247** no. 1, (1990) 88–92. https://www.sciencedirect.com/science/article/pii/037026939091054F.

[45] G. Altarelli, R. Barbieri, and S. Jadach, "Toward a model-independent analysis of electroweak data," *Nuclear Physics B* **369** no. 1, (1992) 3–32. https://www.sciencedirect.com/science/article/pii/055032139290376M.

[46] R. S. Chivukula, S. B. Selipsky, and E. H. Simmons, "Nonoblique effects in the zbb^{-} vertex from extended technicolor dynamics," *Phys. Rev. Lett.* **69** (Jul, 1992) 575–577. https://link.aps.org/doi/10.1103/PhysRevLett.69.575.

[47] E. H. Simmons, R. S. Chivukula, and J. Terning, "Testing extended technicolor with R(b)," *Prog. Theor. Phys. Suppl.* **123** (1996) 87–96, arXiv:hep-ph/9509392.

[48] M. Cepeda *et al.*, "Report from Working Group 2: Higgs Physics at the HL-LHC and HE-LHC," *CERN Yellow Rep. Monogr.* **7** (2019) 221–584, arXiv:1902.00134 [hep-ph].

[49] **ATLAS** Collaboration, "A combination of measurements of Higgs boson production and decay using up to 139 fb^{-1} of proton–proton collision data at $\sqrt{s} = 13$ TeV collected with the ATLAS experiment," Tech. Rep. ATLAS-CONF-2020-027, 2020.

[50] **CMS** Collaboration, A. M. Sirunyan *et al.*, "Measurements of Higgs boson production cross sections and couplings in the diphoton decay channel at $\sqrt{s} =$ 13 TeV," *JHEP* **07** (2021) 027, arXiv:2103.06956 [hep-ex].

[51] **CMS Collaboration** Collaboration, "Sensitivity projections for Higgs boson properties measurements at the HL-LHC," tech. rep., CERN, Geneva, 2018. https://cds.cern.ch/record/2647699.

[52] **CMS** Collaboration, "Combined Higgs boson production and decay measurements with up to 137 fb-1 of proton-proton collision data at sqrts = 13 TeV," Tech. Rep. CMS-PAS-HIG-19-005, 2020.

[53] **CMS** Collaboration, "Measurement of Higgs boson production in association with a W or Z boson in the H $\to$ WW decay channel," Tech. Rep. CMS-PAS-HIG-19-017, 2021.

[54] B. Grzadkowski, M. Iskrzynski, M. Misiak, and J. Rosiek, "Dimension-Six Terms in the Standard Model Lagrangian," *JHEP* **10** (2010) 085, arXiv:1008.4884 [hep-ph].

[55] **ATLAS** Collaboration, G. Aad *et al.*, "Combined measurements of Higgs boson production and decay using up to 80 fb^{-1} of proton-proton collision data at $\sqrt{s} = 13$ TeV collected with the ATLAS experiment," *Phys. Rev. D* **101** no. 1, (2020) 012002, arXiv:1909.02845 [hep-ex].

[56] **CMS** Collaboration, A. M. Sirunyan *et al.*, "Combined measurements of Higgs boson couplings in proton–proton collisions at $\sqrt{s} = 13\,\text{TeV}$," *Eur. Phys. J. C* **79** no. 5, (2019) 421, arXiv:1809.10733 [hep-ex].

[57] J. F. Gunion, H. E. Haber, G. L. Kane, and S. Dawson, "The Higgs Hunter's Guide," *Front. Phys.* **80** (2000) 1–404.

[58] M. McCullough, "An Indirect Model-Dependent Probe of the Higgs Self-Coupling," *Phys. Rev. D* **90** no. 1, (2014) 015001, arXiv:1312.3322 [hep-ph]. [Erratum: Phys.Rev.D 92, 039903 (2015)].

[59] M. Gorbahn and U. Haisch, "Indirect probes of the trilinear Higgs coupling: $gg \to h$ and $h \to \gamma\gamma$," *JHEP* **10** (2016) 094, arXiv:1607.03773 [hep-ph].

[60] G. Degrassi, P. P. Giardino, F. Maltoni, and D. Pagani, "Probing the Higgs self coupling via single Higgs production at the LHC," *JHEP* **12** (2016) 080, arXiv:1607.04251 [hep-ph].

[61] W. Bizon, M. Gorbahn, U. Haisch, and G. Zanderighi, "Constraints on the trilinear Higgs coupling from vector boson fusion and associated Higgs production at the LHC," *JHEP* **07** (2017) 083, arXiv:1610.05771 [hep-ph].

[62] F. Maltoni, D. Pagani, A. Shivaji, and X. Zhao, "Trilinear Higgs coupling determination via single-Higgs differential measurements at the LHC," *Eur. Phys. J. C* **77** no. 12, (2017) 887, arXiv:1709.08649 [hep-ph].

[63] G. Degrassi and M. Vitti, "The effect of an anomalous Higgs trilinear self-coupling on the $h \to \gamma Z$ decay," *Eur. Phys. J. C* **80** no. 4, (2020) 307, arXiv:1912.06429 [hep-ph].

[64] G. Degrassi, B. Di Micco, P. P. Giardino, and E. Rossi, "Higgs boson self-coupling constraints from single Higgs, double Higgs and Electroweak measurements," *Phys. Lett. B* **817** (2021) 136307, arXiv:2102.07651 [hep-ph].

[65] U. Haisch and G. Koole, "Off-shell Higgs production at the LHC as a probe of the trilinear Higgs coupling," arXiv:2111.12589 [hep-ph].

[66] S. Di Vita, C. Grojean, G. Panico, M. Riembau, and T. Vantalon, "A global view on the Higgs self-coupling," *JHEP* **09** (2017) 069, arXiv:1704.01953 [hep-ph].

[67] **ATLAS** Collaboration, "Constraints on the Higgs boson self-coupling from the combination of single-Higgs and double-Higgs production analyses performed with the ATLAS experiment," Tech. Rep. ATLAS-CONF-2019-049, 2019.

[68] R. Frederix, D. Pagani, and M. Zaro, "Large NLO corrections in $t\bar{t}W^{\pm}$ and $t\bar{t}t\bar{t}$ hadroproduction from supposedly subleading EW contributions," *JHEP* **02** (2018) 031, arXiv:1711.02116 [hep-ph].

[69] **CMS** Collaboration, A. M. Sirunyan *et al.*, "Search for the production of four top quarks in the single-lepton and opposite-sign dilepton final states in proton-proton collisions at $\sqrt{s} = 13$ TeV," *JHEP* **11** (2019) 082, arXiv:1906.02805 [hep-ex].

[70] **ATLAS** Collaboration, G. Aad *et al.*, "Evidence for $t\bar{t}t\bar{t}$ production in the multilepton final state in proton–proton collisions at $\sqrt{s} = 13$ TeV with the ATLAS detector," *Eur. Phys. J. C* **80** no. 11, (2020) 1085, arXiv:2007.14858 [hep-ex].

[71] **CMS** Collaboration, A. M. Sirunyan *et al.*, "Measurement of the cross section for $\mathrm{t\bar{t}}$ production with additional jets and b jets in pp collisions at $\sqrt{s} = 13$ TeV," *JHEP* **07** (2020) 125, arXiv:2003.06467 [hep-ex].

[72] **ATLAS** Collaboration, "Measurements of fiducial and differential cross-sections of $t\bar{t}$ production with additional heavy-flavour jets in proton-proton collisions at $\sqrt{s} = 13$ TeV with the ATLAS detector," Tech. Rep. ATLAS-CONF-2018-029, 2018.

[73] J. D'Hondt, A. Mariotti, K. Mimasu, S. Moortgat, and C. Zhang, "Learning to pinpoint effective operators at the LHC: a study of the $\mathrm{t\bar{t}b\bar{b}}$ signature," *JHEP* **11** (2018) 131, arXiv:1807.02130 [hep-ph].

[74] N. P. Hartland, F. Maltoni, E. R. Nocera, J. Rojo, E. Slade, E. Vryonidou, and C. Zhang, "A Monte Carlo global analysis of the Standard Model Effective Field Theory: the top quark sector," *JHEP* **04** (2019) 100, arXiv:1901.05965 [hep-ph].

[75] C. Degrande, G. Durieux, F. Maltoni, K. Mimasu, E. Vryonidou, and C. Zhang, "Automated one-loop computations in the standard model effective field theory," *Phys. Rev. D* **103** no. 9, (2021) 096024, arXiv:2008.11743 [hep-ph].

[76] J. de Blas, M. Chala, and J. Santiago, "Renormalization Group Constraints on New Top Interactions from Electroweak Precision Data," *JHEP* **09** (2015) 189, arXiv:1507.00757 [hep-ph].

[77] **SMEFiT** Collaboration, J. J. Ethier, G. Magni, F. Maltoni, L. Mantani, E. R. Nocera, J. Rojo, E. Slade, E. Vryonidou, and C. Zhang, "Combined SMEFT interpretation of Higgs, diboson, and top quark data from the LHC," *JHEP* **11** (2021) 089, arXiv:2105.00006 [hep-ph].

[78] H. Patel, "Package-X: A Mathematica package for the analytic calculation of one-loop integrals," *Comput. Phys. Commun.* **197** (2015) 276–290, arXiv:1503.01469 [hep-ph].

[79] P. Maierhöfer, J. Usovitsch, and P. Uwer, "Kira—A Feynman integral reduction program," *Comput. Phys. Commun.* **230** (2018) 99–112, arXiv:1705.05610 [hep-ph].

[80] A. Smirnov, "Algorithm FIRE – Feynman Integral REduction," *JHEP* **10** (2008) 107, arXiv:0807.3243 [hep-ph].

[81] A. Alloul, N. D. Christensen, C. Degrande, C. Duhr, and B. Fuks, "FeynRules 2.0 - A complete toolbox for tree-level phenomenology," *Comput. Phys. Commun.* **185** (2014) 2250–2300, arXiv:1310.1921 [hep-ph].

[82] T. Hahn, "Generating Feynman diagrams and amplitudes with FeynArts 3," *Comput. Phys. Commun.* **140** (2001) 418–431, arXiv:hep-ph/0012260.

[83] A. Dedes, W. Materkowska, M. Paraskevas, J. Rosiek, and K. Suxho, "Feynman rules for the Standard Model Effective Field Theory in R_ξ -gauges," *JHEP* **06** (2017) 143, arXiv:1704.03888 [hep-ph].

[84] S. Dawson and P. P. Giardino, "Higgs decays to ZZ and $Z\gamma$ in the standard model effective field theory: An NLO analysis," *Phys. Rev. D* **97** no. 9, (2018) 093003, arXiv:1801.01136 [hep-ph].

[85] E. E. Jenkins, A. V. Manohar, and M. Trott, "Renormalization Group Evolution of the Standard Model Dimension Six Operators I: Formalism and lambda Dependence," *JHEP* **10** (2013) 087, arXiv:1308.2627 [hep-ph].

[86] E. E. Jenkins, A. V. Manohar, and M. Trott, "Renormalization Group Evolution of the Standard Model Dimension Six Operators II: Yukawa Dependence," *JHEP* **01** (2014) 035, arXiv:1310.4838 [hep-ph].

[87] R. Gauld, B. D. Pecjak, and D. J. Scott, "One-loop corrections to $h \to b\bar{b}$ and $h \to \tau\overline{\tau}$ decays in the Standard Model Dimension-6 EFT: four-fermion operators and the large-m_t limit," *JHEP* **05** (2016) 080, arXiv:1512.02508 [hep-ph].

[88] J. Alwall, R. Frederix, S. Frixione, V. Hirschi, F. Maltoni, O. Mattelaer, H. S. Shao, T. Stelzer, P. Torrielli, and M. Zaro, "The automated computation of tree-level and next-to-leading order differential cross sections, and their matching to parton shower simulations," *JHEP* **07** (2014) 079, arXiv:1405.0301 [hep-ph].

[89] G. Ossola, C. G. Papadopoulos, and R. Pittau, "Reducing full one-loop amplitudes to scalar integrals at the integrand level," *Nucl. Phys. B* **763** (2007) 147–169, arXiv:hep-ph/0609007.

[90] G. Ossola, C. G. Papadopoulos, and R. Pittau, "CutTools: A Program implementing the OPP reduction method to compute one-loop amplitudes," *JHEP* **03** (2008) 042, arXiv:0711.3596 [hep-ph].

[91] G. Ossola, C. G. Papadopoulos, and R. Pittau, "On the Rational Terms of the one-loop amplitudes," *JHEP* **05** (2008) 004, arXiv:0802.1876 [hep-ph].

[92] R. Alonso, E. E. Jenkins, A. V. Manohar, and M. Trott, "Renormalization Group Evolution of the Standard Model Dimension Six Operators III: Gauge Coupling Dependence and Phenomenology," *JHEP* **04** (2014) 159, arXiv:1312.2014 [hep-ph].

[93] R. D. Ball *et al.*, "Parton distributions with LHC data," *Nucl. Phys. B* **867** (2013) 244–289, arXiv:1207.1303 [hep-ph].

[94] J. Salvatier, T. V. Wiecki, and C. Fonnesbeck, "Probabilistic programming in python using PyMC3," *PeerJ Computer Science* **2** (Apr, 2016) e55. https://doi.org/10.7717/peerj-cs.55.

[95] R. Kumar, C. Carroll, A. Hartikainen, and O. Martin, "Arviz a unified library for exploratory analysis of bayesian models in python," *Journal of Open Source Software* **4** no. 33, (2019) 1143. https://doi.org/10.21105/joss.01143.

[96] F. James and M. Roos, "Minuit: A System for Function Minimization and Analysis of the Parameter Errors and Correlations," *Comput. Phys. Commun.* **10** (1975) 343–367.

[97] H. Dembinski and P. O. et al., "scikit-hep/iminuit,". https://doi.org/10.5281/zenodo.3949207.

[98] D. Foreman-Mackey, "corner.py: Scatterplot matrices in python," *The Journal of Open Source Software* **1** no. 2, (Jun, 2016) 24. https://doi.org/10.21105/joss.00024.

[99] S. Bocquet and F. W. Carter, "pygtc: beautiful parameter covariance plots (aka. giant triangle confusograms)," *The Journal of Open Source Software* **1** no. 6, (Oct, 2016) . http://dx.doi.org/10.21105/joss.00046.

[100] P. Zivich, "pzivich/Python-for-Epidemiologists: Updates for v0.8.0," July, 2019. https://doi.org/10.5281/zenodo.3339870.

[101] https://github.com/alasfar-lina/trilinear4tops.

[102] J. Ellis, M. Madigan, K. Mimasu, V. Sanz, and T. You, "Top, Higgs, Diboson and Electroweak Fit to the Standard Model Effective Field Theory," *JHEP* **04** (2021) 279, arXiv:2012.02779 [hep-ph].

[103] I. Brivio, S. Bruggisser, F. Maltoni, R. Moutafis, T. Plehn, E. Vryonidou, S. Westhoff, and C. Zhang, "O new physics, where art thou? A global search in the top sector," *JHEP* **02** (2020) 131, arXiv:1910.03606 [hep-ph].

[104] C. Zhang, "Constraining *qqtt* operators from four-top production: a case for enhanced EFT sensitivity," *Chin. Phys. C* **42** no. 2, (2018) 023104, arXiv:1708.05928 [hep-ph].

[105] **ATLAS** Collaboration, "Search for Higgs boson pair production in the two bottom quarks plus two photons final state in pp collisions at $\sqrt{s} = 13$ TeV with the ATLAS detector," Tech. Rep. ATLAS-CONF-2021-016, 2021.

[106] L. Di Luzio, R. Gröber, and M. Spannowsky, "Maxi-sizing the trilinear Higgs self-coupling: how large could it be?," *Eur. Phys. J. C* **77** no. 11, (2017) 788, arXiv:1704.02311 [hep-ph].

[107] L. Alasfar, R. Gröber, C. Grojean, A. Paul, and Z. Qian, "Machine learning augmented probes of light-quark Yukawa and trilinear couplings from Higgs pair production," *In preparation* (2021) .

[108] "Guidelines for extrapolation of cms and atlas lhc/hl-lhc couplings projections to he-lhc." https://twiki.cern.ch/twiki/bin/view/LHCPhysics/GuidelinesCouplingProjections2018#Details%20of%20the%20CMS%20projections.

[109] J. Alison *et al.*, "Higgs boson potential at colliders: Status and perspectives," *Rev. Phys.* **5** (2020) 100045, arXiv:1910.00012 [hep-ph].

[110] **CMS** Collaboration, "Prospects for HH measurements at the HL-LHC," *CMS-PAS-FTR-18-019* (2018) .

[111] **FCC** Collaboration, A. Abada *et al.*, "FCC Physics Opportunities: Future Circular Collider Conceptual Design Report Volume 1," *Eur. Phys. J. C* **79** no. 6, (2019) 474.

[112] **FCC** Collaboration, A. Abada *et al.*, "FCC-ee: The Lepton Collider: Future Circular Collider Conceptual Design Report Volume 2," *Eur. Phys. J. ST* **228** no. 2, (2019) 261–623.

[113] P. Bambade *et al.*, "The International Linear Collider: A Global Project," arXiv:1903.01629 [hep-ex].

[114] **LCC Physics Working Group** Collaboration, K. Fujii *et al.*, "Tests of the Standard Model at the International Linear Collider," arXiv:1908.11299 [hep-ex].

[115] F. An *et al.*, "Precision Higgs physics at the CEPC," *Chin. Phys. C* **43** no. 4, (2019) 043002, arXiv:1810.09037 [hep-ex].

[116] **CEPC Study Group** Collaboration, M. Dong *et al.*, "CEPC Conceptual Design Report: Volume 2 - Physics & Detector," arXiv:1811.10545 [hep-ex].

[117] **CLICdp, CLIC** Collaboration, T. K. Charles *et al.*, "The Compact Linear Collider (CLIC) - 2018 Summary Report," arXiv:1812.06018 [physics.acc-ph].

[118] J. de Blas *et al.*, "The CLIC Potential for New Physics," arXiv:1812.02093 [hep-ph].

[119] S. Di Vita, G. Durieux, C. Grojean, J. Gu, Z. Liu, G. Panico, M. Riembau, and T. Vantalon, "A global view on the Higgs self-coupling at lepton colliders," *JHEP* **02** (2018) 178, arXiv:1711.03978 [hep-ph].

[120] G. Banelli, E. Salvioni, J. Serra, T. Theil, and A. Weiler, "The Present and Future of Four Top Operators," *JHEP* **02** (2021) 043, arXiv:2010.05915 [hep-ph].

[121] J. de Blas, J. C. Criado, M. Perez-Victoria, and J. Santiago, "Effective description of general extensions of the Standard Model: the complete tree-level dictionary," *JHEP* **03** (2018) 109, arXiv:1711.10391 [hep-ph].

[122] Anisha, S. D. Bakshi, S. Banerjee, A. Biekötter, J. Chakrabortty, S. K. Patra, and M. Spannowsky, "Effective limits on single scalar extensions in the light of recent LHC data," arXiv:2111.05876 [hep-ph].

[123] **ATLAS** Collaboration, M. Aaboud *et al.*, "Observation of $H \to b\bar{b}$ decays and VH production with the ATLAS detector," *Phys. Lett. B* **786** (2018) 59–86, arXiv:1808.08238 [hep-ex].

[124] **CMS** Collaboration, A. M. Sirunyan *et al.*, "Observation of Higgs boson decay to bottom quarks," *Phys. Rev. Lett.* **121** no. 12, (2018) 121801, arXiv:1808.08242 [hep-ex].

[125] T. Han and S. Willenbrock, "QCD correction to the p p —> W H and Z H total cross-sections," *Phys. Lett. B* **273** (1991) 167–172.

[126] O. Brein, A. Djouadi, and R. Harlander, "NNLO QCD corrections to the Higgs-strahlung processes at hadron colliders," *Phys. Lett. B* **579** (2004) 149–156, arXiv:hep-ph/0307206.

[127] S. Amoroso *et al.*, "Les Houches 2019: Physics at TeV Colliders: Standard Model Working Group Report," in *11th Les Houches Workshop on Physics at TeV Colliders: PhysTeV Les Houches*. 3, 2020. arXiv:2003.01700 [hep-ph].

[128] C. Englert, M. McCullough, and M. Spannowsky, "Gluon-initiated associated production boosts Higgs physics," *Phys. Rev. D* **89** no. 1, (2014) 013013, arXiv:1310.4828 [hep-ph].

[129] C. Englert, R. Rosenfeld, M. Spannowsky, and A. Tonero, "New physics and signal-background interference in associated $pp \to HZ$ production," *EPL* **114** no. 3, (2016) 31001, arXiv:1603.05304 [hep-ph].

[130] R. V. Harlander, S. Liebler, and T. Zirke, "Higgs Strahlung at the Large Hadron Collider in the 2-Higgs-Doublet Model," *JHEP* **02** (2014) 023, arXiv:1307.8122 [hep-ph].

[131] B. A. Kniehl, "Associated Production of Higgs and Z Bosons From Gluon Fusion in Hadron Collisions," *Phys. Rev. D* **42** (1990) 2253–2258.

[132] D. A. Dicus and C. Kao, "Higgs Boson - Z^0 Production From Gluon Fusion," *Phys. Rev. D* **38** (1988) 1008. [Erratum: Phys.Rev.D 42, 2412 (1990)].

[133] L. Altenkamp, S. Dittmaier, R. V. Harlander, H. Rzehak, and T. J. Zirke, "Gluon-induced Higgs-strahlung at next-to-leading order QCD," *JHEP* **02** (2013) 078, arXiv:1211.5015 [hep-ph].

[134] R. V. Harlander, A. Kulesza, V. Theeuwes, and T. Zirke, "Soft gluon resummation for gluon-induced Higgs Strahlung," *JHEP* **11** (2014) 082, arXiv:1410.0217 [hep-ph].

[135] A. Hasselhuhn, T. Luthe, and M. Steinhauser, "On top quark mass effects to $gg \to ZH$ at NLO," *JHEP* **01** (2017) 073, arXiv:1611.05881 [hep-ph].

[136] R. Harlander, J. Klappert, C. Pandini, and A. Papaefstathiou, "Exploiting the WH/ZH symmetry in the search for New Physics," *Eur. Phys. J. C* **78** no. 9, (2018) 760, arXiv:1804.02299 [hep-ph].

[137] B. Hespel, F. Maltoni, and E. Vryonidou, "Higgs and Z boson associated production via gluon fusion in the SM and the 2HDM," *JHEP* **06** (2015) 065, arXiv:1503.01656 [hep-ph].

[138] J. Davies, G. Mishima, and M. Steinhauser, "Virtual corrections to $gg \to ZH$ in the high-energy and large-m_t limits," arXiv:2011.12314 [hep-ph].

[139] L. Chen, G. Heinrich, S. P. Jones, M. Kerner, J. Klappert, and J. Schlenk, "ZH production in gluon fusion: two-loop amplitudes with full top quark mass dependence," arXiv:2011.12325 [hep-ph].

[140] R. Bonciani, G. Degrassi, P. P. Giardino, and R. Gröber, "Analytical Method for Next-to-Leading-Order QCD Corrections to Double-Higgs Production," *Phys. Rev. Lett.* **121** no. 16, (2018) 162003, arXiv:1806.11564 [hep-ph].

[141] L. Alasfar, G. Degrassi, P. P. Giardino, R. Gröber, and M. Vitti, "Virtual corrections to $gg \to ZH$ via a transverse momentum expansion," *JHEP* **05** (2021) 168, arXiv:2103.06225 [hep-ph].

[142] L. D. Landau, "On the angular momentum of a system of two photons," *Dokl. Akad. Nauk SSSR* **60** no. 2, (1948) 207–209.

[143] C.-N. Yang, "Selection Rules for the Dematerialization of a Particle Into Two Photons," *Phys. Rev.* **77** (1950) 242–245.

[144] G. Passarino and M. J. G. Veltman, "One Loop corrections for e^+e^- annihilation into $\mu^+\mu^-$ in the Weinberg Model," *Nucl. Phys.* **B160** (1979) 151.

[145] S. Larin, "The Renormalization of the axial anomaly in dimensional regularization," *Phys. Lett. B* **303** (1993) 113–118, arXiv:hep-ph/9302240.

[146] M. Spira, A. Djouadi, D. Graudenz, and P. M. Zerwas, "Higgs boson production at the LHC," *Nucl. Phys. B* **453** (1995) 17–82, arXiv:hep-ph/9504378.

[147] U. Aglietti, R. Bonciani, G. Degrassi, and A. Vicini, "Analytic Results for Virtual QCD Corrections to Higgs Production and Decay," *JHEP* **01** (2007) 021, arXiv:hep-ph/0611266.

[148] R. Mertig, M. Bohm, and A. Denner, "FEYN CALC: Computer algebraic calculation of Feynman amplitudes," *Comput. Phys. Commun.* **64** (1991) 345–359.

[149] V. Shtabovenko, R. Mertig, and F. Orellana, "New Developments in FeynCalc 9.0," *Comput. Phys. Commun.* **207** (2016) 432–444, arXiv:1601.01167 [hep-ph].

[150] H. H. Patel, "Package-X 2.0: A Mathematica package for the analytic calculation of one-loop integrals," *Comput. Phys. Commun.* **218** (2017) 66–70, arXiv:1612.00009 [hep-ph].

[151] P. Maierhöfer, J. Usovitsch, and P. Uwer, "Kira—A Feynman integral reduction program," *Comput. Phys. Commun.* **230** (2018) 99–112, arXiv:1705.05610 [hep-ph].

[152] R. Bonciani, P. Mastrolia, and E. Remiddi, "Master integrals for the two loop QCD virtual corrections to the forward backward asymmetry," *Nucl. Phys. B* **690** (2004) 138–176, arXiv:hep-ph/0311145.

[153] S. Borowka and G. Heinrich, "Massive non-planar two-loop four-point integrals with SecDec 2.1," *Comput. Phys. Commun.* **184** (2013) 2552–2561, arXiv:1303.1157 [hep-ph].

[154] S. Borowka, G. Heinrich, S. P. Jones, M. Kerner, J. Schlenk, and T. Zirke, "SecDec-3.0: numerical evaluation of multi-scale integrals beyond one loop," *Comput. Phys. Commun.* **196** (2015) 470–491, arXiv:1502.06595 [hep-ph].

[155] A. V. Smirnov, "FIRE5: a C++ implementation of Feynman Integral REduction," *Comput. Phys. Commun.* **189** (2015) 182–191, arXiv:1408.2372 [hep-ph].

[156] R. N. Lee, "LiteRed 1.4: a powerful tool for reduction of multiloop integrals," *J. Phys. Conf. Ser.* **523** (2014) 012059, arXiv:1310.1145 [hep-ph].

[157] A. von Manteuffel and L. Tancredi, "A non-planar two-loop three-point function beyond multiple polylogarithms," *JHEP* **06** (2017) 127, arXiv:1701.05905 [hep-ph].

[158] R. Bonciani, G. Degrassi, P. P. Giardino, and R. Gröber, "A Numerical Routine for the Crossed Vertex Diagram with a Massive-Particle Loop," *Comput. Phys. Commun.* **241** (2019) 122–131, arXiv:1812.02698 [hep-ph].

[159] L. Naterop, A. Signer, and Y. Ulrich, "handyG —Rapid numerical evaluation of generalised polylogarithms in Fortran," *Comput. Phys. Commun.* **253** (2020) 107165, arXiv:1909.01656 [hep-ph].

[160] S. Buehler and C. Duhr, "CHAPLIN - Complex Harmonic Polylogarithms in Fortran," *Comput. Phys. Commun.* **185** (2014) 2703–2713, arXiv:1106.5739 [hep-ph].

[161] S. Borowka, G. Heinrich, S. Jahn, S. P. Jones, M. Kerner, J. Schlenk, and T. Zirke, "pySecDec: a toolbox for the numerical evaluation of multi-scale integrals," *Comput. Phys. Commun.* **222** (2018) 313–326, arXiv:1703.09692 [hep-ph].

[162] S. Borowka, G. Heinrich, S. Jahn, S. P. Jones, M. Kerner, and J. Schlenk, "A GPU compatible quasi-Monte Carlo integrator interfaced to pySecDec," *Comput. Phys. Commun.* **240** (2019) 120–137, arXiv:1811.11720 [physics.comp-ph].

[163] O. Eboli, G. Marques, S. Novaes, and A. Natale, "Twin higgs-boson production," *Physics Letters B* **197** no. 1, (1987) 269–272.

[164] E. Glover and J. van der Bij, "Higgs boson pair production via gluon fusion," *Nuclear Physics B* **309** no. 2, (1988) 282–294.

[165] D. A. Dicus, C. Kao, and S. S. D. Willenbrock, "Higgs Boson Pair Production From Gluon Fusion," *Phys. Lett.* **B203** (1988) 457–461.

[166] T. Plehn, M. Spira, and P. M. Zerwas, "Pair production of neutral Higgs particles in gluon-gluon collisions," *Nucl. Phys.* **B479** (1996) 46–64, arXiv:hep-ph/9603205 [hep-ph]. [Erratum: Nucl. Phys.B531,655(1998)].

[167] S. Dawson, S. Dittmaier, and M. Spira, "Neutral Higgs boson pair production at hadron colliders: QCD corrections," *Phys. Rev.* **D58** (1998) 115012, arXiv:hep-ph/9805244 [hep-ph].

[168] S. Borowka, N. Greiner, G. Heinrich, S. P. Jones, M. Kerner, J. Schlenk, and T. Zirke, "Full top quark mass dependence in Higgs boson pair production at NLO," *JHEP* **10** (2016) 107, arXiv:1608.04798 [hep-ph].

[169] S. Borowka, N. Greiner, G. Heinrich, S. P. Jones, M. Kerner, J. Schlenk, U. Schubert, and T. Zirke, "Higgs Boson Pair Production in Gluon Fusion at Next-to-Leading Order with Full Top-Quark Mass Dependence," *Phys. Rev. Lett.* **117** no. 1, (2016) 012001, arXiv:1604.06447 [hep-ph]. [Erratum: Phys. Rev. Lett.117,no.7,079901(2016)].

[170] J. Baglio, F. Campanario, S. Glaus, M. Mühlleitner, M. Spira, and J. Streicher, "Gluon fusion into Higgs pairs at NLO QCD and the top mass scheme," *Eur. Phys. J.* **C79** no. 6, (2019) 459, arXiv:1811.05692 [hep-ph].

[171] G. Heinrich, S. P. Jones, M. Kerner, G. Luisoni, and L. Scyboz, "Probing the trilinear Higgs boson coupling in di-Higgs production at NLO QCD including parton shower effects," *JHEP* **06** (2019) 066, arXiv:1903.08137 [hep-ph].

[172] J. Davies, R. Gröber, A. Maier, T. Rauh, and M. Steinhauser, "Top quark mass dependence of the Higgs boson-gluon form factor at three loops," *Phys. Rev.* **D100** no. 3, (2019) 034017, arXiv:1906.00982 [hep-ph].

[173] M. Grazzini, G. Heinrich, S. Jones, S. Kallweit, M. Kerner, J. M. Lindert, and J. Mazzitelli, "Higgs boson pair production at NNLO with top quark mass effects," *JHEP* **05** (2018) 059, arXiv:1803.02463 [hep-ph].

[174] **NNPDF** Collaboration, R. D. Ball *et al.*, "Parton distributions from high-precision collider data," *Eur. Phys. J.* **C77** no. 10, (2017) 663, arXiv:1706.00428 [hep-ph].

[175] A. Buckley, J. Ferrando, S. Lloyd, K. Nordström, B. Page, M. Rüfenacht, M. Schönherr, and G. Watt, "LHAPDF6: parton density access in the LHC precision era," *Eur. Phys. J.* **C75** (2015) 132, arXiv:1412.7420 [hep-ph].

[176] A. Denner, S. Dittmaier, and L. Hofer, "COLLIER - A fortran-library for one-loop integrals," *PoS* **LL2014** (2014) 071, arXiv:1407.0087 [hep-ph].

[177] S. Dittmaier *et al.*, "Handbook of LHC Higgs Cross Sections: 2. Differential Distributions," arXiv:1201.3084 [hep-ph].

[178] **LHC Higgs Cross Section Working Group** Collaboration, D. de Florian *et al.*, "Handbook of LHC Higgs Cross Sections: 4. Deciphering the Nature of the Higgs Sector," arXiv:1610.07922 [hep-ph].

[179] A. D. Martin, W. J. Stirling, R. S. Thorne, and G. Watt, "Uncertainties on alpha(S) in global PDF analyses and implications for predicted hadronic cross sections," *Eur. Phys. J.* **C64** (2009) 653–680, arXiv:0905.3531 [hep-ph].

[180] F. Demartin, S. Forte, E. Mariani, J. Rojo, and A. Vicini, "The impact of PDF and alphas uncertainties on Higgs Production in gluon fusion at hadron colliders," *Phys. Rev.* **D82** (2010) 014002, arXiv:1004.0962 [hep-ph].

[181] J. Baglio, A. Djouadi, R. Gröber, M. M. Mühlleitner, J. Quevillon, and M. Spira, "The measurement of the Higgs self-coupling at the LHC: theoretical status," *JHEP* **04** (2013) 151, arXiv:1212.5581 [hep-ph].

[182] I. Brivio, F. Goertz, and G. Isidori, "Probing the Charm Quark Yukawa Coupling in Higgs+Charm Production," *Phys. Rev. Lett.* **115** no. 21, (2015) 211801, arXiv:1507.02916 [hep-ph].

[183] Y. Soreq, H. X. Zhu, and J. Zupan, "Light quark Yukawa couplings from Higgs kinematics," *JHEP* **12** (2016) 045, arXiv:1606.09621 [hep-ph].

[184] F. Bishara, U. Haisch, P. F. Monni, and E. Re, "Constraining Light-Quark Yukawa Couplings from Higgs Distributions," *Phys. Rev. Lett.* **118** no. 12, (2017) 121801, arXiv:1606.09253 [hep-ph].

[185] G. Bonner and H. E. Logan, "Constraining the Higgs couplings to up and down quarks using production kinematics at the CERN Large Hadron Collider," arXiv:1608.04376 [hep-ph].

[186] **CMS** Collaboration, "Constraints on the Higgs boson self-coupling from ttH+tH, H to gamma gamma differential measurements at the HL-LHC," Tech. Rep. CMS-PAS-FTR-18-020, 2018.

[187] G. Perez, Y. Soreq, E. Stamou, and K. Tobioka, "Prospects for measuring the Higgs boson coupling to light quarks," *Phys. Rev.* **D93** no. 1, (2016) 013001, arXiv:1505.06689 [hep-ph].

[188] **ATLAS** Collaboration, "Direct constraint on the Higgs-charm coupling from a search for Higgs boson decays to charm quarks with the ATLAS detector,".

[189] G. T. Bodwin, F. Petriello, S. Stoynev, and M. Velasco, "Higgs boson decays to quarkonia and the $H\bar{c}c$ coupling," *Phys. Rev.* **D88** no. 5, (2013) 053003, arXiv:1306.5770 [hep-ph].

[190] A. L. Kagan, G. Perez, F. Petriello, Y. Soreq, S. Stoynev, and J. Zupan, "Exclusive Window onto Higgs Yukawa Couplings," *Phys. Rev. Lett.* **114** no. 10, (2015) 101802, arXiv:1406.1722 [hep-ph].

[191] M. König and M. Neubert, "Exclusive Radiative Higgs Decays as Probes of Light-Quark Yukawa Couplings," *JHEP* **08** (2015) 012, arXiv:1505.03870 [hep-ph].

[192] **CMS** Collaboration, A. M. Sirunyan *et al.*, "Search for rare decays of Z and Higgs bosons to J/ψ and a photon in proton-proton collisions at $\sqrt{s} = 13$ TeV," *Eur. Phys. J. C* **79** no. 2, (2019) 94, arXiv:1810.10056 [hep-ex].

[193] F. Yu, "Light Quark Yukawa Couplings and the $W^{\pm}h$ Charge Asymmetry," *Nucl. Part. Phys. Proc.* **285-286** (2017) 123–125.

[194] J. A. Aguilar-Saavedra, J. M. Cano, and J. M. No, "More light on Higgs flavor at the LHC: Higgs boson couplings to light quarks through $h + \gamma$ production," *Phys. Rev. D* **103** no. 9, (2021) 095023, arXiv:2008.12538 [hep-ph].

[195] A. Falkowski, S. Ganguly, P. Gras, J. M. No, K. Tobioka, N. Vignaroli, and T. You, "Light quark Yukawas in triboson final states," *JHEP* **04** (2021) 023, arXiv:2011.09551 [hep-ph].

[196] **ATLAS** Collaboration, A. Sciandra, "Measurement of Triboson Production and aQGCs with the ATLAS detector,".

[197] **CMS** Collaboration, "Observation of heavy triboson production in leptonic final states in proton-proton collisions at $\sqrt{s} = 13$ TeV,".

[198] T. Binoth, S. Karg, N. Kauer, and R. Ruckl, "Multi-Higgs boson production in the Standard Model and beyond," *Phys. Rev.* **D74** (2006) 113008, arXiv:hep-ph/0608057 [hep-ph].

[199] R. Contino, M. Ghezzi, M. Moretti, G. Panico, F. Piccinini, and A. Wulzer, "Anomalous Couplings in Double Higgs Production," *JHEP* **08** (2012) 154, arXiv:1205.5444 [hep-ph].

[200] L. Alasfar, R. Corral Lopez, and R. Gröber, "Probing Higgs couplings to light quarks via Higgs pair production," *JHEP* **11** (2019) 088, arXiv:1909.05279 [hep-ph].

[201] S. Bar-Shalom and A. Soni, "Universally enhanced light-quarks Yukawa couplings paradigm," *Phys. Rev.* **D98** no. 5, (2018) 055001, arXiv:1804.02400 [hep-ph].

[202] M. Bauer, M. Carena, and A. Carmona, "Higgs Pair Production as a Signal of Enhanced Yukawa Couplings," *Phys. Rev. Lett.* **121** no. 2, (2018) 021801, arXiv:1801.00363 [hep-ph].

[203] D. Egana-Ugrinovic, S. Homiller, and P. Meade, "Multi-Higgs Production Probes Higgs Flavor," *Phys. Rev. D* **103** (2021) 115005, arXiv:2101.04119 [hep-ph].

[204] A. Papaefstathiou and K. Sakurai, "Triple Higgs boson production at a 100 TeV proton-proton collider," *JHEP* **02** (Aug, 2015) 006. 10 p, arXiv:1508.06524. https://cds.cern.ch/record/2047255. Corrected version of Figure 6.

[205] C. Delaunay, R. Ozeri, G. Perez, and Y. Soreq, "Probing Atomic Higgs-like Forces at the Precision Frontier," *Phys. Rev.* **D96** no. 9, (2017) 093001, arXiv:1601.05087 [hep-ph].

[206] **ATLAS** Collaboration, G. Aad *et al.*, "Combination of searches for Higgs boson pairs in pp collisions at $\sqrt{s}$ =13 TeV with the ATLAS detector," arXiv:1906.02025 [hep-ex].

[207] A. Falkowski and R. Rattazzi, "Which EFT," arXiv:1902.05936 [hep-ph].

[208] T. Plehn and M. Rauch, "The quartic higgs coupling at hadron colliders," *Phys. Rev.* **D72** (2005) 053008, arXiv:hep-ph/0507321 [hep-ph].

[209] **CMS** Collaboration, V. Khachatryan *et al.*, "Search for a standard model-like Higgs boson in the $\mu^+\mu^-$ and e^+e^- decay channels at the LHC," *Phys. Lett.* **B744** (2015) 184–207, arXiv:1410.6679 [hep-ex].

[210] G. Perez, Y. Soreq, E. Stamou, and K. Tobioka, "Constraining the charm Yukawa and Higgs-quark coupling universality," *Phys. Rev.* **D92** no. 3, (2015) 033016, arXiv:1503.00290 [hep-ph].

[211] J. De Blas *et al.*, "Higgs Boson Studies at Future Particle Colliders," arXiv:1905.03764 [hep-ph].

[212] **ATLAS** Collaboration, M. Aaboud *et al.*, "Constraints on off-shell Higgs boson production and the Higgs boson total width in $ZZ \to 4\ell$ and $ZZ \to 2\ell 2\nu$ final states with the ATLAS detector," *Phys. Lett.* **B786** (2018) 223–244, arXiv:1808.01191 [hep-ex].

[213] **CMS** Collaboration, A. M. Sirunyan *et al.*, "Measurements of the Higgs boson width and anomalous HVV couplings from on-shell and off-shell production in the four-lepton final state," *Phys. Rev.* **D99** no. 11, (2019) 112003, arXiv:1901.00174 [hep-ex].

[214] F. Caola and K. Melnikov, "Constraining the Higgs boson width with ZZ production at the LHC," *Phys. Rev.* **D88** (2013) 054024, arXiv:1307.4935 [hep-ph].

[215] C. Englert and M. Spannowsky, "Limitations and Opportunities of Off-Shell Coupling Measurements," *Phys. Rev.* **D90** (2014) 053003, arXiv:1405.0285 [hep-ph].

[216] M. König and M. Neubert, "Exclusive Radiative Higgs Decays as Probes of Light-Quark Yukawa Couplings," *JHEP* **08** (2015) 012, arXiv:1505.03870 [hep-ph].

[217] **ATLAS** Collaboration, M. Aaboud *et al.*, "Search for exclusive Higgs and Z boson decays to $\phi\gamma$ and $\rho\gamma$ with the ATLAS detector," *JHEP* **07** (2018) 127, arXiv:1712.02758 [hep-ex].

[218] **ATLAS** Collaboration, M. Aaboud *et al.*, "Searches for exclusive Higgs and Z boson decays into $J/\psi\gamma$, $\psi(2S)\gamma$, and $\Upsilon(nS)\gamma$ at $\sqrt{s} = 13$ TeV with the ATLAS detector," *Phys. Lett.* **B786** (2018) 134–155, arXiv:1807.00802 [hep-ex].

[219] **CMS** Collaboration, A. M. Sirunyan *et al.*, "Search for rare decays of Z and Higgs bosons to J/ψ and a photon in proton-proton collisions at $\sqrt{s} = 13$ TeV," *Eur. Phys. J.* **C79** no. 2, (2019) 94, arXiv:1810.10056 [hep-ex].

[220] **ATLAS** Collaboration, "Prospects for $H \to c\bar{c}$ using Charm Tagging with the ATLAS Experiment at the HL-LHC," Tech. Rep. ATL-PHYS-PUB-2018-016, CERN, Geneva, Aug, 2018. http://cds.cern.ch/record/2633635.

[221] **CMS** Collaboration, "Search for the standard model Higgs boson decaying to charm quarks," Tech. Rep. CMS-PAS-HIG-18-031, CERN, Geneva, 2019. http://cds.cern.ch/record/2682638.

[222] C. O. Dib, R. Rosenfeld, and A. Zerwekh, "Double Higgs production and quadratic divergence cancellation in little Higgs models with T parity," *JHEP* **05** (2006) 074, arXiv:hep-ph/0509179 [hep-ph].

[223] R. Gröber and M. Mühlleitner, "Composite Higgs Boson Pair Production at the LHC," *JHEP* **06** (2011) 020, arXiv:1012.1562 [hep-ph].

[224] R. Gröber, M. Mühlleitner, and M. Spira, "Signs of Composite Higgs Pair Production at Next-to-Leading Order," *JHEP* **06** (2016) 080, arXiv:1602.05851 [hep-ph].

[225] G. Blankenburg, J. Ellis, and G. Isidori, "Flavour-Changing Decays of a 125 GeV Higgs-like Particle," *Phys. Lett.* **B712** (2012) 386–390, arXiv:1202.5704 [hep-ph].

[226] G. D'Ambrosio, G. F. Giudice, G. Isidori, and A. Strumia, "Minimal flavor violation: An Effective field theory approach," *Nucl. Phys.* **B645** (2002) 155–187, arXiv:hep-ph/0207036 [hep-ph].

[227] **ATLAS** Collaboration, "Combined measurements of Higgs boson production and decay using up to 80 fb^{-1} of proton–proton collision data at $\sqrt{s} = 13$ TeV collected with the ATLAS experiment," Tech. Rep. ATLAS-CONF-2018-031, CERN, Geneva, Jul, 2018. http://cds.cern.ch/record/2629412.

[228] **CMS** Collaboration, "Measurement of the top quark Yukawa coupling from $\mathrm{t\bar{t}}$ kinematic distributions in the lepton+jets final state in proton-proton collisions at $\sqrt{s} = 13$ TeV," Tech. Rep. CERN-EP-2019-119. CMS-TOP-17-004-003, CERN, Geneva, Jul, 2019. https://cds.cern.ch/record/2681021.

[229] D. Egana-Ugrinovic, S. Homiller, and P. Meade, "Aligned and Spontaneous Flavor Violation," *Phys. Rev. Lett.* **123** no. 3, (2019) 031802, arXiv:1811.00017 [hep-ph].

[230] D. Egana-Ugrinovic, S. Homiller, and P. R. Meade, "Higgs bosons with large couplings to light quarks," arXiv:1908.11376 [hep-ph].

[231] S. R. Coleman, J. Wess, and B. Zumino, "Structure of phenomenological Lagrangians. 1.," *Phys. Rev.* **177** (1969) 2239–2247.

[232] C. G. Callan, Jr., S. R. Coleman, J. Wess, and B. Zumino, "Structure of phenomenological Lagrangians. 2.," *Phys. Rev.* **177** (1969) 2247–2250.

[233] R. Contino, C. Grojean, M. Moretti, F. Piccinini, and R. Rattazzi, "Strong Double Higgs Production at the LHC," *JHEP* **05** (2010) 089, arXiv:1002.1011 [hep-ph].

[234] R. Gröber, A. Maier, and T. Rauh, "Reconstruction of top-quark mass effects in Higgs pair production and other gluon-fusion processes," *JHEP* **03** (2018) 020, arXiv:1709.07799 [hep-ph].

[235] J. Davies, G. Mishima, M. Steinhauser, and D. Wellmann, "Double Higgs boson production at NLO in the high-energy limit: complete analytic results," *JHEP* **01** (2019) 176, arXiv:1811.05489 [hep-ph].

[236] J. Grigo, K. Melnikov, and M. Steinhauser, "Virtual corrections to Higgs boson pair production in the large top quark mass limit," *Nucl. Phys.* **B888** (2014) 17–29, arXiv:1408.2422 [hep-ph].

[237] D. de Florian and J. Mazzitelli, "Higgs Boson Pair Production at Next-to-Next-to-Leading Order in QCD," *Phys. Rev. Lett.* **111** (2013) 201801, arXiv:1309.6594 [hep-ph].

[238] J. Davies and M. Steinhauser, "Three-loop form factors for Higgs boson pair production in the large top mass limit," arXiv:1909.01361 [hep-ph].

[239] R. V. Harlander, M. Prausa, and J. Usovitsch, "The light-fermion contribution to the exact Higgs-gluon form factor in QCD," arXiv:1907.06957 [hep-ph].

[240] D. de Florian and J. Mazzitelli, "Higgs pair production at next-to-next-to-leading logarithmic accuracy at the LHC," *JHEP* **09** (2015) 053, arXiv:1505.07122 [hep-ph].

[241] D. Dicus, T. Stelzer, Z. Sullivan, and S. Willenbrock, "Higgs boson production in association with bottom quarks at next-to-leading order," *Phys. Rev.* **D59** (1999) 094016, arXiv:hep-ph/9811492 [hep-ph].

[242] C. Balazs, H.-J. He, and C. P. Yuan, "QCD corrections to scalar production via heavy quark fusion at hadron colliders," *Phys. Rev.* **D60** (1999) 114001, arXiv:hep-ph/9812263 [hep-ph].

[243] R. V. Harlander and W. B. Kilgore, "Higgs boson production in bottom quark fusion at next-to-next-to leading order," *Phys. Rev.* **D68** (2003) 013001, arXiv:hep-ph/0304035 [hep-ph].

[244] S. Dawson, C. Kao, Y. Wang, and P. Williams, "QCD Corrections to Higgs Pair Production in Bottom Quark Fusion," *Phys. Rev.* **D75** (2007) 013007, arXiv:hep-ph/0610284 [hep-ph].

[245] A. H. Ajjath, P. Banerjee, A. Chakraborty, P. K. Dhani, P. Mukherjee, N. Rana, and V. Ravindran, "Higgs pair production from bottom quark annihilation to NNLO in QCD," *JHEP* **05** (2019) 030, arXiv:1811.01853 [hep-ph].

[246] M. Spira, "Higgs Boson Production and Decay at Hadron Colliders," *Prog. Part. Nucl. Phys.* **95** (2017) 98–159, arXiv:1612.07651 [hep-ph].

[247] V. N. Gribov and L. N. Lipatov, "Deep inelastic e p scattering in perturbation theory," *Sov. J. Nucl. Phys.* **15** (1972) 438–450. [Yad. Fiz.15,781(1972)].

[248] G. Altarelli and G. Parisi, "Asymptotic Freedom in Parton Language," *Nucl. Phys.* **B126** (1977) 298–318.

[249] Y. L. Dokshitzer, "Calculation of the Structure Functions for Deep Inelastic Scattering and e+ e- Annihilation by Perturbation Theory in Quantum Chromodynamics.," *Sov. Phys. JETP* **46** (1977) 641–653. [Zh. Eksp. Teor. Fiz.73,1216(1977)].

[250] A. Djouadi, J. Kalinowski, and M. Spira, "HDECAY: A Program for Higgs boson decays in the standard model and its supersymmetric extension," *Comput. Phys. Commun.* **108** (1998) 56–74, arXiv:hep-ph/9704448 [hep-ph].

[251] A. Djouadi, J. Kalinowski, M. Muehlleitner, and M. Spira, "HDECAY: Twenty$_{++}$ years after," *Comput. Phys. Commun.* **238** (2019) 214–231, arXiv:1801.09506 [hep-ph].

[252] A. Azatov, R. Contino, G. Panico, and M. Son, "Effective field theory analysis of double Higgs boson production via gluon fusion," *Phys. Rev.* **D92** no. 3, (2015) 035001, arXiv:1502.00539 [hep-ph].

[253] U. Baur, T. Plehn, and D. L. Rainwater, "Probing the Higgs selfcoupling at hadron colliders using rare decays," *Phys. Rev.* **D69** (2004) 053004, arXiv:hep-ph/0310056 [hep-ph].

[254] F. Kling, T. Plehn, and P. Schichtel, "Maximizing the significance in Higgs boson pair analyses," *Phys. Rev.* **D95** no. 3, (2017) 035026, arXiv:1607.07441 [hep-ph].

[255] V. Barger, L. L. Everett, C. B. Jackson, and G. Shaughnessy, "Higgs-Pair Production and Measurement of the Triscalar Coupling at LHC(8,14)," *Phys. Lett.* **B728** (2014) 433–436, arXiv:1311.2931 [hep-ph].

[256] A. Adhikary, S. Banerjee, R. K. Barman, B. Bhattacherjee, and S. Niyogi, "Revisiting the non-resonant Higgs pair production at the HL-LHC," *JHEP* **07** (2018) 116, arXiv:1712.05346 [hep-ph].

[257] T. Sjostrand, S. Mrenna, and P. Z. Skands, "PYTHIA 6.4 Physics and Manual," *JHEP* **05** (2006) 026, arXiv:hep-ph/0603175 [hep-ph].

[258] D. C. Hall, "RootTuple: A library enabling ROOT n-tuple output from FORTRAN HEP programs," http://roottuple.hepforge.org.

[259] M. Cacciari, G. P. Salam, and G. Soyez, "FastJet User Manual," *Eur. Phys. J.* **C72** (2012) 1896, arXiv:1111.6097 [hep-ph].

[260] J. M. Butterworth, A. R. Davison, M. Rubin, and G. P. Salam, "Jet substructure as a new Higgs search channel at the LHC," *Phys. Rev. Lett.* **100** (2008) 242001, arXiv:0802.2470 [hep-ph].

[261] **CMS** Collaboration, S. Chatrchyan *et al.*, "Inclusive b-jet production in pp collisions at $\sqrt{s} = 7$ TeV," *JHEP* **04** (2012) 084, arXiv:1202.4617 [hep-ex].

[262] **CMS** Collaboration, "Performance of b tagging at sqrt(s)=8 TeV in multijet, ttbar and boosted topology events," Tech. Rep. CMS-PAS-BTV-13-001, CERN, Geneva, 2013. https://cds.cern.ch/record/1581306.

[263] **ATLAS** Collaboration, "Performance assumptions based on full simulation for an upgraded ATLAS detector at a High-Luminosity LHC," Tech. Rep. ATL-PHYS-PUB-2013-009, CERN, Geneva, 2013. http://cds.cern.ch/record/1604420.

[264] **CMS** Collaboration, "Photon ID performance with 19.6 fb^{-1} of data collected at $\sqrt{s} = 8$ TeV with the CMS detector," Tech. Rep. CMS-DP-2013-010, CERN, Geneva, 2013. http://cds.cern.ch/record/1542855.

[265] G. Cowan, K. Cranmer, E. Gross, and O. Vitells, "Asymptotic formulae for likelihood-based tests of new physics," *Eur. Phys. J.* **C71** (2011) 1554, arXiv:1007.1727 [physics.data-an]. [Erratum: Eur. Phys. J.C73,2501(2013)].

[266] D. Kim and M. Park, "Enhancement of new physics signal sensitivity with mistagged charm quarks," *Phys. Lett.* **B758** (2016) 190–194, arXiv:1507.03990 [hep-ph].

[267] **CMS** Collaboration, S. Chatrchyan *et al.*, "Search for the standard model Higgs boson produced in association with a W or a Z boson and decaying to bottom quarks," *Phys. Rev.* **D89** no. 1, (2014) 012003, arXiv:1310.3687 [hep-ex].

[268] **ATLAS** Collaboration, G. Aad *et al.*, "Search for the $b\bar{b}$ decay of the Standard Model Higgs boson in associated $(W/Z)H$ production with the ATLAS detector," *JHEP* **01** (2015) 069, arXiv:1409.6212 [hep-ex].

[269] N. A. Heard and P. Rubin-Delanchy, "Choosing between methods of combining-values," *Biometrika* **105** no. 1, (2018) .

[270] **ATLAS** Collaboration, G. Aad *et al.*, "Search for Scalar Charm Quark Pair Production in pp Collisions at $\sqrt{s} = 8$ TeV with the ATLAS Detector," *Phys. Rev. Lett.* **114** no. 16, (2015) 161801, arXiv:1501.01325 [hep-ex].

[271] **ATLAS** Collaboration, "Search for single top-quark production via FCNC in strong interaction in $\sqrt{s} = 8$ TeV ATLAS data," Tech. Rep. ATLAS-CONF-2013-063, CERN, Geneva, 2013. http://cds.cern.ch/record/1562777.

[272] **ATLAS** Collaboration, M. Capeans, G. Darbo, K. Einsweiller, M. Elsing, T. Flick, M. Garcia-Sciveres, C. Gemme, H. Pernegger, O. Rohne, and R. Vuillermet, "ATLAS Insertable B-Layer Technical Design Report," Tech. Rep. CERN-LHCC-2010-013. ATLAS-TDR-19, 2010. https://cds.cern.ch/record/1291633.

[273] **ATLAS** Collaboration, "Track Reconstruction Performance of the ATLAS Inner Detector at $\sqrt{s} = 13$ TeV," Tech. Rep. ATL-PHYS-PUB-2015-018, CERN, Geneva, 2015. http://cds.cern.ch/record/2037683.

[274] J. Alonso-Gonzalez, A. de Giorgi, L. Merlo, and S. Pokorski, "Searching for BSM Physics in Yukawa Couplings and Flavour Symmetries," arXiv:2109.07490 [hep-ph].

[275] C. Grojean, A. Paul, and Z. Qian, "Resurrecting $b\bar{b}h$ with kinematic shapes," *JHEP* **04** (2021) 139, arXiv:2011.13945 [hep-ph].

[276] W. Beenakker, S. Dittmaier, M. Kramer, B. Plumper, M. Spira, and P. M. Zerwas, "Higgs radiation off top quarks at the Tevatron and the LHC," *Phys. Rev. Lett.* **87** (2001) 201805, arXiv:hep-ph/0107081.

[277] D. Fäh and N. Greiner, "Diphoton production in association with two bottom jets," *Eur. Phys. J. C* **77** no. 11, (2017) 750, arXiv:1706.08309 [hep-ph].

[278] F. Campanario, R. Roth, and D. Zeppenfeld, "QCD radiation in WH and WZ production and anomalous coupling measurements," *Phys. Rev. D* **91** (2015) 054039, arXiv:1410.4840 [hep-ph].

[279] S. Dawson, C. Jackson, L. Reina, and D. Wackeroth, "Higgs production in association with bottom quarks at hadron colliders," *Mod. Phys. Lett. A* **21** (2006) 89–110, arXiv:hep-ph/0508293.

[280] **LHC Higgs Cross Section Working Group** Collaboration, D. de Florian *et al.*, "Handbook of LHC Higgs Cross Sections: 4. Deciphering the Nature of the Higgs Sector," arXiv:1610.07922 [hep-ph].

[281] T. Sjöstrand, S. Ask, J. R. Christiansen, R. Corke, N. Desai, P. Ilten, S. Mrenna, S. Prestel, C. O. Rasmussen, and P. Z. Skands, "An introduction to PYTHIA 8.2," *Comput. Phys. Commun.* **191** (2015) 159–177, arXiv:1410.3012 [hep-ph].

[282] **DELPHES 3** Collaboration, J. de Favereau, C. Delaere, P. Demin, A. Giammanco, V. Lemaître, A. Mertens, and M. Selvaggi, "DELPHES 3, A modular framework for fast simulation of a generic collider experiment," *JHEP* **02** (2014) 057, arXiv:1307.6346 [hep-ex].

[283] D. de Florian, I. Fabre, G. Heinrich, J. Mazzitelli, and L. Scyboz, "Anomalous couplings in Higgs-boson pair production at approximate NNLO QCD," arXiv:2106.14050 [hep-ph].

[284] G. Heinrich, S. P. Jones, M. Kerner, G. Luisoni, and E. Vryonidou, "NLO predictions for Higgs boson pair production with full top quark mass dependence matched to parton showers," *JHEP* **08** (2017) 088, arXiv:1703.09252 [hep-ph].

[285] G. Heinrich, S. P. Jones, M. Kerner, and L. Scyboz, "A non-linear EFT description of $gg \to HH$ at NLO interfaced to POWHEG," *JHEP* **10** (2020) 021, arXiv:2006.16877 [hep-ph].

[286] G. Buchalla, M. Capozi, A. Celis, G. Heinrich, and L. Scyboz, "Higgs boson pair production in non-linear Effective Field Theory with full m_t-dependence at NLO QCD," *JHEP* **09** (2018) 057, arXiv:1806.05162 [hep-ph].

[287] F. Maltoni, E. Vryonidou, and M. Zaro, "Top-quark mass effects in double and triple Higgs production in gluon-gluon fusion at NLO," *JHEP* **11** (2014) 079, arXiv:1408.6542 [hep-ph].

[288] M. Abadi *et al.*, "TensorFlow: Large-scale machine learning on heterogeneous systems," 2015. https://www.tensorflow.org/. Software available from tensorflow.org.

[289] T. Chen and C. Guestrin, "XGBoost: A Scalable Tree Boosting System," in *Proceedings of the 22nd ACM SIGKDD International Conference on Knowledge Discovery and Data Mining*, KDD '16, p. 785–794. Association for Computing Machinery, New York, NY, USA, 2016. https://dl.acm.org/doi/10.1145/2939672.2939785.

[290] L. Breiman, "Random forests," *Machine Learning* **45** no. 1, (Oct, 2001) 5–32. https://doi.org/10.1023/A:1010933404324.

[291] A. Fisher, C. Rudin, and F. Dominici, "All models are wrong, but many are useful: Learning a variable's importance by studying an entire class of prediction models simultaneously," *Journal of Machine Learning Research* **20** no. 177, (2019) 1–81, arXiv:1801.01489. http://jmlr.org/papers/v20/18-760.html.

[292] M. T. Ribeiro, S. Singh, and C. Guestrin, ""why should i trust you?": Explaining the predictions of any classifier," in *Proceedings of the 22nd ACM SIGKDD International Conference on Knowledge Discovery and Data Mining*, KDD '16, p. 1135–1144. Association for Computing Machinery, New York, NY, USA, 2016. https://doi.org/10.1145/2939672.2939778.

[293] S. M. Lundberg and S.-I. Lee, "A unified approach to interpreting model predictions," in *Advances in Neural Information Processing Systems*, I. Guyon, U. V. Luxburg, S. Bengio, H. Wallach, R. Fergus, S. Vishwanathan, and R. Garnett, eds., vol. 30, pp. 4765–4774. Curran Associates, Inc., 2017. 1705.07874. https://proceedings.neurips.cc/paper/2017/file/8a20a8621978632d76c43dfd28b67767-Paper.pdf.

[294] L. S. Shapley, "Notes on the n-Person Game-II: The Value of an n-Person Game," *Rand Corporation* (1951) . https://www.rand.org/pubs/research_memoranda/RM0670.html.

[295] C. Molnar, *Interpretable Machine Learning*. Lulu, 2020. https://christophm.github.io/interpretable-ml-book/.

[296] D. Alvestad, N. Fomin, J. Kersten, S. Maeland, and I. Strümke, "Beyond Cuts in Small Signal Scenarios - Enhanced Sneutrino Detectability Using Machine Learning," arXiv:2108.03125 [hep-ph].

[297] A. S. Cornell, W. Doorsamy, B. Fuks, G. Harmsen, and L. Mason, "Boosted decision trees in the era of new physics: a smuon analysis case study," arXiv:2109.11815 [hep-ph].

[298] S. M. Lundberg, G. G. Erion, and S.-I. Lee, "Consistent Individualized Feature Attribution for Tree Ensembles," *arXiv e-prints* (Feb., 2018) , arXiv:1802.03888 [cs.LG].

[299] S. M. Lundberg, G. Erion, H. Chen, A. DeGrave, J. M. Prutkin, B. Nair, R. Katz, J. Himmelfarb, N. Bansal, and S.-I. Lee, "From local explanations to global understanding with explainable AI for trees," *Nature Machine Intelligence* **2** no. 1, (2020) 56–67. https://www.nature.com/articles/s42256-019-0138-9.

[300] A. Alves, T. Ghosh, and K. Sinha, "Can We Discover Double Higgs Production at the LHC?," *Phys. Rev. D* **96** no. 3, (2017) 035022, arXiv:1704.07395 [hep-ph].

[301] **ATLAS Collaboration** Collaboration, "Search for Higgs boson pair production in the two bottom quarks plus two photons final state in pp collisions at $\sqrt{s} = 13$ TeV with the ATLAS detector,".

[302] **ATLAS Collaboration** Collaboration, "Measurement prospects of the pair production and self-coupling of the Higgs boson with the ATLAS experiment at the HL-LHC,".

[303] J. Baglio, F. Campanario, S. Glaus, M. Mühlleitner, J. Ronca, and M. Spira, "$gg \to HH$: Combined uncertainties," *Phys. Rev. D* **103** no. 5, (2021) 056002, arXiv:2008.11626 [hep-ph].

[304] **CLICdp, CLIC** Collaboration, T. K. Charles *et al.*, "The Compact Linear Collider (CLIC) - 2018 Summary Report," arXiv:1812.06018 [physics.acc-ph].

[305] J. Gao, "Probing light-quark Yukawa couplings via hadronic event shapes at lepton colliders," *JHEP* **01** (2018) 038, arXiv:1608.01746 [hep-ph].

[306] L. M. Carpenter, T. Han, K. Hendricks, Z. Qian, and N. Zhou, "Higgs Boson Decay to Light Jets at the LHC," *Phys. Rev. D* **95** no. 5, (2017) 053003, arXiv:1611.05463 [hep-ph].

[307] R. Contino, M. Ghezzi, C. Grojean, M. Muhlleitner, and M. Spira, "Effective Lagrangian for a light Higgs-like scalar," *JHEP* **07** (2013) 035, arXiv:1303.3876 [hep-ph].

[308] R. Harnik, J. Kopp, and J. Zupan, "Flavor Violating Higgs Decays," *JHEP* **03** (2013) 026, arXiv:1209.1397 [hep-ph].

[309] Y. Nir and N. Seiberg, "Should squarks be degenerate?," *Phys. Lett. B* **309** (1993) 337–343, arXiv:hep-ph/9304307.

[310] M. Leurer, Y. Nir, and N. Seiberg, "Mass matrix models: The Sequel," *Nucl. Phys. B* **420** (1994) 468–504, arXiv:hep-ph/9310320.

[311] G. C. Branco, W. Grimus, and L. Lavoura, "Relating the scalar flavor changing neutral couplings to the CKM matrix," *Phys. Lett.* **B380** (1996) 119–126, arXiv:hep-ph/9601383 [hep-ph].

[312] A. Peñuelas and A. Pich, "Flavour alignment in multi-Higgs-doublet models," *JHEP* **12** (2017) 084, arXiv:1710.02040 [hep-ph].

[313] A. Falkowski, F. Riva, and A. Urbano, "Higgs at last," *JHEP* **11** (2013) 111, arXiv:1303.1812 [hep-ph].

[314] M. Ciuchini, E. Franco, S. Mishima, and L. Silvestrini, "Electroweak Precision Observables, New Physics and the Nature of a 126 GeV Higgs Boson," *JHEP* **08** (2013) 106, arXiv:1306.4644 [hep-ph].

[315] A. Falkowski and F. Riva, "Model-independent precision constraints on dimension-6 operators," *JHEP* **02** (2015) 039, arXiv:1411.0669 [hep-ph].

[316] J. de Blas, M. Ciuchini, E. Franco, S. Mishima, M. Pierini, L. Reina, and L. Silvestrini, "Electroweak precision observables and Higgs-boson signal strengths in the Standard Model and beyond: present and future," *JHEP* **12** (2016) 135, arXiv:1608.01509 [hep-ph].

[317] J. de Blas, M. Ciuchini, E. Franco, S. Mishima, M. Pierini, L. Reina, and L. Silvestrini, "The Global Electroweak and Higgs Fits in the LHC era," *PoS* **EPS-HEP2017** (2017) 467, arXiv:1710.05402 [hep-ph].

[318] J. Haller, A. Hoecker, R. Kogler, K. Mönig, T. Peiffer, and J. Stelzer, "Update of the global electroweak fit and constraints on two-Higgs-doublet models," *Eur. Phys. J. C* **78** no. 8, (2018) 675, arXiv:1803.01853 [hep-ph].

[319] J. Ellis, C. W. Murphy, V. Sanz, and T. You, "Updated Global SMEFT Fit to Higgs, Diboson and Electroweak Data," *JHEP* **06** (2018) 146, arXiv:1803.03252 [hep-ph].

[320] J. Erler and M. Schott, "Electroweak Precision Tests of the Standard Model after the Discovery of the Higgs Boson," *Prog. Part. Nucl. Phys.* **106** (2019) 68–119, arXiv:1902.05142 [hep-ph].

[321] S. Dawson, S. Homiller, and S. D. Lane, "Putting SMEFT Fits to Work," arXiv:2007.01296 [hep-ph].

[322] B. Bhattacharya, A. Datta, D. London, and S. Shivashankara, "Simultaneous Explanation of the R_K and $R(D^{(*)})$ Puzzles," *Phys. Lett. B* **742** (2015) 370–374, arXiv:1412.7164 [hep-ph].

[323] F. Feruglio, P. Paradisi, and A. Pattori, "Revisiting Lepton Flavor Universality in B Decays," *Phys. Rev. Lett.* **118** no. 1, (2017) 011801, arXiv:1606.00524 [hep-ph].

[324] A. Celis, J. Fuentes-Martin, A. Vicente, and J. Virto, "Gauge-invariant implications of the LHCb measurements on lepton-flavor nonuniversality," *Phys. Rev. D* **96** no. 3, (2017) 035026, arXiv:1704.05672 [hep-ph].

[325] D. Buttazzo, A. Greljo, G. Isidori, and D. Marzocca, "B-physics anomalies: a guide to combined explanations," *JHEP* **11** (2017) 044, arXiv:1706.07808 [hep-ph].

[326] J. Kumar, D. London, and R. Watanabe, "Combined Explanations of the $b \to s\mu^+\mu^-$ and $b \to c\tau^-\overline{\nu}$ Anomalies: a General Model Analysis," *Phys. Rev.* **D99** no. 1, (2019) 015007, arXiv:1806.07403 [hep-ph].

[327] M. Ciuchini, A. M. Coutinho, M. Fedele, E. Franco, A. Paul, L. Silvestrini, and M. Valli, "New Physics in $b \to s\ell^+\ell^-$ confronts new data on Lepton Universality," *Eur. Phys. J.* **C79** no. 8, (2019) 719, arXiv:1903.09632 [hep-ph].

[328] J. Aebischer, W. Altmannshofer, D. Guadagnoli, M. Reboud, P. Stangl, and D. M. Straub, "B-decay discrepancies after Moriond 2019," *Eur. Phys. J.* **C80** no. 3, (2020) 252, arXiv:1903.10434 [hep-ph].

[329] C. Cornella, J. Fuentes-Martin, and G. Isidori, "Revisiting the vector leptoquark explanation of the B-physics anomalies," *JHEP* **07** (2019) 168, arXiv:1903.11517 [hep-ph].

[330] **LHCb** Collaboration, R. Aaij *et al.*, "Test of lepton universality using $B^+ \to K^+\ell^+\ell^-$ decays," *Phys. Rev. Lett.* **113** (2014) 151601, arXiv:1406.6482 [hep-ex].

[331] **LHCb** Collaboration, R. Aaij *et al.*, "Test of lepton universality with $B^0 \to K^{*0}\ell^+\ell^-$ decays," *JHEP* **08** (2017) 055, arXiv:1705.05802 [hep-ex].

[332] **LHCb** Collaboration, R. Aaij *et al.*, "Search for lepton-universality violation in $B^+ \to K^+\ell^+\ell^-$ decays," *Phys. Rev. Lett.* **122** no. 19, (2019) 191801, arXiv:1903.09252 [hep-ex].

[333] **Belle** Collaboration, A. Abdesselam *et al.*, "Test of lepton flavor universality in $B \to K^*\ell^+\ell^-$ decays at Belle," arXiv:1904.02440 [hep-ex].

[334] G. Hiller and M. Schmaltz, "R_K and future $b \to s\ell\ell$ physics beyond the standard model opportunities," *Phys. Rev.* **D90** (2014) 054014, arXiv:1408.1627 [hep-ph].

[335] G. Hiller and M. Schmaltz, "Diagnosing lepton-nonuniversality in $b \to s\ell\ell$," *JHEP* **02** (2015) 055, arXiv:1411.4773 [hep-ph].

[336] M. Bordone, G. Isidori, and A. Pattori, "On the Standard Model predictions for R_K and R_{K^*}," *Eur. Phys. J. C* **76** no. 8, (2016) 440, arXiv:1605.07633 [hep-ph].

[337] G. D'Amico, M. Nardecchia, P. Panci, F. Sannino, A. Strumia, R. Torre, and A. Urbano, "Flavour anomalies after the R_{K^*} measurement," *JHEP* **09** (2017) 010, arXiv:1704.05438 [hep-ph].

[338] L.-S. Geng, B. Grinstein, S. Jäger, J. Martin Camalich, X.-L. Ren, and R.-X. Shi, "Towards the discovery of new physics with lepton-universality ratios of $b \to s\ell\ell$ decays," *Phys. Rev. D* **96** no. 9, (2017) 093006, arXiv:1704.05446 [hep-ph].

[339] B. Capdevila, A. Crivellin, S. Descotes-Genon, J. Matias, and J. Virto, "Patterns of New Physics in $b \to s\ell^+\ell^-$ transitions in the light of recent data," *JHEP* **01** (2018) 093, arXiv:1704.05340 [hep-ph].

[340] M. Ciuchini, A. M. Coutinho, M. Fedele, E. Franco, A. Paul, L. Silvestrini, and M. Valli, "On Flavourful Easter eggs for New Physics hunger and Lepton Flavour Universality violation," *Eur. Phys. J.* **C77** no. 10, (2017) 688, arXiv:1704.05447 [hep-ph].

[341] G. Hiller and I. Nisandzic, "R_K and R_{K^*} beyond the standard model," *Phys. Rev. D* **96** no. 3, (2017) 035003, arXiv:1704.05444 [hep-ph].

[342] A. K. Alok, A. Dighe, S. Gangal, and D. Kumar, "Continuing search for new physics in $b \to s\mu\mu$ decays: two operators at a time," *JHEP* **06** (2019) 089, arXiv:1903.09617 [hep-ph].

[343] M. Algueró, B. Capdevila, A. Crivellin, S. Descotes-Genon, P. Masjuan, J. Matias, M. Novoa, and J. Virto, "Emerging patterns of New Physics with and without Lepton Flavour Universal contributions," *Eur. Phys. J. C* **79** no. 8, (2019) 714, arXiv:1903.09578 [hep-ph].

[344] K. Kowalska, D. Kumar, and E. M. Sessolo, "Implications for new physics in $b \to s\mu\mu$ transitions after recent measurements by Belle and LHCb," *Eur. Phys. J. C* **79** no. 10, (2019) 840, arXiv:1903.10932 [hep-ph].

[345] A. Arbey, T. Hurth, F. Mahmoudi, D. M. Santos, and S. Neshatpour, "Update on the b→s anomalies," *Phys. Rev. D* **100** no. 1, (2019) 015045, arXiv:1904.08399 [hep-ph].

[346] A. Datta, J. Kumar, and D. London, "The B anomalies and new physics in $b \to se^+e^-$," *Phys. Lett. B* **797** (2019) 134858, arXiv:1903.10086 [hep-ph].

[347] S. Descotes-Genon, J. Matias, and J. Virto, "Understanding the $B \to K^*\mu^+\mu^-$ Anomaly," *Phys. Rev.* **D88** (2013) 074002, arXiv:1307.5683 [hep-ph].

[348] S. Descotes-Genon, L. Hofer, J. Matias, and J. Virto, "Global analysis of $b \to s\ell\ell$ anomalies," *JHEP* **06** (2016) 092, arXiv:1510.04239 [hep-ph].

[349] **LHCb** Collaboration, R. Aaij *et al.*, "Measurement of *CP*-averaged observables in the $B^0 \to K^{*0}\mu^+\mu^-$ decay," arXiv:2003.04831 [hep-ex].

[350] A. Khodjamirian, T. Mannel, A. A. Pivovarov, and Y. M. Wang, "Charm-loop effect in $B \to K^{(*)}\ell^+\ell^-$ and $B \to K^*\gamma$," *JHEP* **09** (2010) 089, arXiv:1006.4945 [hep-ph].

[351] J. Lyon and R. Zwicky, "Resonances gone topsy turvy - the charm of QCD or new physics in $b \to s\ell^+\ell^-$?," arXiv:1406.0566 [hep-ph].

[352] V. Chobanova, T. Hurth, F. Mahmoudi, D. Martinez Santos, and S. Neshatpour, "Large hadronic power corrections or new physics in the rare decay $B \to K^*\mu^+\mu^-$," *JHEP* **07** (2017) 025, arXiv:1702.02234 [hep-ph].

[353] T. Blake, U. Egede, P. Owen, K. A. Petridis, and G. Pomery, "An empirical model to determine the hadronic resonance contributions to $\overline{B}^0 \to \overline{K}^{*0}\mu^+\mu^-$ transitions," *Eur. Phys. J. C* **78** no. 6, (2018) 453, arXiv:1709.03921 [hep-ph].

[354] C. Bobeth, M. Chrzaszcz, D. van Dyk, and J. Virto, "Long-distance effects in $B \to K^* \ell\ell$ from analyticity," *Eur. Phys. J. C* **78** no. 6, (2018) 451, arXiv:1707.07305 [hep-ph].

[355] S. Jäger and J. Martin Camalich, "Reassessing the discovery potential of the $B \to K^* \ell^+ \ell^-$ decays in the large-recoil region: SM challenges and BSM opportunities," *Phys. Rev. D* **93** no. 1, (2016) 014028, arXiv:1412.3183 [hep-ph].

[356] M. Ciuchini, M. Fedele, E. Franco, S. Mishima, A. Paul, L. Silvestrini, and M. Valli, "$B \to K^* \ell^+ \ell^-$ decays at large recoil in the Standard Model: a theoretical reappraisal," *JHEP* **06** (2016) 116, arXiv:1512.07157 [hep-ph].

[357] A. Arbey, T. Hurth, F. Mahmoudi, and S. Neshatpour, "Hadronic and New Physics Contributions to $b \to s$ Transitions," *Phys. Rev. D* **98** no. 9, (2018) 095027, arXiv:1806.02791 [hep-ph].

[358] M. Chrzaszcz, A. Mauri, N. Serra, R. Silva Coutinho, and D. van Dyk, "Prospects for disentangling long- and short-distance effects in the decays $B \to K^* \mu^+ \mu^-$," *JHEP* **10** (2019) 236, arXiv:1805.06378 [hep-ph].

[359] M. Ciuchini, A. M. Coutinho, M. Fedele, E. Franco, A. Paul, L. Silvestrini, and M. Valli, "Hadronic uncertainties in semileptonic $B \to K^* \mu^+ \mu^-$ decays," *PoS* **BEAUTY2018** (2018) 044, arXiv:1809.03789 [hep-ph].

[360] T. Hurth, F. Mahmoudi, and S. Neshatpour, "On the new LHCb angular analysis of $B \to K^* \mu^+ \mu^-$: Hadronic effects or New Physics?," arXiv:2006.04213 [hep-ph].

[361] B. Capdevila, S. Descotes-Genon, J. Matias, and J. Virto, "Assessing lepton-flavour non-universality from $B \to K^* \ell\ell$ angular analyses," *JHEP* **10** (2016) 075, arXiv:1605.03156 [hep-ph].

[362] N. Serra, R. Silva Coutinho, and D. van Dyk, "Measuring the breaking of lepton flavor universality in $B \to K^* \ell^+ \ell^-$," *Phys. Rev. D* **95** no. 3, (2017) 035029, arXiv:1610.08761 [hep-ph].

[363] **Belle** Collaboration, S. Wehle *et al.*, "Lepton-Flavor-Dependent Angular Analysis of $B \to K^* \ell^+ \ell^-$," *Phys. Rev. Lett.* **118** no. 11, (2017) 111801, arXiv:1612.05014 [hep-ex].

[364] M. Algueró, B. Capdevila, S. Descotes-Genon, P. Masjuan, and J. Matias, "What R_K and Q_5 can tell us about New Physics in $b \to s\ell\ell$ transitions?," *JHEP* **07** (2019) 096, arXiv:1902.04900 [hep-ph].

[365] **Belle-II** Collaboration, W. Altmannshofer *et al.*, "The Belle II Physics Book," *PTEP* **2019** no. 12, (2019) 123C01, arXiv:1808.10567 [hep-ex]. [Erratum: PTEP 2020, 029201 (2020)].

[366] **LHCb** Collaboration, R. Aaij *et al.*, "Search for the rare decays $B_s^0 \to e^+e^-$ and $B^0 \to e^+e^-$," *Phys. Rev. Lett.* **124** no. 21, (2020) 211802, arXiv:2003.03999 [hep-ex].

[367] **CMS** Collaboration, S. Chatrchyan *et al.*, "Measurement of the $B_s^0 \to \mu^+\mu^-$ Branching Fraction and Search for $B^0 \to \mu^+\mu^-$ with the CMS Experiment," *Phys. Rev. Lett.* **111** (2013) 101804, arXiv:1307.5025 [hep-ex].

[368] **LHCb** Collaboration, R. Aaij *et al.*, "Measurement of the $B_s^0 \to \mu^+\mu^-$ branching fraction and effective lifetime and search for $B^0 \to \mu^+\mu^-$ decays," *Phys. Rev. Lett.* **118** no. 19, (2017) 191801, arXiv:1703.05747 [hep-ex].

[369] **ATLAS** Collaboration, M. Aaboud *et al.*, "Study of the rare decays of B_s^0 and B^0 mesons into muon pairs using data collected during 2015 and 2016 with the ATLAS detector," *JHEP* **04** (2019) 098, arXiv:1812.03017 [hep-ex].

[370] C. Bobeth, M. Gorbahn, T. Hermann, M. Misiak, E. Stamou, and M. Steinhauser, "$B_{s,d} \to l^+l^-$ in the Standard Model with Reduced Theoretical Uncertainty," *Phys. Rev. Lett.* **112** (2014) 101801, arXiv:1311.0903 [hep-ph].

[371] A. Azatov, D. Bardhan, D. Ghosh, F. Sgarlata, and E. Venturini, "Anatomy of $b \to c\tau\nu$ anomalies," *JHEP* **11** (2018) 187, arXiv:1805.03209 [hep-ph].

[372] A. K. Alok, D. Kumar, S. Kumbhakar, and S. Uma Sankar, "Solutions to R_D-R_{D^*} in light of Belle 2019 data," *Nucl. Phys. B* **953** (2020) 114957, arXiv:1903.10486 [hep-ph].

[373] C. Murgui, A. Peñuelas, M. Jung, and A. Pich, "Global fit to $b \to c\tau\nu$ transitions," *JHEP* **09** (2019) 103, arXiv:1904.09311 [hep-ph].

[374] R.-X. Shi, L.-S. Geng, B. Grinstein, S. Jäger, and J. Martin Camalich, "Revisiting the new-physics interpretation of the $b \to c\tau\nu$ data," *JHEP* **12** (2019) 065, arXiv:1905.08498 [hep-ph].

[375] **BaBar** Collaboration, J. Lees *et al.*, "Measurement of an Excess of $\overline{B} \to D^{(*)}\tau^-\overline{\nu}_\tau$ Decays and Implications for Charged Higgs Bosons," *Phys. Rev. D* **88** no. 7, (2013) 072012, arXiv:1303.0571 [hep-ex].

[376] **Belle** Collaboration, M. Huschle *et al.*, "Measurement of the branching ratio of $\overline{B} \to D^{(*)}\tau^-\overline{\nu}_\tau$ relative to $\overline{B} \to D^{(*)}\ell^-\overline{\nu}_\ell$ decays with hadronic tagging at Belle," *Phys. Rev. D* **92** no. 7, (2015) 072014, arXiv:1507.03233 [hep-ex].

[377] **LHCb** Collaboration, R. Aaij *et al.*, "Measurement of the ratio of the $B^0 \to D^{*-}\tau^+\nu_\tau$ and $B^0 \to D^{*-}\mu^+\nu_\mu$ branching fractions using three-prong τ-lepton decays," *Phys. Rev. Lett.* **120** no. 17, (2018) 171802, arXiv:1708.08856 [hep-ex].

[378] L. Di Luzio, A. Greljo, and M. Nardecchia, "Gauge leptoquark as the origin of B-physics anomalies," *Phys. Rev. D* **96** no. 11, (2017) 115011, arXiv:1708.08450 [hep-ph].

[379] L. Calibbi, A. Crivellin, and T. Li, "Model of vector leptoquarks in view of the B-physics anomalies," *Phys. Rev. D* **98** no. 11, (2018) 115002, arXiv:1709.00692 [hep-ph].

[380] M. Bordone, C. Cornella, J. Fuentes-Martin, and G. Isidori, "A three-site gauge model for flavor hierarchies and flavor anomalies," *Phys. Lett. B* **779** (2018) 317–323, arXiv:1712.01368 [hep-ph].

[381] R. Barbieri and A. Tesi, "B-decay anomalies in Pati-Salam SU(4)," *Eur. Phys. J. C* **78** no. 3, (2018) 193, arXiv:1712.06844 [hep-ph].

[382] N. Assad, B. Fornal, and B. Grinstein, "Baryon Number and Lepton Universality Violation in Leptoquark and Diquark Models," *Phys. Lett. B* **777** (2018) 324–331, arXiv:1708.06350 [hep-ph].

[383] J. Heeck and D. Teresi, "Pati-Salam explanations of the B-meson anomalies," *JHEP* **12** (2018) 103, arXiv:1808.07492 [hep-ph].

[384] B. Fornal, S. A. Gadam, and B. Grinstein, "Left-Right SU(4) Vector Leptoquark Model for Flavor Anomalies," *Phys. Rev. D* **99** no. 5, (2019) 055025, arXiv:1812.01603 [hep-ph].

[385] A. Crivellin, C. Greub, D. Müller, and F. Saturnino, "Importance of Loop Effects in Explaining the Accumulated Evidence for New Physics in B Decays with a Vector Leptoquark," *Phys. Rev. Lett.* **122** no. 1, (2019) 011805, arXiv:1807.02068 [hep-ph].

[386] A. Crivellin, D. Müller, and F. Saturnino, "Flavor Phenomenology of the Leptoquark Singlet-Triplet Model," *JHEP* **06** (2020) 020, arXiv:1912.04224 [hep-ph].

[387] M. Bordone, O. Catà, and T. Feldmann, "Effective Theory Approach to New Physics with Flavour: General Framework and a Leptoquark Example," *JHEP* **01** (2020) 067, arXiv:1910.02641 [hep-ph].

[388] **UTfit** Collaboration, M. Bona *et al.*, "Model-independent constraints on $\Delta F = 2$ operators and the scale of new physics," *JHEP* **03** (2008) 049, arXiv:0707.0636 [hep-ph].

[389] L. Silvestrini and M. Valli, "Model-independent Bounds on the Standard Model Effective Theory from Flavour Physics," *Phys. Lett. B* **799** (2019) 135062, arXiv:1812.10913 [hep-ph].

[390] A. Greljo and D. Marzocca, "High-p_T dilepton tails and flavor physics," *Eur. Phys. J.* **C77** no. 8, (2017) 548, arXiv:1704.09015 [hep-ph].

[391] M. J. Baker, J. Fuentes-Martín, G. Isidori, and M. König, "High- p_T signatures in vector–leptoquark models," *Eur. Phys. J.* **C79** no. 4, (2019) 334, arXiv:1901.10480 [hep-ph].

[392] L. Calibbi, A. Crivellin, and T. Ota, "Effective Field Theory Approach to $b \to s\ell\ell^{(')}$, $B \to K^{(*)}\nu\overline{\nu}$ and $B \to D^{(*)}\tau\nu$ with Third Generation Couplings," *Phys. Rev. Lett.* **115** (2015) 181801, arXiv:1506.02661 [hep-ph].

[393] I. Doršner, S. Fajfer, A. Greljo, J. Kamenik, and N. Košnik, "Physics of leptoquarks in precision experiments and at particle colliders," *Phys. Rept.* **641** (2016) 1–68, arXiv:1603.04993 [hep-ph].

[394] **Belle** Collaboration, S. Hirose *et al.*, "Measurement of the τ lepton polarization and $R(D^*)$ in the decay $\overline{B} \to D^*\tau^-\overline{\nu}_\tau$," *Phys. Rev. Lett.* **118** no. 21, (2017) 211801, arXiv:1612.00529 [hep-ex].

[395] **Belle** Collaboration, A. Abdesselam *et al.*, "Measurement of $\mathcal{R}(D)$ and $\mathcal{R}(D^*)$ with a semileptonic tagging method," arXiv:1904.08794 [hep-ex].

[396] D. Bigi and P. Gambino, "Revisiting $B \to D\ell\nu$," *Phys. Rev. D* **94** no. 9, (2016) 094008, arXiv:1606.08030 [hep-ph].

[397] F. U. Bernlochner, Z. Ligeti, M. Papucci, and D. J. Robinson, "Combined analysis of semileptonic B decays to D and D^*: $R(D^{(*)})$, $|V_{cb}|$, and new physics," *Phys. Rev. D* **95** no. 11, (2017) 115008, arXiv:1703.05330 [hep-ph]. [Erratum: Phys.Rev.D 97, 059902 (2018)].

[398] D. Bigi, P. Gambino, and S. Schacht, "$R(D^*)$, $|V_{cb}|$, and the Heavy Quark Symmetry relations between form factors," *JHEP* **11** (2017) 061, arXiv:1707.09509 [hep-ph].

[399] S. Jaiswal, S. Nandi, and S. K. Patra, "Extraction of $|V_{cb}|$ from $B \to D^{(*)}\ell\nu_\ell$ and the Standard Model predictions of $R(D^{(*)})$," *JHEP* **12** (2017) 060, arXiv:1707.09977 [hep-ph].

[400] J. F. Kamenik, Y. Soreq, and J. Zupan, "Lepton flavor universality violation without new sources of quark flavor violation," *Phys. Rev.* **D97** no. 3, (2018) 035002, arXiv:1704.06005 [hep-ph].

[401] P. J. Fox, I. Low, and Y. Zhang, "Top-philic Z' forces at the LHC," *JHEP* **03** (2018) 074, arXiv:1801.03505 [hep-ph].

[402] J. E. Camargo-Molina, A. Celis, and D. A. Faroughy, "Anomalies in Bottom from new physics in Top," *Phys. Lett.* **B784** (2018) 284–293, arXiv:1805.04917 [hep-ph].

[403] L. Di Luzio and M. Nardecchia, "What is the scale of new physics behind the B-flavour anomalies?," *Eur. Phys. J. C* **77** no. 8, (2017) 536, arXiv:1706.01868 [hep-ph].

[404] A. Buras, P. Gambino, M. Gorbahn, S. Jager, and L. Silvestrini, "Universal unitarity triangle and physics beyond the standard model," *Phys. Lett. B* **500** (2001) 161–167, arXiv:hep-ph/0007085.

[405] A. L. Kagan, G. Perez, T. Volansky, and J. Zupan, "General Minimal Flavor Violation," *Phys. Rev. D* **80** (2009) 076002, arXiv:0903.1794 [hep-ph].

[406] A. Efrati, A. Falkowski, and Y. Soreq, "Electroweak constraints on flavorful effective theories," *JHEP* **07** (2015) 018, arXiv:1503.07872 [hep-ph].

[407] R. Coy, M. Frigerio, F. Mescia, and O. Sumensari, "New physics in $b \to s\ell\ell$ transitions at one loop," *Eur. Phys. J. C* **80** no. 1, (2020) 52, arXiv:1909.08567 [hep-ph].

[408] M. Ciuchini, M. Fedele, E. Franco, S. Mishima, A. Paul, L. Silvestrini, and M. Valli, "$B \to K^*\ell^+\ell^-$ in the Standard Model: Elaborations and Interpretations," *PoS* **ICHEP2016** (2016) 584, arXiv:1611.04338 [hep-ph].

[409] M. Ciuchini, M. Fedele, E. Franco, S. Mishima, A. Paul, L. Silvestrini, and M. Valli, "Knowns and Unknowns in the Predictions for $B \to K^*\mu^+\mu^-$," *Nucl. Part. Phys. Proc.* **285-286** (2017) 45–49.

[410] M. Ciuchini, A. M. Coutinho, M. Fedele, E. Franco, A. Paul, L. Silvestrini, and M. Valli, "On hadronic uncertainties polluting the New Physics hunt in $b \to s$ transitions," *Nucl. Part. Phys. Proc.* **303-305** (2018) 8–13.

[411] W. Buchmuller and D. Wyler, "Effective Lagrangian Analysis of New Interactions and Flavor Conservation," *Nucl. Phys. B* **268** (1986) 621–653.

[412] W. Altmannshofer, A. J. Buras, D. M. Straub, and M. Wick, "New strategies for New Physics search in $B \to K^* \nu\overline{\nu}$, $B \to K \nu\overline{\nu}$ and $B \to X_s \nu\overline{\nu}$ decays," *JHEP* **04** (2009) 022, arXiv:0902.0160 [hep-ph].

[413] A. J. Buras, J. Girrbach-Noe, C. Niehoff, and D. M. Straub, "$B \to K^{(*)} \nu\overline{\nu}$ decays in the Standard Model and beyond," *JHEP* **02** (2015) 184, arXiv:1409.4557 [hep-ph].

[414] S. Descotes-Genon, S. Fajfer, J. F. Kamenik, and M. Novoa-Brunet, "Implications of $b \to s\mu\mu$ Anomalies for Future Measurements of $B \to K^{(*)} \nu\overline{\nu}$ and $K \to \pi\nu\overline{\nu}$," arXiv:2005.03734 [hep-ph].

[415] J. Aebischer, A. Crivellin, M. Fael, and C. Greub, "Matching of gauge invariant dimension-six operators for $b \to s$ and $b \to c$ transitions," *JHEP* **05** (2016) 037, arXiv:1512.02830 [hep-ph].

[416] C. Bobeth, A. J. Buras, A. Celis, and M. Jung, "Yukawa enhancement of Z-mediated new physics in $\Delta S = 2$ and $\Delta B = 2$ processes," *JHEP* **07** (2017) 124, arXiv:1703.04753 [hep-ph].

[417] G. Buchalla, A. J. Buras, and M. E. Lautenbacher, "Weak decays beyond leading logarithms," *Rev. Mod. Phys.* **68** (1996) 1125–1144, arXiv:hep-ph/9512380.

[418] A. J. Buras, "Weak Hamiltonian, CP violation and rare decays," in *Les Houches Summer School in Theoretical Physics, Session 68: Probing the Standard Model of Particle Interactions*, pp. 281–539. 6, 1998. arXiv:hep-ph/9806471.

[419] L. Silvestrini, "Effective Theories for Quark Flavour Physics," in *Les Houches summer school: EFT in Particle Physics and Cosmology*. 5, 2019. arXiv:1905.00798 [hep-ph].

[420] J. de Blas, G. Durieux, C. Grojean, J. Gu, and A. Paul, "On the future of Higgs, electroweak and diboson measurements at lepton colliders," *JHEP* **12** (2019) 117, arXiv:1907.04311 [hep-ph].

[421] B. Capdevila, A. Crivellin, C. A. Manzari, and M. Montull, "Explaining $b \to s\ell^+\ell^-$ and the Cabbibo Angle Anomaly with a Vector Triplet," arXiv:2005.13542 [hep-ph].

[422] B. Belfatto, R. Beradze, and Z. Berezhiani, "The CKM unitarity problem: A trace of new physics at the TeV scale?," *Eur. Phys. J. C* **80** no. 2, (2020) 149, arXiv:1906.02714 [hep-ph].

[423] Y. Grossman, E. Passemar, and S. Schacht, "On the Statistical Treatment of the Cabibbo Angle Anomaly," arXiv:1911.07821 [hep-ph].

[424] J. de Blas *et al.*, "HEPfit: a Code for the Combination of Indirect and Direct Constraints on High Energy Physics Models," *Eur. Phys. J. C* **80** no. 5, (2020) 456, arXiv:1910.14012 [hep-ph].

[425] A. Caldwell, D. Kollár, and K. Kröninger, "BAT - The Bayesian analysis toolkit," *Computer Physics Communications* **180** no. 11, (Nov., 2009) 2197–2209, arXiv:0808.2552 [physics.data-an].

[426] **SLD** Collaboration, K. Abe *et al.*, "First direct measurement of the parity violating coupling of the Z0 to the s quark," *Phys. Rev. Lett.* **85** (2000) 5059–5063, arXiv:hep-ex/0006019 [hep-ex].

[427] **ALEPH, DELPHI, L3, OPAL, LEP Electroweak** Collaboration, S. Schael *et al.*, "Electroweak Measurements in Electron-Positron Collisions at W-Boson-Pair Energies at LEP," *Phys. Rept.* **532** (2013) 119–244, arXiv:1302.3415 [hep-ex].

[428] **ATLAS** Collaboration, M. Aaboud *et al.*, "Measurement of the W-boson mass in pp collisions at $\sqrt{s} = 7$ TeV with the ATLAS detector," *Eur. Phys. J. C* **78** no. 2, (2018) 110, arXiv:1701.07240 [hep-ex]. [Erratum: Eur.Phys.J.C 78, 898 (2018)].

[429] **CMS** Collaboration, V. Khachatryan *et al.*, "Measurement of the t-channel single-top-quark production cross section and of the $| V_{tb} |$ CKM matrix element in pp collisions at $\sqrt{s}$= 8 TeV," *JHEP* **06** (2014) 090, arXiv:1403.7366 [hep-ex].

[430] **D0** Collaboration, V. Abazov *et al.*, "Measurement of $\sin^2\theta^{\ell}_{\text{eff}}$ and Z-light quark couplings using the forward-backward charge asymmetry in $p\overline{p} \to Z/\gamma^* \to e^+e^-$ events with $\mathcal{L} = 5.0$ fb^{-1} at $\sqrt{s} = 1.96$ TeV," *Phys. Rev. D* **84** (2011) 012007, arXiv:1104.4590 [hep-ex].

[431] **ATLAS** Collaboration, M. Aaboud *et al.*, "Angular analysis of $B^0_d \to K^*\mu^+\mu^-$ decays in pp collisions at $\sqrt{s} = 8$ TeV with the ATLAS detector," *JHEP* **10** (2018) 047, arXiv:1805.04000 [hep-ex].

[432] **CMS** Collaboration, V. Khachatryan *et al.*, "Angular analysis of the decay $B^0 \to K^{*0}\mu^+\mu^-$ from pp collisions at $\sqrt{s} = 8$ TeV," *Phys. Lett.* **B753** (2016) 424–448, arXiv:1507.08126 [hep-ex].

[433] **CMS** Collaboration, A. M. Sirunyan *et al.*, "Measurement of angular parameters from the decay $\mathrm{B}^0 \to \mathrm{K}^{*0}\mu^+\mu^-$ in proton-proton collisions at $\sqrt{s} = 8$ TeV," *Phys. Lett.* **B781** (2018) 517–541, arXiv:1710.02846 [hep-ex].

[434] **LHCb** Collaboration, R. Aaij *et al.*, "Angular analysis of the $B^0 \to K^{*0}e^+e^-$ decay in the low-q^2 region," *JHEP* **04** (2015) 064, arXiv:1501.03038 [hep-ex].

[435] **LHCb** Collaboration, R. Aaij *et al.*, "Measurements of the S-wave fraction in $B^0 \to K^+\pi^-\mu^+\mu^-$ decays and the $B^0 \to K^*(892)^0\mu^+\mu^-$ differential branching fraction," *JHEP* **11** (2016) 047, arXiv:1606.04731 [hep-ex]. [Erratum: JHEP04,142(2017)].

[436] A. Paul and D. M. Straub, "Constraints on new physics from radiative B decays," *JHEP* **04** (2017) 027, arXiv:1608.02556 [hep-ph].

[437] **HFLAV** Collaboration, Y. S. Amhis *et al.*, "Averages of b-hadron, c-hadron, and τ-lepton properties as of 2018," arXiv:1909.12524 [hep-ex].

[438] **LHCb** Collaboration, R. Aaij *et al.*, "Differential branching fractions and isospin asymmetries of $B \to K^{(*)}\mu^+\mu^-$ decays," *JHEP* **06** (2014) 133, arXiv:1403.8044 [hep-ex].

[439] **LHCb** Collaboration, R. Aaij *et al.*, "Angular analysis and differential branching fraction of the decay $B_s^0 \to \phi\mu^+\mu^-$," *JHEP* **09** (2015) 179, arXiv:1506.08777 [hep-ex].

[440] **LHCb** Collaboration, R. Aaij *et al.*, "Measurement of the ratio of branching fractions $BR(B_0 \to K^{\star 0}\gamma)/BR(B_{s0} \to \phi\gamma)$ and the direct CP asymmetry in $B_0 \to K^{\star 0}\gamma$," *Nucl. Phys.* **B867** (2013) 1–18, arXiv:1209.0313 [hep-ex].

[441] T. Hurth, F. Mahmoudi, and S. Neshatpour, "Global fits to $b \to s\ell\ell$ data and signs for lepton non-universality," *JHEP* **12** (2014) 053, arXiv:1410.4545 [hep-ph].

[442] **CCFR** Collaboration, S. Mishra *et al.*, "Neutrino tridents and W Z interference," *Phys. Rev. Lett.* **66** (1991) 3117–3120.

[443] **ATLAS** Collaboration, M. Aaboud *et al.*, "Search for new high-mass phenomena in the dilepton final state using 36 fb^{-1} of proton-proton collision data at $\sqrt{s} = 13$ TeV with the ATLAS detector," *JHEP* **10** (2017) 182, arXiv:1707.02424 [hep-ex].

[444] **CMS** Collaboration, A. M. Sirunyan *et al.*, "Search for standard model production of four top quarks with same-sign and multilepton final states in proton–proton collisions at $\sqrt{s} = 13\,\text{TeV}$," *Eur. Phys. J. C* **78** no. 2, (2018) 140, arXiv:1710.10614 [hep-ex].

[445] **ATLAS** Collaboration, M. Aaboud *et al.*, "Search for pair production of heavy vector-like quarks decaying into high-p_T gy bosons and top quarks in the

lepton-plus-jets final state in pp collisions at $\sqrt{s} = 13$ TeV with the ATLAS detector," *JHEP* **08** (2018) 048, arXiv:1806.01762 [hep-ex].

[446] **CMS** Collaboration, A. M. Sirunyan *et al.*, "Search for vector-like leptons in multilepton final states in proton-proton collisions at $\sqrt{s} = 13$ TeV," *Phys. Rev. D* **100** no. 5, (2019) 052003, arXiv:1905.10853 [hep-ex].

[447] S. D. Thomas and J. D. Wells, "Phenomenology of Massive Vectorlike Doublet Leptons," *Phys. Rev. Lett.* **81** (1998) 34–37, arXiv:hep-ph/9804359.

[448] F. del Aguila, J. de Blas, and M. Perez-Victoria, "Effects of new leptons in Electroweak Precision Data," *Phys. Rev. D* **78** (2008) 013010, arXiv:0803.4008 [hep-ph].

[449] K. Kannike, M. Raidal, D. M. Straub, and A. Strumia, "Anthropic solution to the magnetic muon anomaly: the charged see-saw," *JHEP* **02** (2012) 106, arXiv:1111.2551 [hep-ph]. [Erratum: JHEP10,136(2012)].

[450] N. Kumar and S. P. Martin, "Vectorlike Leptons at the Large Hadron Collider," *Phys. Rev. D* **92** no. 11, (2015) 115018, arXiv:1510.03456 [hep-ph].

[451] P. N. Bhattiprolu and S. P. Martin, "Prospects for vectorlike leptons at future proton-proton colliders," *Phys. Rev. D* **100** no. 1, (2019) 015033, arXiv:1905.00498 [hep-ph].

[452] J. C. Pati and A. Salam, "Lepton Number as the Fourth Color," *Phys. Rev. D* **10** (1974) 275–289. [Erratum: Phys.Rev.D 11, 703–703 (1975)].

[453] H. Georgi and S. L. Glashow, "Unity of all elementary-particle forces," *Phys. Rev. Lett.* **32** (Feb, 1974) 438–441. https://link.aps.org/doi/10.1103/PhysRevLett.32.438.

[454] D. Bečirević and O. Sumensari, "A leptoquark model to accommodate $R_K^{\rm exp} < R_K^{\rm SM}$ and $R_{K^*}^{\rm exp} < R_{K^*}^{\rm SM}$," *JHEP* **08** (2017) 104, arXiv:1704.05835 [hep-ph].

[455] W. Buchmuller, R. Ruckl, and D. Wyler, "Leptoquarks in Lepton - Quark Collisions," *Phys. Lett. B* **191** (1987) 442–448. [Erratum: Phys.Lett.B 448, 320–320 (1999)].

[456] F. del Aguila, J. de Blas, and M. Perez-Victoria, "Electroweak Limits on General New Vector Bosons," *JHEP* **09** (2010) 033, arXiv:1005.3998 [hep-ph].

[457] R. Alonso, B. Grinstein, and J. Martin Camalich, "Lepton universality violation and lepton flavor conservation in B-meson decays," *JHEP* **10** (2015) 184, arXiv:1505.05164 [hep-ph].

[458] A. Angelescu, D. Beˇ cirević, D. Faroughy, and O. Sumensari, "Closing the window on single leptoquark solutions to the B-physics anomalies," *JHEP* **10** (2018) 183, arXiv:1808.08179 [hep-ph].

[459] **LHCb** Collaboration, R. Aaij *et al.*, "Physics case for an LHCb Upgrade II - Opportunities in flavour physics, and beyond, in the HL-LHC era," arXiv:1808.08865 [hep-ex].

[460] **FCC** Collaboration, A. Abada *et al.*, "FCC Physics Opportunities: Future Circular Collider Conceptual Design Report Volume 1," *Eur. Phys. J. C* **79** no. 6, (2019) 474.

[461] **FCC** Collaboration, A. Abada *et al.*, "FCC-ee: The Lepton Collider: Future Circular Collider Conceptual Design Report Volume 2," *Eur. Phys. J. ST* **228** no. 2, (2019) 261–623.

[462] **LCC Physics Working Group** Collaboration, K. Fujii *et al.*, "Tests of the Standard Model at the International Linear Collider," arXiv:1908.11299 [hep-ex].

[463] Z. Han and W. Skiba, "Effective theory analysis of precision electroweak data," *Phys. Rev. D* **71** (2005) 075009, arXiv:hep-ph/0412166.

[464] F. del Aguila and J. de Blas, "Electroweak constraints on new physics," *Fortsch. Phys.* **59** (2011) 1036–1040, arXiv:1105.6103 [hep-ph].

[465] J. de Blas, "Electroweak limits on physics beyond the Standard Model," *EPJ Web Conf.* **60** (2013) 19008, arXiv:1307.6173 [hep-ph].

[466] L. Berthier and M. Trott, "Towards consistent Electroweak Precision Data constraints in the SMEFT," *JHEP* **05** (2015) 024, arXiv:1502.02570 [hep-ph].

[467] J. de Blas, M. Ciuchini, E. Franco, S. Mishima, M. Pierini, L. Reina, and L. Silvestrini, "Electroweak precision constraints at present and future colliders," *PoS* **ICHEP2016** (2017) 690, arXiv:1611.05354 [hep-ph].

[468] S. Dawson and P. P. Giardino, "Electroweak and QCD corrections to Z and W pole observables in the standard model EFT," *Phys. Rev. D* **101** no. 1, (2020) 013001, arXiv:1909.02000 [hep-ph].